INVESTIGATION ON MAGNETO-STRUCTURAL TRANSITION AND CALORIC EFFECTS IN Ni-Mn-Sn-BASED MAGNETIC ALLOYS

MA SIYAO

PhD

The Hong Kong Polytechnic University

This programme is jointly offered by The Hong Kong Polytechnic University and Harbin Institute of Technology

2026

The Hong Kong Polytechnic University

Department of Mechanical Engineering

Harbin Institute of Technology

School of Materials Science and Engineering

Investigation on Magneto-structural Transition and Caloric Effects in Ni-Mn-Sn-based Magnetic Alloys

Ma Siyao

A thesis submitted in partial fulfilment of the requirements for the degree of Doctor of Philosophy

November 2025

CERTIFICATE OF ORIGINALITY

I hereby declare that this thesis is my own work and that, to the best of my knowledge and belief, it reproduces no material previously published or written, nor material that has been accepted for the award of any other degree or diploma, except where due acknowledgement has been made in the text.

(Signed)

MA Siyao (Name of student)

Abstract

Ni-Mn-Sn-based magnetic alloys, which exhibit both magnetocaloric and elastocaloric effects, hold significant application potential in solid-state refrigeration. However, their intrinsic brittleness leads to structural fatigue issues. This study focuses on Ni-Mn-Sn magnetic alloys, employing first-principles calculations to investigate the effects of Fe and Cu doping on the crystal structure, magneto-structural phase transitions, and magnetic properties of Ni-Mn-Sn alloys, as well as the influence of B doping on their mechanical properties. Building on the computational results, the research systematically explores the magneto-structural phase transitions, magnetocaloric and elastocaloric effects, their stability, and the multi-field regulation and optimization of caloric effects in Fe-, Cu-, and B-doped Ni-Mn-Sn-based magnetic alloys. The study reveals the mechanism by which reversible components during martensitic phase transitions influence caloric effects, providing a theoretical foundation for the development of low-cost, high-performance Ni-Mn-Sn alloy refrigeration materials.

First-principles calculations reveal that Fe atoms preferentially occupy Ni sublattice sites in the $Ni_{43.75}Mn_{37.5}Sn_{12.5}Fe_{6.25}$ alloy. The energy difference between the austenite and non-modulated martensite phases gradually decreases with Fe doping, resulting in a decrease in the martensitic transformations temperature. Phase transitions become difficult when the Fe doping exceeds 6 at.%. Fe doping also enhances alloy stability and magnetic properties. In $Ni_{43.75}Mn_{37.5}Sn_{12.5}Cu_{6.25}$ and $Ni_{37.5}Mn_{37.5}Sn_{12.5}Cu_{12.5}$ alloys, Cu atoms preferentially occupy Ni lattice sites. The Curie temperature of $Ni_{43.75}Mn_{37.5}Sn_{12.5}Cu_{6.25}$ alloy decreases with increasing Cu content. Cu doping also gradually lowers the martensitic transformations

temperature, although its effect on enhancing the alloy's magnetic moment is slightly lower than that of Fe.

Research on $Ni_{50-y}Mn_{38}Sn_{12}Fe_y$ (y=0, 1, 2, 3, 4, 5) alloys shows that there are no second phase precipitates when the Fe doping level is low, and the microstructure at room temperature consists of 10M martensite. In alloys with Fe doping reaching 3 at.%, there exists an extremely small amount of the second phase precipitates. Fe doping enables the magnetic-structural coupling regulation of the alloy. The $Ni_{47}Mn_{38}Sn_{12}Fe_3$ alloy undergoes two-step reverse martensitic transformations: 10M→$L2_1$ and 10M→4O, followed by 4O→$L2_1$. These two-step transformations lead to two entropy change (ΔS_m) peaks of 15.2 J/kg·K and 9 J/kg·K at 259 K and 267 K, respectively, with a working temperature range of 255–268 K and a refrigeration capacity (*RC*) of 142.5 J/kg.

Studies on $Ni_{50-x}Mn_{38}Sn_{12}Cu_x$ (x=0, 2, 3, 4, 5, 6) alloys indicate that Cu doping significantly improves the mechanical properties of the alloys through solid solution strengthening, with both compressive strength and strain increased by more than 1.8 times. Cu doping also enhances the cyclic stability of the alloys. During rapid adiabatic loading-unloading cycles, the elastocaloric effect remains stable after about 30 cycles for the 3 at.% Cu-doped alloy. The $Ni_{48}Mn_{38}Sn_{12}Cu_2$ alloy achieves partial magneto-structural coupling, with ΔS_m reaching 10.3 J/kg·K under a 5 T magnetic field. The $Ni_{47}Mn_{38}Sn_{12}Cu_3$ alloy achieves complete magneto-structural coupling, with ΔS_m reaching 21.2 J/kg·K under 5 T, an average hysteresis loss of only 45 J/kg, and a relative cooling power of 108 J/kg.

Modulated Differential Scanning Calorimetry (MDSC), which superimposes a small sinusoidal temperature variation on a constant heating rate, allows for the separation of reversible and nonreversible components during martensitic

transformations, establishing a direct link between thermal hysteresis and frictional dissipation during the transition. Additionally, an accurate method for characterizing adiabatic temperature changes based on MDSC is developed. Calculations reveal that when Cu doping is x=3, the alloy exhibits a high reversible latent heat, low frictional dissipation, and a high ΔT_{ad}, closely approaching the directly measured ΔT_{ad} result of 10.3 K.

Research shows that B doping in $(Ni_{47}Mn_{38}Sn_{12}Cu_3)_{100-z}B_z$ (z=0, 0.2, 0.4, 0.6) alloys gradually refines the grains and leads to the precipitation of a small amount of second phases. When the B doping level increases to 0.6 at.%, the martensitic transformation temperature decreases by approximately 1 K. The B element effectively inhibits alloy fracture along grain boundaries, with the strengthening mechanism mainly originating from grain refinement and grain boundary strengthening due to microalloying. The $(Ni_{47}Mn_{38}Sn_{12}Cu_3)_{99.4}B_{0.6}$ alloy exhibits excellent cyclic stability during 500 heating-cooling cycles, 10^5 magnetic cycles, and 200 rapid adiabatic loading-unloading cycles.

Research demonstrates that stress assistance can broaden the working temperature range for caloric effects. The $(Ni_{47}Mn_{38}Sn_{12}Cu_3)_{99.4}B_{0.6}$ alloy achieves a large and reversible caloric effect within the temperature range of 260−336 K. With hydrostatic pressure coupling, the magnetic entropy change of the alloy remains constant, while the working temperature window for refrigeration expands. At H=3 T and 10 kbar, the RC value reaches 100.2 J/kg, representing a 20.8% increase in refrigeration capacity compared to 0 kbar.

The optimal preparation parameters for $(Ni_{47}Mn_{38}Sn_{12}Cu_3)_{99.4}B_{0.6}$ ribbons are a heating power of 8 kW and a copper roller speed of 1800 rpm. The as-spun ribbons have an average thickness of 20 μm. After heat treatment, the ribbons can

reach saturation in a low magnetic field (0.02 T) parallel to the grain growth direction. Under a 2 T magnetic field, ΔS_m reaches 7.6 J/kg·K, and the maximum ΔS_m value is 15.2 J/kg·K under a 5 T magnetic field. The ribbons achieve *RC* values of 143 J/kg and 119 J/kg for parallel and perpendicular magnetic fields, respectively, and corresponding *RCP* values of 187 J/kg and 156 J/kg.

Keywords: Ni-Mn-Sn-based Alloys; Martensitic Transformation; Caloric Effects; First-Principles Calculations; Element Doping

List of publications

[1] S. Ma, X. Zhang, G. Zheng, M. Qian, L. Geng. Toughening of Ni‐Mn‐Based Polycrystalline Ferromagnetic Shape Memory Alloys, Materials. (2023) 16, 5725.

[2] S. Ma, X. Zhang, G. Zheng, M. Qian, L. Geng. Cu- and Fe-Doped Ni-Mn-Sn Shape Memory Alloys with Enhanced Mechanical and Magnetocaloric Properties, Materials. (2024) 17, 3172.

[3] S. Ma, X. Zhang, G. Zheng, M. Qian, L. Geng. A study on martensitic transformation behavior in shape memory alloys via a modulated differential scanning calorimetry technique, Applied Physics Letters. (2024) 125 (25): 252202

[4] S. Ma, G. Zheng, X. Zhang, M. Qian. Broad refrigeration temperature window associated with multicaloric effects in Ni-Mn-Sn-Cu-B alloys, Materials Science and Engineering B. (2025) 321, 118462

Acknowledgments

The completion of this doctoral dissertation marks the culmination of over a decade of academic pursuit. As I reflect on this journey, my heart is filled with profound gratitude for all the support and encouragement I have received.

First and foremost, I wish to express my deepest and most sincere appreciation to my supervisor, Professor Guangping Zheng. I am truly fortunate to have been under his guidance. His profound knowledge, rigorous scholarly standards, and innovative research thinking have been instrumental in shaping the direction of my PhD study. During times of research difficulty, his unique insights consistently provided clarity and direction. Throughout the process of thesis writing, he devoted immense effort, offering invaluable advice on everything from the overarching framework to the finest details. Furthermore, his diligence and dedication to scientific research serve as an inspiring model I will strive to emulate throughout my life. I consider it a great privilege to have been his student.

I also wish to acknowledge all the technicians in the Department of Mechanical Engineering for their help.

Finally, and most importantly, I must reserve my deepest gratitude for my family. To my parents, words cannot fully express my thankfulness for your unconditional love, unwavering belief, and endless patience throughout these years

Table of contents

Chapter 1 Introduction

1.1 Background, Research Objectives and Significance

Green development is the cornerstone of high-quality development. China is currently in a critical period of economic transformation and upgrading toward high-quality development and ecological civilization construction. Refrigeration energy consumption accounts for nearly 20% of the world's total energy use. However, the widely used vapor-compression refrigeration technology has an energy efficiency of less than 40%, and the hydrofluorocarbon (HFC) refrigerants employed contribute to ozone depletion and exacerbate the greenhouse effect. Against this backdrop, developing a refrigeration technology that is environmentally friendly, energy-efficient, and highly effective has become a crucial challenge to address[1]. Solid-state cooling technology offers advantages such as compact size and high energy conversion efficiency. Additionally, it is environmentally benign and energy-saving, holding great potential to replace conventional vapor-compression refrigeration systems. Over the past decade, this technology has undergone rapid development[2-5].

Solid-state cooling is based on the caloric effects generated by phase transitions in refrigerant materials. Depending on the nature of the external stimuli (e.g., applied fields), these caloric effects can be classified into the following categories: (1) Elastocaloric effect (eCE)[6, 7]: A caloric effect induced by applying or removing uniaxial stress. (2) Magnetocaloric effect (MCE)[8, 9]: A caloric effect induced by applying or removing a magnetic field. (3) Barocaloric effect (BCE)[10, 11]: A caloric effect induced by applying or removing hydrostatic pressure. (4) Electrocaloric effect (ECE)[12]: A caloric effect induced by applying or removing

an electric field. Among the emerging solid-state cooling technologies, magnetic refrigeration (based on MCE) and elastocaloric cooling (based on eCE) are considered the two most promising approaches. Given that refrigerant materials play a pivotal role in enhancing the energy conversion efficiency and heat transfer of solid-state cooling devices, the development of high-performance solid-state refrigerants is crucial for advancing the practical application of this technology[13-16].

Significant magnetocaloric effects have been observed in alloy systems exhibiting magneto-structural phase transitions, such as La-Fe-Si[17, 18], Gd-Si-Ge[19], Fe-Rh[20], and Ni-Mn-based alloys[21, 13, 22, 23]. However, rare-earth metals like La and Rh are costly and challenging for room-temperature refrigeration applications. In contrast, Ni-Mn-based alloys (Ni-Mn-X, X=In, Sn, Sb, Ga) offer lower costs, and their martensitic transformation (MT) temperature can be adjusted near room temperature through doping, enabling practical room-temperature cooling.

The elastocaloric effect originates from stress-induced martensitic transformation (SIMT)[24], with metallic systems including Ni-Ti[25, 26], Cu-Zn-Al[27], Fe-Pd[28], Ni-Fe-Ga-(Co)[29, 30], and Ni-Mn-based alloys[16, 31-34]. Ni-Mn-based alloys are particularly noteworthy as they exhibit both first-order structural phase transitions and second-order magnetic phase transitions. This dual nature enables them to demonstrate not only magnetocaloric effects under magnetic fields but also elastocaloric or barocaloric effects induced by structural phase transitions under stress fields[35]. Such multi-field responsive caloric effects present substantial development potential in solid-state refrigeration.

Current research on Ni-Mn-based alloys has predominantly focused on their

magnetocaloric performance. The elastocaloric effect requires reversible superelastic deformation under uniaxial stress, demanding excellent mechanical properties and fatigue resistance. However, Ni-Mn-based alloys suffer from intrinsic brittleness and environmental embrittlement, showing strong intergranular fracture tendencies[36-38], This leads to structural fatigue (crack initiation and propagation) and functional degradation fatigue (elastocaloric effect deterioration and reversibility reduction)[2, 39], severely limiting their practical applications in solid-state refrigeration.

Performance enhancement of Ni-Mn-based magnetic alloys can be achieved through: (1) Composition design using elemental doping for solid solution strengthening to improve matrix mechanical properties and introduce ductile secondary phases; (2) Grain boundary purification through doping to enhance grain boundary cohesion and reduce intergranular fracture; (3) Microstructural design controlling grain size and crystallographic orientation. Therefore, strategic selection of doping elements, precise composition control, and rational microstructural design represent viable approaches to optimize Ni-Mn-based magnetic alloys.

This research focuses on Ni-Mn-Sn-based magnetic alloys with two primary objectives: Investigating the effects of Fe, Cu, and B doping on martensitic transformation, magnetic properties, and mechanical performance. First-principles calculations will predict lattice structure and phase stability, while induction melting will prepare variously doped alloys for characterization of crystal structure, phase transition behavior, and magnetocaloric properties. Developing Ni-Mn-Sn-Cu-B alloys with both excellent elastocaloric and magnetocaloric effects at room temperature by studying elastocaloric cycling reversibility and stability.

Additionally, this study systematically investigates the reversible and nonreversible components during martensitic transformation. Theoretically, it elucidates the relationship between the reversible transformation components and adiabatic temperature change, while clarifying the intrinsic connections among nonreversible components, frictional dissipation, and transformation hysteresis. These investigations aim to achieve precise control of magneto-structural phase transitions in Ni-Mn-Sn-based alloys, providing theoretical guidance for improving their magnetocaloric/elastocaloric performance and cycling stability toward practical applications.

1.2 Structure, Phase Transition, and Properties of Ni-Mn-Sn-based Magnetic Alloys

1.2.1 Crystal Structure of Ni-Mn-Sn Alloy

The non-stoichiometric Ni_2MnSn alloy belongs to the Heusler alloy family[40]. Its parent phase exhibits a highly ordered $L2_1$ type face-centered cubic structure, which can be described as four interpenetrating face-centered sublattices along the diagonal direction. These sublattices are occupied by Sn, Ni, Mn, and Ni atoms at the (0, 0, 0), (1/4, 1/4, 1/4), (1/2, 1/2, 1/2), and (3/4, 3/4, 3/4) positions, respectively. From an electronic structure perspective, Ni ($3d^8 4s^2$) and Mn ($3d^5 4s^2$) are transition metals with valence electrons primarily in the d-orbitals of their penultimate shells, while Sn ($4d^{10} 5s^2 5p^2$) is a main-group s-p element with valence electrons in the outermost p-orbitals. The relatively weak p-d covalent hybridization between these orbitals contributes to the significant intrinsic brittleness of Ni-Mn-Sn-based alloys[36-38].

In the crystal structure of Ni_2MnSn, atomic spacings exhibit notable variations: the Mn-Ni distance is the shortest, followed by Mn-Sn, while Mn-Mn pairs have

the largest separation. This structural feature necessitates that the magnetic coupling between Mn-Mn atoms relies on itinerant electrons mediated by Ni/Sn atoms. Notably, Mn and Sn atoms are prone to site interchange, leading to a transformation from a highly ordered $L2_1$ structure to a disordered B_2-type arrangement. Moreover, the martensitic phase of Ni-Mn-Sn alloys can adopt diverse crystal structures depending on composition. Fig. 1-1 illustrates three typical modulated structures of martensite in Ni-Mn-Sn alloys[41, 42].

Martensitic phases with modulated structures exhibit periodic stacking along the <110> direction of the $L2_1$ parent phase. Sutou et al.[41] identified a 4O orthorhombic martensite in $Ni_{50}Mn_{37.5}Sn_{12.5}$ alloy, characterized by a high-density twinned modulated structure with lattice parameters a=4.313 Å, b=2.870 Å, c=8.401 Å, and a monoclinic angle β of 90 °. The 5M martensite adopts a near-orthogonal structure with β≈90 °, while the $Ni_{50}Mn_{40}Sn_{10}$ alloy forms a 7M martensite at room temperature, with β=93.84 °.

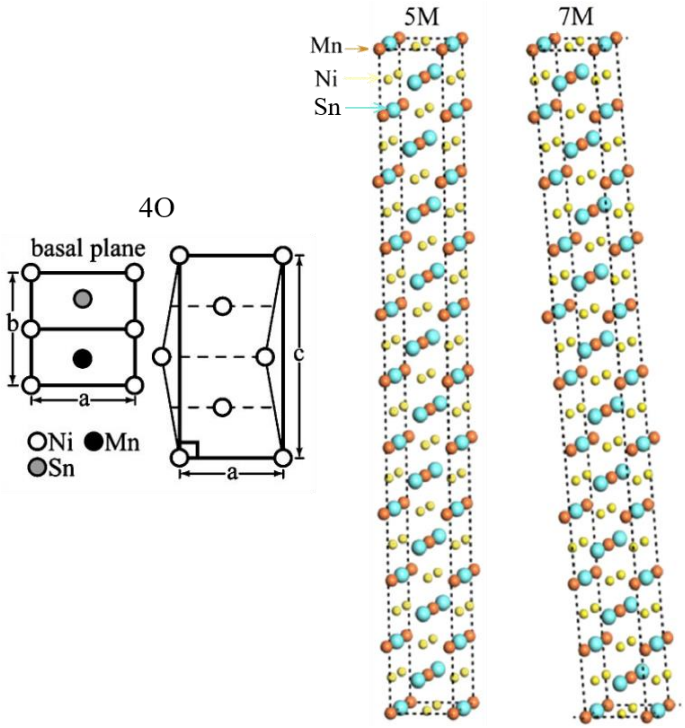

Fig. 1-1 Schemes diagram of the 4O, 5M and 7M martensites in Ni-Mn-Sn alloys[41, 42]

Krenke et al.[43]demonstrated that in the $Ni_{50}Mn_{50-x}Sn_x$ (0<x<25 at.%) system, cooling from high temperatures induces sequential phase transitions: from the $L2_1$ austenite to a six-layer modulated monoclinic (6M) martensite, five-layer modulated near-orthogonal (5M) martensite, four-layer modulated orthorhombic (4O) martensite, seven-layer modulated monoclinic (7M) martensite, and finally a non-modulated $L1_0$ martensite. The structural details and lattice parameters of these phases are summarized in Table 1-1[43]. These findings differ from those of Sutou et al.[41], highlighting the complexity of modulated structures in this compositional range.

Table 1-1 Crystal structures and lattice parameters of $Ni_{50}Mn_{50-x}Sn_x$ (0<x<25 at.%) alloys at room temperature[43]

x	Crystal structure	Lattice parameter (Å)		
		a	*b*	*c*
0.25	$L2_1$	6.046	6.046	6.046
0.2	$L2_1$	6.024	6.024	6.024
0.18	$L2_1$	6.009	6.009	6.009
0.15	$L2_1$	5.995	5.995	5.995
0.13	5M	4.317	5.621	21.808
0.1	7M	4.333	5.570	29.971
0.05	$L1_0$	7.595	7.595	6.980

1.2.2 Magnetic Properties and Martensitic Transformation Behavior of Ni-Mn-Sn Alloy

In the stoichiometric Ni_2MnSn alloy, the magnetic moment primarily originates from the magnetic coupling between Mn atoms[44], with a localized magnetic moment of approximately 4 μB near each Mn atom. In the $L2_1$-phase Ni_2MnSn alloy, the nearest Mn-Sn distance is 3 Å, while the Mn-Mn distance is

4.2 Å—significantly larger than the 2.24 Å spacing of Mn atoms in pure metallic Mn. This observation confirms the earlier assertion that the magnetic coupling between Mn atoms in Ni-Mn-Sn alloys predominantly relies on itinerant electrons provided by Ni/Sn atoms.

For non-stoichiometric $Ni_2Mn(Mn_xSn_{1-x})$ alloys, as Mn atoms progressively substitute Sn sites, two distinct Mn occupancies emerge in the lattice: Mn atoms occupying original Sn sites and those at native Mn sites. The magnetic exchange interaction between these Mn atoms exhibits an antiferromagnetic state, leading to a marked reduction in individual atomic moments and consequently diminishing the total magnetic moment of the alloy.

Fig. 1-2 illustrates the structural phase transition process in Ni-Mn-Sn magnetic alloys. At low temperatures, the alloy adopts a weakly magnetic martensitic state with antiparallel alignment of Mn atomic moments. Upon heating, the alloy undergoes a reverse martensitic transformation[45], characterized by: (1) preserved nearest-neighbor atomic relationships, (2) atomic displacements smaller than the interatomic spacing, confirming a diffusionless transformation mechanism. During this process, the crystal structure reconstructs via instantaneous shear, transitioning from the low-symmetry monoclinic martensite phase (weakly magnetic state) to the high-symmetry face-centered cubic austenite phase (ferromagnetic state), accompanied by significant macroscopic deformation. Notably, in the early stages of transformation, partial parallel alignment of Mn moments becomes observable, corresponding to a coexisting martensite-austenite state. Upon complete transformation at higher temperatures, the alloy fully converts to austenite with uniformly parallel-aligned Mn moments. Thermodynamically, this austenite formation during heating represents a typical

non-equilibrium phase transition that cannot be predicted by equilibrium phase diagrams.

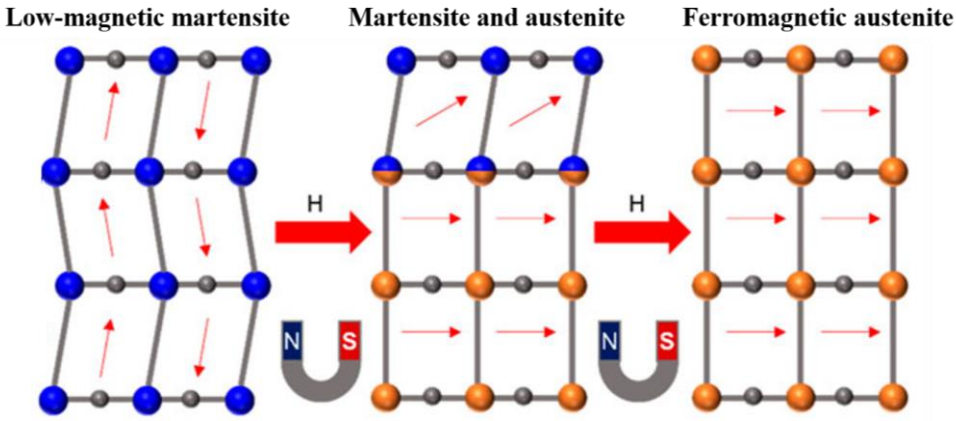

Fig. 1-2 Structural phase transition of Ni-Mn-Sn alloy[45]

With further temperature increase, the alloy experiences a second-order phase transition where the austenite transforms from a ferromagnetic to paramagnetic state. The corresponding transition temperature, termed the Curie temperature of austenite (T_C^A), marks the onset of disordered Mn moment orientations.

1.2.3 Mechanical Properties of Ni-Mn-Sn-based Alloys

As discussed, Ni-Mn-Sn alloys are prone to intergranular fracture, and their brittle fracture originates from intrinsic brittleness and environmental brittleness. In addition, polycrystalline Ni-Mn-Sn alloys have strong elastic anisotropy, and stress concentration easily occurs at grain boundaries. Furthermore, Ni-Mn-Sn alloys have an ordered structure with a large volume of unit cells and a large Burgers vector of dislocations, leading to difficulty in dislocation slips and a reduction in independent slip systems, which could result in the intrinsic brittleness of the alloy. Consequently, research on the elastocaloric effect in Ni-Mn-Sn-based alloys has been significantly limited by their intrinsic brittleness. As demonstrated in existing studies[34, 46], the inherent brittleness of these alloys leads to structural instability prior to the completion of stress-induced martensitic transformation,

thereby preventing accurate theoretical determination of both superelastic strain and adiabatic temperature change.

To address these challenges, viable approaches to improving the plasticity and toughness of Ni-Mn-Sn-based alloys are proposed, which mainly include: (1) the improvement of the mechanical properties of the parent phase through element doping, solid solution strengthening, or introducing a ductile second phase; (2) the purification and modification of the grain boundary by element doping, which could improve the bonding forces at the grain boundary and reduce the tendency of intergranular fracture; (3) the design of microstructure or the adjustment of grain size and crystal orientation (texture). A comprehensive analysis of these approaches will be presented in the following section.

1.2.4 Elastocaloric Effect of Ni-Mn-Sn-based Alloys

The caloric effects accompanying phase transitions can be classified according to their driving fields into: magnetocaloric effect (MCE)[47], elastocaloric effect (eCE)[6], and barocaloric effect (BCE)[48], corresponding to magnetic fields, uniaxial stress, and hydrostatic pressure, respectively. Magnetic alloy materials possess magneto-elastic coupling characteristics, enabling their phase transitions to be driven by two or more combined external fields to generate caloric effects[49]. While research on the magnetocaloric effect of magnetic alloys was initiated earlier, mechanical phase transition refrigeration based on elastocaloric and barocaloric effects has gradually gained widespread attention. Particularly, multi-field regulated caloric effects have emerged as a cutting-edge research frontier in solid-state refrigeration materials[5, 50, 51]. The elastocaloric effect is typically quantified by either isothermal entropy change (ΔS_m) or adiabatic temperature change (ΔT_{ad})[2]. Consequently, the effective characterization of these

two physical parameters constitutes a fundamental requirement for studying caloric effects in magnetic alloys and serves as a crucial criterion for evaluating their suitability as solid-state refrigeration materials.

1.2.4.1 Generation and Principle of Elastocaloric Effect

The phenomenon where a material undergoes temperature changes upon mechanical stress application is termed the elastocaloric effect. Fig. 1-3 schematically illustrates the refrigeration process via elastocaloric effect in magnetic alloys[52].

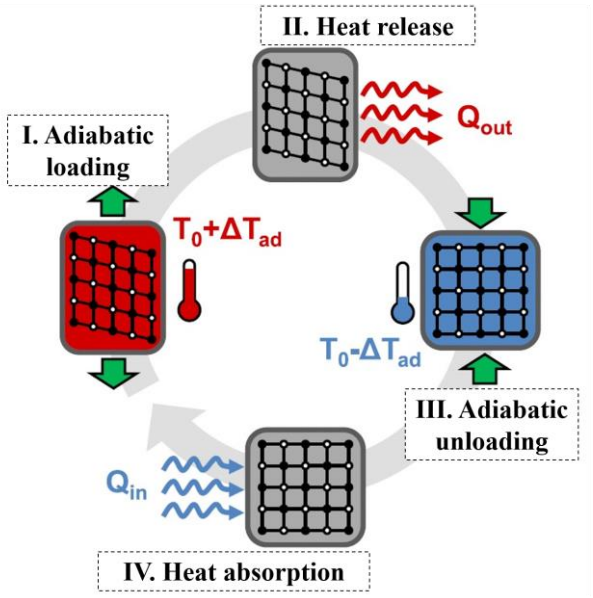

Fig. 1-3 Schematic diagram of the elastocaloric effect refrigeration process[52]

The material exhibits reversible deformation at high strains due to its superelasticity, resulting in a characteristic stress plateau in the stress-strain curve caused by the austenite-to-martensite phase transition.

When the alloy is in the austenitic state (temperature T_0), applying uniaxial stress beyond a critical value triggers an exothermic austenite→martensite transformation. Under sufficiently high loading strain rates, this process can be approximated as adiabatic, causing the alloy temperature to rise to ($T_0+\Delta T_{ad}$). During the transformation, the alloy's entropy decreases, releasing latent heat (ΔT_{ad})

to the environment and returning the temperature to its initial value T_0. During unloading, removal of the applied stress induces an endothermic martensite→austenite reverse transformation. If the unloading strain rate is sufficiently rapid, this process can also be treated as adiabatic, leading to temperature reduction to ($T_0-\Delta T_{ad}$). The alloy absorbs heat from the environment during reverse transformation, restoring the temperature to T_0 and thereby achieving the refrigeration effect.

1.2.4.2 Thermodynamic Description of Elastocaloric Effect

The internal energy of a stress-deformable solid can be expressed as[5]:

$$dU=TdS+V_0\sigma_{ij}d\varepsilon_{ij} \tag{1.1}$$

Where U is the system internal energy, T is temperature, S denotes entropy, V_0 is stress-free solid volume, σ_{ij} is Cauchy stress and ε_{ij} represents linear strain.

For analytical convenience, by taking temperature and stress as independent variables, the system's Gibbs free energy G can be derived through Legendre transformation as:

$$G=U-TS-V_0\sigma_{ij}\varepsilon_{ij} \tag{1.2}$$

The differential equation of Gibbs free energy can be expressed as:

$$dG=-SdT-V_0\varepsilon_{ij}d\sigma_{ij} \tag{1.3}$$

From this, the Maxwell relation can be derived:

$$\frac{\partial S}{\partial \sigma_{ij}}=V_0\frac{\partial \varepsilon_{ij}}{\partial T} \tag{1.4}$$

In the above discussion, the temperature dependence of the stress-free solid volume V_0 is negligible.

The elastocaloric effect is induced by variations in the magnitude of uniaxial stress. The application of stress along a given direction μ can be expressed as

$\sigma_{ij}=\sigma\delta_{i\mu}\delta_{j\mu}$. In this expression, δ_{ij} represents the Kronecker delta function, where $\sigma>0$ corresponds to tensile stress and $\sigma<0$ corresponds to compressive stress. Thus, σ can be treated as a scalar quantity.

To quantify the response function of the elastocaloric effect, we can write:

$$\xi_{iso}=\left(\frac{\partial S}{\partial f}\right)_T \tag{1.5}$$

and

$$\xi_{adi}=\left(\frac{\partial T}{\partial f}\right)_S \tag{1.6}$$

where f is a scalar field of σ. These two response functions satisfy the following relationship:

$$\xi_{iso}=-\frac{C\xi_{adi}}{T} \tag{1.7}$$

Here, C represents the heat capacity under constant force. For solids, the heat capacity at constant stress can be assumed equal to that at constant deformation.

Under isothermal conditions, the isothermal entropy change (ΔS) induced by stress-driven martensitic transformation is expressed as:

$$\Delta S(T, 0\rightarrow\sigma)=V_0\int_0^{\sigma}\left(\frac{\partial\varepsilon}{\partial T}\right)_{\sigma}\mathrm{d}\sigma \tag{1.8}$$

Under adiabatic conditions, the adiabatic temperature change (ΔT) induced by stress-driven martensitic transformation is given by:

$$\Delta T(S, 0\rightarrow\sigma)=-V_0\int_0^{\sigma}\frac{T}{C}\left(\frac{\partial\varepsilon}{\partial T}\right)_{\sigma}\mathrm{d}\sigma \tag{1.9}$$

When the temperature variation is small and the heat capacity remains unaffected by stress, the calculation of ΔT can be simplified to:

$$\Delta T(S, 0\rightarrow f=\sigma)\backsimeq-\frac{T\Delta S(T_i, 0\rightarrow f=\sigma)}{C} \tag{1.10}$$

where T_i denotes the initial temperature at which the stress is applied.

1.2.4.3 Characterization of Elastocaloric Effect

As mentioned earlier, the elastocaloric effect of materials can be characterized by two physical parameters: the isothermal entropy change (ΔS_m) or the adiabatic temperature change (ΔT_{ad}). The specific evaluation approaches include the following methods:

(1) Calculation of isothermal entropy change by measuring stress-strain curves at different temperatures or strain-temperature curves under varying applied stresses.

The isothermal entropy change can be initially determined by testing stress-strain curves (σ-ε curves) at different temperatures, from which it can be calculated as:

$$\Delta S(T_K, 0\rightarrow\varepsilon)=\frac{1}{\rho\Delta T}\left[\int_0^{\varepsilon}\sigma_{T_{k+1}}\mathrm{d}\varepsilon-\int_0^{\varepsilon}\sigma_{T_k}\mathrm{d}\varepsilon\right] \tag{1.11}$$

where ρ is the density, T_K represents the average temperature of two measurement points, ΔT is the temperature difference between two measurement points, T_k and T_{k+1} denote two selected measurement temperatures, respectively (here $T_{k+1}>T_k$).

The isothermal entropy change can also be determined by first measuring the strain-temperature curves (ε-T curves) under different stresses and then calculating:

$$\Delta S(\sigma_1\rightarrow\sigma_2)=v_0\int_{\sigma_1}^{\sigma_2}\left(\frac{\partial\varepsilon}{\partial T}\right)_{\sigma}\mathrm{d}\sigma \tag{1.12}$$

where v_0 is the specific volume.

(2) Calculating isothermal entropy change by measuring differential scanning calorimetry (DSC) curves under different stresses

Since the elastocaloric effect in magnetic alloys originates from martensitic transformation, which is a first-order phase transition, the latent heat during phase

transition can be directly measured using DSC under external fields, from which the entropy change during transformation can be calculated:

$$\Delta S=\frac{|\Delta H|}{T_p} \tag{1.13}$$

where ΔH is the latent heat of transformation between austenite and martensite phases, and T_p represents the temperature value corresponding to the endothermic or exothermic peak in the DSC curve

(3) Calculation of adiabatic temperature change based on isothermal entropy change results

After obtaining the isothermal entropy change, the adiabatic temperature change ΔT can be calculated as follows:

$$\Delta T=\frac{T}{C_p}\Delta S \tag{1.14}$$

where T is the ambient temperature, and C_p represents the specific heat capacity.

Here, ΔS represents the entropy change values obtained through the two aforementioned methods, resulting in different values for the adiabatic temperature change. The two distinct calculation approaches will be analyzed in detail in subsequent sections.

(4) Adiabatic temperature change measurement using direct methods

The measurement methods can be classified into contact and non-contact methods. The contact method involves fixing thermocouples to the elastocaloric material surface using solder or specialized adhesives for temperature measurement, while the non-contact method typically employs infrared thermography for direct temperature change detection. Under adiabatic conditions, elastocaloric materials exhibit significant temperature variations during stress application or removal. It should be noted that the loading/unloading rate must be sufficiently high in

practical measurements to approximate adiabatic conditions. Experimental studies by Pataky et al.[53] demonstrated that when the strain rate exceeds 0.1 s^{-1}, the material state approaches adiabatic conditions, and the measured temperature change can be reasonably regarded as the adiabatic temperature change. Insufficient strain rates, however, lead to significant deviations between measured ΔT_{ad} values and theoretical predictions.

Comparative analysis reveals that ΔT_{ad} values estimated through indirect methods are generally higher than those obtained from direct measurements. This discrepancy stems partially from heat dissipation at the contact interfaces between thermocouples/stress fixtures and the specimen during actual measurements. Another contributing factor may be the frictional dissipation occurring at the moving interphase during martensitic transformation. A detailed investigation and discussion of these phenomena will be presented in Chapter 4.

1.2.5 Magnetocaloric Effect of Ni-Mn-Sn-based Alloys

1.2.5.1 Generation and Principle of Magnetocaloric Effect

The magnetocaloric effect represents an intrinsic property of magnetic materials, originating from the coupling interaction between magnetic fields and magnetic sublattices. Under constant pressure conditions, the total entropy $S(T, H)$ of a magnetic material (as a function of magnetic field strength H and absolute temperature T) can be expressed as the sum of three components: the magnetic entropy $S_M(T, H)$, the lattice vibrational entropy $S_L(T)$, and the electronic entropy $S_E(T)$:

$$S(T, H)=S_M(T, H)+S_L(T)+S_E(T) \tag{1.15}$$

The lattice vibrational entropy and electronic entropy are essentially independent of the magnetic field, with the contribution from electronic entropy

being negligible in most cases. When subjected to an external magnetic field, the magnetic entropy decreases due to the ordering of magnetic spins. Under adiabatic conditions, this reduction in magnetic entropy leads to a corresponding increase in lattice vibrational entropy. It should be noted that in magnetocaloric cycles, only the magnetic entropy is capable of responding to changes in the external magnetic field. Based on the sign of the magnetic entropy change, the magnetocaloric effect can be classified into two categories: the conventional magnetocaloric effect and the inverse magnetocaloric effect, which will be discussed separately below.

The conventional magnetocaloric effect (CMCE) exhibits the characteristic phenomenon of "Heating upon magnetization and cooling upon demagnetization." Fig. 1-4 illustrates a schematic diagram of the refrigeration cycle based on CMCE[13].

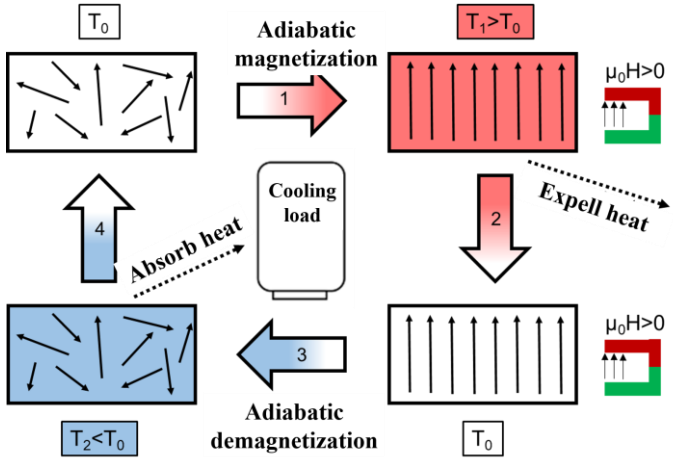

Fig. 1-4 Schematic diagram of the CMCE refrigeration process[13]

Under adiabatic conditions, when a magnetic field is applied, the reduction in magnetic entropy is compensated by an increase in lattice entropy. This entropy transfer results in a temperature rise of the material (Step 1). Subsequently, the excess heat is dissipated through a heat-transfer medium (e.g., a thermal fluid), returning the material to its initial temperature but in a magnetized state (Step 2). Upon adiabatic removal of the magnetic field, the material's magnetic entropy

increases while its lattice entropy decreases, leading to temperature reduction (Step 3). The material then absorbs heat from the cooling target, thereby lowering its temperature to meet refrigeration requirements (Step 4). This cycle repeats to initiate the next refrigeration process.

In contrast to CMCE, materials exhibiting the inverse magnetocaloric effect (IMCE) demonstrate "cooling upon magnetization and heating upon demagnetization". When a magnetic field is applied to IMCE materials, the heat absorbed during structural phase transition significantly exceeds that released through magnetic ordering. This phenomenon is commonly observed in first-order phase transitions of Ni-Mn-X (X=Sn, In, Sb) alloys[54, 55], and originates from their metamagnetic transition. The refrigeration process is detailed in Fig. 1-5[13].

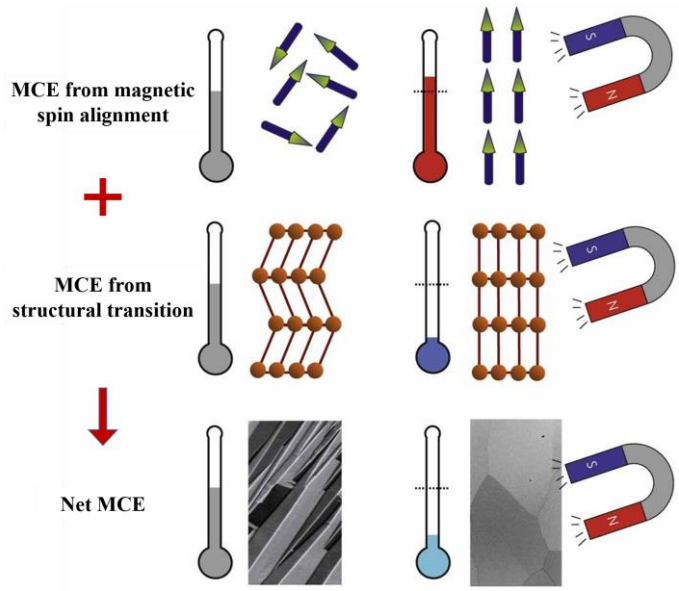

Fig. 1-5 Schematic diagram of the IMCE refrigeration process[13]

Under adiabatic conditions, magnetic field application aligns the magnetic moments, causing temperature increase; simultaneously, the field induces a phase transition from weakly magnetic low-symmetry monoclinic martensite to ferromagnetic high-symmetry cubic austenite, resulting in significant temperature decrease. The superposition of these opposing effects ultimately leads to net

temperature reduction in the material under adiabatic magnetization.

1.2.5.2 Thermodynamic Description of Magnetocaloric Effect

Using the principle of energy conservation, introducing magnetocaloric effects into thermodynamic systems through magnetic work:

$$\mathrm{d}U=\mathrm{d}Q-\mathrm{d}W \tag{1.16}$$

In the formula, U—Internal energy, J;

Q—Heat, J;

W—Work, J

In a closed system, the law of conservation of energy can be expressed as:

$$\mathrm{d}U=T\mathrm{d}S-p\mathrm{d}V+\mu_0 H\mathrm{d}M \tag{1.17}$$

In the formula, T—Temperature, K;

S—Entropy, J/kg·K;

p—Pressure, N/m^2;

V—Volume, m^3;

μ_0—Free space magnetic permeability, N/m^2;

H—Magnetic field, T;

M—Magnetization, $A\cdot m^2/kg$

Among them, internal energy is a function of entropy, volume, and magnetization, expressed as $U(S, V, M)$. Usually, experiments are conducted under constant pressure, so Gibbs free energy can be written as:

$$G(T, p, H)=U-TS=pV-M\mu_0 H \tag{1.18}$$

Its differential form is:

$$\mathrm{d}G=V\mathrm{d}p-S\mathrm{d}T-M\mu_0\mathrm{d}H \tag{1.19}$$

From this equation, entropy can be obtained:

$$S=-\left(\frac{\partial G}{\partial T}\right)_{p,H} \tag{1.20}$$

And can also obtain the magnetization:

$$M=-\frac{1}{\mu_0}\left(\frac{\partial G}{\partial H}\right)_{p,T} \tag{1.21}$$

The second derivative can obtain the following relationship (Maxwell's equation):

$$\left(\frac{\partial S}{\partial H}\right)_{p,T}=\mu_0\left(\frac{\partial M}{\partial T}\right)_{p,H} \tag{1.22}$$

The Maxwell relationship can be extended to obtain the expression of magnetocaloric effect (MCE). MCE is a reversible temperature change caused by changes in magnetic field during adiabatic processes. Therefore, entropy can be expressed as a function of magnetic field and temperature:

$$\mathrm{d}S=\left(\frac{\partial S}{\partial T}\right)_{p,H}\mathrm{d}T+\left(\frac{\partial S}{\partial H}\right)_{p,T}\mathrm{d}H \tag{1.23}$$

Considering dS=0, we can obtain:

$$\mathrm{d}T=-\mu_0\left[\left(\frac{\partial S}{\partial T}\right)_{p,H}\right]^{-1}+\left(\frac{\partial S}{\partial H}\right)_{p,T}\mathrm{d}H \tag{1.24}$$

According to the definition of heat capacity (C), at a constant x (where x=p, H):

$$C_x=\left(\frac{\mathrm{d}Q}{\mathrm{d}T}\right)_x=T\left(\frac{\mathrm{d}S}{\mathrm{d}T}\right)_x \tag{1.25}$$

According to Maxwell's equation (Eq. 1.22), we can obtain:

$$\mathrm{d}T=-\mu_0\frac{T}{C_{p,H}}\left(\frac{\partial M}{\partial T}\right)_{p,H}\mathrm{d}H \tag{1.26}$$

And the total temperature change caused by magnetic field changes is:

$$\Delta T_{\mathrm{ad}}=-\mu_0\int_{H_I}^{H_F}\frac{T}{C_{p,H}}\left(\frac{\partial M}{\partial T}\right)_{p,H}\mathrm{d}H \tag{1.27}$$

Here, H_F and H_I represent the final magnetic field and initial magnetic field,

respectively. Although ΔT_{ad} depends on magnetization, it must be pointed out that heat capacity is not a state function, and this method eliminates the dependence of ΔT_{ad} on sample size. In addition, magnetocaloric effect is usually defined as the change in magnetic entropy caused by changes in magnetic field under isothermal conditions (i.e., dT=0). So the form of Eq. (1.23) can be rewritten as:

$$\mathrm{d}S=\left(\frac{\partial S}{\partial H}\right)_{p,T}\mathrm{d}H=\mu_0\left(\frac{\partial M}{\partial T}\right)_{p,H}\mathrm{d}H \tag{1.28}$$

The entropy change caused by changes in magnetic field is expressed as:

$$\Delta S_{\mathrm{m}}=-\mu_0\int_{H_I}^{H_F}\left(\frac{\partial M}{\partial T}\right)_{p,H}\mathrm{d}H \tag{1.29}$$

When ΔS_{m} is negative, it is the conventional magnetocaloric effect (CMCE). If it is positive, it becomes the inverse magnetocaloric effect (IMCE).

In addition, by linking magnetic entropy with heat capacity, the total entropy under a constant magnetic field can be expressed as the following equation:

$$S_H(T)=S_0+\int_0^T\frac{C_{p,H}}{T}\mathrm{d}T \tag{1.30}$$

Among them, S_0 is the zero entropy term, from which the expression of magnetocaloric effect can be obtained:

$$\Delta S_{\mathrm{m}}(T,\Delta H)=\left[S_{H_F}(T)-S_{H_I}(T)\right]_T \tag{1.31}$$

$$\Delta T_{\mathrm{ad}}(T,\Delta H)=\left[T_{H_F}(S)-T_{H_I}(S)\right]_S \tag{1.32}$$

1.2.5.3 Characterization of Magnetocaloric Effect

Similar to the characterization of the elastocaloric effect, the magnetocaloric effect of a material can also be characterized by the isothermal entropy change (ΔS_{m}) or the adiabatic temperature change (ΔT_{ad}). Among them, Δ Sm is generally obtained through indirect methods, one of which is to measure the isothermal magnetization curves at different temperatures, another method is to measure the

specific heat capacity curves under different magnetic fields and then calculate ΔS_m. For adiabatic temperature changes, it can be calculated by measuring the specific heat capacity curves under different magnetic fields.

(1) The isothermal entropy change is determined by measuring the isothermal magnetization (*M*-*H*) curves at different temperatures and performing subsequent calculations using Maxwell's equations:

$$\Delta S_m(T, H)=\sum_i \frac{M(T_{i+1}, H)-M(T_i, H)}{T_{i+1}-T_i}\Delta H_i \tag{1.33}$$

In the formula, T_{i+1}—Test temperature when obtaining the $(i+1)^{th}$ *M*-*H* curve, K;

T_i—Test temperature when obtaining the i^{th} *M*-*H* curve, K;

M_{i+1}—The magnetization corresponding to the $(i+1)^{th}$ *M*-*H* curve, A·m^2/kg;

M_i—The magnetization corresponding to the i^{th} *M*-*H* curve, A·m^2/kg

It should be noted that when calculating the magnetic entropy change of first-order phase transitions using the Maxwell relations, the coexistence of multiple magnetic phases may occur within the phase transition temperature range. This can lead to an artificially sharp and overestimated peak in the ΔS_m-*T* curve, exceeding the actual value[56]. To eliminate this phenomenon, the Loop method is typically employed for correction.

(2) Measure the specific heat capacity curve under different magnetic fields and calculate the isothermal entropy change.

The isothermal entropy change can be calculated by measuring the C_p (*T*, *H*) curves under different magnetic fields:

$$\Delta S_m(T)=\int_0^T \frac{C_p(T, H)-C_p(T, 0)}{T}\mathrm{d}T \tag{1.34}$$

In the formula, C_p(*T*, *H*)—Heat capacity value at temperature of *T* and magnetic

field of $\mu_0 H$, J/kg·K;

$C_p(T, 0)$—Heat capacity value at temperature of T and zero magnetic field, J/kg·K.

(3) The adiabatic temperature change is calculated by measuring the specific heat capacity curves under different magnetic fields

Similar to the approach for measuring the isothermal entropy change mentioned earlier, the specific heat capacity $C_p(T, H)$ curves under different magnetic fields are first measured to obtain the entropy change versus temperature curves at various fields. The adiabatic temperature change is then calculated using the following equation:

$$\Delta T_{ad}(T)_{\Delta H}=[T(S)_H-T(S)_0]_s \tag{1.35}$$

Additionally, for practical applications, magnetic refrigeration materials must possess a broad operating temperature range, defined as the full width at half maximum (ΔT_{FWHM}) of the ΔS_m-T curve. To comprehensively evaluate the magnetocaloric effect of materials, the refrigerant capacity (RC) is defined using the following equation:

$$RC=\int_{T_2}^{T_1}|\Delta S_m(T)|\,dT \tag{1.36}$$

RC represents the area under the ΔS_m-T curve within the temperature range at half of the peak value. As can be inferred from its definition, the RC value does not represent the maximum energy transfer between the hot and cold ends during the refrigeration cycle. In addition to RC, the relative cooling power (RCP) is another parameter used to characterize the magnetocaloric effect of materials:

$$RCP=|\Delta S_m|\cdot\Delta T_{FWHM} \tag{1.37}$$

Here, $|\Delta S_m|$ represents the maximum magnetic entropy change value during one

complete cycle. In existing research reports[57, 54], both the refrigerant capacity (*RC*) and relative cooling power (*RCP*) parameters are typically employed to evaluate the refrigeration performance

1.2.6 Thermodynamics of Martensitic Transformation Process in Ni-Mn-Sn-based Alloy

Based on the aforementioned analysis of martensitic transformation mechanisms and the principles underlying elastocaloric and magnetocaloric effects, the martensitic transformation in Ni-Mn-Sn-based magnetic alloys belongs to thermoelastic martensitic transformation. This serves as the common physical foundation for various functional properties of the alloys, including superelasticity, elastocaloric effect, and magnetocaloric effect. Thermoelastic martensitic transformation exhibits three characteristic features[58]: (1) small critical transformation driving force with narrow thermal hysteresis; (2) reversible interfacial motion between austenite and martensite phases; and (3) elastic strain energy of martensite acting as the driving force for reverse transformation.

Accurate characterization of the relevant thermophysical parameters during martensitic transformation is a prerequisite for investigating the associated caloric effects. Differential scanning calorimetry (DSC) has been widely employed to characterize the heat flow and temperature changes during thermoelastic martensitic transformation. However, DSC measures the cumulative thermal events throughout the transformation process and cannot precisely resolve the nature of multiple transition processes occurring within the transformation temperature range.

In the 1990s, Reading et al.[59]developed modulated differential scanning calorimetry (MDSC), which provides a potential solution to overcome the current

limitations of DSC in studying thermoelastic martensitic transformations. MDSC has been successfully applied to investigate polymers and multicomponent polymer blends, achieving significant results in measuring glass transition temperatures[60, 61], studying crystallization and melting processes[62, 63], and separating complex thermal transitions[64, 65]. This capability stems from MDSC's unique approach of simultaneously employing two heat flow signals during thermal analysis: one using the conventional constant heating rate of standard DSC, and the other incorporating a small sinusoidal temperature modulation. The constant heating rate ensures high resolution, while the sinusoidal modulation creates instantaneous temperature variations that enhance sensitivity.

However, the dominant mechanisms of martensitic transformation in Ni-Mn-Sn-based alloys differ fundamentally from those in polymers. The thermoelastic martensitic transformation involves two crucial energy components: (1) the energy stored during cooling that drives the reverse transformation, and (2) the internal friction work associated with interface migration and defect formation. To achieve the separation and individual study of these thermodynamic components through MDSC, further analysis and clarification of the underlying principles and mechanisms are still required. This research direction holds promise for addressing the resolution limitations of conventional DSC in characterizing thermodynamic parameters during martensitic transformation.

1.3 Composition and Element Doping of Ni-Mn-Sn Alloy

1.3.1 First-principles Calculations and Element Doping Design

The microstructure of materials determines their various properties. The physical phenomena exhibited by Ni-Mn-Sn alloys, such as the elastocaloric effect [46], magnetocaloric effect[66], and magnetoresistance effect[67], are fundamentally

governed by their intrinsic electronic structures. Compared with traditional experimental approaches, first-principles calculation methods developed based on quantum mechanical theories can more conveniently and accurately obtain the electronic structures of alloys, thereby explaining the intrinsic mechanisms behind the macroscopic physical properties of materials. This approach significantly reduces both the development cycle and the costs of materials, powerfully advancing the progress of materials science.

In Heusler alloys, atoms may exhibit paramagnetic, ferromagnetic, or antiferromagnetic coupling. The ground-state magnetic structure can be determined by fitting the energy-volume relationships under different coupling states and selecting the configuration with the lowest total energy. Once the cubic crystal structure is established, atomic migration during the martensitic transformation does not disrupt the nearest-neighbor relationships, and the relative atomic arrangement remains unchanged. However, during tetragonal distortion, the magnetic properties of the atoms may undergo transitions, i.e., the coupling states may change. Xiao et al.[68] employed first-principles calculations to investigate the magnetic properties and martensitic transformation in $Ni_8Mn_6Sn_{2-x}Al_x$ alloys. They found that as the Al doping concentration increased, the *c/a* ratio of the martensitic phase increased from 1.30 to 1.34, and the cubic austenitic phase gradually transitioned from a ferromagnetic state to an antiferromagnetic state.

Tan et al.[69] employed first-principles calculations to investigate the fundamental configurations of $Ni_2Mn_{1+x}In_{1-x}$ magnetic alloys. From an energetic perspective, they proposed that excess Mn atoms directly occupy In atomic sites, considering two magnetic configurations: parallel or antiparallel alignment between the magnetic moments of Mn atoms and those occupying In sites. Their

study on martensitic transformation revealed that only the $Ni_2Mn_{1.5}In_{0.5}$ composition undergoes martensitic transformation, with Mn atomic moments exhibiting antiparallel alignment in the tetragonal phase. The researchers further attributed this phenomenon to changes in Mn-Mn interatomic distances, which play a decisive role in both magnetic properties and martensitic transformations.

Numerous studies[70, 71] have demonstrated that the transformation temperatures and Curie temperatures of Ni-Mn-based alloys exhibit high sensitivity to material composition. Ye et al.[72] investigated the tetragonal distortion and electronic structure of $Ni_2Mn_{1+x}Sn_{1-x}$ (x=0, 0.25, 0.5) using first-principles methods. They found that for $x \leqslant 0.25$, the alloys cannot undergo martensitic transformation based on energetic considerations. With increasing x, the density of states peaks formed by hybridization between Ni 3d electrons and Mn 3d electrons occupying Sn sites gradually shift toward the Fermi level, exhibiting antiferromagnetic coupling. He et al.[73] studied the effects of Mn and Co doping on the structure, magnetic properties, and phase transitions of Ni_2MnZ (Z=In, Sn, Sb) alloys. Through formation energy calculations, they determined that excess Mn preferentially occupies Z atomic sites while Co atoms preferentially occupy Ni sites. The energy difference between austenite and martensite decreases with Co doping, a finding consistent with experimental results.

1.3.2 Effect of Doping on the Phase Transition Characteristic Temperature of Ni-Mn-Sn-based Alloys

The transformation characteristic temperatures of Ni-Mn-based alloys are highly sensitive to their composition[74], Statistical analysis of extensive experimental results indicates that the martensitic transformation temperature increases with the average valence electron concentration (*e/a*) of the alloy. As

shown in Fig. 1-6[75], the phase transition characteristic temperature of most Heusler-type Ni-Mn-based magnetic alloys exhibits a linear relationship with *e/a*. In addition, unit cell volume and grain size are also critical factors influencing the transformation temperature of these alloys[76-78].

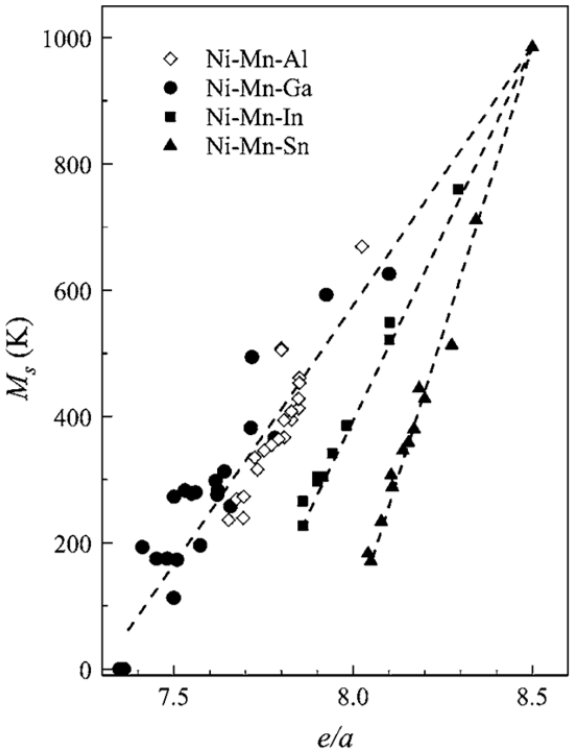

Fig. 1-6 Relationship between MT characteristic temperature and electron concentration of Ni-Mn-based alloy[75]

Magneto-structural coupling refers to the phenomenon where the structural transformation and magnetic transition of a magnetic alloy occur within the same temperature range. This coupling effect can significantly enhance the difference in saturation magnetization between the austenite and martensite phases. Therefore, precise control of magneto-structural coupling serves as an effective approach to improve the caloric effect of Ni-Mn-based magnetic alloys[79]. In particular, alloying doping provides a viable method to adjust the phase transition temperatures, thereby enabling effective modulation of the alloy's magneto-structural coupling behavior.

1.3.3 Effect of Doping on the Magnetocaloric Performance of Ni-Mn-Sn-based Alloys

As mentioned previously, when Ni-Mn-X (X=Sn, In, Sb) based alloys undergo the first-order structural phase transition from austenite to martensite, they simultaneously experience a second-order magnetic transition from ferromagnetism to weak magnetism. The significant difference in saturation magnetization before and after the phase transition provides substantial driving force for the martensitic transformation. Under an applied magnetic field, these magnetic alloys exhibit field-induced magneto-structural phase transitions accompanied by magnetocaloric effects. In 2005, Krenke et al.[21] investigated the magnetocaloric effects in $Ni_{50}Mn_{35}Sn_{15}$ and $Ni_{50}Mn_{37}Sn_{13}$ metamagnetic alloys, achieving magnetic entropy changes of 15 and 18 J/kg·K, respectively, under a 5 T magnetic field. Since then, numerous research teams have conducted extensive studies on the magnetocaloric effects in Ni-Mn-based magnetic alloys and the influence of alloying doping on these effects. Table 1-2 summarizes the impact of Fe, Cu, and Co as doping elements on the magnetocaloric properties of Ni-Mn-Sn alloys.

Table 1-2 Effect of Fe, Cu and Co doping on magnetocaloric properties of Ni-Mn-Sn alloys

Composition	$\Delta\mu_0 H$ (T)	ΔS_m (J/kg·K)	T_p (K)	Reference
$Ni_{49.1}Mn_{36.7}Sn_{13.3}Fe_{0.9}$	5	15	241	[80]
$Ni_{46.9}Mn_{36.8}Sn_{13.3}Fe_3$	5	28	177	[80]
$Ni_{43}Mn_{45}Cu_1Sn_{11}$	1	14.1	220	[81]
$Ni_{43}Mn_{44}Cu_2Sn_{11}$	1	18	250	[81]
$Ni_{43}Mn_{43}Cu_3Sn_{11}$	1	15.8	256	[81]
$Ni_{48.7}Mn_{36.9}Sn_{13.2}Co_{1.2}$	5	9	289	[80]
$Ni_{47.0}Mn_{36.6}Sn_{13}Co_{3.1}$	5	8	259	[80]

$Ni_{50}Mn_{36}Co_1Sn_{13}$	2	10.4	282	[82]
$Ni_{40}Co_{10}Mn_{40}Sn_{10}$	5	14.9	275	[83]
$Ni_{48}Co_2Mn_{38}Sn_{12}$	5	37	328	[84]
$Ni_{46}Co_4Mn_{38}Sn_{12}$	5	30	291	[84]
$Ni_{44}Co_6Mn_{38}Sn_{12}$	5	15	210	[84]

1.3.4 Effect of Doping on the Mechanical Properties of Ni-Mn-Sn-based Alloys

Based on the aforementioned analysis of the causes of brittleness in Ni-Mn-based magnetic alloys, alloying doping has become the primary approach to improving the mechanical properties of Ni-Mn-based alloys. By summarizing existing research findings, the mechanisms for enhancing mechanical properties can be categorized into the following two major types: (1) Improving the mechanical properties of the parent phase through element doping and solid solution strengthening, while introducing a ductile second phase; (2) Purifying and modifying grain boundaries through elemental doping to enhance grain boundary cohesion and reduce intergranular fracture tendency.

Transition metal elements, such as Cu, Fe, Co, Cr, etc., can be doped into Ni-Mn-based alloys, resulting in either a solid solution or a second-phase toughening effect. Doping Cu into Ni-Mn-Ga alloys promotes the coupling of martensitic transformation and magnetic transformation, which can generates giant magnetocaloric effect and a large magnetically induced strain[85, 86]. Meanwhile, Cu doping can improve the plasticity of Ni-Mn-based alloys and reduce the cost of materials. In 2010, Wang et al.[82] pointed out that the $Ni_{50}Mn_{25}Ga_{17}Cu_8$ alloy has a single-phase structure at room temperature, and its compressive strength and fracture strain are 878 MPa and 22%, respectively. Subsequently, Wang et al.[87]

reported a more ductile dual-phase $Ni_{30}Cu_{20}Mn_{41.5}Ga_{8.5}$ alloy with a compressive fracture strain exceeding 70%. In situ observations during dynamic stretching indicated that the second phase distributed along the grain boundaries is the key to the enhancement of the plasticity of the alloy. Li et al.[46] used Cu to replace Mn in Ni-Mn-Sn alloys and found that the fracture strength of the $Ni_{44}Mn_{43}Sn_{11}Cu_2$ alloy with a dual-phase structure was as high as 1150 MPa. The elastic modulus could reach 400 GPa, which was twice that of the single-phase Ni-Mn-Sn-Cu alloy.

It has been reported that the doping of a certain amount of the ferromagnetic element Fe into Ni-Mn-Ga alloys can improve the magnetic properties of the alloy; thus, the doping of the Fe element, which might be effective in enhancing the mechanical properties of Ni-Mn-based magnetic SMAs, has attracted attention[88]. Similar to Cu doping, Fe doping can also improve the plasticity of the alloy, but Fe doping more likely results in the formation of a second phase. In 2001, Cherechukin et al.[89] found that polycrystalline Ni-Mn-Ga alloy doped with a small amount of Fe could improve the plasticity of the alloy without affecting its magnetocaloric properties. Later, Feng et al.[88] replaced Mn with Fe in the Ni-Mn-Ga alloy; the as-spun $Ni_{52}Mn_9Fe_{15}Ga_{24}$ single crystal had significantly improved plasticity, and its Young's modulus along the [001] direction and Vickers hardness reached 13.7 GPa and 6.4 GPa, respectively. Wang et al.[90] systematically studied the effects of Fe content on the hardness and toughness of the $Ni_{48.7}Mn_{30.1-x}Fe_xGa_{21.2}$ alloy and found that the hardness and toughness increased after Fe doping. Studies on the fracture of alloys indicated that the $Ni_{48.7}Mn_{30.1}Ga_{21.2}$ (x=0) alloy had an intergranular fracture with a fracture toughness of 12 $N/mm^{3/2}$; while the $Ni_{48.7}Mn_{19.1}Fe_{11}Ga_{21.2}$ (x=11) alloy possessed a transgranular fracture with a fracture toughness of 18 $N/mm^{3/2}$. The results indicated that Fe doping could

strengthen the grain boundaries and suppress the tendency of intergranular fracture. Feng et al.[91] found that with an increase in Fe content, the compressive strength and fracture strain of the $Ni_{50}Mn_{34}In_{16-y}Fe_y$ alloy increased, and a transition from intergranular to transgranular fractures occurred; when the Fe content was more than 5 at.%, the second phase was precipitated at the grain boundaries and inside the grain interiors; when the Fe content was 8 at.%, the compressive strength and maximum compressive strain reached 1200 MPa and 15.8%, respectively.

The ductile second phase formed after doping can improve the plasticity of Ni-Mn-based alloys. However, the second phase hinders the martensitic transformation and increases the hysteresis. The reason is that during the phase transition, the interface between the matrix and the second phase has lattice distortion, which generates dislocations and hinders the migration of the phase interface. As a result, the phase transition hysteresis increases.

The ductility of Ni-Mn-based alloys can be improved by doping the B element, introducing second-phase particles at grain boundaries. In 2011, Nong et al.[92] studied Ni-Mn-Sb alloys with B doping and found that if the content of the B element was increased from 1 at.% to 3 at.%, the Curie temperature increased from 330 K to 345 K, and the martensitic transformation temperature decreased from 300 K to 262 K. Prusik et al.[93] investigated the Ni-Mn-Co-In alloy doped with the B element and found that the B element facilitated the formation of “Co-rich and In-deficient” γ phase and $M_{23}B_6$ phase. When the B content reached 1 at.%, the second phases formed a “sub grain” structure within the grain interiors and at the grain boundaries. Aydogdu et al.[94] added the B element to Ni-Mn-Ga alloys and found that the compressive strength and plasticity of the alloys were improved. When the content B doping was 1 at.%, the compressive strength reached 1100

MPa, and the fracture strain reached 30%. The compressive strength and fracture strain of the undoped $Ni_{51}Mn_{28.5}Ga_{19.5}$ alloy were only 300 MPa and 11.5%, respectively. However, when the content of B doping increased from 1% to 3%, the yield strength of the alloy increased, and the ductility decreased. Zhang et al.[95] found that by doping B, the grains of the $(Ni_{54}Mn_{25}Ga_{21})_{100-x}B_x$ alloy were significantly refined. When the content of B doping was 3 at.%, the grain size decreased from several hundred microns in undoped alloys to 20 μm in the doped ones, and the compressive strength of the alloys with B doping first increased and then decreased with increased content of B doping. When the content of B doping was 1 at.%, the compressive strength of the alloy was the highest (1100 MPa), which was about 700 MPa higher than that of the undoped $Ni_{54}Mn_{25}Ga_{21}$ alloy.

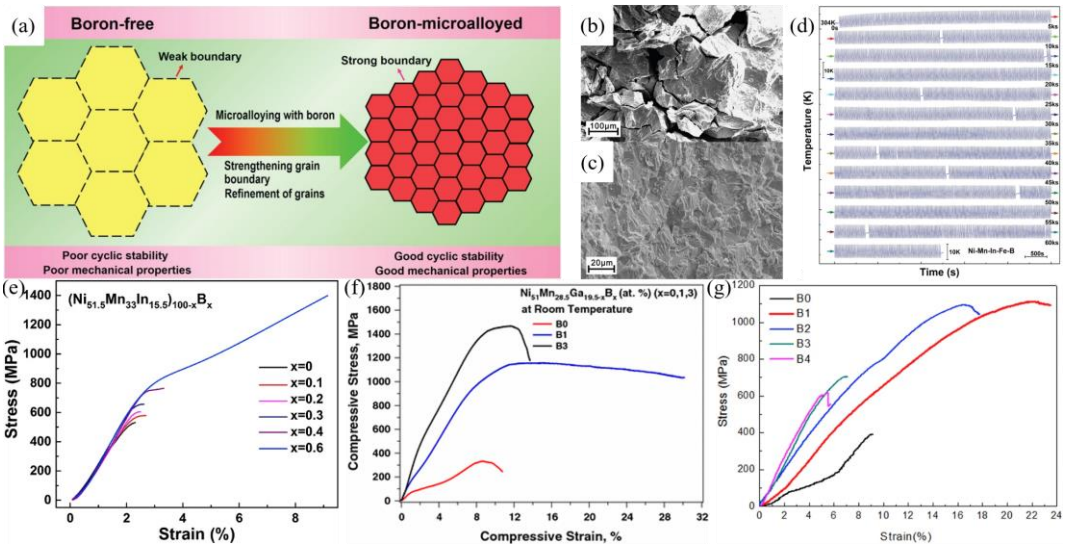

Fig. 1-7 Toughening effect of boron in Ni-Mn-based magnetic alloy

(a) schematic of boron microalloying[96]; (b) fracture SEM of $Ni_{51.5}Mn_{33}In_{15.5}$[96]; (c) fracture SEM of $(Ni_{51.5}Mn_{33}In_{15.5})_{99.4}B_{0.6}$[96]; (d) temperature variation during cyclic loading[96]; (e) compressive stress-strain curves for the $(Ni_{51.5}Mn_{33}In_{15.5})_{100-x}B_x$ alloys[97]; (f) ductility behavior of the $Ni_{51}Mn_{28.5}Ga_{19.5-x}B_x$ alloys[94]; (g) compressive stress-strain curves of alloys[95]

According to the microalloying theory, which is different from the second phase strengthening and toughening mechanisms, Yang et al.[97] proposed that

micro-alloying could enhance the grain boundary strength and refine the grains, thereby improving the mechanical properties and cycling stability of alloys with B doping, as shown in Fig. 1-7(e). For example, the $Ni_{51.5}Mn_{33}In_{15.5}$ alloy failed after 20 stress cycles, while the $(Ni_{51.5}Mn_{33}In_{15.5})_{99.7}B_{0.3}$ alloy remained basically stable after more than 150 stress cycles[96]. Tang et al.[3] studied the Ni-Mn-In alloy with co-doped Cu and B elements. With increasing content of Cu doping, the Ni-rich second phase was precipitated in the matrix, which improved the mechanical properties of the alloy; during 100 cycles elastocaloric tests on the $(Ni_{52}Mn_{31}In_{16}Cu_1)_{99.8}B_{0.2}$ polycrystalline alloys can maintain stable adiabatic temperature changes even after 100 stress cycles. The results indicate that stability in the plasticity and elasticity of the alloy were improved after Cu and B co-doping.

It is worth noting that although the doping amount of B element in Ni-Mn-based alloys can be as high as 5 at.%, the content of microalloying generally does not exceed 0.6 at.%. This can be explained by the differences in the toughening mechanisms related to B element microalloying and the formation of second phase, as follows: the microalloying of the B element promotes the formation of the coordination compound $NiBH^+$, and $NiBH^+$ exhibits strong grain boundary segregation. Hydrogen is bonded to B and Ni and trapped in the NiBH clusters, effectively reducing hydrogen diffusion along grain boundaries and suppressing hydrogen embrittlement. Therefore, B element microalloying increases grain boundary strengthening, which inhibits the formation and propagation of cracks along the grain boundaries, thereby improving the toughness of the alloy.

1.4 Optimization of Refrigeration Performance in Ni-Mn-Sn-based Alloys

1.4.1 Optimization of Refrigeration Performance in Ni-Mn-Sn-based Alloys via Size Effect

In the practical application of refrigeration technology, heat exchange performance is a crucial consideration factor. To improve heat exchange efficiency, solid refrigeration materials should have a high specific surface area, for example, by designing special shapes such as ribbons and fibers. Using the material size effect, it can significantly affect the mechanical behavior of materials at micro and nano scales. Nanoindentation, tensile and torsion tests of micron diameter fibers, as well as ribbon bending and micro tensile tests show that the yield strength of the material increases with the decrease of diameter / thickness. Therefore, when the size of Ni-Mn-based alloy is in micro nano scale, the material size is equivalent to the characteristic length related to the main deformation mechanism, and the mechanical properties will change greatly. Therefore, it is necessary to investigate the internal relationships among microstructure, material size, and properties.

In single-crystal Ni-Mn-Ga alloys, large strains can be induced by an applied magnetic field[98-100], which could be related to the low resistance of the motions of twin boundaries. However, single-crystal alloys are difficult and expensive to prepare. Polycrystalline alloys can be prepared rapidly and at a low cost by casting, but they have small magnetic field-induced strain due to the constraint effects of grain boundaries on the motion of the twin boundary. Dunand and Müllner[101] proposed that when the grain size of the Ni-Mn-Ga alloy is compatible with the characteristic sizes of the samples, such as the powder diameter, fiber diameter, film thickness, and the pore node diameter of porous materials, as shown in Fig. 1-8(a), the resistance of the motions of the twin boundary in the alloy can be reduced. In this way, there are more free surfaces around the grains, and the constraint effects

of the grain boundaries are greatly reduced during the reorientation of the martensitic variant, improving the magnetic field-induced strain.

Studies have shown that micron-diameter fibers are fabricated to reduce grain boundary and sample size constraints. At the same time, the introduction of texture can improve the superelasticity and plasticity of the material. Ueland et al.[102] first proposed the concept of "Oligocrystalline structure", and defined "Oligocrystalline structure" as the grain morphology in which the total surface area of the alloy exceeds the total grain boundary area. The Cu-Zn-Al shape memory alloy is prepared into fibers, and the bamboo-like oligocrystalline structure is obtained by heat treatment. The fatigue life of the shape memory alloy is about 10^3, which is two orders of magnitude higher than that of the polycrystalline bulk alloy. Subsequently, Zhukov et al.[103-107] prepared Ni-Mn-Ga, Ni-Mn-In and Ni-Co-Mn-In series fibers by the glass coating method, and studied the microstructure, phase composition and magnetic properties of the fibers. They enriched the research of Ni-Mn-based "oligocrystalline structure" alloy. Zhang et al.[108] found that the maximum recoverable strain of superelasticity was 11.2% and the critical stress was 115 MPa in $Ni_{54.0}Mn_{24.1}Ga_{21.9}$ alloy fibers, as shown in Fig. 1-8(c). Glock et al.[109] studied the effect of Annealing on the mechanical behavior and magnetic properties of the original 7M martensitic fiber. It is found that long-time annealing makes the grain grow, the fiber changes from polycrystalline to oligocrystalline structure, and the reorientation stress of twin variants decreases. Liu et al.[32] observed a large recoverable strain of 6.0% in $Ni_{44.5}Co_{5.5}Mn_{39.5}Sn_{10.5}$ fibers with a superelastic stress hysteresis of only 23 MPa. Fig. 1-8(d) shows the stress-strain curves of the fibers under different stress levels. Ding et al.[110] reported that the $Ni_{52.8}Mn_{23.8}Ga_{23.4}$ alloy fiber has a recoverable strain of 14.0%. Li et al.[111]

obtained 20% tensile recoverable strain in the <001>$_A$ direction of $Ni_{50.0}Mn_{31.4}Sn_{9.6}Fe_{9.0}$ alloy fiber, which is the largest recoverable strain of Ni-Mn-based alloys reported so far. In conclusion, if the free surface area caused by the reduction of material size is increased, the formation of an oligocrystalline structure can significantly increase the shape memory and superelastic strain recovery rate of the alloy, and improve the fatigue life compared with the oligocrystalline state produced by heat treatment. However, oligocrystalline structures tend to be easily formed in small-scale materials.

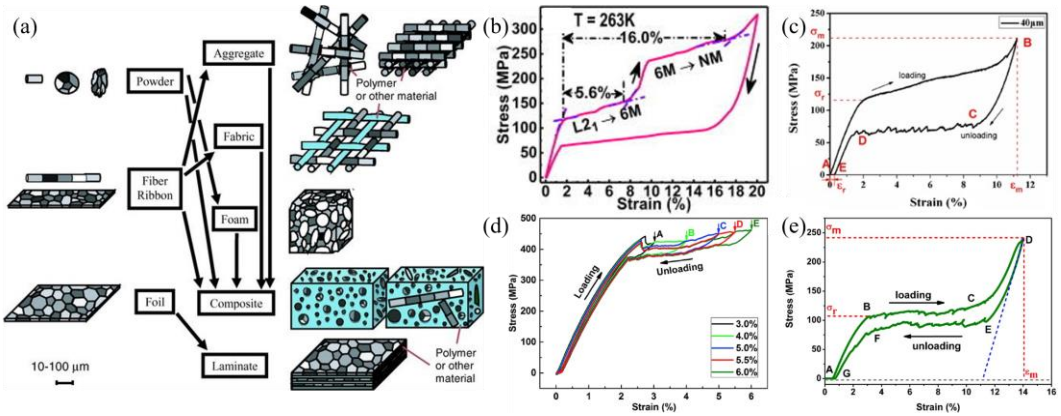

Fig. 1-8 Toughening effect of the size effect in Ni-Mn-based magnetic alloy (a) schematic illustration of the size effect[101]; tensile stress-strain curve of the (b) $Ni_{50.0}Mn_{31.4}Sn_{9.6}Fe_{9.0}$ microwire[111]; (c) $Ni_{53.96}Mn_{24.12}Ga_{21.92}$ microwires[108]; (d) $Ni_{44.5}Co_{5.5}Mn_{39.5}Sn_{10.5}$ microwire[32]; (e) $Ni_{52.87}Mn_{23.82}Ga_{23.32}$ microwire[110]

The Ni-Mn-In thin ribbons prepared by the rapid cooling strip method have uniform composition, well-developed columnar crystals and texture, and the brittleness of the material is also improved to a certain extent. Feng et al.[112] prepared $Ni_{45}Mn_{36.6}In_{13.4}Co_5$ alloy ribbons with different thicknesses. The ribbons have a texture in the [001] crystal direction, and the fracture strength in this direction is improved. In addition, the texture of the ribbon is affected by the heat treatment method, and the texture weakens after annealing. The higher the temperature, the more obvious the weakening phenomenon. Hernando et al.[113]

prepared $Mn_{50}Ni_{40}In_{10}$ ribbon under the high cooling speed strip throwing process ($\sim 10^4-10^6$ Ks^{-1}). The growth directions of austenite and martensite are [400] and [040] respectively, which are perpendicular to the strip surface. By applying magnetic fields in different directions, it is found that the magnetocaloric properties of the ribbons are improved in a specific direction. Inspired by the work of Hernando et al., researchers further studied the effect of texture on microstructure and mechanical properties. Akkera et al.[114] prepared Ni-Mn-In films with a thickness of 90−655 nm by magnetron sputtering, it was found that the grain size and crystallinity increased with the film thickness. Nanoindentation studies show that the film thickness of 153 nm has the highest hardness value (7.2 GPa) and an elastic modulus of 190 GPa.

It should be noted that during the preparation of ribbon by rapid solidification, the melt crystallizes under a large degree of undercooling, resulting in a metastable structure. At the same time, substructures such as high-density dislocations are generated in the process; their stored deformation energy can be used as the driving force of recrystallization, but it will also affect the mechanical and functional properties of the alloy. Therefore, the ribbon alloy prepared by rapid solidification process often needs an annealing treatment.

1.4.2 Optimization of Refrigeration Performance in Ni-Mn-Sn-based Alloys via Multi-field Cooperative Regulation

Ni-Mn-Sn-based magnetic alloys exhibit concurrent structural and magnetic phase transitions, accompanied by changes in physical properties such as magnetic moment, lattice parameters, and heat capacity during the transition process[2]. These materials can undergo phase transitions induced by temperature, stress (or hydrostatic pressure), and magnetic fields, thereby acquiring various functional

characteristics. Consequently, the caloric effects based on magnetoelastic coupling and multi-field stimulation have attracted significant attention in recent years. The central research focus involves understanding the coupling mechanisms between uniaxial stress (or hydrostatic pressure) and magnetic fields in magneto-structural phase transition materials, along with their influence on phase transition caloric effects. This understanding constitutes the key to effectively regulating multi-field caloric effects.

Oliveira first theoretically discussed the magnetocaloric effect under pressure assistance and the barocaloric effect under magnetic field assistance in first-order magneto-structural phase transition compounds[115]. Subsequently, Stern-Taulats et al.[51] building upon the thermodynamic framework established by Planes et al.[116] investigated the relationship between isothermal entropy change and variations in both pressure and magnetic field, as illustrated in Fig. 1-9.

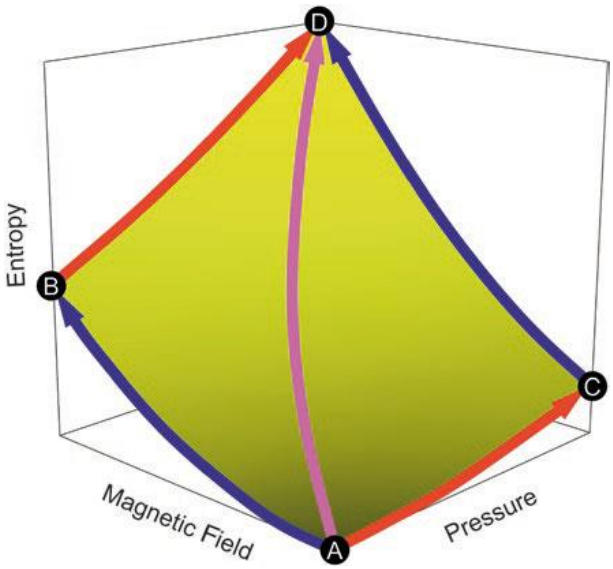

Fig. 1-9 Entropy change under the combined action of pressure and magnetic field[51]

Since entropy is a state function, the caloric effects can be driven either simultaneously or sequentially by multiple external fields. To achieve the entropy change along path A→D, pressure can be applied under zero magnetic field (path

A→C), followed by magnetic field application under constant pressure (path C→D). Alternatively, the magnetic field can be applied first under zero pressure (path A→B), then pressure under constant magnetic field (path B→D). The resulting entropy change is independent of the driving path of external fields. However, it should be noted that due to cross-coupling effects, the magnitude of the caloric effect driven by one field is influenced by the concurrent application of another field. For instance, the magnetocaloric effect differs when driven under zero pressure (path A→B) versus under pressure (path C→D).

Compared with caloric effects induced by a single external field, multi-field cooperative regulation of caloric effects offers the following advantages[51, 117, 118]: (1) Broadening the phase transition temperature window to achieve caloric effects over a wider refrigeration working range; (2) Providing a larger parameter space through multi-field regulation, which can effectively reduce the critical field for phase transitions and consequently enhance the material's fatigue life; (3) Overcoming hysteresis through multi-field regulation to improve phase transition reversibility; (4) Increasing the entropy change during phase transition to boost refrigeration efficiency.

1.5 Main Research Contents of this Subject

Based on the comprehensive review, Ni-Mn-Sn magnetic alloys stand out among first-order phase transition refrigerants due to their remarkable advantages: low production costs and absence of toxic elements; tunable phase transition temperatures through alloying doping, demonstrating potential for near-room-temperature applications; and simultaneous ferroelastic and ferromagnetic ordering characteristics, which provide a fundamental basis for multi-field regulation of caloric effects.

Through systematic analysis of research progress on Ni-Mn-Sn alloys, this Thesis addresses three critical scientific challenges hindering their room-temperature refrigeration applications: (1) Unclear mechanisms of quaternary alloying doping, with current studies lacking systematic understanding of microscopic mechanisms for Fe, Cu, and B doping; (2) Poor refrigeration performance, including low isothermal entropy change, narrow operating temperature range, and phase transition temperature not near room temperature; (3) The structural damage caused by intrinsic brittleness restricts the full utilization of the elastocaloric effect.

To overcome these challenges, the proposed research focuses on the following aspects:

(1) Using first-principles calculations to investigate how Fe, Cu, and B doping as fourth elements affects total energy characteristics, lattice constant evolution, and electronic density of states in the base $Ni_{50}Mn_{37.5}Sn_{12.5}$ ($Ni_8Mn_6Sn_2$) alloy configuration. Based on computational results, Fe-doped Ni-Mn-Sn alloys were designed and fabricated to study doping effects on crystal structure, martensitic transformation temperature, latent heat, and transformation hysteresis, achieving magneto-structural coupling in $Ni_{47}Mn_{38}Sn_{12}Fe_3$ alloy with near-room-temperature transitions.

(2) From a thermodynamic perspective, this study systematically investigates the martensitic transformation process by decoupling the reversible and nonreversible components during phase transition. The intrinsic relationship between nonreversible components and energy dissipation during phase transition is revealed, along with their influence on transformation hysteresis. By elucidating the impact of reversible components on the alloy's refrigeration performance, this

work addresses the characterization challenges of adiabatic temperature changes in elastocaloric effects, thereby providing guidance for developing high-performance Ni-Mn-Sn magnetic alloys.

Building upon first-principles calculation results and analysis of reversible thermal components during phase transition, Cu-doped Ni-Mn-Sn alloys were designed and fabricated. The research examines the effects of Cu doping on the alloy's crystal structure and magnetic properties, analyzing how two distinct magneto-structural coupling states influence the magnetocaloric effect. Special focus is given to investigating the elastocaloric performance, operational temperature range, and cyclic stability of the optimized $Ni_{47}Mn_{38}Sn_{12}Cu_3$ alloy composition.

(3) Through co-doping with Cu and B, this study investigates the superelasticity and elastocaloric effects of the alloys. While enhancing the cyclic stability of the elastocaloric effect in Ni-Mn-Sn-Cu-B alloys, we explore multi-field cooperative regulation to develop methods for broadening the working temperature range of caloric effects. The Ni-Mn-Sn-Cu-B alloy polycrystalline ribbons were fabricated using the melt-spinning technique, with subsequent optimization of the preparation and heat treatment processes for high-quality ribbons. The influence of crystallographic orientation on the ribbons' magnetic properties and magnetocaloric performance was systematically analyzed.

Chapter 2 Materials and Experimental Methods

2.1 Raw Materials and Fabrication Process

2.1.1 Raw Materials

The Ni-Mn-Sn-Fe, Ni-Mn-Sn-Cu, and Ni-Mn-Sn-Cu-B alloy ingots were prepared using induction melting technology, while the Ni-Mn-Sn-Cu-B ribbons were fabricated via the single-roller melt-spinning method. All metallic raw materials employed were elemental metals with purity exceeding 99.98 wt.%, with Table 2-1 detailing the purity specifications of metals and boron powder.

Table 2-1 Composition, purity, shape, and manufacturer of the raw materials

Composition	Purity (wt.%)	Shape	Manufacturer
Ni	99.99%	Bulk	Alfa Aesar
Mn	99.98%	Flaky	Alfa Aesar
Sn	99.99%	Bulk	GRINM
Cu	99.99%	Bulk	GRINM
Fe	99.99%	Granular	GRINM
B	99.99%	Powder	GRINM

2.1.2 Fabrication and Heat Treatment Method

2.1.2.1 Fabrication and Heat Treatment Method of Bulk Ingot

A German Induret-Compact high-frequency induction melting furnace was used to prepare the alloy ingots. Fig. 2-1 shows the furnace and its internal chamber. The main steps for ingot preparation were as follows:

(1) Raw Material Cleaning:

The oxide film on Ni surfaces was removed using a mixed solution of HNO_3

and HCl with a volume ratio of 1:3, followed by distilled water rinsing and drying. The oxide film on Sn surfaces was eliminated with 10% NaOH solution, then rinsed with distilled water and dried. The oxide film on Cu surfaces was removed with 10% dilute nitric acid, subsequently cleaned with acetone and oven-dried. For pure Mn metal which oxidizes easily, its surface oxide layer was removed using 5% nitric acid-alcohol solution, with immediate melting after cleaning.

(2) Raw Material Weighing:

The metallic raw materials were weighed according to nominal composition using a G324A high-precision balance. Considering Mn's high volatility, an additional 2 wt.% of Mn was added.

(3) Loading Weighed Materials into the Crucible:

To prevent volatilization loss, volatile Mn was placed at the crucible bottom, while high-melting-point, less-volatile metals were positioned above.

(4) Equipment Operation:

Power was activated, cooling water circulation initiated, and after adjusting the copper mold position, melting commenced.

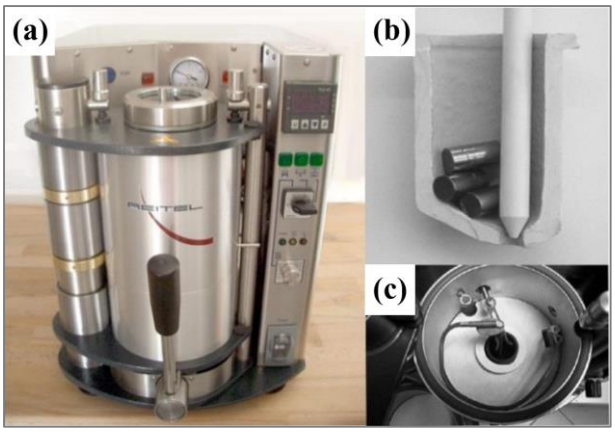

Fig. 2-1 Schematic diagram of induction melting furnace
(a) entire appearance; (b) ceramic crucible; (c) cavity

To minimize compositional segregation and enhance homogeneity of the as-

cast ingots, homogenization heat treatment was performed following this procedure:

(1) Alloy Cleaning and Drying:

The ingots were immersed in acetone and ultrasonically cleaned for 5−10 min;

Subsequently dried at 373 K for 10 min.

(2) Quartz Tube Preparation:

Two perforated quartz tubes of different diameters were selected;

Ultrasonically cleaned in 5 wt.% dilute nitric acids for 20 min;

Rinsed with distilled water and oven-dried;

Joined at one end using oxy-acetylene flame;

After ingot loading, the larger tube end was sealed;

The smaller tube was necked down to Φ3−5 mm at 1/3 length from its end.

(3) Sample Preparation for Heat Treatment:

Cleaned ingots were placed in the sealed end of quartz tube;

100 μm-thick Ti foil strips (2 mm wide) were twisted into loose balls;

Positioned at tube midpoint as oxygen getter;

Mn particles were added to compensate for volatilization;

The tube was evacuated to 0.5 Pa and backfilled with high-purity Ar (1 atm);

This purge cycle was repeated three times before final sealing;

Heat treatment at 1173 K for 24 h in resistance furnace;

Rapid quenching in ice water by fracturing the quartz tube.

2.1.2.2 Fabrication and Heat Treatment Method of Ribbon

Alloy ribbons were fabricated using a single-roller melt-spinning apparatus. The as-cast alloy ingots were machined into slender strips and loaded into quartz tubes with a 1 mm diameter nozzle at the bottom, with the tube height properly adjusted. The melt-spinning chamber was first evacuated and then backfilled with

high-purity argon. Under argon protection, the alloy was heated to its molten state and rapidly ejected onto a water-cooled copper roller through argon pressurization, resulting in the formation of metallic ribbons. A GDJ500C high-vacuum melt-spinning system was employed, with the schematic diagram shown in Fig. 2-2. This equipment utilizes induction coil heating for metal melting, with the following detailed procedures:

(1) Material Preparation:

The alloy ingots were cut into ~5×5×5 mm^3 pieces;

Loaded into pre-cleaned quartz tubes (150 mm length, 18 mm diameter) with 1 mm nozzle;

Positioned within the induction coil at optimal height and secured by clamps.

(2) Equipment Setup:

The chamber was sealed and evacuated to 9×10^{-4} Pa;

The vacuum valve was closed and high-purity argon was introduced to ~0.5 Pa;

(3) Melt Ejection:

Cooling water circulation was initiated and roller speed adjusted;

Induction heating was activated with proper power setting;

Quartz tube position was fine-tuned relative to the coil;

Upon complete melting, the foot pedal was pressed for instant argon injection;

The molten metal was ejected onto the high-speed rotating copper roller;

Rapid solidification yielded continuous ribbons.

(4) Ribbon Collection:

The solidified ribbons were detached by centrifugal force;

Partial ribbons were collected automatically while others remained in chamber;

After ~15 min cooling, the chamber was opened for collection;

The final ribbons measured 15−50 μm in thickness and 2−4 mm in width;

Table 2-2 summarizes the detailed processing parameters for Ni-Mn-Sn-Cu-B ribbon fabrication.

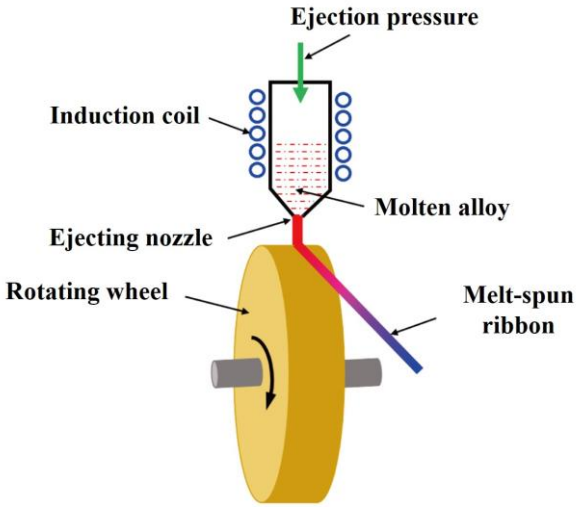

Fig. 2-2 Schematic of the melt-spinning process

Table 2-2 Ribbon preparation parameters

No.	Heating power (kW)	Rotational speed (rpm)	Spray casting pressure (MPa)	Nozzle diameter (mm)
1	5	1200	0.1	0.5
2	5	1800	0.1	0.5
3	8	1200	0.1	0.5
4	8	1800	0.2	0.5
5	8	1800	0.1	1.0
6	8	1800	0.1	1.5
7	11	1200	0.1	0.5
8	11	1800	0.1	0.5
9	13	1200	0.1	0.5
10	15	1800	0.1	0.5

To enhance the ordering degree and adjust the grain size of the as-spun ribbons, appropriate heat treatments were performed after fabrication. The cleaning and

drying procedures for both the ribbon alloys and quartz tubes, as well as the sample preparation for heat treatment, followed the same protocols as those described previously for alloy ingots. The heat treatment process consisted of two stages:

(1) Grain Growth Treatment:

Conducted at 1173 K with varying holding times: 10 min, 30 min, and 60 min.

(2) Ordering Treatment:

Primary stage: 973 K for 2 h;

Secondary stage: 773 K for 24 h;

Controlled cooling at 5 K/min between 1173 K to 973 K and 973 K to 773 K.

2.2 Calculations Research Methods

The effects of doping of Cu, Fe and B on the crystal structure, energy, and density of states of Ni-Mn-Sn alloys were systematically studied by first-principles calculation using the Vienna Ab-initio Software Package (VASP)[119] package. The exchange-correlation were based on Perdew-Burke-Enzerh (PBE) functional in the generalized gradient approximation (GGA)[120] framework, with spin-polarized treatment for electrons. Using the plane wave pseudopotentials, the interaction between ions and electrons was described by the projected augmented wave (PAW) method[121].

The electronic configurations of the involved elements were Ni($3d^8 4s^2$), Mn($3d^6 4s^1$), Sn($5s^2 5p^2$), Cu($3d^{10} 4s^1$), Fe($3d^6 4s^2$), B($2s^2 2p^1$). The convergence tolerance for the calculations was selected as 10^{-5} eV, and the cutoff of the energy plane wave was set to be 600 eV. The Brillouin zone was sampled using the Monkhorst-Pack method[122], and there is a 15×15×15 *k*-point mesh for a unit cell containing 16 atoms with the $L2_1$ structure.

2.3 Analytical Testing and Characterization Methods

2.3.1 Microstructure and Characterization

2.3.1.1 Microstructure Observation

(1) Optical Microscope Observation

The metallographic microstructure of the alloy was observed using an Olympus PMG3 optical microscope (OM). Before examining the morphology of martensitic twins under polarized light, the samples underwent a cold-hot air cycling pretreatment to induce martensitic surface relief. The metallographic sample preparation steps were as follows:

The specimens were initially ground sequentially with 400#, 800#, 1000#, 1500#, 2000#, and 3000# abrasive papers. Mechanical polishing was then performed using a 0.5 μm diamond polishing suspension. The sample surface was subsequently etched with a solution composed of 1 g $CuCl_2$, 30 g $FeCl_3$, 0.5 g $SnCl_2$, 50 mL concentrated hydrochloric acid, 500 mL ethanol, and 500 mL deionized water to reveal the grain morphology.

For ribbon samples, hot mounting was required before observation. The ribbons were embedded in HM2 conductive mounting resin using an XQ-2B metallographic mounting press at a temperature of 400 K, followed by a 5-minute holding period. The mounted samples were then ground with 1000#, 1500#, and 2000# abrasive papers and mechanically polished with a 0.5 μm diamond polishing suspension.

(2) Scanning Electron Microscope Observation

The surface morphology, microstructure, and compressive fracture morphology of bulk alloys and ribbon samples were observed using a Zeiss-SUPRA55 scanning electron microscope (SEM). The elemental composition and content on the sample surfaces were analyzed using the equipped Oxford energy-

dispersive X-ray spectroscopy (EDS) system.

To ensure the relative accuracy of compositional analysis, the operating parameters were standardized as follows: accelerating voltage of 20 kV, emission current of 97 μA, working distance of 8−10 mm, probe current of 50 μA, and signal acquisition time exceeding 60 s. For EDS analysis, at least five different regions were selected for data collection, and the average composition was calculated. The obtained compositional results were considered valid only when the deviation between measurements was confirmed to be less than 0.5 at.%.

(3) Transmission Electron Microscopy Observation

Transmission electron microscopy (TEM, Tecnai G^2F30) and high-resolution TEM (HRTEM) were used at room temperature to study the microstructures. Samples were cut from the specimens before and after loading-unloading cycles using a focused ion beam (FIB).

2.3.1.2 Phase Identification

The phase composition of both bulk alloys and ribbons was determined using an Empyrean X-ray diffractometer (XRD). Measurements were conducted with Cu-Kα radiation (λ=1.54 Å) at an operating current of 40 mA and voltage of 40 kV, with a scanning range of 20−90 ° and a scan rate of 10 °/min. For bulk specimens, surface preparation involving "coarse grinding-fine grinding-polishing" was performed before testing. Ribbon specimens were carefully aligned and mounted on single-crystal Si substrates for measurement. The acquired diffraction patterns were analyzed and indexed using Jade 6.0 software.

2.3.1.3 Thermal Analysis

(1) Phase Transition Behavior Characterization

The phase transition behavior of the alloy samples was analyzed using a TA-

Q200 differential scanning calorimeter (DSC). To ensure relative accuracy of the results, standardized working parameters were applied as follows: all test samples were uniformly processed into small discs measuring Φ2×0.1 mm^3, acid-washed to remove surface oxide layers, and then loaded into the instrument's aluminum crucibles. Measurements were conducted under a helium atmosphere with a heating/cooling rate of 10 K/min. The transformation latent heat for austenite-to-martensite ($\Delta H_{A\rightarrow M}$) and martensite-to-austenite ($\Delta H_{M\rightarrow A}$) transitions were calculated through integration of the endothermic and exothermic peaks in the DSC curves, respectively.

(2) Reversible and Nonreversible Components Characterization

To investigate the relationship between energy dissipation at moving interfaces and thermal hysteresis during phase transitions, the evolution of reversible and nonreversible signals during thermoelastic martensitic transformations was analyzed using modulated differential scanning calorimetry (MDSC).

Using a reference sample of high-purity indium, the calorimeter was calibrated for cell constant, baseline slope and temperature reading. The C_p was calibrated utilizing a standard sample of sapphire using the same experimental conditions at the target temperature. Since MDSC is sensitive to sample size and surface condition, the test samples of Φ2×0.7 mm^3 were used. The modulation heat flow period and heating/cooling rate need to be coordinated to ensure an appropriate number of oscillation cycles in the MT temperature range. The heating/cooling rate is selected as 5 K/min, with modulation periods of 40 s, 60 s, 80 s, 100 s, and 120 s. The modulation amplitude is selected as 5 K.

2.3.2 Performance Test

2.3.2.1 Compression Test

(1) Compression Stress-strain Test

The compressive mechanical properties of the samples were tested using an Instron-5966 universal testing machine. The equipment is equipped with an environmental chamber, an electrical resistance heating system, and a liquid nitrogen cooling system, enabling mechanical property testing of samples within a temperature range of 213−473 K. The test samples were machined into cylinders (Φ3×4.5 mm^3) by wire cutting. Prior to testing, the environmental chamber temperature was adjusted to the target test temperature and maintained for 10 minutes. Subsequently, the yield strength and fracture strength of the samples were measured.

(2) Superelastic Training

Place the test sample at its A_f temperature using an environmental chamber, hold for 10 minutes, and load unload at a strain rate of 3.3×10^{-4} s^{-1} for 10 cycles to complete superelastic training.

(3) Superelastic Testing

Prior to testing, the environmental chamber temperature was adjusted to the target test temperature and maintained for 10 minutes. Subsequently, compressive stress was applied at a strain rate of 3.3×10^{-4} s^{-1} while recording the stress-strain curve.

(4) Elastocaloric Performance Testing

The characterization of elastocaloric properties can be performed through indirect and direct methods. The indirect method involves acquiring a series of superelastic curves at different temperatures, followed by computational analysis.

For direct characterization, a FLIR-A325sc infrared camera system is employed to directly measure temperature variations on the sample surface. The infrared data is processed using FLIR's Research IR software for temperature reading of target regions.

To ensure measurement accuracy, K-type thermocouples are welded onto the compressed sample surface, with temperature data acquired through an Omega OM-DAQ-USB-2401 data acquisition module at 1 Hz sampling frequency. The adiabatic temperature change measurement was performed with loading at a strain rate of 3.3×10^{-2} s^{-1} followed by 30 s of load maintenance, subsequent rapid unloading at the same strain rate of 3.3×10^{-2} s^{-1}, and finally a 30 s temperature stabilization period.

2.3.2.2 Magnetism and Magnetocaloric Properties Measurement

The magnetic properties of the samples were measured using Quantum Design's Physical Property Measurement System (PPMS) to obtain both magnetization curves (*M-T* curves) and isothermal magnetization curves (*M-H* curves). Before *M-T* curve measurement, the sample was first heated above the A_f temperature and held for 5 min, followed by application of a magnetic field. The sample was then cooled at 3 K/min to below the M_f temperature and held for 5 min, before being reheated at 3 K/min to above the A_f point while recording the complete *M-T* curve throughout the process.

For *M-H* curve measurements, the Loop method was employed to eliminate "spurious peak" effects by first cooling the sample to complete martensitic state (approximately 150K), then heating at 10 K/min to 10K below the test temperature ($T_{test}-10$), followed by slow heating at 1 K/min to the target temperature (T_{test}) with a 2-minute stabilization before conducting *M-H* curve measurements, with this

procedure repeated before each magnetization curve test.

Furthermore, a series of *M-H* curves were obtained near first-order and second-order phase transitions at various temperatures, and the Maxwell relation or Clausius-Clapeyron equation was applied to calculate the isothermal entropy change ΔS_m for evaluating the magnetocaloric effect. The specific method is as follows: Determine the temperature at which the magnetization intensity changes most dramatically during the phase transition process by taking the first derivative of the magnetization curve. Using this temperature as the center, select 1 K, 3 K, 5 K, and 10 K as temperature intervals to determine the test temperature.

When the magnetic field is measured perpendicular to the grain growth direction in the ribbon, the demagnetizing field is negligible. However, when measured parallel to the grain growth direction, the ribbon sample exhibits a demagnetizing effect that requires correction. The effective magnetic field is given by $H_{eff}=H_{ext}-N_dM$, where the demagnetizing factor N_d is taken as 1.

The magnetization curve under hydrostatic pressure was measured using a vibrating sample magnetometer (VSM, Versalab, Quantum Design) equipped with a copper-beryllium clamp pressure chamber (Quantum Design) in the temperature range of 200 to 400 K, under a magnetic field variation of up to 3 T and a hydrostatic pressure of up to 10 kbar. The pressure transmission medium was Daphne 7373 oil. The value of the hydrostatic pressure was calibrated by measuring the shift of the curie transition temperature of Gd which was used as a reference manometer.

Chapter 3 Design of Element Doping for Ni-Mn-Sn-based Magnetic Alloy

3.1 Introduction

As previously mentioned, first-order phase transition solid-state refrigeration materials should meet the following requirements in terms of composition design: (1) a first-order phase transition temperature near room temperature; (2) a large and reversible caloric effect under low magnetic fields; and (3) the best possible mechanical properties to ensure a long service life under cyclic external fields and the ability to be processed into complex shapes conducive to heat exchange. To address these three requirements, element doping can be employed as an effective composition optimization method to synergistically regulate the magneto-structural transition of the alloy while enhancing its mechanical and magnetocaloric properties. According to literature reports, ferromagnetic excitation factors represented by Fe, transition elements represented by Cu, and interstitial atoms represented by B have significant effects on the crystal structure, martensitic transformation, mechanical properties, and electronic structure of Ni-Mn-Sn alloys. So far, researchers have not provided a systematic explanation or comparison of the influence mechanisms of these three types of atoms on the martensitic transformation and properties of Ni-Mn-Sn alloys. Therefore, elucidating the impact mechanisms of these three atoms on the crystal structure, martensitic transformation, and properties of Ni-Mn-Sn alloys is a highly meaningful work.

Based on the above analysis, this chapter first employs density functional theory (DFT) to analyze the influence of Fe, Cu, and B as fourth-component dopants on the total energy variation, lattice constant evolution, and electronic

density of states distribution in Ni-Mn-Sn alloys. It reveals the electronic-level mechanisms by which these three elements affect the martensitic transformation temperature and ferromagnetic transition temperature, while also predicting the range of doping concentrations that meet the design requirements for Ni-Mn-Sn-based magnetic alloys.

Based on the computational results, this chapter selects Fe as the "ferromagnetic excitation factor" to design and prepare a series of $Ni_{50-y}Mn_{38}Sn_{12}Fe_y$ (y=0, 1, 2, 3, 4, 5) alloys. The study investigates the effects of Fe doping on the magneto-structural transition, magnetocaloric effect, and room-temperature compressive properties of the alloys.

3.2 First Principles Investigations of Fe Doped Ni-Mn-Sn Alloy

In 2005, the research results of Krenke et al.[43] demonstrated that only $Ni_2Mn(Mn_xSn_{1-x})$ alloys with non-stoichiometric compositions containing excess Mn atoms exhibit martensitic transformation behavior. Their study revealed that the compositional ratio of ternary alloys directly influences the martensitic transformation temperature. Krenke et al. summarized the relationship between the characteristic martensitic transformation temperature and the Sn content (x) in $Ni_{0.50}Mn_{0.50-x}Sn_x$ alloys (where $0.05 \leqslant x \leqslant 0.25$), as shown in Fig. 3-1[43]. When the Sn content in the alloy is too high, the alloy does not undergo a first-order structural phase transition but instead exhibits a second-order magnetic phase transition in the 300−400 K range. As the Mn content increases, martensitic transformation begins to occur in the alloy, and the martensitic transformation temperature gradually rises with increasing Mn content. Furthermore, they categorized the phase transition temperatures of the alloys based on the range of x values: (1) For $0.12<x \leqslant 0.25$, the alloys undergo a second-order magnetic phase transition, and

the Curie temperature of the austenite phase (T_C^A) slightly increases with increasing x. (2) For 0.05≤x<0.15, the alloys undergo a first-order structural phase transition, and the martensitic transformation start temperature (M_s) decreases with increasing x. (3) For 0.1≤x≤0.12, the martensite phase undergoes a Curie transition, and the Curie temperature of the martensite phase (T_C^M) increases with increasing x. More importantly, within the range of 0.12≤x≤0.15, M_s and T_C^A gradually converge as x decreases[41].

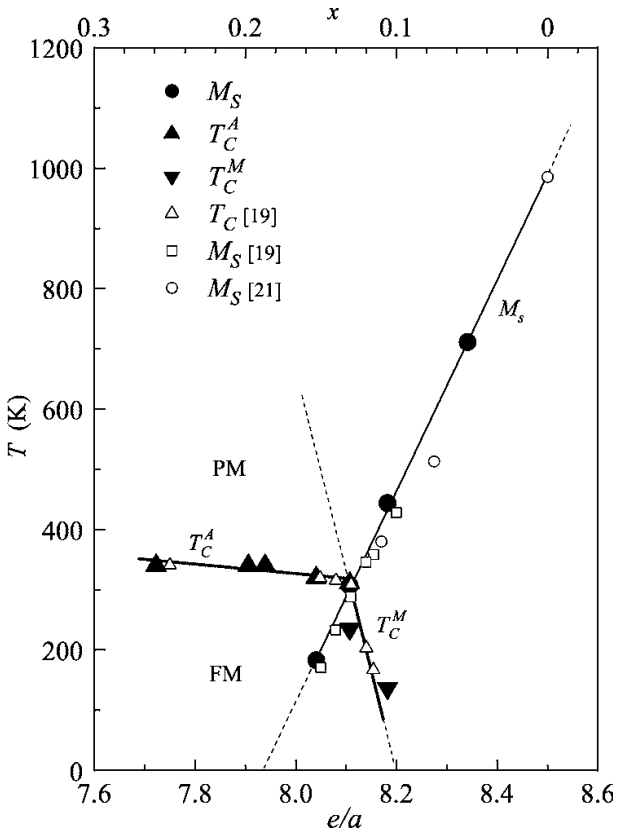

Fig. 3-1 The MT characteristic temperatures as a function of Sn (x) for Ni-Mn-Sn alloys[43]

The regulatory mechanisms of alloy composition on characteristic phase transition temperatures differ from each other, making it impossible to conduct composition design based on a single factor. However, it is certain that the characteristic phase transition temperatures of Ni-Mn-Sn alloys are highly sensitive to composition.

This study aims to achieve a favorable caloirc effect near room temperature, requiring the martensitic transformation temperature of the alloy to be in the vicinity of room temperature (practically controlled within 273−303 K). Considering the influence of element doping on the phase transition temperature of Ni-Mn-Sn-based alloys, it is deduced that the martensitic transformation temperature of the ternary Ni-Mn-Sn alloy should preferably be controlled within the range of 323−353 K. Based on the above theoretical analysis, the $Ni_{50}Mn_{38}Sn_{12}$ alloy composition was selected for investigation.

Based on the first-principles plane-wave pseudopotential method of density functional theory, the electronic structure of alloys can be conveniently obtained to explain their macroscopic physical properties. This section investigates the influence of Fe doping on the total energy variation, lattice constant evolution, and electronic density of states distribution in Ni-Mn-Sn alloys. The study focuses on elucidating the electronic-level mechanisms by which Fe doping regulates the martensitic transformation temperature and ferromagnetic transition temperature of the alloy. Furthermore, it provides an in-depth analysis of the modulation effect of Fe doping on the magnetic properties of the alloy system and its underlying physical nature.

3.2.1 Fe Atomic Preferential Site Occupation

The experimental methods are inadequate for accurately determining the specific lattice site occupation of the fourth component Fe in Ni-Mn-Sn alloys. To address this critical issue, it is essential to systematically investigate the preferential site occupation tendency of Fe atoms from a thermodynamic perspective. This involves constructing models with different site occupation configurations, calculating and comparing their energies to determine the most

stable occupation mode of Fe atoms in the Ni-Mn-Sn alloy lattice.

The stoichiometric $Ni_8Mn_4Sn_4$ alloy has a crystal structure with the space group $Fm\bar{3}m$, where the unit cell consists of 16 atoms. However, the stoichiometric alloy cannot undergo martensitic transformation. Existing studies[123, 124] have shown that martensitic transformation behavior is only observed in non-stoichiometric $Ni_8Mn_{4+x}Sn_{4-x}$ alloys. Based on the selected $Ni_{50}Mn_{38}Sn_{12}$ alloy, an approximate 16-atom $L2_1$ structure was constructed with the composition $Ni_{50}Mn_{37.5}Sn_{12.5}$ ($Ni_8Mn_6Sn_2$) as the base configuration, as illustrated in Fig. 3-2(a). Building upon the $Ni_{50}Mn_{37.5}Sn_{12.5}$ alloy crystal structure[125, 126], three cubic $L2_1$ structures of $Ni_{43.75}Mn_{37.5}Sn_{12.5}Fe_{6.25}$ were established: (1) Fe atoms occupying Ni sites; (2) Fe atoms occupying Mn sites, with Mn atoms substituting Ni atoms; and (3) Fe atoms occupying Sn sites, with Sn atoms substituting Ni atoms. For clarity in discussion, Fe atoms occupying Ni, Mn, and Sn sites are denoted as Fe_{Ni}, Fe_{Mn} and Fe_{Sn}, respectively, as illustrated in the substitution diagrams in Fig. 3-2(b-d).

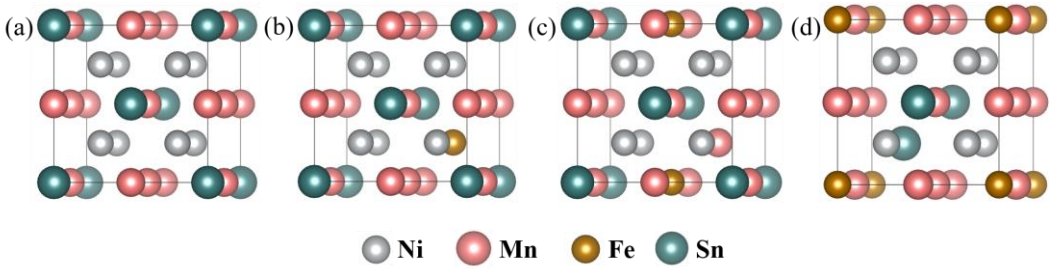

Fig. 3-2 The unit cell of the cubic structure of austenite

(a) $Ni_8Mn_6Sn_2$; (b) $(Ni_7Fe_1)Mn_6Sn_2$; (c) $(Ni_7Mn_1)(Mn_5Fe_1)Sn_2$; (d) $(Ni_7Sn_1)Mn_6(Sn_1Fe_1)$

In non-stoichiometric $Ni_8Mn_{4+x}Sn_{4-x}$ Mn-rich alloys, the magnetic moment exhibits two distinct configurations: the magnetic moments of Mn atoms occupying Sn sites can align either parallel or antiparallel to those of Mn atoms in the stoichiometric structure. These are denoted as ferromagnetic (FM) and antiferromagnetic (AFM) magnetic structures, respectively.

Therefore, when calculating the properties of the $Ni_{43.75}Mn_{37.5}Sn_{12.5}Fe_{6.25}$ alloy, the total energy of the system under two different magnetic configurations—ferromagnetic (FM) and antiferromagnetic (AFM)—was evaluated as a function of volume to determine which magnetic structure is more stable in the cubic phase. Fig. 3-3 shows the variation of total energy with lattice constant for $Ni_{50}Mn_{37.5}Sn_{12.5}$ alloy and $Ni_{43.75}Mn_{37.5}Sn_{12.5}Fe_{6.25}$ alloy under both FM and AFM magnetic structures. For the austenitic phase $Ni_{50}Mn_{37.5}Sn_{12.5}$, the antiferromagnetic configuration consistently exhibits a lower total energy across the entire range of calculated lattice constants. When the lattice constant reaches 0.593 nm, the system attains its most stable state with the lowest energy. At this lattice parameter, the total energy of the antiferromagnetic state is significantly lower than that of the corresponding ferromagnetic state, indicating that the antiferromagnetic state is the thermodynamically stable state of the system. This result is consistent with the theoretical calculations results reported by Sokolovskiy et al.[127]

After substituting 6.25 at.% Fe for Ni, as shown in Fig. 3-3(b), the total energy-lattice constant curves for both ferromagnetic (FM) and antiferromagnetic (AFM) states shift downward simultaneously. The system reaches its most stable state with the lowest energy when the lattice constant reaches 0.595 nm. It can be observed that the total energy of the configuration where Fe substitutes Sn and subsequently replaces Ni is higher than that of the configuration where Fe substitutes Mn and then replaces Ni, while the configuration with Fe directly substituting Ni exhibits the lowest total energy. This confirms that when one Fe atom (6.25 at.%) is doped into the alloy system, it directly substitutes for Ni.

When the lattice constant exceeds 0.60 nm, the energy-lattice constant

relationship between the AFM and FM states undergoes a trend reversal, with the two curves intersecting. This indicates a change in the magnetic ground state of the system, as the ferromagnetic stage gradually becomes the energetically more favorable magnetic configuration. The magnetic moments of Mn atoms occupying Sn sites and the original Mn atoms transition from antiparallel to parallel alignment, demonstrating that Fe doping alters the magnetic moment relationship between Mn-Mn and Mn-Sn pairs, thereby stabilizing the ferromagnetic state of the alloy[128].

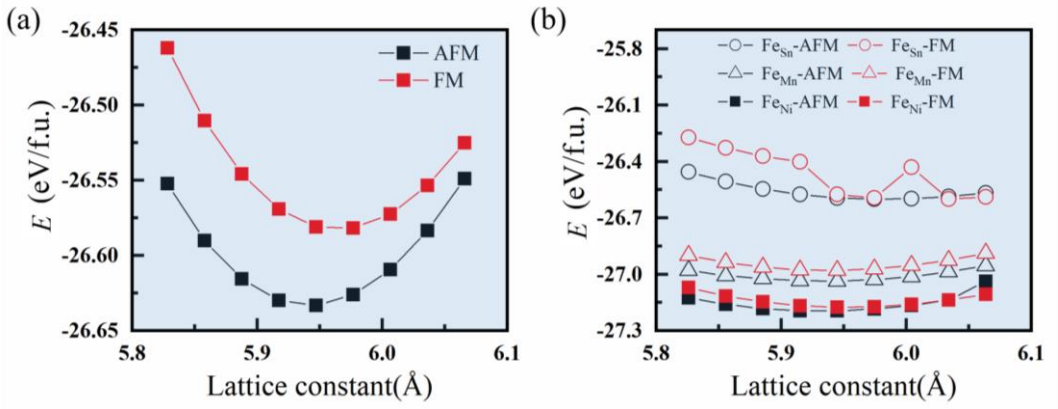

Fig. 3-3 Relationships between total energies and lattice constant for austenitic-type alloys (a) $Ni_{50}Mn_{37.5}Sn_{12.5}$; (b) $Ni_{43.75}Mn_{37.5}Sn_{12.5}Fe_{6.25}$

In Ni-Mn-X (X=Ga, Sn, In, Sb) alloys, the non-modulated martensite (NM) with a tetragonal crystal structure is typically the most stable phase and serves as the final transformation product of the martensitic transformation process[129]. Martensitic transformation is a non diffusive transformation, once the site occupation configuration of the fourth element Fe atoms in the austenite phase is determined, the atomic site configuration of the resulting NM-type martensite phase is consequently established. Based on this theoretical foundation, the study first determined the most stable atomic occupancy configuration of the austenite phase through the minimum energy criterion, and then carried out computational research on other physical properties of the alloy on this basis.

3.2.2 Phase Stability and Phase Transition of Fe Doping in Ni-Mn-Sn Alloy

Building upon the lattice constant data obtained in the previous section, calculate the evolution of total energy with tetragonal distortion (*c/a* ratio) for both $Ni_{50}Mn_{37.5}Sn_{12.5}$ and $Ni_{43.75}Mn_{37.5}Sn_{12.5}Fe_{6.25}$ alloy systems at absolute zero temperature. The calculations considered both ferromagnetic and antiferromagnetic configurations, with the results presented in Fig. 3-4.

Although the first-principles calculations are performed under absolute zero conditions, the stable phase structure of the alloy can still be effectively inferred by analyzing the characteristic curve of total energy versus *c/a* ratio, particularly the distribution of extremum points. As shown in Fig. 3-4(a), for $Ni_{50}Mn_{37.5}Sn_{12.5}$, the antiferromagnetic configuration consistently exhibits lower total energy across the entire range of *c/a* variations. This indicates that in both austenite and martensite phases, the magnetic moments of Mn atoms occupying Sn atomic sites exhibit antiferromagnetic coupling with those of Mn atoms in the stoichiometric configuration. Using the energy of the ferromagnetic austenite phase as a reference baseline, it can be observed that the total energy of the ferromagnetic state increases with the degree of tetragonal distortion. Notably, two local minima appear in the energy curve of the antiferromagnetic state: the first minimum occurs near *c/a*=0.9, while the second is located at *c/a*=1.30. According to the energy minimization principle, the non-modulated martensite phase with *c/a*=1.30 is determined to be the stable structure of the system at extremely low temperatures, this result can be found as evidence in the literature[129]. During the cooling process of Ni-Mn-based alloys, the NM martensite phase has the lowest total energy, making it more stable compared to other types of martensite (e.g., 5M, 6M, 7M, etc.)[130, 131]. For the alloy

doped with 6.25 at.% Fe, the energy values of the AFM and FM states nearly coincide near *c/a*=1, suggesting enhanced ferromagnetism in the austenite phase. Fig. 3-4(b) reveals that Fe doping reduces the *c/a* ratio of the martensite phase to approximately 1.2, while the antiferromagnetic interactions between Mn-Mn and Mn-Sn remain antiparallel, meaning the martensite phase retains its antiferromagnetic state. This also directly leads to a significant magnetization difference between the austenite and martensite phases.

To investigate the effect of Fe doping on the Curie temperature of Ni-Mn-Sn alloys, according to Stoner theory[132, 133], T_C^A is linearly correlated with the total energy difference (ΔE) between its paramagnetic and ferromagnetic states. As the Fe doping concentration increases, ΔE decreases, leading to a reduction in the alloy's Curie temperature with increasing Fe content.

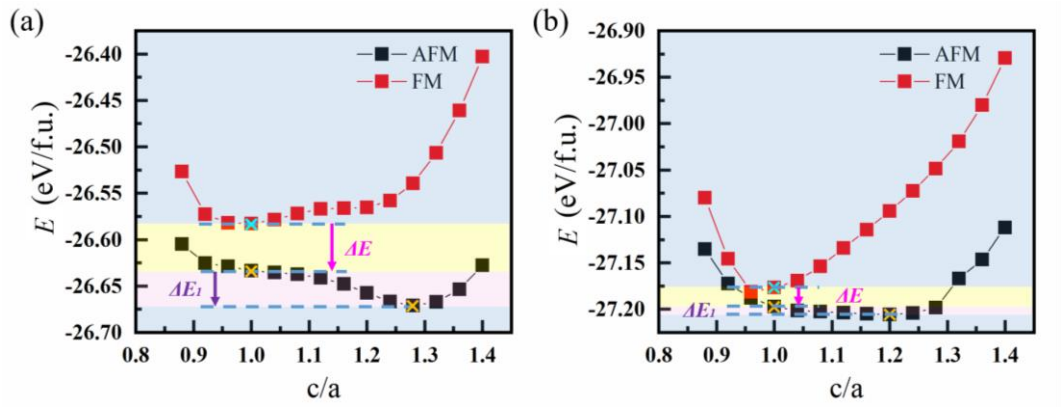

Fig. 3-4 Relationships between total energies and *c/a*

(a) $Ni_{50}Mn_{37.5}Sn_{12.5}$; (b) $Ni_{43.75}Mn_{37.5}Sn_{12.5}Fe_{6.25}$

To investigate the regulation mechanism of doping elements on the martensitic transformation temperature, the thermodynamic characteristics of the phase transition were qualitatively analyzed by calculating the total energy difference between the austenite and martensite phases (ΔE_1, $\Delta E_1 = E_{AP(Cub.)} - E_{P(Tetra.)}$)[134, 135]. The variation trend of the martensitic transformation temperature is closely related to ΔE_1. A larger ΔE_1 value indicates a higher energy barrier between the austenite

and martensite phases, which provides stronger driving force for the phase transition. This promotes the structural transformation from austenite to martensite, ultimately leading to a significant increase in the alloy's martensitic transformation temperature.

Comparing Fig. 3-4(a) and (b), Fe doping gradually reduces the martensitic transformation temperature. When the Fe doping concentration reaches 6.25 at.%, ΔE_1 approaches zero, indicating that the $Ni_{43.75}Mn_{37.5}Sn_{12.5}Fe_{6.25}$ alloy exhibits nearly identical energy levels between its austenite and martensite phases, resulting in weakened driving force for martensitic transformation. Notably, within the *c/a* range of 1.1 to 1.25, no energy extremum is observed, meaning there is no appearance of a stable martensite phase. This suggests that multiple types of martensite may form during the transformation process, raising the possibility of two-step or even multi-step phase transitions[131]. Research has shown that doped $Ni_{50}Mn_{37.5}Sn_{12.5}$ alloys may exhibit 5M or 4O martensite during phase transition[41, 136-140].

Based on the *c/a* variation trend of the AFM state $Ni_{43.75}Mn_{37.5}Sn_{12.5}Fe_{6.25}$ in Fig. 3-4(b), the 5M and 4O structures were constructed by stacking (110) planes along the $[1\bar{1}0]$ direction of the austenitic cubic $L2_1$ structure, using *c/a*=1.2 as the basis. To accurately model the 5M and 4O phase structures, relaxation was performed in two steps[131]. First, the shape was optimized with a fixed modulated structure, followed by full relaxation under the optimized shape to obtain the trend of total energy changes with respect to the deformation parameter δ. The results are shown in Fig. 3-5.

For both 5M and 4O structures, the minimum energies were obtained at deformation parameters of 0.050 and 0.059, respectively, with the 4O structure

exhibiting lower energy than 5M. To investigate the driving force for martensitic transformation, the energy differences between austenite and NM martensite ($\Delta E_1 = E_{AP(Cub.)} - E_{P(Tetra.)}$), austenite and 5M martensite ($\Delta E_2 = E_{AP(Cub.)} - E_{P(5M.)}$), and austenite and 4O martensite ($\Delta E_3 = E_{AP(Cub.)} - E_{P(4O.)}$) were calculated. The results were 20 meV/f.u., 7 meV/f.u., and 11 meV/f.u., respectively, with all ΔE_1, ΔE_2 and ΔE_3 values being greater than 0. This indicates that, from a thermodynamic perspective, the $Ni_{43.75}Mn_{37.5}Sn_{12.5}Fe_{6.25}$ alloy has the potential to undergo two-step or even multi-step martensitic transformations. This observation aligns with the findings reported by Zhang et al.[141], who noted the coexistence of 4O and NM phases in $Ni_2Mn_{1.5-x}Fe_xSn_{0.5}$ alloys. It can thus be inferred that when the Fe doping concentration in the alloy exceeds 6 at.%, the energy difference between austenite and martensite becomes very small, resulting in insufficient driving force for martensitic transformation and making phase transition difficult to occur in the alloy.

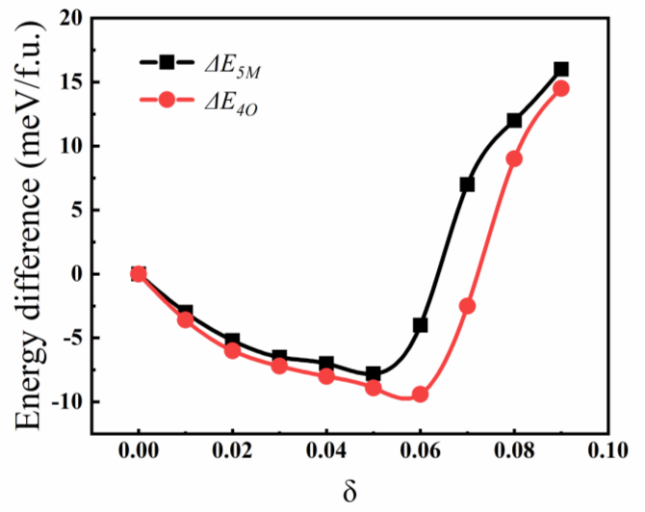

Fig. 3-5 The energy of 5M and 4O as a function of the displacement

3.2.3 Magnetic Properties of Fe Doping in Ni-Mn-Sn Alloy

Building upon the equilibrium lattice constants obtained in the previous

section, this study investigates the microscopic mechanism of Fe doping's influence on the magnetic properties of Ni-Mn-Sn alloys. The total spin density of states (DOS) was calculated for both the $Ni_{50}Mn_{37.5}Sn_{12.5}$ and $Ni_{43.75}Mn_{37.5}Sn_{12.5}Fe_{6.25}$ alloys in their austenite phase and stable martensite phase. The results are presented in Fig. 3-6.

Both spin-up and spin-down states are distinctly divided into bonding and antibonding regions. Notably, the variation in the alloy's total magnetic moment originates from the asymmetric distribution of spin-up and spin-down electronic density of states in the bonding region below the Fermi level (E_F). E_F is indicated by a vertical dashed line at 0 eV.

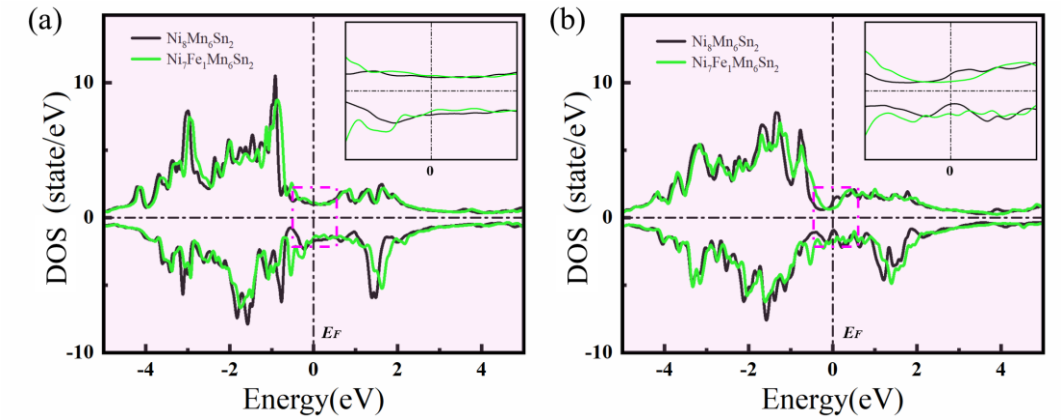

Fig. 3-6 DOS of $Ni_{50}Mn_{37.5}Sn_{12.5}$ and $Ni_{43.75}Mn_{37.5}Sn_{12.5}Fe_{6.25}$ alloys
(a) austenite state; (b) martensite states

As shown in Fig. 3-6(a), the spin-up DOS exhibits only slightly changes with Fe doping, with the curves for $Ni_{50}Mn_{37.5}Sn_{12.5}$ and $Ni_{43.75}Mn_{37.5}Sn_{12.5}Fe_{6.25}$ alloys nearly overlapping. In contrast, Fig. 3-6(b) reveals that the spin-down DOS is highly sensitive to the doping of the fourth element. Compared to $Ni_{50}Mn_{37.5}Sn_{12.5}$, the energy at the E_F is reduced in $Ni_{43.75}Mn_{37.5}Sn_{12.5}Fe_{6.25}$. A lower energy at the Fermi level corresponds to higher stability of the austenite phase. This fundamentally explains why doping enhances the stability of the austenite phase

and further predicts that Fe doping can lower the martensitic transformation temperature of the $Ni_{50}Mn_{37.5}Sn_{12.5}$[142].

The doping of Fe atoms induces modifications in the electronic structure of the system. Below the Fermi level, the spin-up DOS exhibits a marginal increase, while the spin-down DOS demonstrates a more substantial reduction. This enhanced spin asymmetry directly contributes to the elevation of the total magnetic moment in the alloy system. Notably, upon substitution of a single Fe atom for Ni, the minimum of the spin-down DOS precisely coincides with the Fermi level, establishing a characteristic pseudogap effect. This Fe doping configuration consequently enhances the overall stability of the alloy system.

3.3 First Principles Investigations of Cu Doped Ni-Mn-Sn Alloy

3.3.1 Cu Atomic Preferential Site Occupation

Similar to the research approach for Fe doping, it is necessary to construct models with different occupation configurations to systematically investigate the preferential site occupation tendency of Cu atoms from a thermodynamic perspective. Based on the crystal structure of $Ni_{50}Mn_{37.5}Sn_{12.5}$ ($Ni_8Mn_6Sn_2$) alloy (shown in Fig. 3-7(a)), three cubic $L2_1$ structures of $Ni_{43.75}Mn_{37.5}Sn_{12.5}Cu_{6.25}$ ($Ni_7Mn_6Sn_2Cu_1$) were established: (1) Cu atoms occupying Ni sites; (2) Cu atoms occupying Mn sites, with Mn atoms substituting Ni atoms; and (3) Cu atoms occupying Sn sites, with Sn atoms substituting Ni atoms. The corresponding unit cell structure diagrams are shown in Fig. 3-7(b-d). Additionally, a $Ni_{37.5}Mn_{37.5}Sn_{12.5}Cu_{12.5}$ ($Ni_6Cu_2Mn_6Sn_2$) structure was established where two Cu atoms occupying Ni sites, as illustrated in Fig. 3-7(e).

When 6.25 at.% Cu substitutes for Ni, as shown in Fig. 3-8(b), the total energy-lattice constant curves for both ferromagnetic and antiferromagnetic states

shift upward simultaneously. The system reaches its lowest-energy stable state when the lattice constant attains 0.595 nm. It can be observed that the configuration with direct Cu substitution for Ni exhibits the lowest total energy. From a thermodynamic perspective, lower energy indicates higher stability of the atomic occupation configuration. These results conclusively demonstrate that in the 6.25 at.% Cu-doped alloy, Cu directly substitutes for Ni atoms.

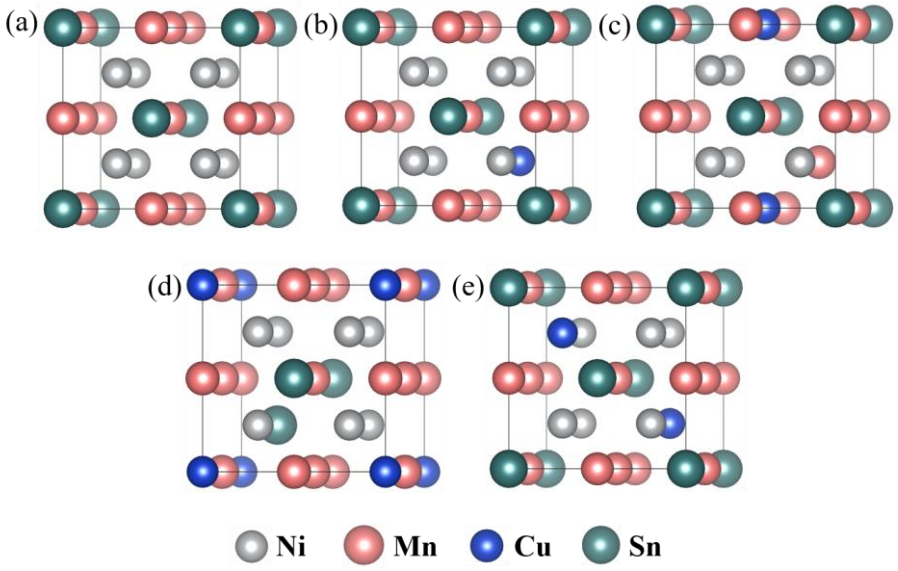

Fig. 3-7 The unit cell of the cubic structure of alloys

(a) $Ni_8Mn_6Sn_2$; (b) $(Ni_7Cu_1)Mn_6Sn_2$; (c) $(Ni_7Mn_1)(Mn_5Cu_1)Sn_2$; (d) $(Ni_7Sn_1)Mn_6(Sn_1Cu_1)$; (e) $(Ni_6Cu_2)Mn_6Sn_2$

Fig. 3-8(c) shows the total energy-lattice constant curves for both ferromagnetic and antiferromagnetic states when two Cu atoms (12.5 at.%) substitute for Ni. With increasing Cu doping concentration in the alloy, these curves continue to shift upward simultaneously. The system reaches its lowest-energy stable state at a lattice constant of 0.597 nm. Moreover, the lattice constant increases with higher Cu doping content. This phenomenon occurs because Cu's 3d orbitals are fully occupied, resulting in a larger atomic radius for Cu compared to Ni, which consequently occupies more space.

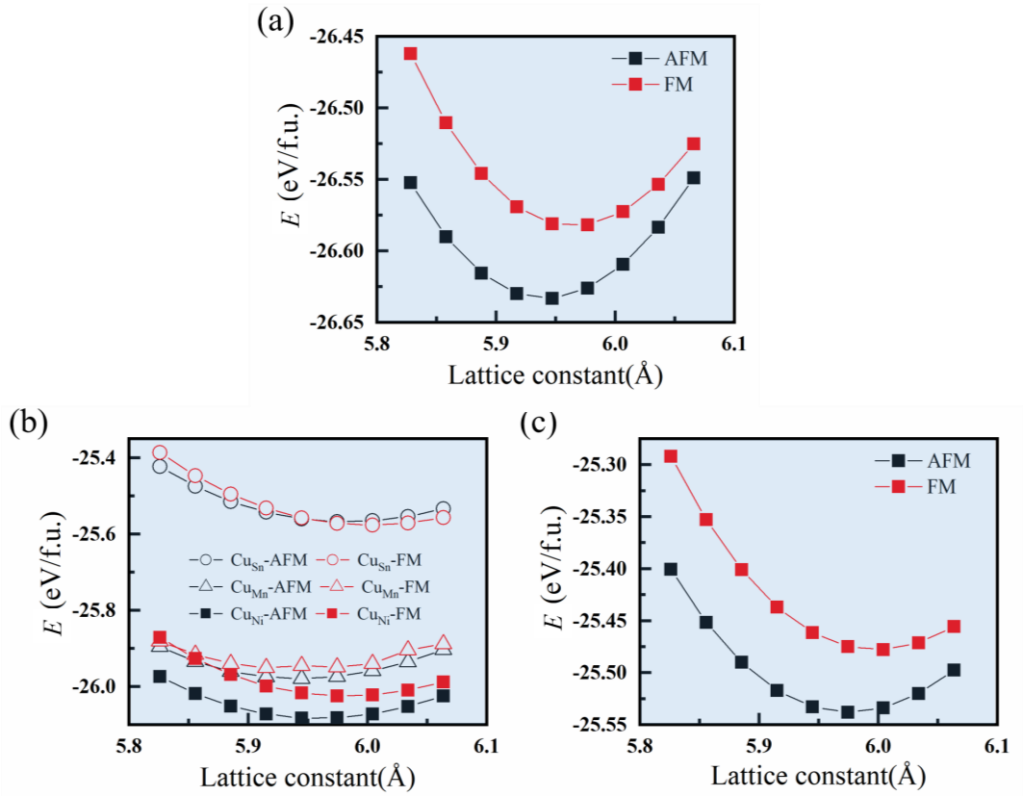

Fig. 3-8 Relationships between total energies and lattice constant for austenitic-type alloys (a) $Ni_{50}Mn_{37.5}Sn_{12.5}$; (b) $Ni_{43.75}Mn_{37.5}Sn_{12.5}Cu_{6.25}$; (c) $Ni_{37.5}Mn_{37.5}Sn_{12.5}Cu_{12.5}$

3.3.2 Phase Transition of Cu Doping in Ni-Mn-Sn Alloy

The phase stability of alloys directly influences phase transition and can significantly affect their transition temperatures. Considering both ferromagnetic and antiferromagnetic configurations, we calculated the evolution of total energy with tetragonal distortion (*c/a* ratio) for three alloy systems at absolute zero temperature, as shown in Fig. 3-9. The energy difference between austenite and martensite (ΔE_1) was calculated to analyze the effect of Cu doping on the martensitic transformation temperature.

By comparing Fig. 3-9(b) and (c), it becomes evident that the reduction in ΔE_1 decreases with increasing Cu content. When doping 6.25 at.% Cu, ΔE_1 significantly decreases, while when the Cu doping amount increases from 6.25 at.% to 12.5 at.%, ΔE_1 slightly decreases. This suggests that Cu doping has limited capability in

adjusting the phase transition temperature, which aligns with findings reported in other literature[143]. For both 6.25 at.% and 12.5 at.% Cu-doped alloys, the magnetic states of austenite and martensite remain unchanged. However, the increase in Cu doping content leads to an increase in the *c/a* ratio of martensite.

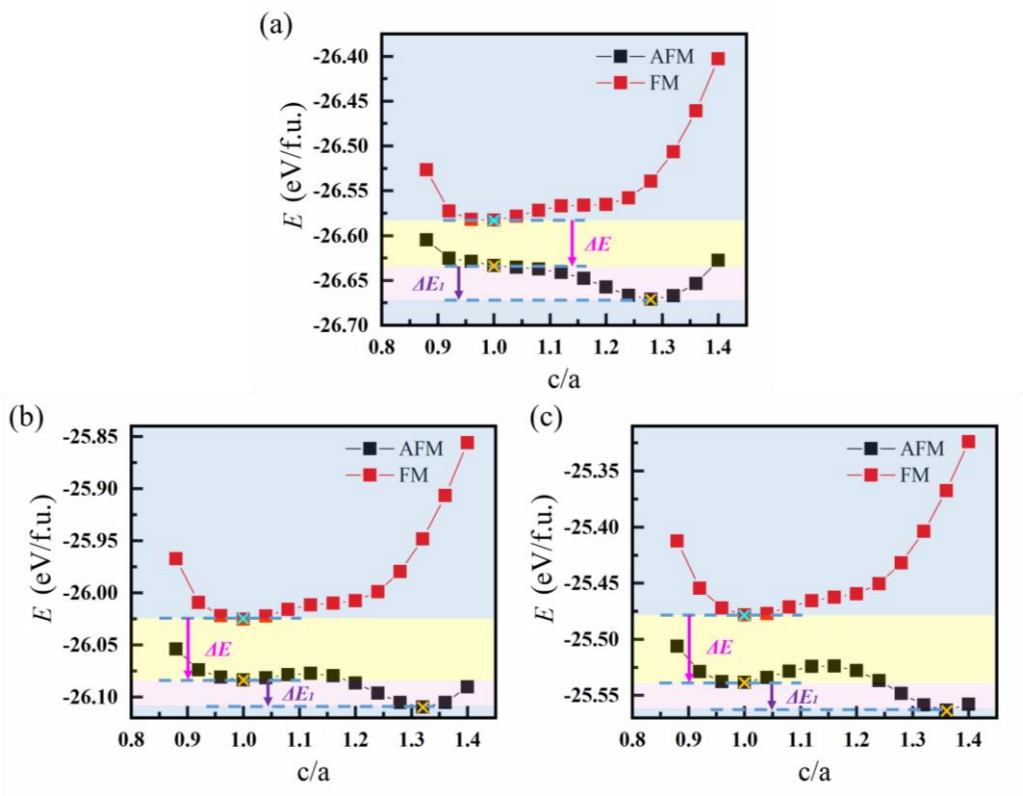

Fig. 3-9 Relationships between total energies and *c/a*

(a) $Ni_{50}Mn_{37.5}Sn_{12.5}$; (b) $Ni_{43.75}Mn_{37.5}Sn_{12.5}Cu_{6.25}$; (c) $Ni_{37.5}Mn_{37.5}Sn_{12.5}Cu_{12.5}$

3.3.3 Magnetic Properties of Cu Doping in Ni-Mn-Sn Alloy

Building upon the previous predictive analysis of phase transition temperatures through the energy difference between austenite and martensite, it has been found that the substitution of Cu atoms for Ni atoms enhances the stability of the austenite phase while simultaneously reducing the martensitic transformation temperature. To gain deeper insight into the mechanisms underlying this phenomenon, we calculated and obtained comparative diagrams of the total density of states for $Ni_{50}Mn_{37.5}Sn_{12.5}$ alloy with Cu and Fe doping, as shown in Fig. 3-10.

Cu doping modifies the characteristics of spin-down DOS near the Fermi level. In the $Ni_{50}Mn_{37.5}Sn_{12.5}$ alloy, the spin-down DOS at the Fermi level does not reside at a valley position, and there exists a minor peak in the spin-down bonding region. This electronic structure feature changes with Cu doping, with one Cu atom substitutes for Ni, the peak shifts toward the Fermi level, and with two Cu atoms doping per unit cell, the peak disappears completely and a valley emerges at the Fermi level, exhibiting typical pseudogap effect. This pseudogap formation process reflects the gradual enhancement of stability.

In contrast, Fe doping leads to a slight increase in spin-up electrons below E_F while causing a more pronounced reduction in spin-down electrons, resulting in enhanced total magnetic moment for Fe-doped alloys. These findings are consistent with calculated total and atomic magnetic moments presented in Table 3-1.

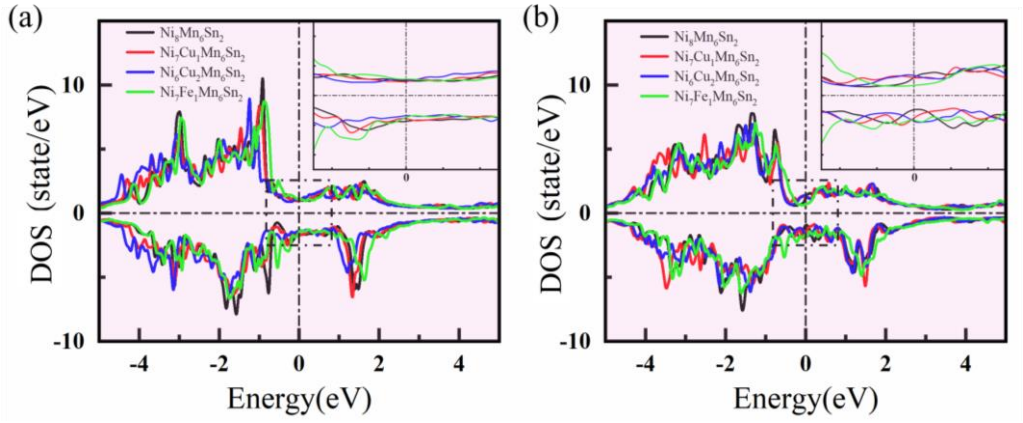

Fig. 3-10 DOS of $Ni_{50}Mn_{37.5}Sn_{12.5}$, $Ni_{43.75}Mn_{37.5}Sn_{12.5}Cu_{6.25}$, $Ni_{37.5}Mn_{37.5}Sn_{12.5}Cu_{12.5}$, and $Ni_{43.75}Mn_{37.5}Sn_{12.5}Fe_{6.25}$ alloys
(a) austenite and (b) martensite

Fig. 3-11 presents the projected density of states diagrams for $Ni_{50}Mn_{37.5}Sn_{12.5}$, $Ni_{43.75}Mn_{37.5}Sn_{12.5}Cu_{6.25}$, $Ni_{37.5}Mn_{37.5}Sn_{12.5}Cu_{12.5}$ and $Ni_{43.75}Mn_{37.5}Sn_{12.5}Fe_{6.25}$ alloys in both austenite and martensite phases. The charge density of states distribution for Sn atoms exhibits highly symmetric characteristics, rendering their contribution to magnetic moments negligible.

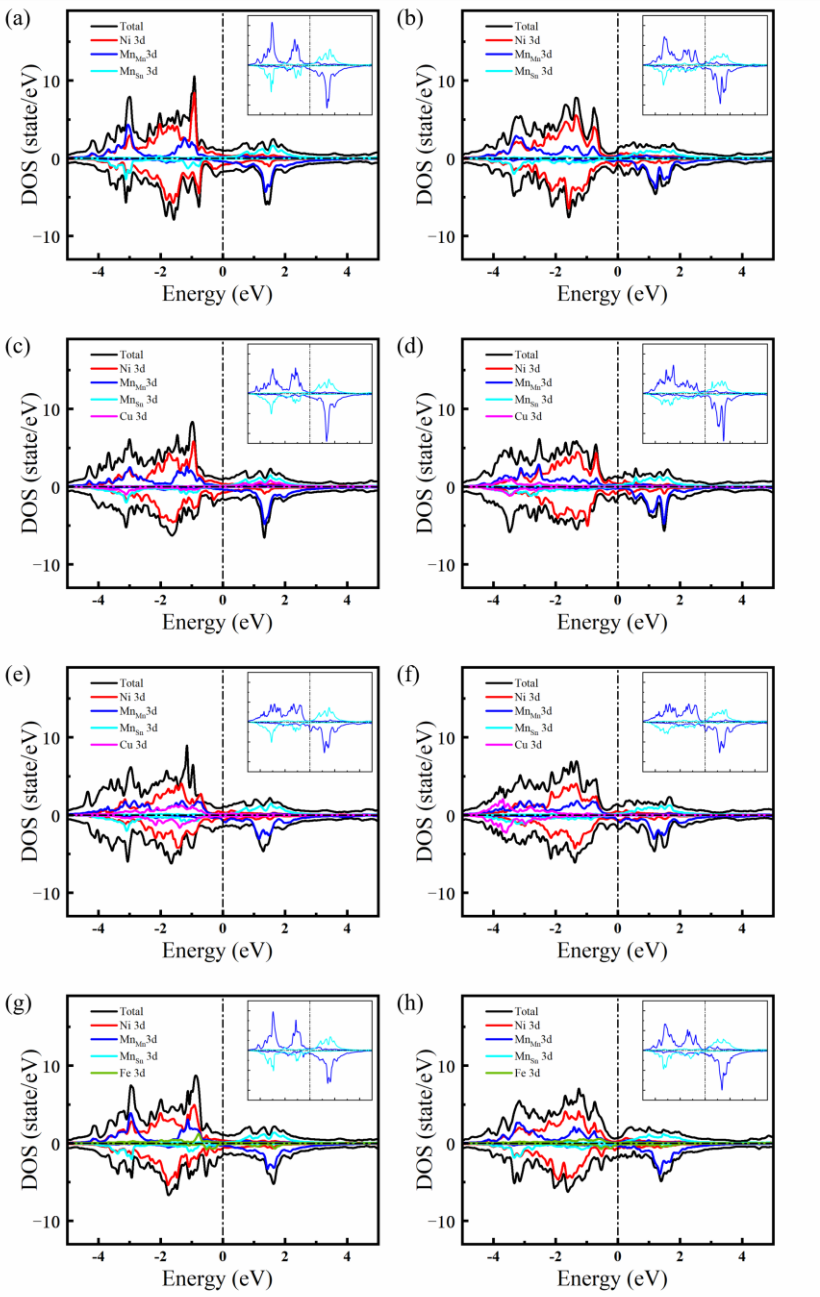

Fig. 3-11 PDOS of $Ni_{50}Mn_{37.5}Sn_{12.5}$, $Ni_{43.75}Mn_{37.5}Sn_{12.5}Cu_{6.25}$, $Ni_{37.5}Mn_{37.5}Sn_{12.5}Cu_{12.5}$ and $Ni_{43.75}Mn_{37.5}Sn_{12.5}Fe_{6.25}$ alloys

(a) (c) (e) (g) austenite phase; (b) (d) (f) (h) martensite phase (The inset is the near-E_F total densities of states in the energy range marked by the dot-dashed rectangle)

In the region below the Fermi level, the 3d DOS of Ni atoms, Mn_{Mn} atoms, and Mn_{Sn} atoms dominates in both spin up and down orbitals. Above the Fermi level, the 3d DOS of Mn_{Mn} and Mn_{Sn} demonstrate stronger contributions. Notably, the DOS for Ni atoms shows nearly symmetric distribution between both spin

channels, with minimal splitting at the Fermi level. This characteristic indicates that Ni atoms contribute relatively little to the system's total magnetic moment.

Detailed analysis of the Mn_{Mn}3d DOS reveals two distinct spin-up density peaks below the Fermi level and one prominent spin-down density peak above the Fermi level. This density of states distribution exhibits markedly asymmetric characteristics, particularly evidenced by the pronounced state splitting observed at the Fermi level. Such electronic structure features demonstrate that Mn atoms make significant contributions to the system's magnetic moment and serve as the primary source of the alloy's magnetism. These findings are consistent with the calculated atomic magnetic moment results (3.48 μB).

Table 3-1 Equilibrium lattice parameters, total and partial spin moments of the cubic austenite (Cub.) and NM martensite (Tel.) for $Ni_{50}Mn_{37.5}Sn_{12.5}$, $Ni_{43.75}Mn_{37.5}Sn_{12.5}Cu_{6.25}$, $Ni_{37.5}Mn_{37.5}Sn_{12.5}Cu_{12.5}$ and $Ni_{43.75}Mn_{37.5}Sn_{12.5}Fe_{6.25}$ alloys

Composition		Lattice parameters (nm)			Moment (μB)					
		a	*c*	*c/a*	Total	Ni	Mn_{Mn}	Mn_{Sn}	Cu	Fe
$Ni_{50}Mn_{37.5}Sn_{12.5}$	Cub.	5.94479			1.87	0.13	3.48	-3.66		
	Tet.	5.47399	7.01136	1.28084	1.71	0.1	3.37	-3.6		
$Ni_{43.75}Mn_{37.5}Sn_{12.5}$	Cub.	5.96170			1.79725	0.11	3.481	-3.678	0.003	
$Cu_{6.25}$	Tet.	5.43446	7.17461	1.32020	1.7795	0.12471	3.38525	-3.566	0.016	
$Ni_{37.5}Mn_{37.5}Sn_{12.5}$	Cub.	5.97804			1.7175	0.09	3.4785	-3.698	-0.003	
$Cu_{12.5}$	Tet.	5.39669	7.33535	1.35923	1.6665	0.08833	3.35525	-3.538	0.013	
$Ni_{43.75}Mn_{37.5}Sn_{12.5}$	Cub.	5.92856			2.1425	0.13342	3.36225	-3.613		1.597
$Fe_{6.25}$	Tet.	5.58899	6.67086	1.19357	2.0115	0.10085	3.3135	-3.541		1.357

Notably, at specific energy positions (e.g., −1 eV and −2.8 eV), overlapping density peaks appear in the spin-up channel for both Ni and Mn_{Mn}3d atomic orbitals. This characteristic stems from the energy level hybridization effect between Ni-Mn 3d electron orbitals, which enhances the bonding interaction between Ni and Mn

atoms. Furthermore, the non-zero DOS at the Fermi level and the small peaks formed on both sides constitute typical pseudogap effect, fully demonstrating the existence of strong covalent bonding interactions in the alloy system.

3.4 First Principles Investigations of B doped Ni-Mn-Sn alloy

3.4.1 B Atomic Preferential Site Occupation

Following the research approach similar to that of Fe and Cu doping in previous sections, to investigate the effect of B doping on the properties of Ni-Mn-Sn alloys, it is first necessary to establish an accurate structural model of Ni-Mn-Sn-B alloys. However, the study of B doping presents distinctions compared to Fe and Cu doping. Due to the small atomic radius of B, in addition to substitutional doping, B may also alloy through occupying interstitial sites. Therefore, this scenario requires further discussion. In the $L2_1$ crystal structure shown in Fig. 3-12, there exist three types of interstitial sites: one tetragonal site (labeled as T) and two octahedral sites (labeled as O−I and O−II).

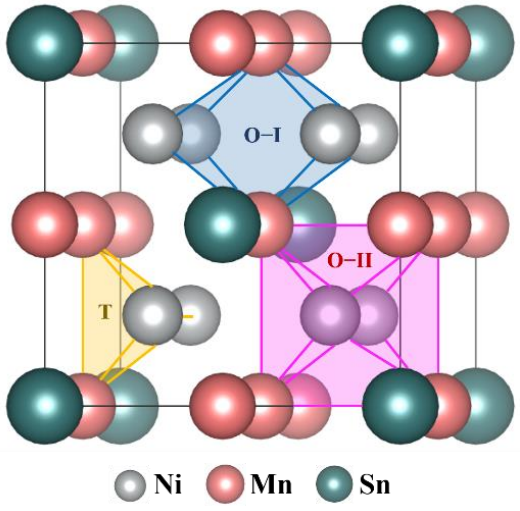

Fig. 3-12 Configurations occupying interstitial sites

The formation energies of different occupation configurations were calculated to evaluate their stability, with the results listed in Table 3-2. It can be readily

observed that the tetragonal interstitial occupation leads to a higher formation energy compared to the undoped $Ni_8Mn_6Sn_2$ alloy, whereas both octahedral interstitial occupation modes result in lower formation energies than the undoped $Ni_8Mn_6Sn_2$ alloy. Among these, the occupation of the O−I octahedral interstitial site corresponds to the lowest formation energy.

Table 3-2 summarizes the formation energies of the undoped ternary alloy, B occupying one tetragonal interstitial site, and B occupying octahedral interstitial sites under both antiferromagnetic and ferromagnetic states. By comparing the energies, the following conclusions can be drawn: (1) The austenite phase in all four configurations exhibits an antiferromagnetic state; (2) The aforementioned B doping methods enhance the energetic stability of the austenite phase.

Table 3-2 Formation energies and formation energy difference of austenite and martensite for the undoped, T, O−I and O−II configurations (eV/f.u.)

	Undoped		T		O−I		O−II	
	AFM	FM	AFM	FM	AFM	FM	AFM	FM
Cub.	−1.23	−1.17	−0.72	−0.66	−1.69	−1.41	−1.54	−1.38
Tet.	−1.89	−1.62	−0.88	−0.73	−1.74	−1.55	−1.73	−1.53
ΔE_{f1}	−0.66	−0.45	−0.16	−0.07	−0.05	−0.14	−0.19	−0.15

From an energetic perspective, alloys with different B substitution configurations all exhibit antiferromagnetic properties, indicating that the magnetism of $Ni_8Mn_6Sn_2$ alloy is insensitive to B doping. Considering thermodynamic stability, the total energy difference (ΔE_{f1}) between austenite and martensite phases is also included in Table 3-2. All three B doping approaches reduce ΔE_{f1}, thereby decreasing the tendency for martensitic phase transition in the alloy.

3.4.2 Elastic Properties of B Doping in Ni-Mn-Sn Alloy

To further evaluate the effect of B doping on the mechanical stability of Ni-Mn-Sn alloys, the elastic constants C_{ij} of both the undoped alloy and the alloy with B occupying the O−I octahedral interstitial site were calculated using first-principles methods. The specific results are presented in Table 3-3. Since the strain energy must be positive, the elastic constant matrix must satisfy positive definiteness, i.e., the Born-Huang stability criteria:

$$C_{11}-C_{12}>0 \tag{3.1}$$

$$C_{11}>0 \tag{3.2}$$

$$C_{44}>0 \tag{3.3}$$

As can be seen from Table 3-3, the elastic constants of the configuration with B occupying the O−I octahedral interstitial site satisfy the criteria for mechanical stability, indicating a stable phase structure. In summary, based on the analysis of both energetics and mechanical stability, B doping is most likely to occupy the O−I octahedral interstitial site. Furthermore, mechanical property parameters such as bulk modulus (B), shear modulus (G), Young's modulus (Y), and Poisson's ratio (v) can be calculated from the elastic constants:

$$B=(C_{11}+2C_{12})/3 \tag{3.4}$$

$$G=[3(C_{11}-C_{12})+4C_{44}]/10 \tag{3.5}$$

$$Y=9BG/(3B+G) \tag{3.6}$$

$$v=(3B-2G)/2(3B+G) \tag{3.7}$$

The calculated results are presented in Table 3-3. The shear elastic constant C', defined as $(C_{11}-C_{12})/2$, serves as a key mechanical parameter characterizing the structural stability of the austenite phase. The occupation of the O−I octahedral interstitial site by B increases the shear elastic constant of austenite, indicating

enhanced resistance to shear deformation along the <110> direction and improved stabilization of the austenitic phase in the alloy. This trend aligns with the results obtained from the formation energy analysis discussed earlier. As shown in Table 3-3, when B occupies the O−I octahedral interstitial site, the bulk modulus (B) of the alloy increases, suggesting improved incompressibility and fracture strength.

According to the Pugh criterion[144], a B/G ratio of 1.75 serves as the critical value for distinguishing between ductile and brittle behavior in materials. Generally, ductile metals with a face-centered cubic structure exhibit higher B/G values, while brittle metals with a body-centered cubic structure display relatively lower B/G values[145]. The computational results of this study reveal that although the B/G ratio of the Ni-Mn-Sn(B) alloy system exceeds 1.75, the unique characteristics of Ni-Mn-based magnetic materials[146] prevent a definitive assessment of ductility based solely on this parameter. A comprehensive evaluation incorporating additional mechanical parameters is required. With B doping, the elastic constant C_{44} increases, indicating enhanced resistance to shear deformation along the <001> direction.

Table 3-3 Elastic constants and related mechanical properties for the undoped and O−I configuration (GPa)

System	C_{11}	C_{12}	C_{44}	B	G	Y	v	B/G
Undoped	141.84	127.61	95.58	132.35	42.50	115.18	0.35	3.11
O−I	232.70	123.85	113.53	160.13	78.07	201.46	0.29	2.05

3.5 Magneto-Structural Phase Transitions and Magnetocaloric Effect of Ni-Mn-Sn-Fe Alloys

Based on first-principles calculations, the Fe doping concentration was designed not to exceed 6 at.% to ensure sufficient energy driving force for the phase

transition between austenite and martensite phases. Following this theoretical analysis, this section experimentally investigates a series of $Ni_{50-y}Mn_{38}Sn_{12}Fe_y$ (y=0, 1, 2, 3, 4, 5) alloys prepared by substituting Fe for partial Ni content.

3.5.1 Microstructure of Ni-Mn-Sn-Fe Alloys

Fig. 3-13 shows the backscattered electron images of heat-treated $Ni_{50-y}Mn_{38}Sn_{12}Fe_y$ (y=0, 1, 2, 3, 4, and 5) alloys. The undoped $Ni_{50}Mn_{38}Sn_{12}$ alloy exhibits a single-phase solid solution at room temperature. With increasing Fe doping content, the alloy's microstructure demonstrates distinct evolutionary patterns. Under low doping conditions (y=1 and 2), the room-temperature microstructure maintains a single-phase structure. It can be observed that when y=3, a small amount of γ phase precipitates appear locally. As for the alloy with y=4, the γ phase is noticeably larger at the grain boundaries compared with itself within the grain, indicating that the γ phase nucleates and grows primarily at the grain boundaries. As the Fe content increases, the quantity and grain size of the second phase gradually increase. Furthermore, the distribution of the second phase expands from the grain boundaries into the grain interiors.

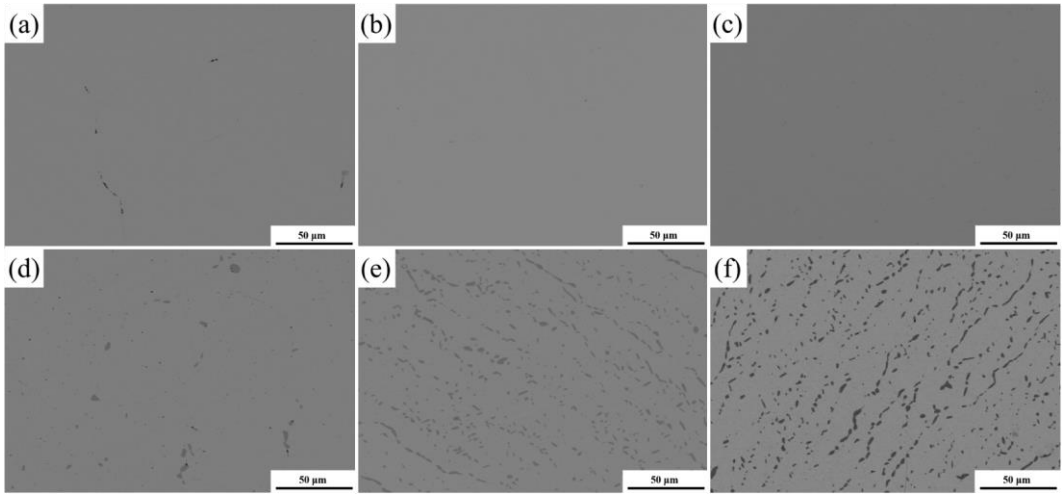

Fig. 3-13 BSE micrographs of $Ni_{50-y}Mn_{38}Sn_{12}Fe_y$ alloys
(a) y=0; (b) y=1; (c) y=2; (d) y=3; (e) y=4; (f) y=5

The precipitation of secondary phases alters the matrix composition, which in turn affects its *e/a* ratio. Consequently, the precipitation of secondary phases modifies the characteristic martensitic transformation temperatures while simultaneously influencing both the latent heat and entropy change of the phase transition. Compositional analyses were conducted separately for the alloy matrix and secondary phases, with results presented in Table 3-4. The data demonstrate that the maximum solid solubility of Fe in the $Ni_{50}Mn_{38}Sn_{12}$ alloy matrix is approximately 3.6 at.%.

Table 3-4 Compositions of the matrix and second phase of $Ni_{50-y}Mn_{38}Sn_{12}Fe_y$ alloys

y	Matrix (at.%)				Second phase (at.%)			
	Ni	Mn	Sn	Fe	Ni	Mn	Sn	Fe
0	49.8±0.4	38.2±0.2	12.0±0.2	—	—	—	—	—
1	48.9±0.5	38.1±0.3	12.0±0.1	1.0±0.02	—	—	—	—
2	48.1±0.5	38.0±0.2	11.9±0.2	2.0±0.04	—	—	—	—
3	46.7±0.3	38.2±0.3	12.1±0.1	3.0±0.03	35.7±0.2	45.2±0.3	2.1±0.1	17.0±0.2
4	45.9±0.4	38.0±0.3	12.6±0.1	3.5±0.06	34.2±0.2	44.8±0.1	2.3±0.2	18.7±0.1
5	45.2±0.5	38.2±0.3	13.0±0.2	3.6±0.03	32.6±0.2	44.0±0.3	1.8±0.1	21.6±0.1

Fig. 3-14 displays polarized metallographic images of $Ni_{50-y}Mn_{38}Sn_{12}Fe_y$ (y=0, 1 and 2), revealing the presence of martensitic variants of various scales. Under polarized light, the different colors indicating the martensite variants of the Ni-Mn-Sn alloy suggest distinct crystallographic orientations among the variants. The lamellar and spearhead-shaped martensite structures exhibit a self-cooperative arrangement, with visible fine substructures inside. Furthermore, the grains appear to be relatively coarsened after undergoing heat treatment, with the average grain size of the central equiaxed crystal measured at about 270 μm.

The microstructures of the $Ni_{50-y}Mn_{38}Sn_{12}Fe_y$ alloys with y=0, y=1, and y=2

at room temperature suggest that they are single-phase solid solutions. However, as the Fe doping content increases, the microstructure gradually transforms into a two-phase mixed microstructure of austenite and martensite. The martensite phase extends from one side of the austenite grain boundary towards the interior of the austenite grain, forming a distinct spearhead-shaped deformed morphology, which is attributed to the process of martensite formation. Initially, self-cooperative variants nucleate and grow at the grain boundaries, stimulating the growth of other variants. As the phase transition progresses, spearhead-like self-cooperative morphologies develop at the ends of the variants.

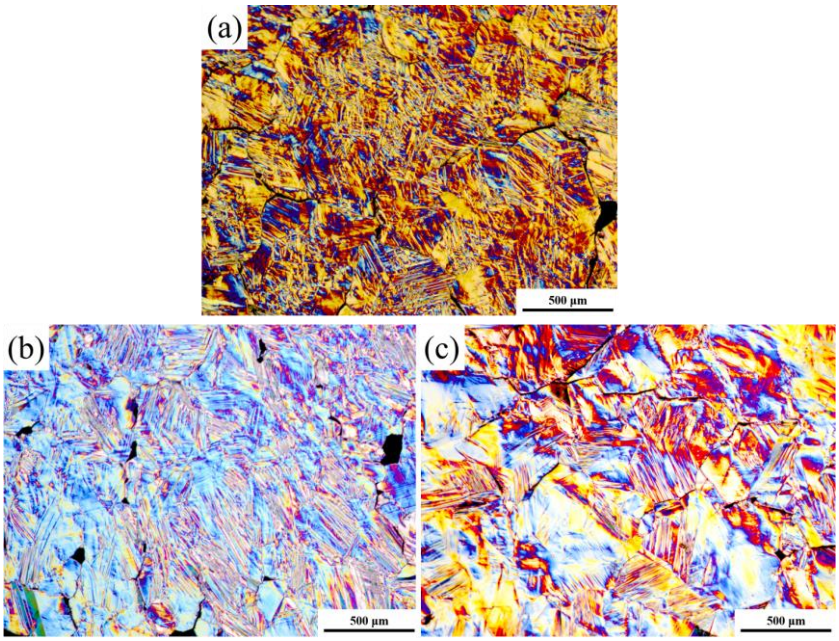

Fig. 3-14 Polarized optical micrograph of $Ni_{50-y}Mn_{38}Sn_{12}Fe_y$ (y=0, 1, and 2) alloys (a) y=0; (b) y=1; (c) y=2

The austenite phase of Ni-Mn-Sn alloys possesses a highly ordered $L2_1$ structure. Through alloy doping, both the alloy composition and sublattice site occupation are modified, while the martensite phase exhibits various modulated structures[147, 148]. Room-temperature XRD phase analysis results are presented in Fig. 3-15. In the ternary alloy, the martensite phase adopts an orthorhombic 10M

modulated structure with lattice parameters a_0=0.434 nm, b_0=0.559 nm, and c_0=2.195 nm, consistent with the findings reported by Krenke et al[43].

With increasing Fe doping content, the y=2 alloy exhibits two sets of diffraction peaks in Fig. 3-15, indicating coexistence of orthorhombic 10M modulated martensite and austenite phases at room temperature. The y=4 alloy primarily consists of $L2_1$-type austenite matrix at room temperature, accompanied by additional diffraction peaks from secondary phases[7], in agreement with the BSE results shown in Fig. 3-13.

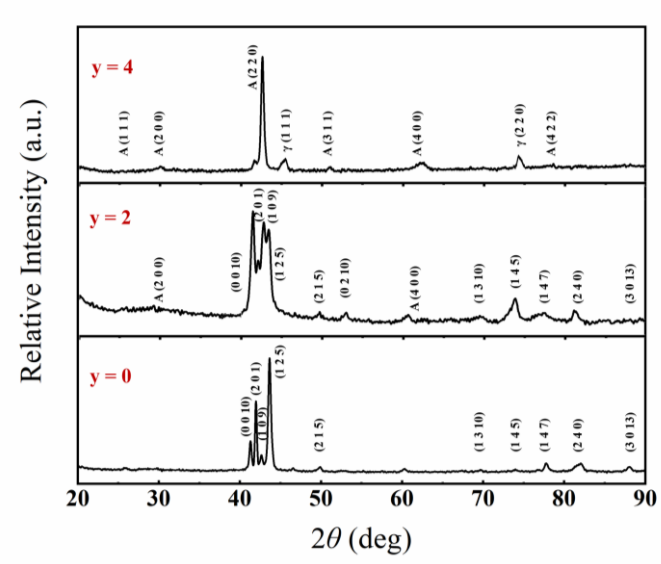

Fig. 3-15 XRD patterns of $Ni_{50-y}Mn_{38}Sn_{12}Fe_y$ alloys measured at room temperature

3.5.2 Compressive Mechanical Properties of Ni-Mn-Sn-Fe Alloys

Ni-Mn-Sn alloys exhibit strong elastic anisotropy, making grain boundaries prone to stress concentration and inherently brittle. The mechanical properties of Ni-Mn-Sn can be effectively improved through doping such as Fe or Cu[46, 91]. To avoid the influence of stress-induced martensitic transformation on mechanical properties, compressive stress-strain curves were measured for $Ni_{50-y}Mn_{38}Sn_{12}Fe_y$ (y=0, 1, 2, 3, 4, 5) alloys at temperatures corresponding to A_f+60 K (where A_f is the finishing temperature of reverse martensitic transformation). The results are shown

in Fig 3-16.

The results demonstrate a gradual increase in yield strength with higher Fe doping concentrations. The y=5 alloy exhibits fracture strength and strain of 1105 MPa and 5.8% respectively, representing a 2.1-fold improvement compared to the undoped $Ni_{50}Mn_{38}Sn_{12}$ alloy (512 MPa and 2.6%). Both y=4 and y=5 alloys show significant enhancement in elastic modulus relative to the undoped $Ni_{50}Mn_{38}Sn_{12}$. The secondary phases distributed along grain boundaries in the alloy matrix effectively inhibit crack propagation, thereby improving both strength and toughness.

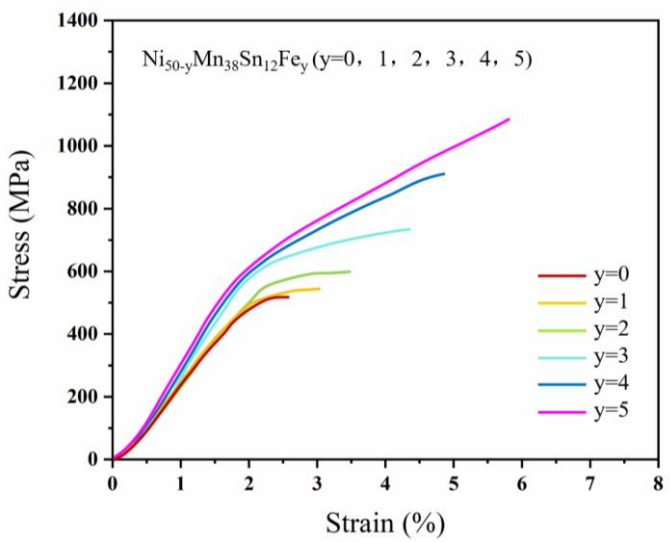

Fig. 3-16 Stress-strain curves of $Ni_{50-y}Mn_{38}Sn_{12}Fe_y$ alloys at temperature of A_f+60K

Fig. 3-17 presents the microscopic morphology of the fracture surface for the y=4 alloy after the aforementioned compression test, analyzing the influence of secondary phases on mechanical properties through crack propagation paths. As shown in Fig. 3-17(a), the secondary phases in the alloy (indicated by yellow circles) undergo plastic deformation under stress, effectively releasing stress concentration at crack tips and impeding crack propagation. In Fig. 3-17(b), the detachment of secondary phases (within yellow circles) during stress application causes cracks to

propagate along the interface between secondary phases and the matrix, forming tortuous fracture paths that dissipate more energy and enhance mechanical performance.

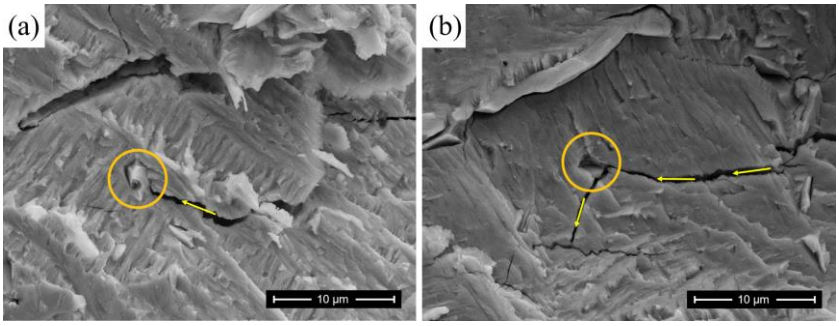

Fig. 3-17 SEM fracture surface morphology of $Ni_{50-y}Mn_{38}Sn_{12}Fe_y$ (y=4) alloy (a) local magnified image; (b) local magnified image (The yellow arrow indicates the direction of crack propagation)

Experimental results demonstrate that when Fe doping exceeds 4 at.%, the gradual formation of secondary phases significantly increases transformation hysteresis. These secondary phases hinder martensitic transformation, adversely affecting the alloy's caloric effects. Therefore, the role of secondary phases in Ni-Mn-Sn alloys requires balanced consideration—acknowledging their positive impact on mechanical properties while recognizing their potential drawbacks for caloric effects.

3.5.3 Martensitic Transformation and Magneto-structural Phase Diagram of Ni-Mn-Sn-Fe Alloys

Since the characteristic phase transition temperatures of solid-state refrigeration materials are closely related to their operational temperature range, DSC was employed to analyze the characteristic phase transition temperatures during endothermic and exothermic processes. Fig. 3-18(a) shows the DSC curves of $Ni_{50-y}Mn_{38}Sn_{12}Fe_y$ alloys. The curves reveal that during cooling, the alloys exhibit an exothermic peak corresponding to the martensitic transformation, while

during heating, an endothermic peak appears corresponding to the reverse martensitic transformation. The characteristic phase transition temperatures were determined using the tangent method: martensitic transformation start temperature (M_s), martensitic transformation finish temperature (M_f), reverse martensitic transformation start temperature (A_s), and reverse martensitic transformation finish temperature (A_f). Additionally, the peak temperatures of martensitic transformation (T_M) and reverse martensitic transformation (T_A) were obtained from the DSC curves.

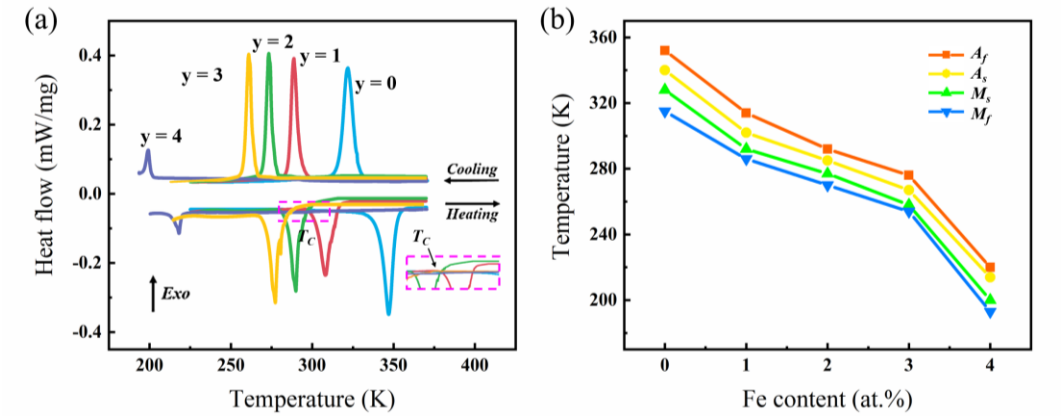

Fig. 3-18 Martensite transformation characteristics of $Ni_{50-y}Mn_{38}Sn_{12}Fe_y$ alloys
(a) DSC curves; (b) MT characteristic temperatures v.s. Fe content curves

The DSC curves also show a distinct thermal hysteresis between the exothermic and endothermic peaks, consistent with typical first-order phase transition behavior. A notable inflection point (indicated by arrows in the figure) appears in both the heating and cooling processes, corresponding to the Curie temperature of the austenite phase (T_C^A). The Curie transition exhibits almost no thermal hysteresis, which is characteristic of a second-order phase transition. Fig. 3-18(b) illustrates the variation in characteristic phase transition temperatures with Fe content (y-value) in $Ni_{50-y}Mn_{38}Sn_{12}Fe_y$ alloys. As y increases, M_s, M_f, A_s, and A_f all exhibit a decreasing trend. Previous studies[78, 76, 77, 75] have shown that the phase transition temperatures of Heusler alloys are regulated by the *e/a* ratio and unit cell

volume. For $Ni_{50-y}Mn_{38}Sn_{12}Fe_y$ alloys, an increase in y reduces the *e/a* ratio. Moreover, doping with Fe (atomic radius 0.127 nm), which replaces Ni (atomic radius 0.124 nm), leads to an expansion of the unit cell volume, thereby lowering the characteristic phase transition temperatures of the alloy.

DSC was employed to investigate the latent heat during phase transitions in $Ni_{50-y}Mn_{38}Sn_{12}Fe_y$ alloys with varying compositions. During the cooling process of magnetic alloys, a paramagnetic-to-ferromagnetic transition occurs, which represents a second-order phase transition. This magnetic transformation involves minimal latent heat, manifesting as a small step-like change in heat flow during DSC measurements, making the results less visually distinct. Therefore, magnetization-temperature (*M-T*) curves obtained under a low magnetic field of 100 Oe can be utilized to characterize the martensitic transformation temperatures of the alloys.

Fig. 3-19 shows the *M-T* curves of the $Ni_{50-y}Mn_{38}Sn_{12}Fe_y$ alloy under a 100 Oe external field. The tangent method can also be employed to determine the characteristic phase transition temperatures (M_s, M_f, A_s and A_f), which are largely consistent with the results obtained from DSC analysis in the previous section. From Fig. 3-19, it can be observed that the y=0 alloy exhibits weak magnetism near the phase transition temperature. As the Fe doping concentration increases, the magnetization of the alloy strengthens. In the FC (field-cooled) curve of the y=1 alloy, the alloy is in the paramagnetic austenite (PA) state at high temperatures. Below 310 K (i.e., the T_C^A temperature), the magnetization of the alloy rapidly increases, transitioning into ferromagnetic austenite (FA), followed by the transformation from ferromagnetic austenite to paramagnetic martensite (PM).

However, upon examining the FH (field-heated) curve of the y=1 alloy, no

significant magnetic change is observed during the reverse martensitic transformation. This is due to the coupling between the martensitic phase transition and the magnetic transition in the y=1 alloy, where the magnetic transition hinders the reverse martensitic transformation, resulting in the absence of a distinct peak in the FH curve. In the lower temperature region, the magnetization gradually increases as the temperature decreases, as the paramagnetic martensite (PM) transforms into ferromagnetic martensite (FM) at 215 K (the T_C^M temperature).

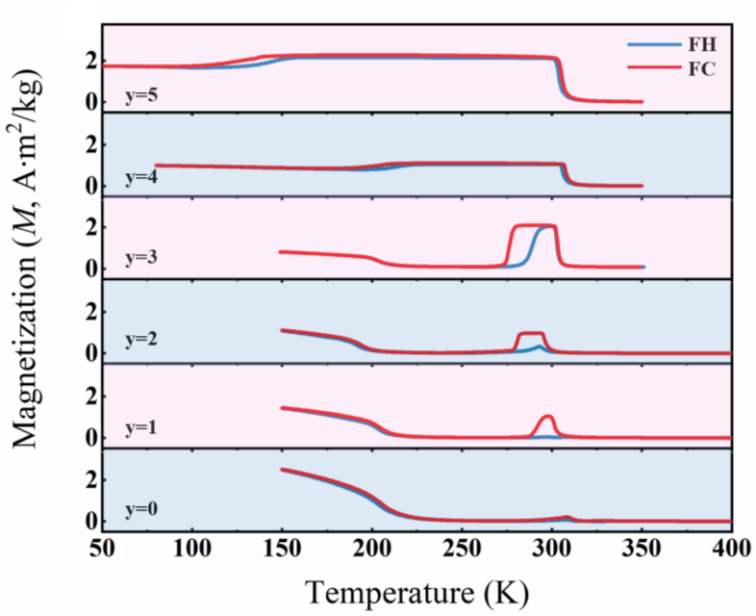

Fig. 3-19 *M-T* curve for $Ni_{50-y}Mn_{38}Sn_{12}Fe_y$ alloys under 100 Oe

For the y=2 alloy (as shown in Fig. 3-19), it undergoes an incomplete reverse martensitic transformation from martensite to austenite, accompanied by a jump in magnetization. When y=3, the alloy experiences a complete reverse martensitic transformation. As demonstrated by the FC curve of the $Ni_{47}Mn_{38}Sn_{12}Fe_3$ alloy, after the transformation from paramagnetic austenite to ferromagnetic austenite, the magnetization sharply decreases at 279 K (i.e., M_s temperature) as the temperature further drops, until the magnetization reaches its minimum, marking the completion of the martensitic transformation. For the y=5 alloy, the FC curve indicates that the transition from paramagnetic austenite to ferromagnetic austenite

near T_C^A follows the same process as in other alloys. Upon further cooling, the alloy directly transforms into ferromagnetic martensite.

Based on the DSC results and the T_A, T_C^A and T_C^M values determined from the *M-T* curves in Fig. 3-19, combined with experimental data reported by Zhang[149] and Tan et al.[150], the magneto-structural phase diagram of $Ni_{50-y}Mn_{38}Sn_{12}Fe_y$ alloys was obtained, as shown in Fig. 3-20. The Fe content in the alloys has a minor influence on T_C^A and T_C^M, whereas the T_A value of $Ni_{50-y}Mn_{38}Sn_{12}Fe_y$ alloys decreases linearly with increasing Fe content, which can be fitted as $T_{A(y)}$=347−31.36y. By fitting the T_A, T_C^A and T_C^M temperatures for each composition, the phase diagram can be divided into four regions, represented by different colors, corresponding to PA, FA, PM and FM, respectively.

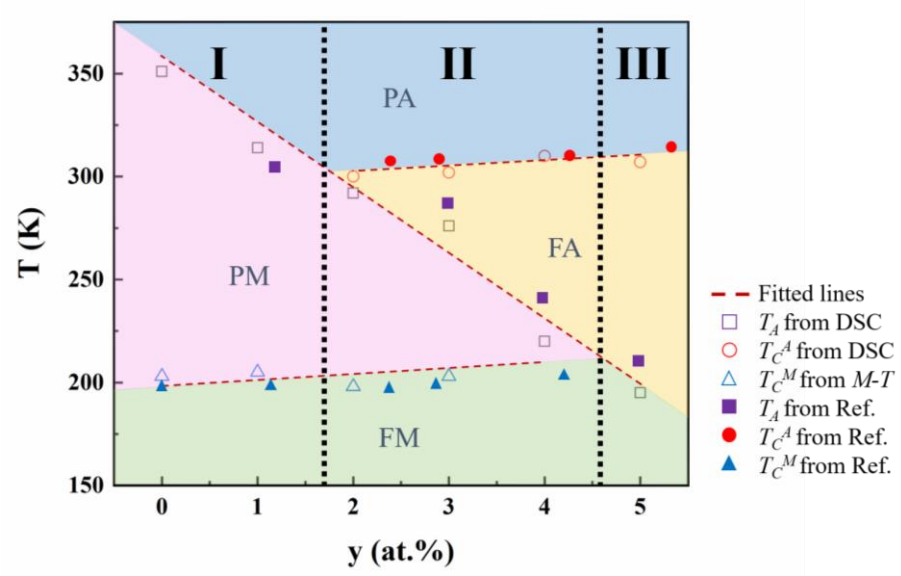

Fig. 3-20 Magneto-structural phase diagram of the $Ni_{50-y}Mn_{38}Sn_{12}Fe_y$ alloys

Additionally, based on the changes in the magnetic states of the alloys during cooling, the phase diagram can be divided into three regions (I, II, and III), as demarcated by the black dashed lines in Fig. 3-20. In Region I, the cooling process involves the PA→PM→FM transformation, where the martensitic phase transition occurs without an accompanying magnetic transition. In Region II, the cooling

process follows the PA → FA → PM → FM transformation sequence. Here, the martensitic phase transition takes place between ferromagnetic austenite and paramagnetic martensite, accompanied by a magnetic transition. Consequently, research on the magneto-structural coupling and related magnetic driving properties[151, 152] has been a key focus in the study of Ni-Mn-X (X = In, Sn, Sb, Al) magnetic alloys. In Region III, the cooling process undergoes a PA → FA → FM transformation, where the martensitic phase transition occurs between ferromagnetic austenite and ferromagnetic martensite. Since both austenite and martensite phases exhibit ferromagnetism, the difference in their saturation magnetization remains significant.

3.5.4 Magnetocaloric Effect of $Ni_{47}Mn_{38}Sn_{12}Fe_3$ Alloys

On the basis of the $Ni_{50-y}Mn_{38}Sn_{12}Fe_y$ phase diagram, achieving reversible phase transitions and large magnetocaloric effects under low magnetic fields makes it particularly important to regulate the magneto-structural transitions of the alloys. Research has shown that the transformation hysteresis (ΔT_{hys}), phase transition interval (ΔT_{int}), and the magnetic field sensitivity parameter of the magneto-structural transition temperature ($\Delta T_A/\Delta\mu_0 H$) all influence the magneto-structural transitions[153, 154]. Among these, the transformation hysteresis is calculated by the formula:

$$\Delta T_{hys}=\frac{(A_s+A_f-M_s-M_f)}{2} \tag{3.8}$$

The formula for calculating the phase transition interval is:

$$\Delta T_{int}=\frac{(A_f-A_s+M_s-M_f)}{2} \tag{3.9}$$

The sensitivity parameters of critical magnetic field to temperature can be estimated using the Clausius-Clapeyron equation:

$$\frac{\Delta T_A}{\Delta \mu_0 H} \approx \frac{\Delta M}{\Delta S_{\mathrm{A}}} \tag{3.10}$$

where ΔM is the magnetization difference between the two phases, ΔS_{A} is the entropy change of reverse martensitic transformation.

The minimum magnetic field required to achieve a complete and reversible magneto-structural phase transition can be calculated using the following equation:

$$\mu_0 H_{\min} \approx \frac{\left(\Delta T_{\mathrm{hys}} + \Delta T_{\mathrm{int}}\right)}{\left(\frac{\Delta M}{\Delta S_{\mathrm{A}}}\right)} \tag{3.11}$$

According to Eq. (3.11), to obtain large and reversible magnetocaloric effects under low magnetic fields, it is necessary to simultaneously regulate ΔT_{hys}, ΔT_{int} and $\Delta M/\Delta S_A$—factors that are mutually constraining. Magnetic alloys should possess small ΔT_{hys} and ΔT_{int}, while $\Delta M/\Delta S_A$ requires comprehensive consideration. Here, ΔS_A represents the maximum theoretical entropy change during the reverse martensitic transformation, and an increase in ΔM value plays a beneficial role in enhancing the alloy's magnetic properties. To determine ΔM, the M-T curves of $Ni_{50-y}Mn_{38}Sn_{12}Fe_y$ alloys were measured under a 5 T magnetic field, as shown in Fig. 3-21(a).

Fig. 3-21(b) shows the variation curves of austenite magnetization, martensite magnetization, and their magnetization difference (ΔM) with Fe content in the alloys under a 5 T external magnetic field. Analysis of Fig. 3-21(a) reveals that as the Fe content increases, the T_M (or T_A) gradually decreases, while the magnetization of both austenite and martensite phases progressively increases. Notably, the magnetization of austenite rises at a faster rate than that of martensite, leading to an increase in ΔM with higher Fe content. According to literature reports[155-157], the value of $\Delta M/\Delta S_A$ is closely related to the temperature difference between the Curie point and the peak temperature of the reverse martensitic

transformation ($T_C{}^A - T_A$). As observed in the earlier DSC results, ΔS_A decreases while ΔM increases with a larger ($T_C{}^A - T_A$). Consequently, $\Delta M/\Delta S_A$ also increases as ($T_C{}^A - T_A$) grows.

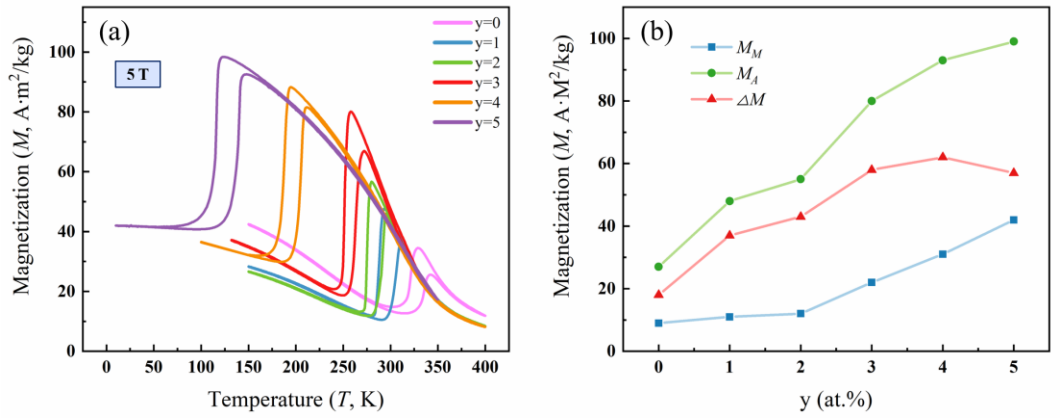

Fig. 3-21 The magnetization curve of $Ni_{50-y}Mn_{38}Sn_{12}Fe_y$ series alloy under a 5 T magnetic field and the magnetization difference between the two phases during phase transition

(a) *M-T* curves at 5 T; (b) relationships between Fe content and ΔM

Through coordinated regulation of magneto-structural phase transition parameters, the $Ni_{47}Mn_{38}Sn_{12}Fe_3$ alloy exhibits small ΔT_{hys} and ΔT_{int} while maintaining a large ΔS_A. According to the phase diagram, among the three compositions with magneto-structural coupling, the y=4 alloy has a relatively low phase transition temperature, limiting its practical application at room temperature. Additionally, it shows significant ΔT_{hys} due to the high content of secondary phases in the matrix that do not undergo martensitic transformation. The y=2 alloy has a low ΔM, which is unfavorable for achieving high phase transition driving force and consequently affects the alloy's magnetocaloric effect. Therefore, considering both the working temperature range and magnetic properties, the $Ni_{47}Mn_{38}Sn_{12}Fe_3$ alloy was selected for studying its room-temperature magnetocaloric effect.

As demonstrated by previous research, the phase transition temperature of $Ni_{47}Mn_{38}Sn_{12}Fe_3$ alloy has been adjusted to near room temperature. The doping

process make the alloy with a high ΔM of 57 A·m^2/kg, along with substantial entropy change and minimal ΔT_{hys}, which are conducive to achieving superior magnetocaloric properties. Fig. 3-22(a) presents the *M-T* curve of $NNi_{47}Mn_{38}Sn_{12}Fe$ alloy under a 100 Oe magnetic field and its DSC curves in the 255−295 K range. The *M-T* curve aligns with the characteristic phase transition temperatures determined from the DSC curves. M_s, M_f, A_s and A_f are identified as 265.5 K, 262.5 K, 268 K, and 281 K, respectively.

Notably, within the reverse martensitic transformation temperature range, the *M-T* curve exhibits three distinct slope variations. Correspondingly, the DSC results reveal not only a main peak at 275 K but also additional transformation peaks near 274 K and 278 K, indicating the occurrence of intermartensitic transformation. Fig. 3-22(b) displays the first derivative (d*M*/d*T*-*T* curve) of the *M-T* curve obtained under a 100 Oe magnetic field. Multiple irregular minor peaks appear within the MT temperature range. These observations are consistent with the thermodynamic calculations of phase transitions discussed in Section 3.2.2.

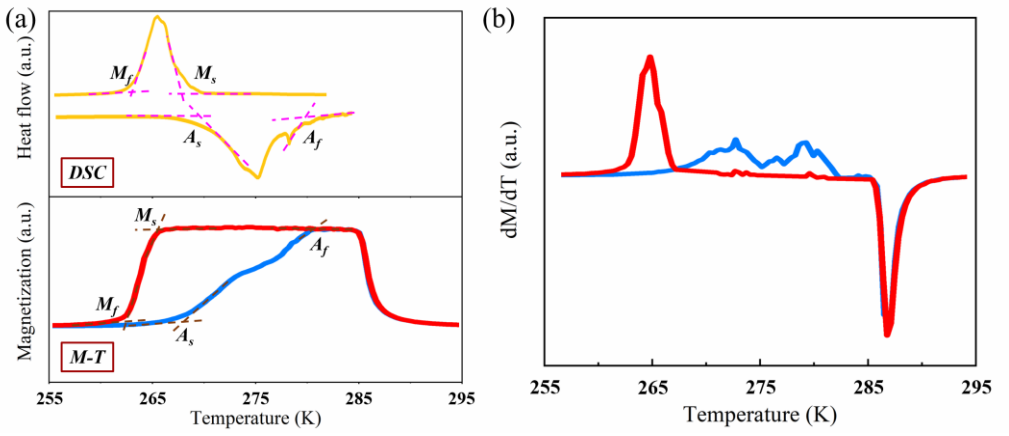

Fig. 3-22 Martensite transformation behaviors of $Ni_{47}Mn_{38}Sn_{12}Fe_3$ alloy
(a) DSC curve and *M-T* curve at 100 Oe; (b) first-derivative (d*M*/d*T*-*T*) plots of *M-T*

To determine the crystal structure during phase transition, in-situ XRD analysis was conducted at different temperatures covering the reverse martensitic

transformation range. Fig. 3-23 shows the XRD patterns of $Ni_{47}Mn_{38}Sn_{12}Fe_3$ alloy measured under isothermal conditions within the 240−290 K range during heating. At 250 K (<M_f), the $Ni_{47}Mn_{38}Sn_{12}Fe_3$ alloy consists of a mixture of orthorhombic four-layered modulated martensite (4O), five-layered orthorhombic martensite (10M), and residual $L2_1$ austenite. When the temperature increases to 260 K, the peak intensities corresponding to 4O martensite and $L2_1$ austenite strengthen, while those of 10M martensite weaken. The 10M martensite peaks nearly disappear at 270 K, indicating that within this temperature range, the 10M martensite transforms into 4O martensite and $L2_1$ austenite. As the temperature further rises to 280 K, the Bragg diffraction peaks of the martensite phase are replaced by those of a new phase, signifying the complete transformation of the alloy into $L2_1$ austenite.

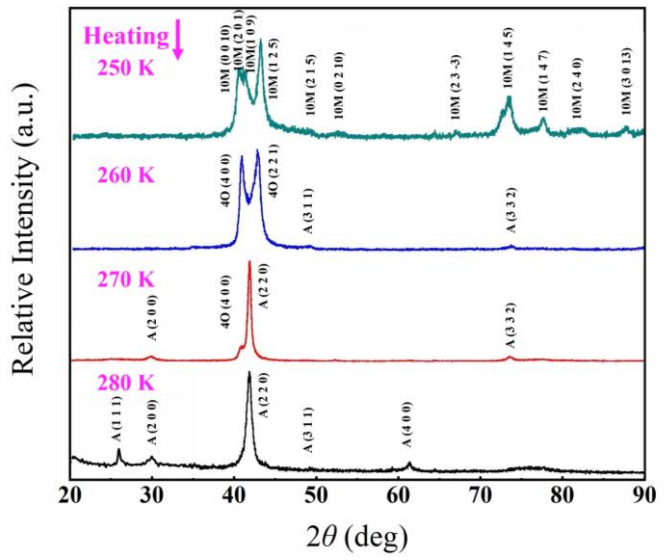

Fig. 3-23 XRD patterns of $Ni_{47}Mn_{38}Sn_{12}Fe_3$ alloy under different temperatures

From these results, it can be concluded that the reverse martensitic transformation in $Ni_{47}Mn_{38}Sn_{12}Fe_3$ alloy occurs within the temperature range of 260−280 K. This range is essentially consistent with the results obtained from previous PPMS and DSC measurements. The metamagnetic transformation of $Ni_{47}Mn_{38}Sn_{12}Fe_3$ alloy proceeds in two stages: In the first stage, a portion of the

10M martensite transforms into $L2_1$ austenite while another portion transforms into 4O martensite, while in the second stage, the 4O martensite transforms into $L2_1$ austenite. This two-stage transformation process explains the complex phase evolution observed during heating.

To investigate the metamagnetic transition behavior of $Ni_{47}Mn_{38}Sn_{12}Fe_3$ near its phase transition temperature, *M-H* curves were measured separately within the martensitic transformation temperature range (246−270 K) and near the Curie point (275−350 K). The testing method employed here was the Loop method mentioned in Section 2.3.2, with results shown in Fig. 3-24(a). When T>270 K, $Ni_{47}Mn_{38}Sn_{12}Fe_3$ alloy exhibits ferromagnetic behavior, with magnetization decreasing as temperature increases. Within the temperature range of 248−270 K, the alloy demonstrates strong characteristics of metamagnetic phase transition. When the magnetic field reaches a critical value, the slope of the *M-H* curve abruptly increases significantly, indicating rapid enhancement of magnetization, which is particularly favorable for achieving large magnetocaloric effects.

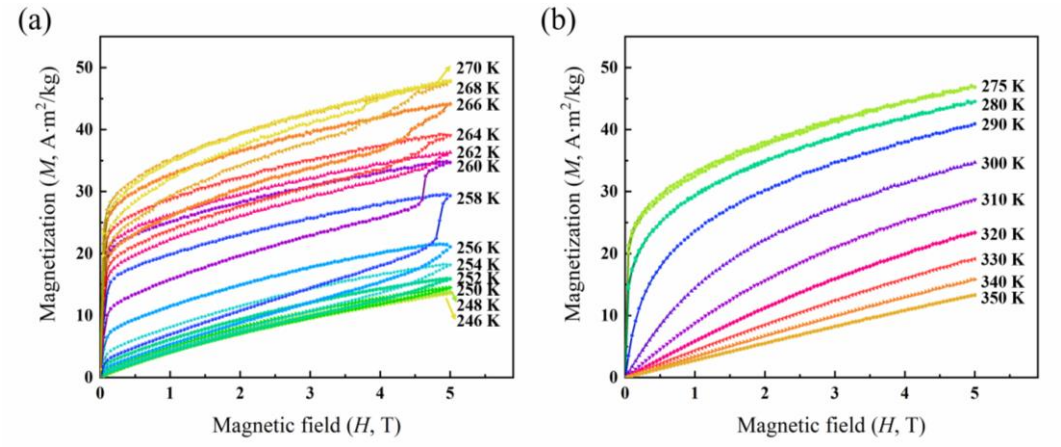

Fig. 3-24 *M-H* curves under 5 T at different temperatures for $Ni_{47}Mn_{38}Sn_{12}Fe_3$ alloy (a) 246 K≤T≤270 K; (b) 275 K≤T≤350 K

To elucidate the nature of the metamagnetic transition, Arrott plots were constructed based on the *M-H* curves in Fig. 3-24, with results shown in Fig. 3-25.

According to Banerjee's criterion[158], when Arrott curves exhibit an "S" shape or negative slope, the magneto-structural transition is first-order; when the slope is positive, it indicates a second-order transition. As seen in Fig. 3-25(a), the Arrott curves of $Ni_{47}Mn_{38}Sn_{12}Fe_3$ alloy show negative slopes in the 252−268 K range, confirming a first-order magneto-structural transition. Above 275 K (as shown in Fig. 3-25(b)), the positive slope indicates a second-order transition. Notably, in the temperature range above 290 K, the negative y-axis intercept of the curves suggests 280 K<T_C^A<290 K[159]. Combining information from both *M-T* curves and Arrott plots, at 258 K the Arrott curve exhibits its maximum negative slope, while the *M-H* curve simultaneously shows the maximum rate of magnetization increase. This demonstrates that the phase transition reaches its fastest kinetics at 258 K[13].

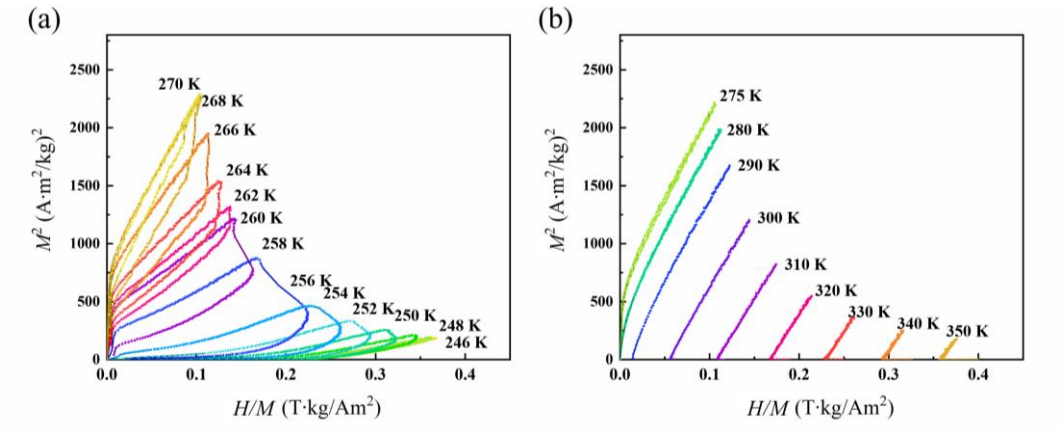

Fig. 3-25 Arrott curves at different temperatures for $Ni_{47}Mn_{38}Sn_{12}Fe_3$ alloy
(a) 246 K≤T≤270 K; (b) 275 K≤T≤350 K

The determination of magnetic hysteresis can be achieved by integrating the area enclosed between the magnetization and demagnetization curves of *M-H* curves at specific temperatures. The temperature dependence of magnetic hysteresis is shown in Fig. 3-26. Since the temperature range of 262−264 K corresponds to the transformation from 10M martensite to 4O martensite without significant field-induced reverse martensitic transformation, the magnetic

hysteresis consequently decreases in this temperature range. The nonreversible magnetic hysteresis reduces the refrigeration efficiency of first-order phase transition solid-state refrigerants. Both applied stress (or hydrostatic pressure) and reduced material dimensions can be utilized to modulate the hysteresis of the alloy, which will be discussed in Chapter 5.

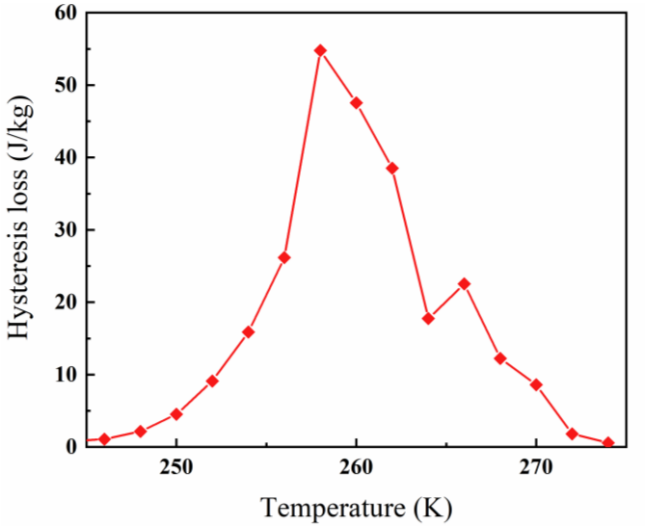

Fig. 3-26 The hysteresis loss at 5 T as a function of temperature for $Ni_{47}Mn_{38}Sn_{12}Fe_3$ alloy

The relationship between ΔS_m and temperature for the $Ni_{47}Mn_{38}Sn_{12}Fe_3$ alloy under various magnetic fields was calculated using Eq. (1.33) and is shown in Fig. 3-27. This calculation was based on the *M-H* curves measured at different temperatures. Two distinct ΔS_m peaks of 15.2 J/kg·K and 9 J/kg·K appear at 259 K and 267 K respectively under a 5 T magnetic field. It should be noted that these two consecutive metamagnetic transitions result in corresponding dual peaks in ΔS_m, which is consistent with the phase transition process revealed in the previously discussed *M-H* curves.

The working temperature interval of the alloy (define as the full width at half maximum of the ΔS_m-*T* curve, ΔT_{FWHM}) spans from 255 K to 268 K. The ΔT_{FWHM} value of $Ni_{47}Mn_{38}Sn_{12}Fe_3$ alloy exceeds that of many Ni-Mn-based polycrystalline alloys[160-162]. As mentioned in Section 1.2.5, the magnetic refrigeration capacity

represents the maximum energy transferred during one refrigeration cycle, and thus can be evaluated using *RC*. The *RC* value can be estimated by integrating the area under the ΔS_m-T curve within the ΔT_{FWHM} range. $Ni_{47}Mn_{38}Sn_{12}Fe_3$ alloy demonstrates a *RC* value of 142.5 J/kg under a 5 T magnetic field.

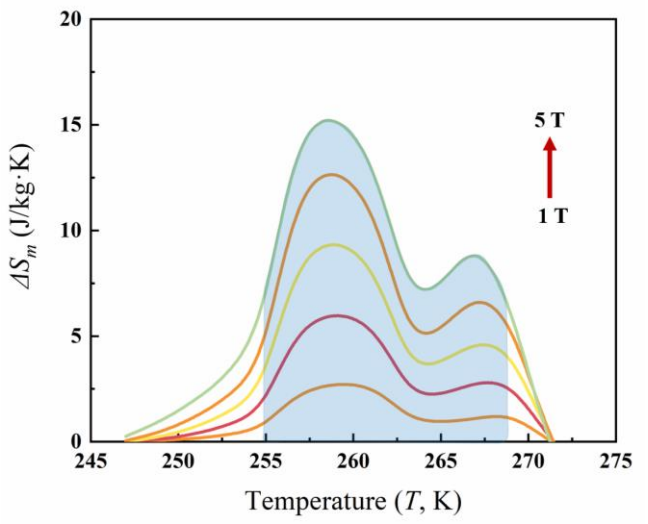

Fig. 3-27 ΔS_m-T curve for $Ni_{47}Mn_{38}Sn_{12}Fe_3$ alloy under magnetic fields of 1−5 T

3.6 Summary

This chapter first employs first-principles calculations to analyze the effects of Fe, Cu, and B as fourth-component dopants on the total energy, lattice parameters, and electronic structure of the alloys. The mechanisms by which these three elements influence the stability and properties of the martensitic phase are revealed, and the composition ranges meeting the design requirements for Ni-Mn-Sn-based magnetic alloys are predicted. Subsequently, a series of $Ni_{50-y}Mn_{38}Sn_{12}Fe_y$ (y=0, 1, 2, 3, 4, 5) alloys were prepared to investigate the influence of Fe doping on the magneto-structural phase transition coupling state, room-temperature compressive properties, and magnetocaloric performance. The main conclusions are as follows:

(1) First-principles calculations indicate that when one Fe atom is doped into the alloy system, it preferentially occupies the Ni sublattice sites. The magnetic

order between Mn atoms occupying Sn sites and original Mn atoms exhibits antiferromagnetic alignment. During tetragonal distortion, the austenite phase can transform into various types of martensite (e.g., 4O and 5M), possessing the energetic conditions for two-step or even multi-step phase transitions.

(2) First-principles results show that in $Ni_7Cu_1Mn_6Sn_2$ and $Ni_6Cu_2Mn_6Sn_2$ alloys, Cu atoms preferentially occupy Ni sublattice sites. Cu doping reduces the energy difference between austenite and martensite phases, suppressing the tendency for austenite-to-martensite transformation while enhancing the stability of the alloy system.

(3) From energetic and mechanical stability perspectives, B atoms most likely occupy the O−I octahedral interstitial sites. After doping, the alloy exhibits enhanced incompressibility, fracture resistance, and improved shear deformation resistance, though its magnetic properties remain insensitive to B doping.

(4) A magneto-structural phase diagram was established for $Ni_{50-y}Mn_{38}Sn_{12}Fe_y$ alloys. Complete magneto-structural coupling can be achieved within the Fe content range of 1.7−4.5 at.%. The $Ni_{47}Mn_{38}Sn_{12}Fe_3$ alloy demonstrates compressive fracture strength and strain of 723 MPa and 4.4%, respectively, representing more than 1.4-fold improvement compared to the undoped alloy (493 MPa and 2.6%). Under a 5 T magnetic field, the $Ni_{47}Mn_{38}Sn_{12}Fe_3$ alloy undergoes a two-stage reverse martensitic transformation: first stage (10M→$L2_1$ and 10M→4O) and second stage (4O→$L2_1$).

Chapter 4 Magneto-structural Phase Transition and Magnetocaloric/ Elastocaloric Properties of Ni-Mn-Sn-Cu Alloy

4.1 Introduction

According to the findings presented in the previous chapter, Fe-doped Ni-Mn-Sn-Fe magnetic alloys exhibit a large and reversible magnetocaloric effect, making them suitable for refrigeration applications driven solely by a magnetic field. However, similar to other first-order magnetocaloric alloys (such as Gd-Si-Ge, La-Fe-Si, and Fe-Rh alloys), their reversible refrigeration temperature range remains relatively narrow. The MT temperature of the $Ni_{47}Mn_{38}Sn_{12}Fe_3$ alloy is around 250 K, below room temperature, which somewhat limits its practical application in room-temperature refrigeration. Additionally, magnetic alloys require good mechanical properties—both to withstand sufficient stress for a substantial elastocaloric effect and to ensure excellent processability. However, the strengthening effect of Fe doping on the alloy's mechanical performance remains insufficient, further restricting the potential applications of Ni-Mn-Sn-Fe magnetic alloys.

This chapter initiates a systematic investigation of the reversible and nonreversible components during martensitic transformation using modulated differential scanning calorimetry (MDSC). The intrinsic correlation between the nonreversible component and energy dissipation during phase transition was analyzed, with the transformation hysteresis of martensite examined from an energy dissipation perspective. Furthermore, the relationship between the reversible component of martensitic transformation and the elastocaloric effect was

elucidated, leading to the development of an accurate method for estimating adiabatic temperature changes.

Based on first-principles calculations, a series of $Ni_{50-x}Mn_{38}Sn_{12}Cu_x$ (x=0, 2, 3, 4, 5, 6) alloys were prepared to investigate the influence of Cu doping on the microstructure, martensitic transformation, and mechanical properties of the alloys. The elastocaloric effect and its cyclic stability were also studied, with an analysis of the impact of strain rate, temperature, and maximum applied stress on the elastocaloric performance. Through Cu doping, two types of magneto-structural coupling states were successfully regulated.

4.2 Study on the Behavior of Thermoelastic Martensitic Transformation

4.2.1 Reversible and Nonreversible Components of Martensitic Transformation Caloric Effect

Various properties, such as the magnetocaloric effect and the elastocaloric effect, originate from martensitic transformation. Therefore, a more in-depth analysis of the martensitic transformation process is required to guide the design of alloy compositions. In Ortin and Planes' work[163, 164], they proposed two main driving forces for MT: (1) The chemical driving force, represented by the difference between Gibbs free energy of the two crystalline structures, (2) Non-chemical driving force, i.e. the strain energy generated by the change in the volume of the two phases during MT. The thermal-related signal recorded during the calorimetric tests originated from the combination of these two energies. That is to say, conventional calorimetric test such as differential scanning calorimetry (DSC) can only measures the sum of both thermal events, making it impossible to

distinguish the reversible (strain energy part) and nonreversible (Gibbs free energy part) transitions. In this regard, modulated differential scanning calorimetry (MDSC) appears to be an effective method for this study.

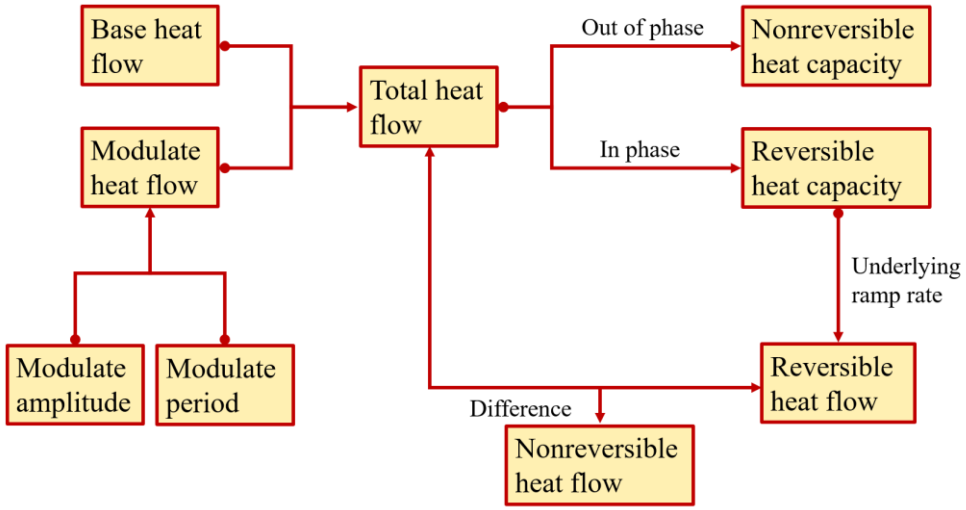

Fig. 4-1 Scheme of modulated differential scanning calorimetry

Unlike traditional DSC, MDSC can decompose the total heat flow into two distinct components: reversible heat flow and nonreversible heat flow. A pictorial representation of the signals by MDSC technique is given in Fig. 4-1. MDSC uses two ramp rates simultaneously for thermal analysis, *i.e.*, a linear ramp rate used in a conventional DSC and a periodically varying sinusoidal ramp rate. In this case, the changes in modulation temperature and modulation heat flow are illustrated in Fig. 4-2, and the actual change in sample temperature can be written as:

$$T=T_0+\beta t+T_A\sin(\omega t) \tag{4.1}$$

where T_0 is the initial temperature, β is the linear heating rate, T_A is the modulation amplitude, and ω is the frequency.

The measured heat flow is the total of all the thermal responses. The total heat flow (H) can be divided into the part related to heat capacity (C_p) and that related to the nonreversible heat flow:

$$\frac{dH}{dt} = C_P \frac{dT}{dt} + f(T, t) \tag{4.2}$$

where dH/dt is the total heat flow under a linear heating rate, C_p is the heat capacity, dT/dt is the heating rate. The heat flow resulting from the C_p change or heating rate is related to the reversible heat flow. $f(T, t)$ (where T is absolute temperature and t time) represents the nonreversible heat flow and is associated with the kinetics of heat transfer.

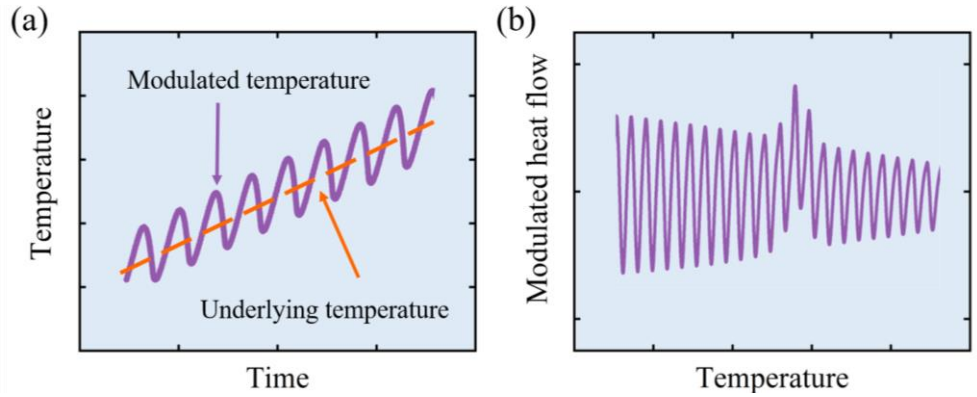

Fig. 4-2 The relationship between various physical quantities in MDSC analysis process (a) the modulated temperature changes as a function of time; (b) modulated heat flow as a function of temperature

As shown in Eq. (4.2), the first term on the right side represents the thermodynamic phase, generated by heat capacity or heating rate variations, and is defined as the reversible heat flow. The second term, being a function of temperature and time, is kinetically controlled and constitutes the nonreversible heat flow. Conventional DSC measures the aggregate of all thermal events, encompassing both the aforementioned reversible and nonreversible components (i.e., the sum of thermodynamic and kinetic contributions). However, traditional DSC cannot separate or detect the nonreversible energy dissipation caused by frictional losses due to interface migration, defect formation, and plastic transformation work. With MDSC, the heat flow patterns can be resolved into two parts. It is also possible to calculate directly the heat capacity of a sample with the

MDSC analysis:

$$C_p = \frac{K_{C_p} A_{M\text{-}HF}}{A_{M\text{-}HR}} \tag{4.3}$$

where $A_{M\text{-}HF}$ is the amplitude of modulated heat flow, $A_{M\text{-}HR}$ is the amplitude of modulated heating rate, and K_{Cp} is C_p calibration constant. It is possible to resolve the contribution of reversible and nonreversible heat flow by superposing the temperature-modulated signals.

During a DSC test, the temperature changes linearly at a constant heat or cooling rate. But in MDSC test, the temperature sinusoidal modulation may overlap on the linear temperature ramp. Therefore, it can be used to differentiate the exothermic and endothermic processes involved during MT. Fig. 4-3 shows the reversible, nonreversible and total heat flow of a $Ni_{47}Mn_{38}Sn_{12}Cu_3$ alloy obtained at various modulation periods. As shown in Fig. 4-3(a), when the modulation period is 40 s, the direction of the reversible heat-flow peak is opposite to that of the total heat flow. That indicated that the reversible heat flow is an endothermic process when the total heat flow exhibits an exothermic process. When the modulation period is extended to 60 s, as shown in Fig. 4-3 (b), the reversible heat flow successively exhibited both exothermic and endothermic peaks. When the modulation period is increased to more than 80 s, as shown in Fig. 4-3 (c-e), the reversible heat flow and the total heat flow always have peaks in the same direction.

It is noticed that the modulation period did not affect the nonreversible heat flow peaks, which always followed the direction of the total heat flow. This is often related to the inevitable occurrence of defects in the crystal, which induced stored elastic strain ($\Delta H_{el}^{P\text{-}M}$) at the phase interface between parent and martensite phases. In addition, the energy dissipation in friction ($E_{fr}^{P\text{-}M}$) during interface movement is

often heterogeneous. As a result, different martensitic plates or different parts of the same martensitic plate may exhibit different thermal hysteresis. For example, in the cooling process shown in Fig. 4-3(a), a transition from austenite to martensite occurred under the temperature disturbance (ΔT_1). At this point, the modulated heat flow of the MDSC provides a temperature disturbance (ΔT_2) in the heating direction, which triggers a portion of martensite reverting to the parent phase. Since ΔT_1 is always greater than ΔT_2 during cooling process, the phase transition from martensite to austenite is incomplete.

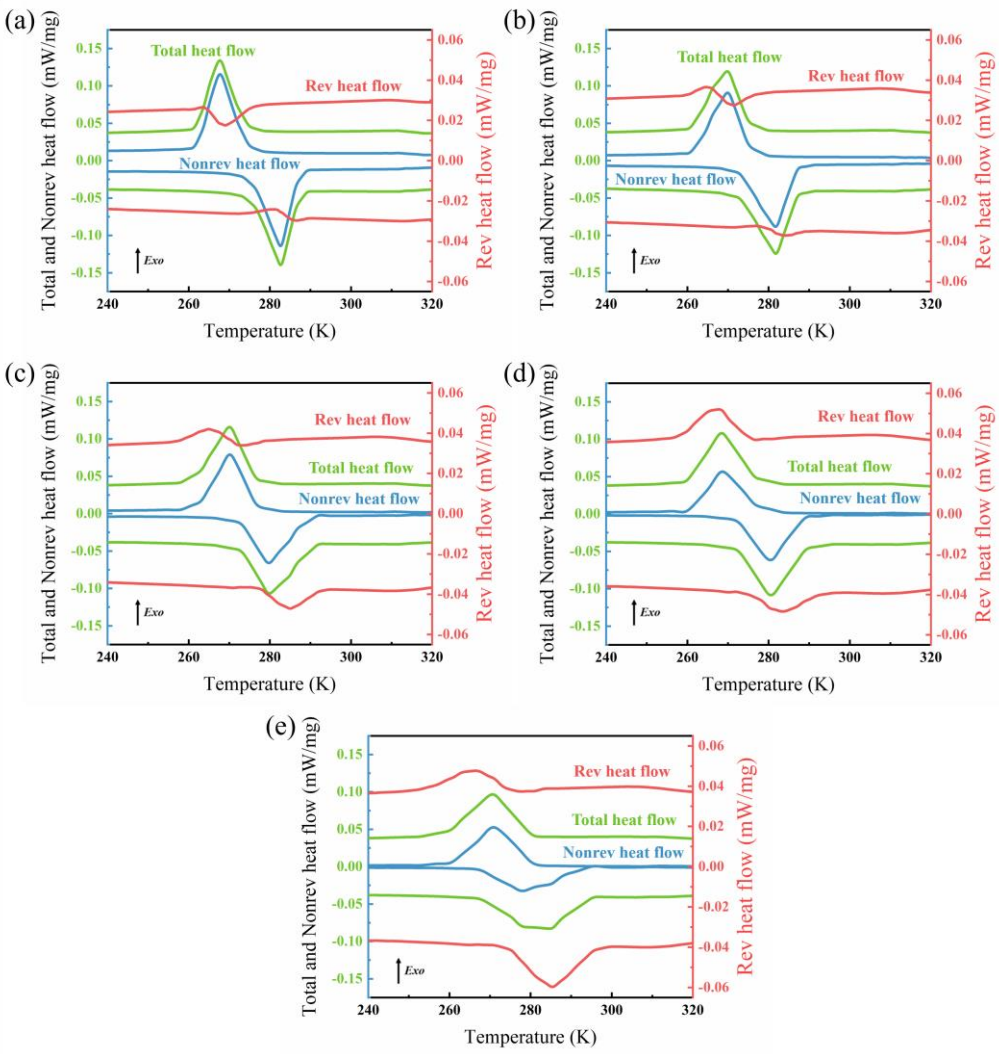

Fig. 4-3 Reversible, nonreversible and total heat flow of $Ni_{47}Mn_{38}Sn_{12}Cu_3$ alloy at various modulation periods

(a) 40 s; (b) 60 s; (c) 80 s; (d) 100 s; (e) 120 s

Therefore, within a given temperature modulation amplitude, a portion of martensite plates exhibit reversible properties, while the remaining exhibit nonreversible properties. The frictional work dissipation and thermal hysteresis during MT can be further analyzed from these nonreversible signals.

Meanwhile, the MDSC method enables simultaneous investigation of heat flow and heat capacity variations in the alloy. Fig. 4-4 illustrates the heat capacity evolution of the $Ni_{47}Mn_{38}Sn_{12}Cu_3$ alloy. Notably, abrupt changes and extremum values emerge in the reversible, nonreversible, and total heat capacities near both the martensitic transformation and reverse transformation temperatures, which are related to the first-order martensitic transformation.

A step-like feature appears near the Curie temperature (approximately 310 K), which arises from the second-order magnetic transition where the heat capacity exhibits an inflection rather than an abrupt change. In the vicinity of the martensitic transformation temperature, the total heat capacities of austenite and martensite are essentially comparable. However, the reversible heat capacity of austenite is higher than that of martensite, while its nonreversible heat capacity is lower.

This behavior can be attributed to two key factors: (1) The specific heat capacity depends on the number of available degrees of freedom (DOF) in the alloy. Each DOF is influenced by the potential vibration of individual atoms around their lowest-energy positions, and the material can store energy when quantum energy levels are reached[165]. As the temperature decreases to a specific threshold, these degrees of freedom begin to "freeze", preventing individual atoms from storing additional energy. Therefore, in the austenitic state, the value of DOF is higher than that in the martensitic state. (2) Austenite and martensite possess distinct crystal structures. Austenite has a body-centered cubic (bcc) lattice, whereas martensite

exhibits a monoclinic crystal system with a disordered structure. The higher lattice symmetry of austenite grants its atoms a greater number of DOF.

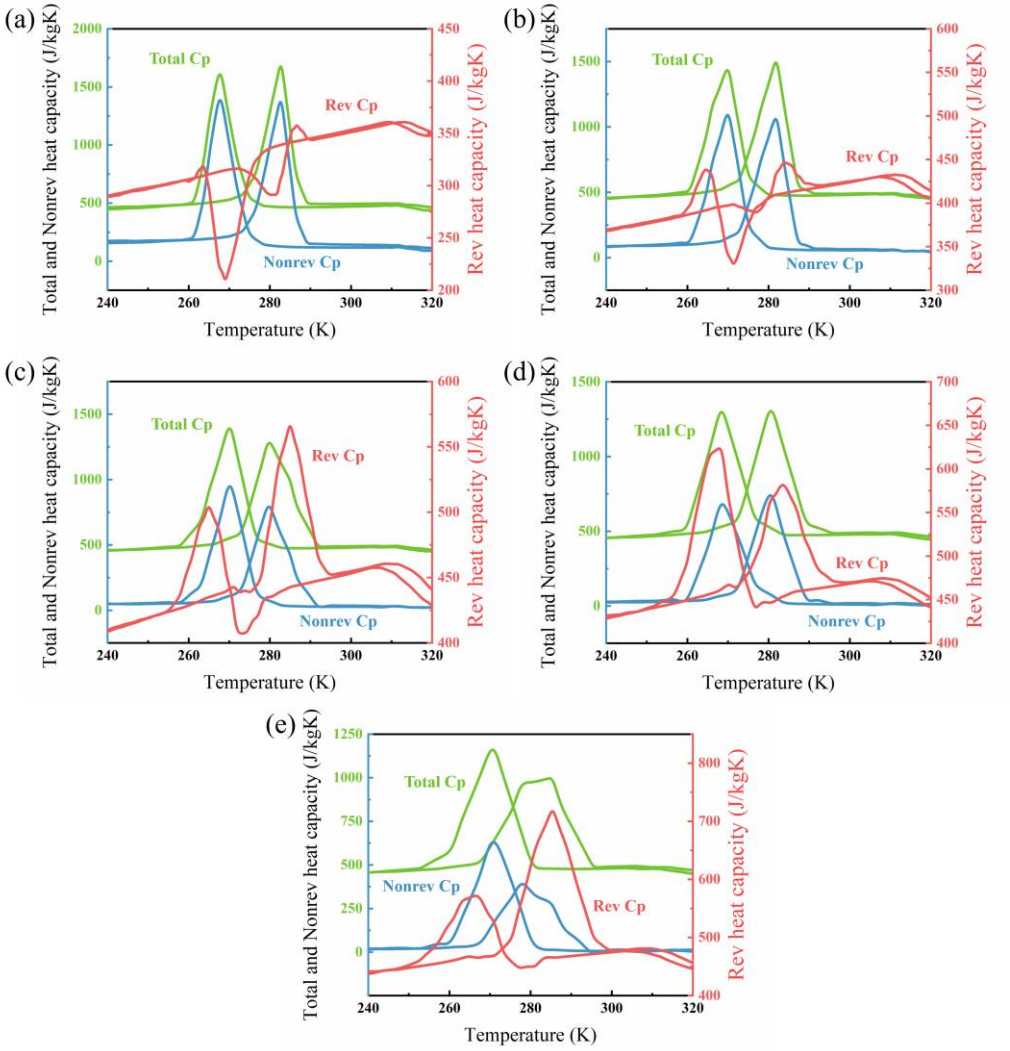

Fig. 4-4 Reversible, nonreversible and total heat capacity of $Ni_{47}Mn_{38}Sn_{12}Cu_3$ alloy at various modulation periods

(a) 40 s; (b) 60 s; (c) 80 s; (d) 100 s; (e)120 s

4.2.2 Influence of Nonreversible Components on Friction Dissipation

As proposed by Planes et al.[166], the heat ($-Q_M$) released during MT can be expressed as:

$$-Q_M = -\Delta H_{ch}^{P\text{-}M} + \Delta H_{el}^{P\text{-}M} + E_{fr}^{P\text{-}M} \tag{4.4}$$

where $-\Delta H_{ch}^{P\text{-}M}$ is the latent heat related to phase transition, $\Delta H_{el}^{P\text{-}M}$ is the latent

heat associated with storage elastic strain, $E_{fr}^{P\text{-}M}$ is the energy dissipation in friction during interface movement. In the reverse MT process, the heat (Q_A) released during forward MT can be expressed as:

$$Q_A=\Delta H_{ch}^{M\text{-}P}+\Delta H_{el}^{M\text{-}P}+E_{fr}^{M\text{-}P} \tag{4.5}$$

For Ni-Mn-Sn-based magnetic SMAs, it is found that the magnetization curves in the forward and reverse transition processes are approximately parallel[167, 21], indicating that the elastic strain energy stored in the forward MT is approximately equal to that released in the reverse MT. So, the frictional energy (E_{fr}) can be obtained from Eqs. (4.4) and (4.5) that:

$$E_{fr}=E_{fr}^{P\text{-}M}+E_{fr}^{M\text{-}P}=Q_A\text{-}Q_M+\Delta H_{ch}^{P\text{-}M}\text{-}\Delta H_{ch}^{M\text{-}P} \tag{4.6}$$

Assuming that the interface between parent and martensite phases is a single-phase interface during MT, the entropy change $-\Delta H_{ch}^{P\text{-}M}$ can be written as:

$$\Delta H_{ch}^{P\text{-}M}=T_0\frac{Q_M}{T_M} \tag{4.7}$$

and

$$\Delta H_{ch}^{M\text{-}P}=T_0\frac{Q_A}{T_A} \tag{4.8}$$

where T_0 is the thermodynamic equilibrium temperature[168], at which the Gibbs energies of martensite and austenite phases are equal, which can be estimated by: $T_0=(M_s+A_f)/2$

Fig. 4-5(a) shows the DSC thermal analysis curve of $Ni_{50\text{-}x}Mn_{38}Sn_{12}Cu_x$ alloy in the range of 190−370 K. Use the double tangent method to calibrate M_s, M_f, A_s, A_f, T_M, and T_A on the DSC curve, and list them in Table 4-1. Fig. 4-5 (b) shows the variation trend of the phase transition characteristic temperature of $Ni_{50\text{-}x}Mn_{38}Sn_{12}Cu_x$ alloy with Cu content. In $Ni_{50\text{-}x}Mn_{38}Sn_{12}Cu_x$ alloy, M_s, M_f, A_s, and A_f

decrease with the increase of x.

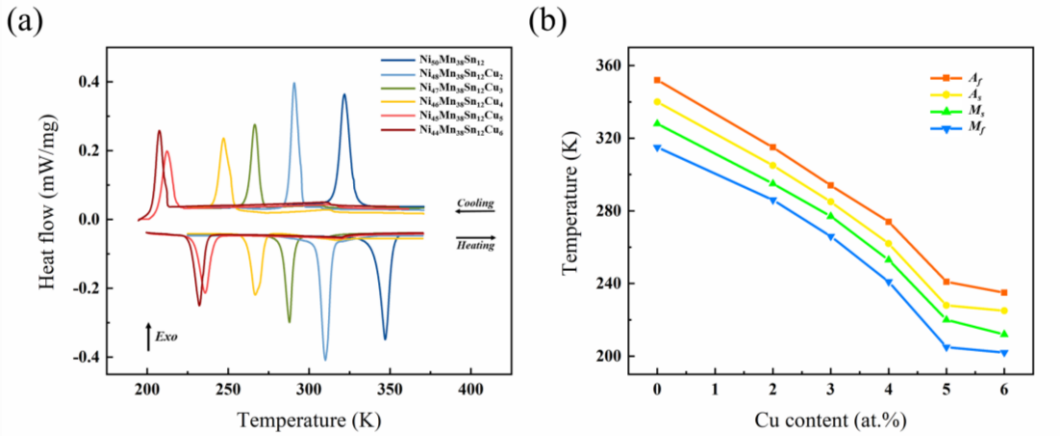

Fig. 4-5 Martensite transformation characteristics of $Ni_{50-x}Mn_{38}Sn_{12}Cu_x$ alloys (a) DSC curves; (b) MT characteristic temperatures v.s. Cu content curves

It is worth mentioning that according to the theory of valence electron concentration (*e/a*), the *e/a* of $Ni_{50-x}Mn_{38}Sn_{12}Cu_x$ alloy increases with the increase of Cu content, which means that the phase transition characteristic temperature should increase accordingly. However, as shown in Fig. 4-5(b), with the increase of Cu content in the alloy, both T_M and T_A temperatures show a decreasing trend. This is because the valence electron configuration of Cu is $3d^{10}4s^1$, and its 3d orbitals are fully filled structures with a relatively large atomic radius (0.128 nm). Cu doping increases the volume of the alloy unit cell and changes the distance between Mn-Mn atoms, which also affects the phase transition temperature of the alloy.

In fact, the concentration of valence electrons, Mn-Mn atomic distance, and grain size are all important factors affecting the phase transition temperature[76-78, 169]. In addition, an increase in Mn-Mn atomic distance can also lead to a decrease in hybridization between Ni-3d and Mn-*d* states, which may also result in a decrease in the phase transition characteristic temperature[169].

The frictional work consumed in the $Ni_{50-x}Mn_{38}Sn_{12}Cu_x$ alloys with different

contents x during a MT cycle can be calculated and is also listed in Table 4-1. It is noticed that the hysteresis of the MT is related to E_{fr}, demonstrating that E_{fr} can be a good measure for the MT processes.

Table 4-1 Characteristic temperature and thermal hysteresis of phase transition (A_f, A_s, M_s and M_f), the latent heat of forward and reverse phase transitions (Q_A and Q_M), and the frictional energy consumption in the process of phase transition (E_{fr}) of the $Ni_{50-x}Mn_{38}Sn_{12}Cu_x$ alloys

x	A_f (K)	A_s (K)	M_s (K)	M_f (K)	Q_A ($J \cdot g^{-1}$)	Q_M ($J \cdot g^{-1}$)	E_{fr} ($J \cdot g^{-1}$)	ΔT_{hys} (K)
0	352	340	328	315	9.094	9.472	0.722	24.5
2	315	305	295	286	8.566	8.616	0.57	19.5
3	294	285	277	266	8.064	8.345	0.549	18
4	274	262	253	241	7.045	7.309	0.606	21
5	240	227	221	206	5.334	5.647	0.577	20

E_{fr} can also be extended to the study of nonreversible C_p. According to the working principle of MDSC, the nonreversible C_p is obtained by the difference between the measured total C_p and reversible C_p[170]. It is found from Fig. 4-6 that, for $Ni_{50-x}Mn_{38}Sn_{12}Cu_x$ alloys, the dependence of E_{fr} on x is consistent with the nonreversible specific C_p. The relation between nonreversible C_p and E_{fr} during MT can be established:

$$E_{fr}=C_{p\text{-}non}\Delta T_{int} \tag{4.9}$$

where ΔT_{int} is the transformation temperature interval ($\Delta T_{int} = (A_f - A_s + M_s - M_f)/2$). In this way, the nonreversible C_p can be directly characterized by E_{fr}. Although there remain some uncertainties in the interpretation of the data, the reversible and nonreversible signals provide much richer useful information than the conventional DSC.

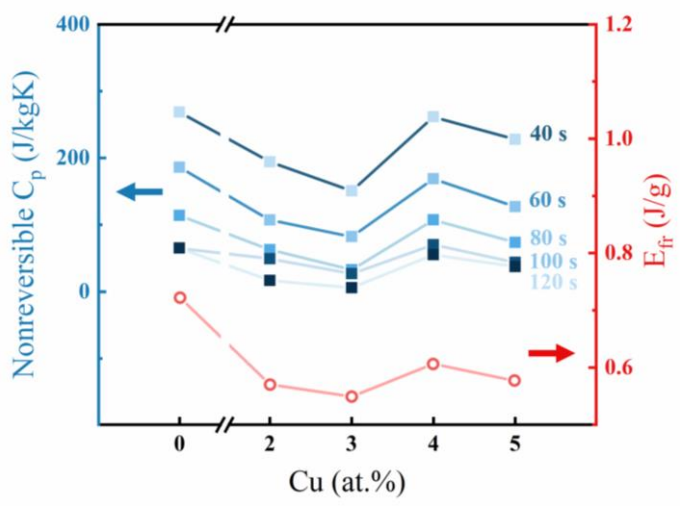

Fig. 4-6 Nonreversible specific heat capacity and frictional work dissipation under different modulation periods of $Ni_{50-x}Mn_{38}Sn_{12}Cu_x$ alloys

4.2.3 Influence of Reversible Components on Latent Heat

Here, we take $Ni_{50-x}Mn_{38}Sn_{12}Cu_x$ alloy as an example to analyze the ΔT_{ad} based on the MDSC data. The latent heat of $Ni_{50-x}Mn_{38}Sn_{12}Cu_x$ alloys under different modulation periods are plotted in Fig. 4-7. Fig. 4-7(a) shows that the total latent heat of the alloys decreases with increasing Cu content. Such total latent heat is actually the same as those obtained from conventional DSC. The nonreversible latent heat shows a minimum for x=3 alloy (Fig. 4-7(b)), while the reversible latent heat shows a maximum (Fig. 4-7(c)).

As discussed in Section 1.2.4.3 regarding the characterization methods for the elastocaloric effect of martensitic transformation, ΔT_{ad} can be calculated using Eq. (1.14). In this equation, ΔH (transformation latent heat) can be obtained by integrating the exothermic peak of the DSC curve, while C_p represents the total heat capacity of the alloy. However, the results calculated by this method are consistently higher than the experimentally measured data[171]. As previously mentioned, the reversible component during martensitic transformation is related to the material's heat capacity, whereas the nonreversible component is determined

by physicochemical processes within the material. According to the discussion in Section 4.2.1, the reversible component correlates with the alloy's heat capacity, while the nonreversible component depends on the alloy's physical and chemical processes. These processes are governed by changes in internal variables far from equilibrium, rather than being driven by heating rates.

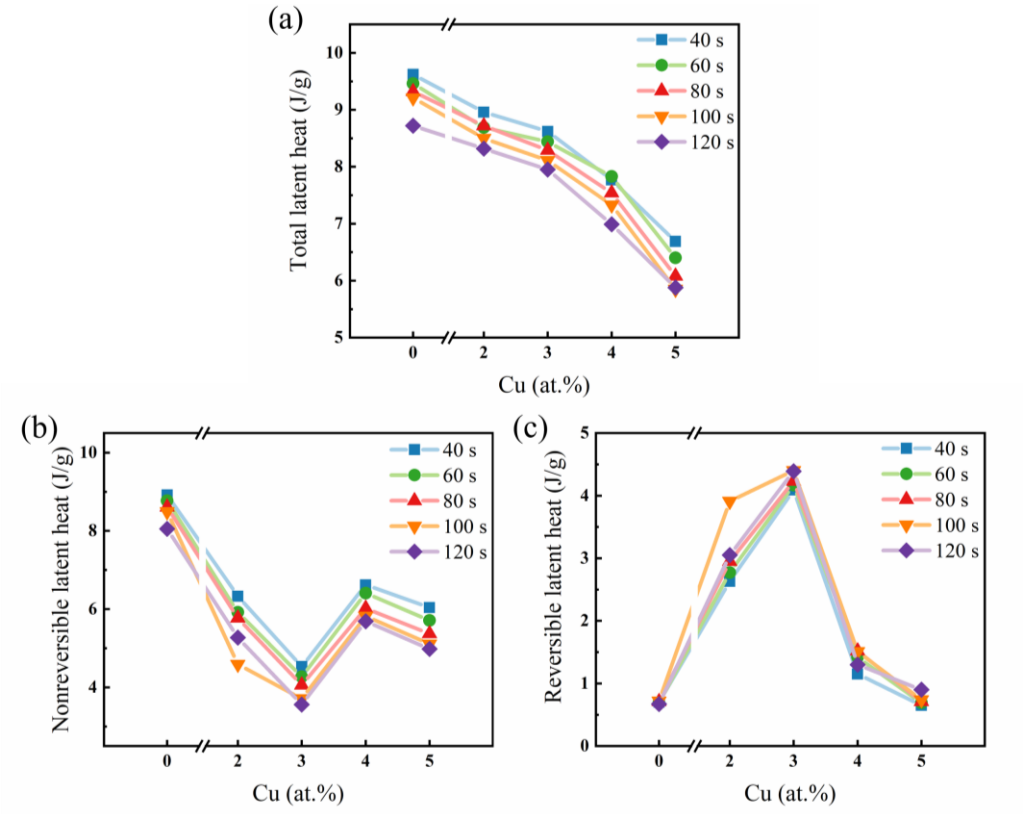

Fig. 4-7 Latent heat of $Ni_{50-x}Mn_{38}Sn_{12}Cu_x$ alloys under different modulation periods (a) total latent heat; (b) nonreversible latent heat; (c) reversible latent heat

Therefore, after resolving the reversible and nonreversible components using MDSC, the reversible latent heat and reversible heat capacity can be utilized to more accurately estimate the alloy's elastocaloric effect. To achieve a substantial elastocaloric effect through material design, elastocaloric materials should possess both large reversible latent heat and low reversible heat capacity. Fig. 4-8 presents the adiabatic temperature change results of $Ni_{50-x}Mn_{38}Sn_{12}Cu_x$ alloys obtained via MDSC, demonstrating that Cu doping significantly enhances the elastocaloric

performance. Notably, when the Cu doping level reaches x=3, the alloy exhibits a markedly higher adiabatic temperature change compared to other compositions. This enhancement results from the combined effects of the reversible latent heat value and reversible heat capacity.

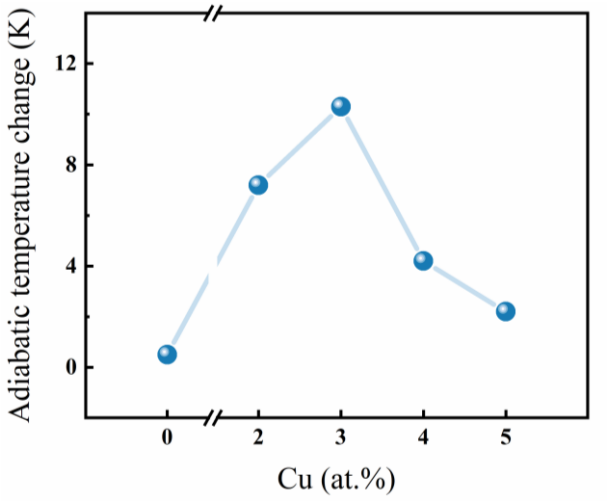

Fig. 4-8 Calculated ΔT_{ad} via MDSC method in $Ni_{50-x}Mn_{38}Sn_{12}Cu_x$ alloys

The MDSC method enables the acquisition of a series of thermodynamic parameters crucial for investigating martensitic transformation processes. Not only does it facilitate the analysis of the intrinsic relationship between nonreversible components and thermal hysteresis from an energy dissipation perspective, but it also provides an accurate characterization method for determining adiabatic temperature changes. Furthermore, the reversible and nonreversible components obtained through MDSC offer novel perspectives for phase transition regulation and compositional optimization.

4.3 Microstructure of Ni-Mn-Sn-Cu Alloys

A systematic analysis was conducted on the alloy's microstructure. Fig. 4-9 presents the optical microstructures of $Ni_{50-x}Mn_{38}Sn_{12}Cu_x$ (x=0, 2, 3, 4, 5, 6) alloys. Observations revealed that the samples exhibited equiaxed grains in the central region and columnar grains at the edges. As shown in Fig. 4-9(a), the $Ni_{50}Mn_{38}Sn_{12}$

ternary alloy primarily consisted of coarse equiaxed grains. Due to the inherent brittleness of intermetallic compounds, numerous fine cracks were observed on the surface of the $Ni_{50}Mn_{38}Sn_{12}$ alloy. Fig. 4-9(b) displays the microstructure of the alloy doped with 2 at.% Cu, where significant grain refinement was evident. When the Cu content reached 3 at.%, the grain size further decreased to an average of approximately 200 μm, as illustrated in Fig. 4-9(c). Fig. 4-9(d) shows that with an increase in Cu content to 4 at.%, the grains continued to refine, reaching sizes of about 150 μm. At 5 at.% Cu (Fig. 4-9(e)), the average grain size decreased further to approximately 80 μm, and no precipitates were observed in the matrix. However, the x=6 alloy exhibited distinct differences from the others, displaying dendritic structures that aggregated at grain boundaries.

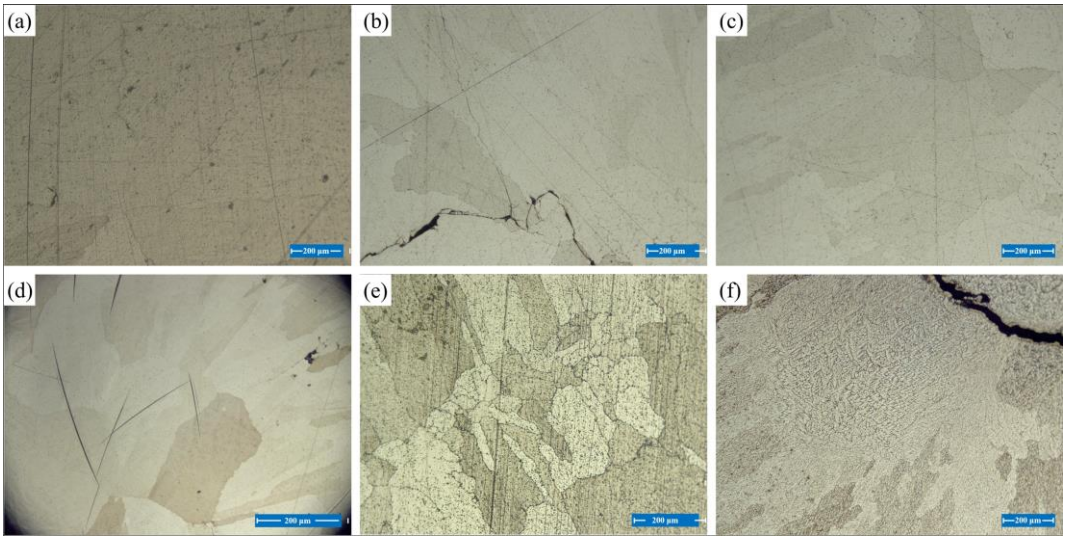

Fig. 4-9 Optical micrographs of $Ni_{50-x}Mn_{38}Sn_{12}Cu_x$ alloys
(a) x=0; (b) x=2; (c) x=3; (d) x=4; (e) x=5; (f) x=6

In summary, Cu played a significant role in refining the alloy's microstructure. It can be inferred that the solubility limit of Cu in the $Ni_{50}Mn_{38}Sn_{12}$ alloy is approximately 5−6 at.%. The effect of secondary phases should be considered dialectically: while they can effectively enhance mechanical properties, their precipitation may lead to deviations in the matrix composition from the designed

composition. This deviation could reduce the martensitic transformation temperature, thereby increasing the temperature difference between the Curie point and the reverse martensitic transformation peak ($T_C^A - T_A$) and decreasing the entropy change. Additionally, secondary phases may increase internal stress at phase interfaces, leading to greater transformation hysteresis.

Room-temperature XRD phase analysis was conducted on the alloys, with the results presented in Fig. 4-10. In the $Ni_{50}Mn_{38}Sn_{12}$ ternary alloy, the martensite phase exhibited an orthorhombic ten-layered modulated structure (10M) with lattice parameters of a_0=0.434 nm, b_0=0.559 nm, and c_0=2.195 nm. With increasing Cu doping content, both the room-temperature microstructure and lattice parameters of the alloys changed, with specific data summarized in Table 4-2.

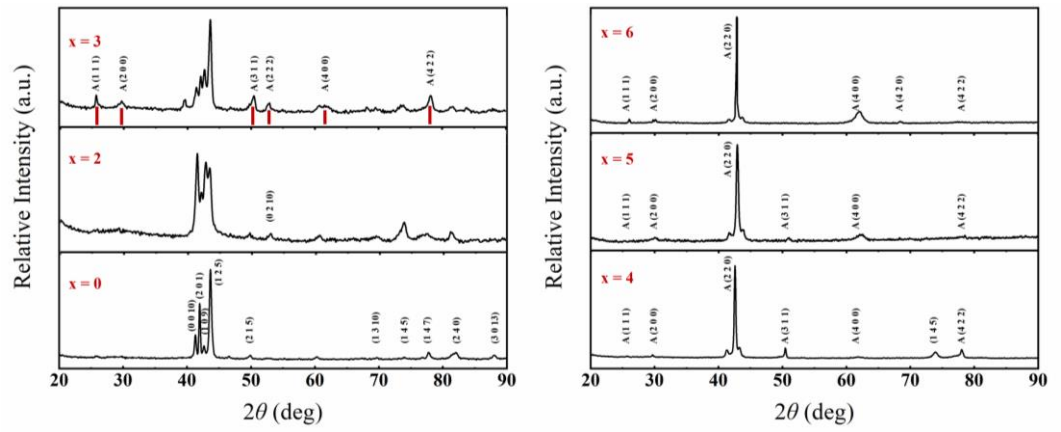

Fig. 4-10 XRD patterns of $Ni_{50-x}Mn_{38}Sn_{12}Cu_x$ alloys measured at room temperature

By calculating the unit cell volume based on the lattice parameters of x=0 and x=2 alloys, it can be observed that the unit cell volume increases with Cu doping, which is also consistent with the fact that the atomic radius of Cu is larger than that of Ni. As shown in Fig. 4-10, the x=3 and x=4 alloys exhibit two sets of diffraction peaks, indicating the coexistence of 10M martensite and austenite phase at room temperature. The appearance of superlattice diffraction peaks such as (111) and (311), where the Miller indices h, k, and l satisfy the 2n+1 condition, demonstrates

that the austenite phase in these alloys possesses the $L2_1$-type structure.

Table 4-2 Crystal structures and lattice parameters of $Ni_{50-x}Mn_{38}Sn_{12}Cu_x$ alloys measured at room temperature

x	Crystal structure	Lattice parameter (nm)		
		a	b	c
0	10M Martensite	0.434	0.559	2.195
2	10M Martensite	0.433	0.564	2.186
3	10M Martensite	0.431	0.572	2.168
	$L2_1$ Austenite	0.602	0.602	0.602
4	10M Martensite	0.426	0.575	2.153
	$L2_1$ Austenite	0.600	0.600	0.600
5	$L2_1$ Austenite	0.599	0.599	0.599
6	$L2_1$ Austenite	0.599	0.599	0.599

When the Cu doping content reaches 5 at.% and 6 at.%, the matrix microstructure of the alloys transforms completely into $L2_1$-type austenite. To further confirm the phase structure of the Cu-doped alloys, TEM analysis was performed on the $Ni_{47}Mn_{38}Sn_{12}Cu_3$ alloy, with the results presented in Fig. 4-11.

Fig. 4-11(a) shows the TEM bright-field image of the $Ni_{47}Mn_{38}Sn_{12}Cu_3$ alloy, where modulated 10M martensite plates can be observed. The lath martensite contains high-density nanoscale twin structures, while the $L2_1$ austenite phase is also present in the $Ni_{47}Mn_{38}Sn_{12}Cu_3$ alloy. Fig. 4-11(b) presents a high-resolution TEM image of the 10M martensite in the $Ni_{47}Mn_{38}Sn_{12}Cu_3$ alloy, revealing a periodic atomic stacking structure (along the c-axis direction) in the modulated 10M martensite, with c=2.17 nm corresponding to the interlayer distance of ten atomic planes. Fig. 4-11(d) displays the selected-area electron diffraction (SAED) pattern of the orthorhombic five-layered 10M martensite phase, showing four equally spaced superlattice spots (indicated by white arrows) between two bright

spots, dividing the distance between them into five equal parts. Fig. 4-11(c) and (e) show the HRTEM image and SAED pattern of the $L2_1$ austenite, respectively. Notably, while XRD analysis suggests that the $Ni_{47}Mn_{38}Sn_{12}Cu_3$ alloy at room temperature consists of a mixture of $L2_1$ austenite phase[172] and orthorhombic five-layered 10M martensite[173], TEM observations reveal that the content of 10M martensite is significantly lower than that of the $L2_1$ austenite phase.

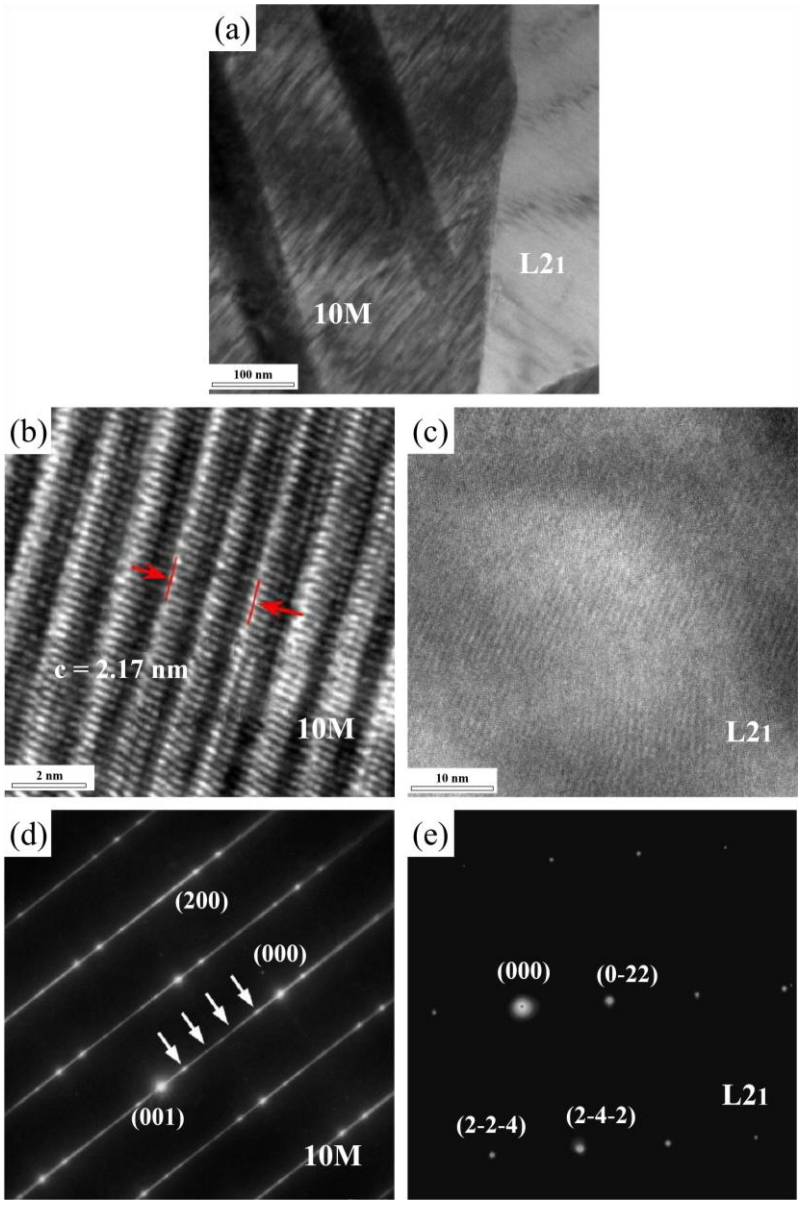

Fig. 4-11 TEM bright field images and corresponding electron diffraction patterns (a) TEM bright-field images of $Ni_{47}Mn_{38}Sn_{12}Cu_3$ alloy at room temperature; (b) and (c) HRTEM images of 10M martensites and $L2_1$ austenite taken from the areas in (a); (d) and (e) the corresponding SAEDPs of 10M martensites and $L2_1$ austenite

4.4 Elastocaloric Effect of Ni-Mn-Sn-Cu Alloys

4.4.1 Compressive Mechanical Properties of Ni-Mn-Sn-Cu Alloys

The elastocaloric effect in first-order phase transition solid-state refrigeration materials is closely related to their mechanical properties. As previously analyzed, the martensitic transformation temperature of $Ni_{50-x}Mn_{38}Sn_{12}Cu_x$ alloys is significantly influenced by their Cu content. According to the Clausius-Clapeyron relationship[174], the difference between the test temperature and the martensitic transformation point ($T_{test}-A_f$) directly affects the critical stress value for stress-induced martensitic transformation. Therefore, it is necessary to identify the origin of any yield plateau observed in test results, which could stem from either stress-induced martensitic transformation or material yield deformation. To eliminate the factor of stress-induced martensitic transformation, compression stress-strain curves of $Ni_{50-x}Mn_{38}Sn_{12}Cu_x$ (x=0, 2, 3, 4, 5, 6) alloys were measured at 60 K above their respective A_f temperatures, with the results shown in Fig. 4-12.

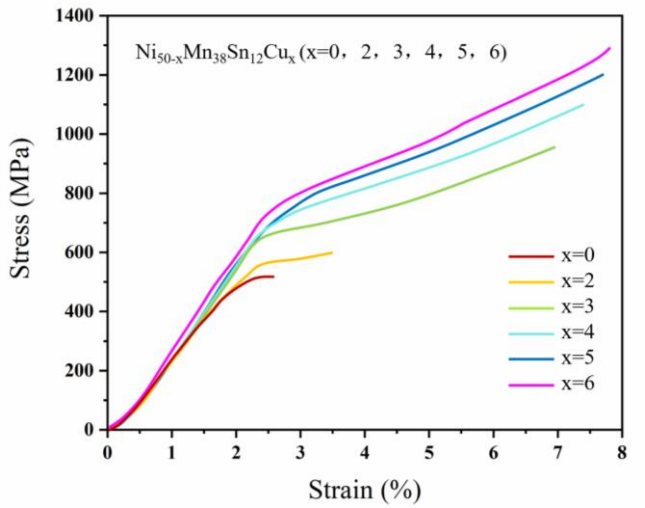

Fig. 4-12 The stress-strain curves of $Ni_{50-x}Mn_{38}Sn_{12}Cu_x$ alloys at A_f+60K

With increasing Cu content in the alloys, both the yield strength and the critical stress for austenite yielding progressively increase. Cu alloying effectively enhances the mechanical properties of Ni-Mn-Sn alloys, thereby enabling the

alloys to withstand higher stresses and meet the requirements for complete stress-induced martensitic transformation, which provides an essential prerequisite for achieving superior elastocaloric effects.

4.4.2 Elastocaloric Effect of Ni-Mn-Sn-Cu Alloys

4.4.2.1 Superelasticity and Adiabatic Temperature Change under Different Conditions

The thermal analysis results in Section 4.2 reveal that when the Cu doping content reaches x=3, the alloy exhibits substantial reversible latent heat, creating favorable conditions for achieving superior elastocaloric performance. Considering that the elastocaloric effect originates from stress-induced martensitic transformation, the alloy with x=3 Cu doping was selected for recording stress-strain curves over 10 loading-unloading cycles to investigate the stress-induced martensitic transformation behavior and analyze the changes before and after cyclic loading. The stress-strain curves obtained from room temperature testing are shown in Fig. 4-13.

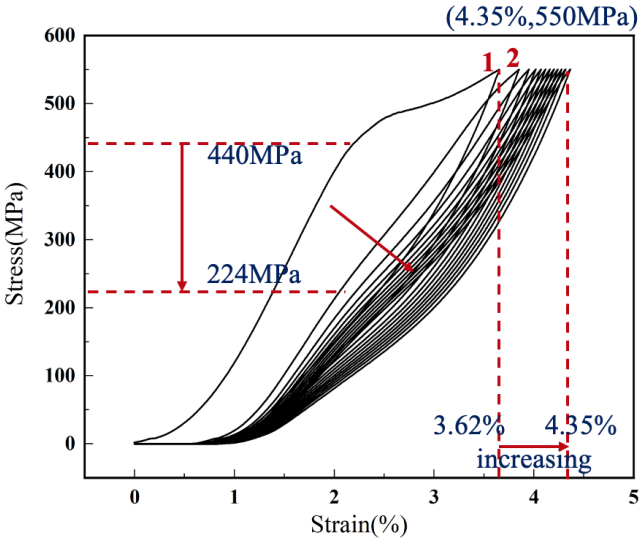

Fig. 4-13 Compressive stress-strain curves of $Ni_{47}Mn_{38}Sn_{12}Cu_3$ alloy recorded during 10 loading-unloading cycles at room temperature

The results demonstrate that during the first loading-unloading cycle, the critical stress for inducing martensitic transformation is approximately 440 MPa, accompanied by a relatively wide superelastic plateau. Approximately 0.5% residual strain remains after unloading, indicating incomplete strain recovery and demonstrating that the martensitic transformation is not fully reversible during the initial cycle. This phenomenon occurs because dislocations generated during the transformation process prevent some residual martensite from undergoing reverse transformation upon stress removal.

During the second loading-unloading cycle, the critical stress significantly decreased from the initial 440 MPa to 224 MPa, and stabilized thereafter without further noticeable reduction starting from the third cycle. This behavior stems from the "training effect"[174], where dislocations and residual martensite formed during the first cycle arrange in "favorable" positions that facilitate subsequent martensitic transformations by providing additional driving force[174], thereby substantially reducing the critical stress for stress-induced martensitic transformation in the second cycle. Furthermore, the retained dislocations and martensite in the alloy matrix suppress the generation of new dislocations during subsequent cycles[174].

As mentioned in Section 1.2.4, the elastocaloric effect is represented by the caloric effect induced by stress under adiabatic conditions, meaning both adiabatic conditions and applied stress influence the caloric effect and require separate discussion. Adiabatic conditions refer to a state where the system exchanges no heat with its surroundings, yet this concept is idealized and nearly impossible to achieve in practical elastocaloric refrigeration characterization. The closest approximation involves adjusting the strain rate to apply/remove stress as quickly as possible, making test conditions near-adiabatic and bringing the measured

adiabatic temperature change closer to theoretical values. In summary, the strain rate should be as high as possible without causing structural instability, while the uniaxial stress must induce complete martensitic transformation without exceeding the sample's yield limit, as excessive stress would produce residual strain and reduce reversibility.

To prevent sample cracking, a slow isothermal loading-fast adiabatic unloading approach was adopted. Based on the superelasticity test results in Fig. 4-13, a uniaxial stress of 500 MPa was selected at an ambient temperature of 296 K to ensure complete stress-induced martensitic transformation. The loading process maintained a constant strain rate of 3.3×10^{-4} s^{-1}, with thermocouples welded to the sample surface for direct temperature measurement during unloading. Fig. 4-14(a) shows the ΔT_{ad} of $Ni_{47}Mn_{38}Sn_{12}Cu_3$ alloy under different unloading rates, where increasing the strain rate from 0.5×10^{-2} s^{-1} to 2.5×10^{-2} s^{-1} significantly enhanced the ΔT_{ad} from 3.6 K to 7 K. At 3.3×10^{-2} s^{-1}, the ΔT_{ad} reached about 8.2 K, showing no further substantial increase even when raising the rate to 4.0×10^{-2} s^{-1}, indicating this strain rate sufficiently achieved quasi-adiabatic conditions. Therefore, 3.3×10^{-2} s^{-1} was selected for subsequent ΔT_{ad} tests to maximize quasi-adiabatic performance while maintaining structural integrity.

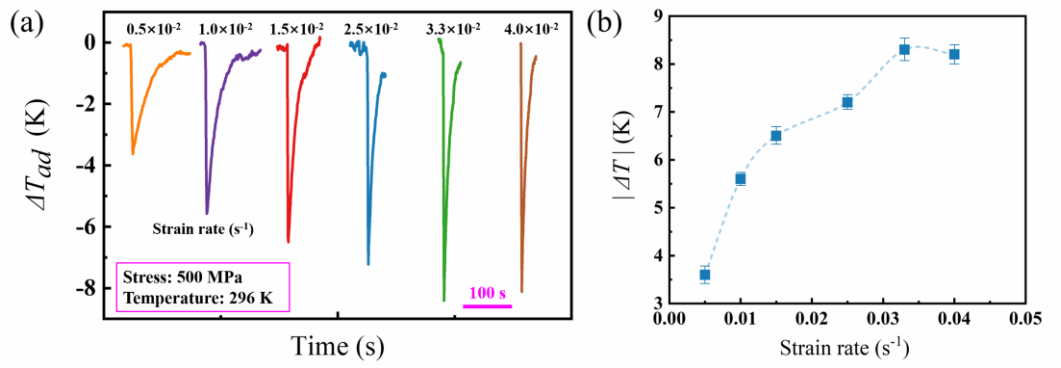

Fig. 4-14 ΔT_{ad} measured at different unloading strain rates

(a) ΔT_{ad} as a function of time; (b) ΔT_{ad} as a function of strain rate

In addition to investigating the influence of strain rate, it is essential to examine the effect of external stress on the elastocaloric effect. Fig. 4-15(a) shows ΔT_{ad} of $Ni_{47}Mn_{38}Sn_{12}Cu_3$ alloy under different applied stresses, tested at a strain rate of 3.3×10^{-2} s^{-1} and an ambient temperature of 296 K. Based on the superelastic curve of $Ni_{47}Mn_{38}Sn_{12}Cu_3$ alloy at room temperature shown in Fig. 4-15(b), uniaxial stresses of 100, 250, 400, and 550 MPa were selected for testing, corresponding to different transformation stages on the loading curve as indicated by the red dots in Fig. 4-15(b).

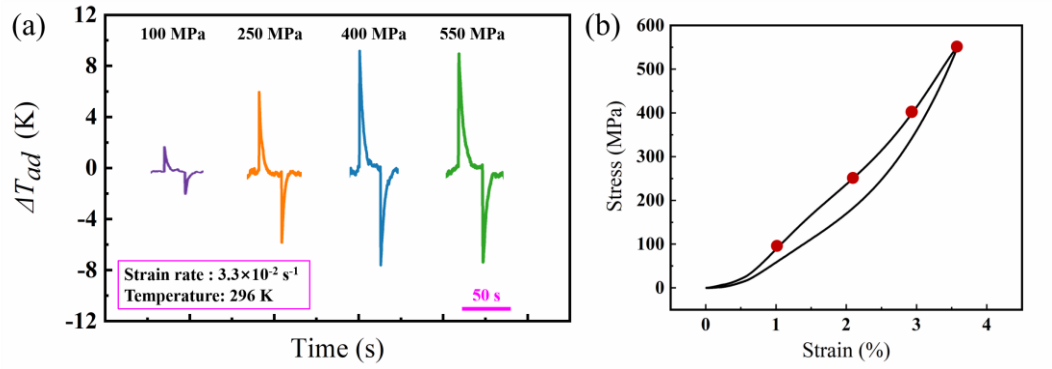

Fig. 4-15 ΔT_{ad} measured at different applied stress

(a) ΔT_{ad} as a function of time; (b) superelastic curve at 296 K

When the stress was 100 MPa, as shown in Fig. 4-15(b), it approached but did not reach the critical stress value required for complete stress-induced martensitic transformation, resulting in a relatively small temperature change of approximately 2 K. Increasing the stress to 250 MPa enhanced the adiabatic temperature change to 5.7 K. At 400 MPa, corresponding to the completion of stress-induced martensitic transformation in Fig. 4-15(b), the elastocaloric effect approached its theoretical maximum while maintaining excellent reversibility. Throughout the 100–400 MPa range, the adiabatic temperature changes during reverse transformation increased proportionally with the applied stress due to the rising fraction of stress-induced martensite. When the stress reached 550 MPa, though

theoretically inducing the same martensite fraction as 400 MPa, the system exhibited martensitic elastic deformation. The measured adiabatic temperature change at 550 MPa showed a slight decrease (8.2 K during loading vs 7.3 K during unloading) compared to 400 MPa, accompanied by reduced reversibility. This degradation may stem from either enhanced energy dissipation (E_{fr}) through grain boundary motion during unloading or partial plastic deformation of martensite under excessive stress, where residual strains decreased the participating martensite fraction during reverse transformation, ultimately diminishing the temperature change.

4.4.2.2 Effect of Cu Doping on Adiabatic Temperature Change and Cyclic Stability

The influence of Cu doping on the elastocaloric effect was investigated by recording temperature variations during loading-holding-unloading processes in $Ni_{50-x}Mn_{38}Sn_{12}Cu_x$ alloys. Based on previous discussions regarding strain rate and stress effects on the elastocaloric performance, the experimental parameters were established as follows: a strain rate of 3.3×10^{-2} s^{-1}, applied stress of 500 MPa, and test temperatures set at A_f+3 K for each alloy composition. The measured adiabatic temperature changes of $Ni_{50-x}Mn_{38}Sn_{12}Cu_x$ alloys are presented in Fig. 4-16.

Fig. 4-13 demonstrates that during the initial loading-unloading cycle, both the critical stress and transformation reversibility remain unstable. Therefore, to ensure the obtained results accurately reflect the genuine elastocaloric effect, all samples underwent 10 cycles of mechanical training before formal testing. However, due to the intrinsic brittleness characteristic of Ni-Mn-based magnetic alloys, the ternary $Ni_{50}Mn_{38}Sn_{12}$ alloy fractured after only four loading-unloading cycles during superelastic training.

The testing procedure of loading-holding-unloading is illustrated by the x=2

annotation in Fig. 4-16, with all alloy compositions tested following the same protocol. The results show that for $Ni_{50-x}Mn_{38}Sn_{12}Cu_x$ (x=2, 3, 4, 5) alloys, $|\Delta T_{ad\text{-}loading}| > |\Delta T_{ad\text{-}unloading}|$, indicating incomplete reverse transformation of stress-induced martensite during unloading due to significant frictional dissipation[32], which causes the adiabatic temperature change during loading to exceed that during unloading. Quantitative analysis of frictional dissipation will be detailed in the following chapter.

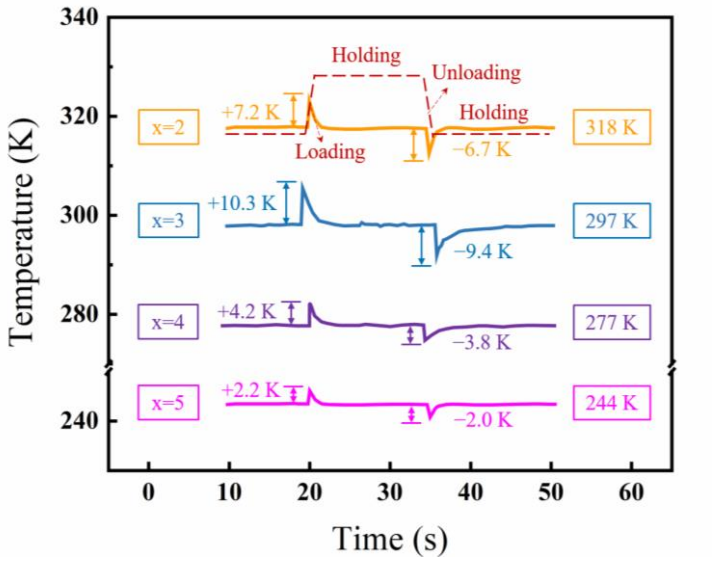

Fig. 4-16 ΔT_{ad} of the $Ni_{50-x}Mn_{38}Sn_{12}Cu_x$ alloy during loading-unloading compressive test

In Section 4.2, MDSC method was employed to predict the adiabatic temperature changes of $Ni_{50-x}Mn_{38}Sn_{12}Cu_x$ (x=2, 3, 4, 5) alloys. Comparison between directly measured ΔT_{ad} and MDSC-predicted values, as plotted in Fig. 4-17, reveals close agreement between experimental results and theoretical calculations. This confirms nearly complete stress-induced reverse martensite transformation during quasi-adiabatic compression and demonstrates that the reversible component of martensitic transformation accurately reflects caloric effects while the nonreversible component contributes negligibly to adiabatic temperature changes.

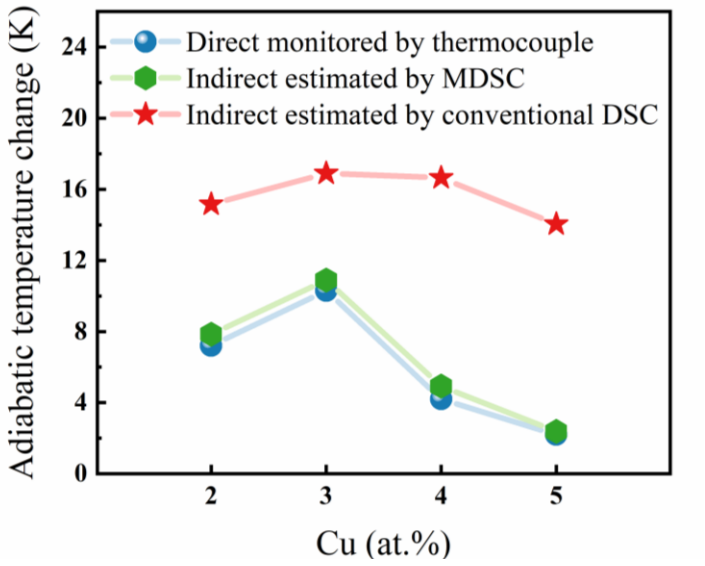

Fig. 4-17 The comparison of the experimentally tested ΔT_{ad} and calculated data

From a practical application perspective, elastocaloric refrigeration materials must not only possess excellent cooling performance but also demonstrate good cyclic stability. According to the definition of the elastocaloric effect, it can be reasonably inferred that the stress loading method is not the primary factor affecting the alloy's elastocaloric performance. As long as sufficient superelastic strain can be obtained, reverse martensitic transformation will occur after rapid unloading (when the strain rate exceeds 0.1 s^{-1}, the material approaches the adiabatic limit), thereby generating the elastocaloric refrigeration effect. Based on the research results of strain rate and stress in the previous section, the cyclic stability study of the elastocaloric effect involved testing stress-strain curves under 35 loading-unloading cycles with a strain rate of 3.3×10^{-2} s^{-1}, maximum applied stress of 250 MPa, and test temperature set at A_f+3 K for each alloy. The stability curves of adiabatic temperature changes versus cycle numbers are presented in Fig. 4-18. For each loading-unloading cycle test, the sample was loaded and held for 20 s, then unloaded to 0 MPa, followed by another 20 s holding period before commencing the next loading-unloading cycle test.

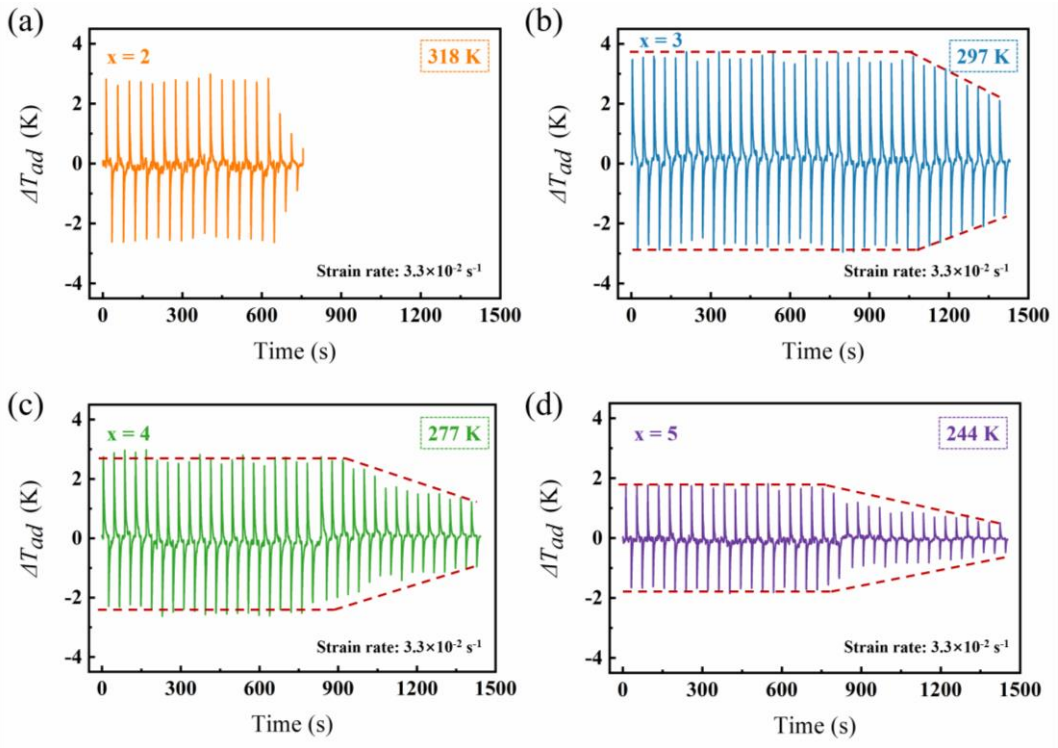

Fig. 4-18 ΔT_{ad} of the $Ni_{50-x}Mn_{38}Sn_{12}Cu_x$ alloy during the superelastic cycle
(a) x=2; (b) x=3; (c) x=4; (d) x=5

Without the superelastic training, the critical stress for stress-induced martensitic transformation would rapidly decrease during the initial stress cycles, leading to enhanced adiabatic temperature changes[175]. Therefore, to obtain stable ΔT_{ad} measurements, all tested alloys underwent preliminary superelastic training. As shown in Fig. 4-18(a), the $Ni_{48}Mn_{38}Sn_{12}Cu_2$ alloy maintained relatively stable performance during the first 15 cycles, achieving temperature changes of approximately 2.5 K, but experienced sample splitting and instability at the 17th cycle. In contrast, the $Ni_{47}Mn_{38}Sn_{12}Cu_3$ alloy demonstrated stable elastocaloric effects for about 30 cycles as shown in Fig. 4-18(b), though significant attenuation occurred thereafter, with the adiabatic temperature change decreasing from 3 K to 1.8 K. While the $Ni_{46}Mn_{38}Sn_{12}Cu_4$ and $Ni_{45}Mn_{38}Sn_{12}Cu_5$ alloys maintained structural integrity until the end of cycling, gradual attenuation became observable after approximately 20 cycles, as evidenced in Fig. 4-18(c) and (d).

Here, the discussion focuses on the rapid adiabatic loading-unloading method, which can achieve caloric effects and be applied in heat pump design[176]. When the applied stress approaches the yield strength of the martensite phase and operates with high loading rates and numerous cycles, the parent phase undergoes plastic deformation. This plastic deformation hinders the martensitic transformation in subsequent loading-unloading cycles. As cycle numbers increase, accumulated plastic deformation in the parent phase gradually reduces the adiabatic temperature change.

Some studies have reported using isothermal loading-adiabatic unloading methods to investigate the cyclic stability of elastocaloric materials, where lower strain rates are employed during loading and temperature changes during loading are not the primary research focus. While this approach prevents early sample cracking, it prolongs loading time, reduces refrigeration efficiency per unit time, and proves difficult for practical applications. Therefore, adjusting loading methods can only slightly increase stress cycle numbers without fundamentally solving structural instability issues. Functional fatigue and structural instability still occur with increasing cycles. Only through material performance enhancement can we fundamentally improve the stability of elastocaloric cycles.

4.5 Magnetocaloric Effect of Ni-Mn-Sn-Cu Alloys

4.5.1 Magneto-structural Phase Diagram of Ni-Mn-Sn-Cu Alloys

To investigate the magnetism of $Ni_{50-x}Mn_{38}Sn_{12}Cu_x$ alloys with varying compositions, the temperature-dependent magnetization curves of alloy compositions were measured. Fig. 4-19 presents the *M-T* curves of $Ni_{50-x}Mn_{38}Sn_{12}Cu_x$ alloys under a 100 Oe magnetic field. A 100 Oe magnetic field was first applied, and the field-cooled (FC) curve was obtained by cooling under the

field, followed by reheating to a high temperature under the same field to obtain the field-heated (FH) curve. Due to the structural differences between ferromagnetic martensite and austenite, the characteristic phase transition temperatures (M_s, M_f, A_s, A_f) could be determined using the tangent method from the *M-T* curves obtained under a low magnetic field. With increasing Cu content, the characteristic martensitic transformation temperatures gradually decreased. Additionally, during the cooling process, the alloys underwent a second-order phase transition from paramagnetic to ferromagnetic, manifested as a sharp change in magnetization in the *M-T* curves, accompanied by a very small hysteresis of approximately 1 K, corresponding to the T_C^A temperature. A comparison with the characteristic phase transition temperatures obtained via DSC in Table 4-1 showed generally consistent results.

The ternary alloy exhibits weak magnetism near its phase transition temperature. While the magnetization of the alloy strengthens with Cu doping, when x=2, as shown in Fig. 4-19, the alloy undergoes a transition from paramagnetic martensite to paramagnetic austenite during heating, with a low peak in the FH curve and an indistinct change in magnetization. When x reaches 3, the alloy undergoes a complete reverse martensitic transformation. As indicated by the FC curve of the $Ni_{47}Mn_{38}Sn_{12}Cu_3$ alloy, the alloy transforms from paramagnetic austenite to ferromagnetic austenite at approximately 315 K (the T_C^A temperature), accompanied by a rapid increase in magnetization. As the temperature further decreases to around 262 K (the M_s temperature), the magnetization sharply drops to a minimum, marking the completion of the martensitic transformation. Upon further cooling to about 240 K (the Curie point of the martensitic phase, T_C^M), the magnetization gradually increases again as the paramagnetic martensite transitions

into ferromagnetic martensite. When the Cu doping reaches 5 at.%, the FC curve reveals that the alloy's second-order phase transition process is similar to those of the x=3 and x=4 alloys. However, since T_C^M is higher than the M_s temperature, ferromagnetic austenite directly transforms into ferromagnetic martensite when the temperature approaches M_s. A comparison with the *M-T* curves of the x=3 and x=4 alloys shows that this transition results in a smaller magnetization difference (ΔM) between the two phases.

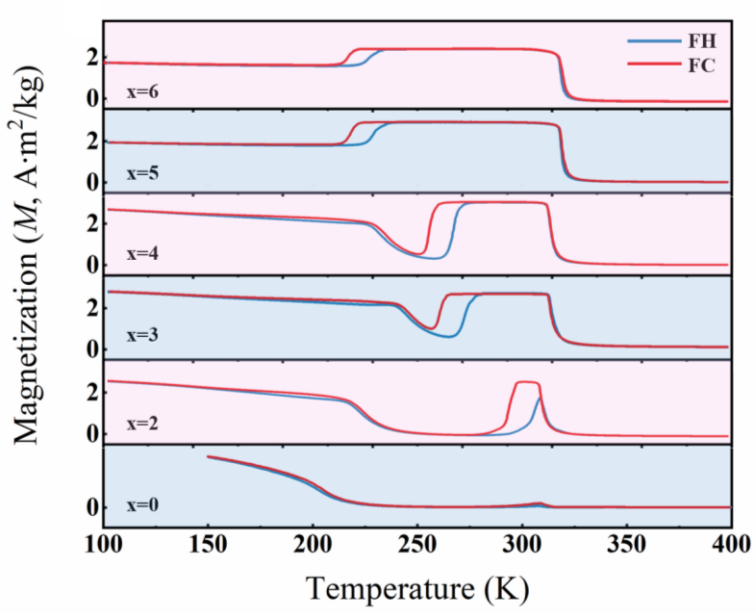

Fig. 4-19 Temperature dependence magnetization for $Ni_{50-x}Mn_{38}Sn_{12}Cu_x$ alloys under 100 Oe

Based on the DSC results in Fig. 4-5 and the T_A, T_C^A, T_C^M temperatures determined from the *M-T* curves in Fig. 4-19, combined with the experimental data reported by Jing et al.[173], the magneto-structural phase diagram of $Ni_{50-x}Mn_{38}Sn_{12}Cu_x$ alloys was obtained, as shown in Fig. 4-20. It can be observed that with increasing Cu content, the martensitic transformation temperature gradually decreases, while the Curie point slightly increases. The T_A temperature of $Ni_{50-x}Mn_{38}Sn_{12}Cu_x$ alloys decreases linearly with increasing Cu content and can be fitted by the following relationship: $T_{A(x)}$=347−18.34x. Similar to the results for Fe-doped alloys, the T_A, T_C^A and T_C^M temperatures of the alloys with different compositions

were fitted, allowing the phase diagram to be divided into four regions: paramagnetic austenite, ferromagnetic austenite, paramagnetic martensite, and ferromagnetic martensite. Additionally, the phase diagram can be categorized into three regions. In region I, upon cooling, paramagnetic austenite transforms into paramagnetic martensite without any accompanying magnetic transition. In region II, ferromagnetic austenite transforms into paramagnetic martensite during cooling, where both structural and magnetic transitions occur simultaneously. Research on the magneto-structural coupling of Cu-doped Ni-Mn-Sn alloys has primarily focused on this compositional range[151, 152]. In region III, ferromagnetic austenite transforms into ferromagnetic martensite upon cooling.

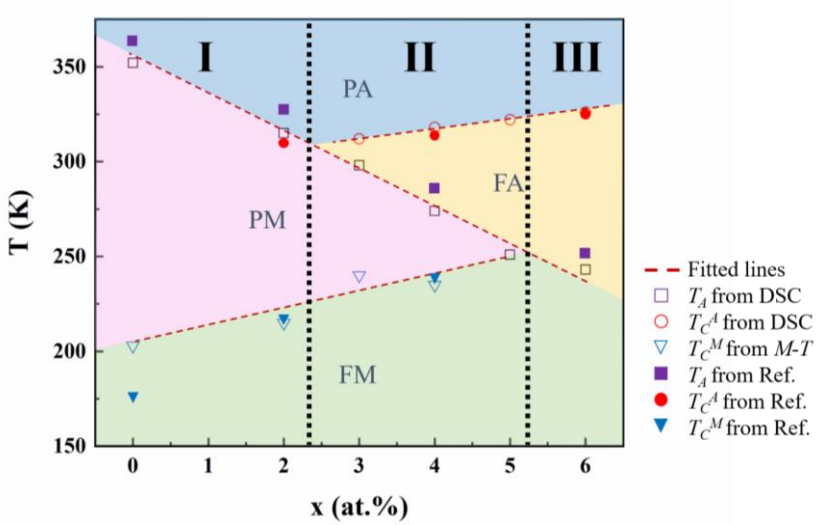

Fig. 4-20 Magneto-structural phase diagram of the $Ni_{50-x}Mn_{38}Sn_{12}Cu_x$ alloys

4.5.2 Partial Magneto-Structural Coupling and Magnetocaloric Effect in Ni-Mn-Sn-Cu Alloys

Fig. 4-21 shows the magnetization curve of the x=2 alloy under a low magnetic field (100 Oe). During the cooling process, a second-order phase transition from paramagnetic austenite to ferromagnetic austenite occurs at approximately 310 K, followed by a metamagnetic transition from ferromagnetic austenite to paramagnetic martensite at about 295 K. However, during the heating process, as

shown in the inset of Fig. 4-21, a small peak appears at the reverse martensitic transformation. Similar phenomena have been reported in polycrystalline $Ni_{45}Mn_{42}Sn_{11}Fe_2$ alloys [177]. By taking the first derivative of the *M*-*T* curve during heating, the d*M*/d*T*-*T* curve was obtained, where the minimum value determines T_C^A, as indicated by the pink arrow in the inset of Fig. 4-21. In other words, during the reverse martensitic transformation, a second-order magnetic transition occurs, referred to as the partial coupling phenomenon between the first-order martensitic structural transformation and the second-order magnetic transition, resulting in the formation of a small peak near the reverse martensitic transformation. However, in reference[177], the appearance of such a small peak was caused by an intermediate martensitic transformation, indicating a different underlying mechanism between the two cases.

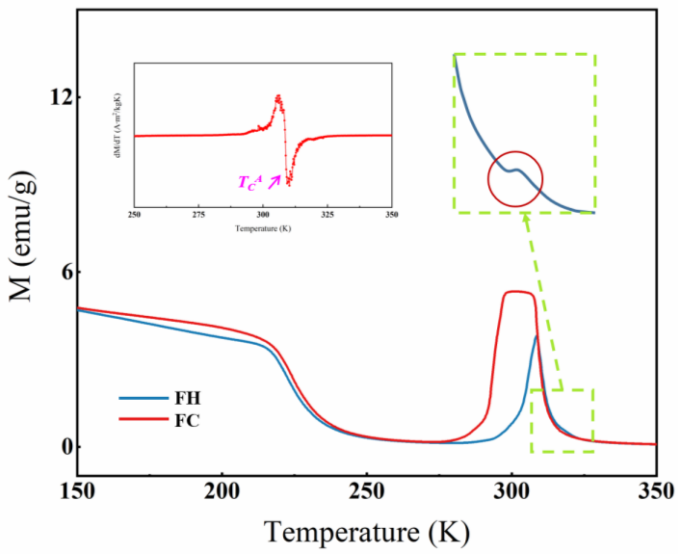

Fig. 4-21 *M*-*T* curves for $Ni_{48}Mn_{38}Sn_{12}Cu_2$ alloy at 100 Oe (Inset is the enlarged magnetization of the FH plot and d*M*/d*T*-*T* curve)

Isothermal magnetization curves were measured in the temperature ranges of 297−310 K and 311−323 K, as shown in Fig. 4-22. From Fig. 4-22(a), it can be observed that the x=2 alloy undergoes a magnetic-field-induced reverse martensitic transformation in the temperature range of 301−310 K. At test temperatures of 307

K and 308 K, the S-shaped curves during magnetization and the hysteresis between magnetization-demagnetization processes both indicate the occurrence of a field-induced reverse martensitic transformation. At the A_f temperature, even when the applied magnetic field is increased to 5 T, the magnetization of the alloy still fails to reach saturation, demonstrating that the reverse martensitic transformation remains incomplete. This phenomenon results from the interruption of the first-order martensitic structural transformation by the second-order magnetic transition. When the temperature exceeds 311 K, as illustrated in Fig. 4-22(b), the magnetization decreases with increasing temperature, exhibiting conventional magnetocaloric effect (CMCE) behavior.

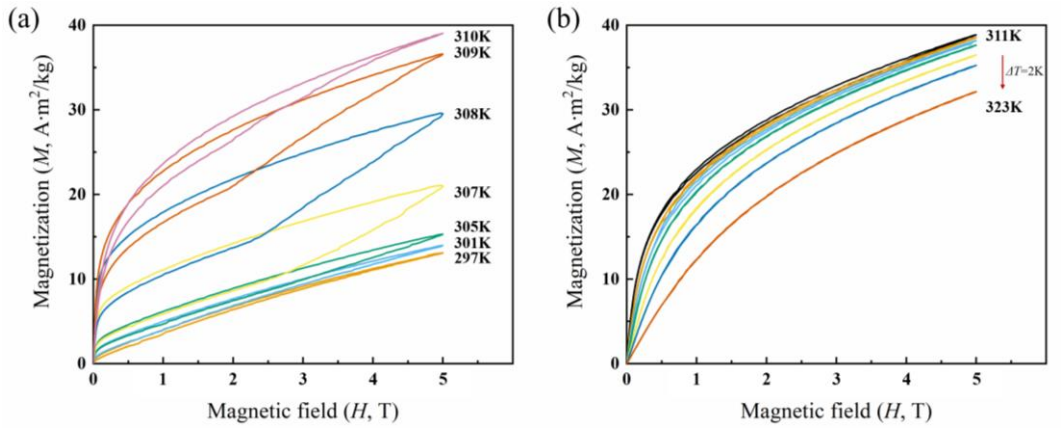

Fig. 4-22 *M-H* curves of $Ni_{48}Mn_{38}Sn_{12}Cu_2$ alloy under a magnetic field cycle of 0 T−5 T−0 T (a) 297 K≤T≤310 K; (b) 311 K≤T≤323 K

Fig. 4-23 presents the Arrott plots near the first-order phase transition temperature and the second-order magnetic transition temperature. According to Banerjee's criterion[158], Arrott plots exhibit negative slopes or "S"-shaped curves near first-order transitions, while showing positive slopes at second-order magnetic transitions. As shown in Fig. 4-23(a), the Arrott plots demonstrate negative slopes at 307 K and adjacent temperatures, indicating the occurrence of a first-order transition at these temperatures. When the temperature exceeds 310 K, the positive

slope of the curves suggests the emergence of a second-order magnetic transition. Furthermore, in the temperature range of 311 K and above, the Arrott plots display negative intercepts on the M^2 axis (Fig. 4-23(b)), revealing that T_C^A < 311 K, which can also be confirmed from literature[159]. These results demonstrate that the first-order martensitic transformation in $Ni_{48}Mn_{38}Sn_{12}Cu_2$ alloy partially overlaps with the second-order magnetic transition of austenite, indicating a partial magneto-structural coupling state.

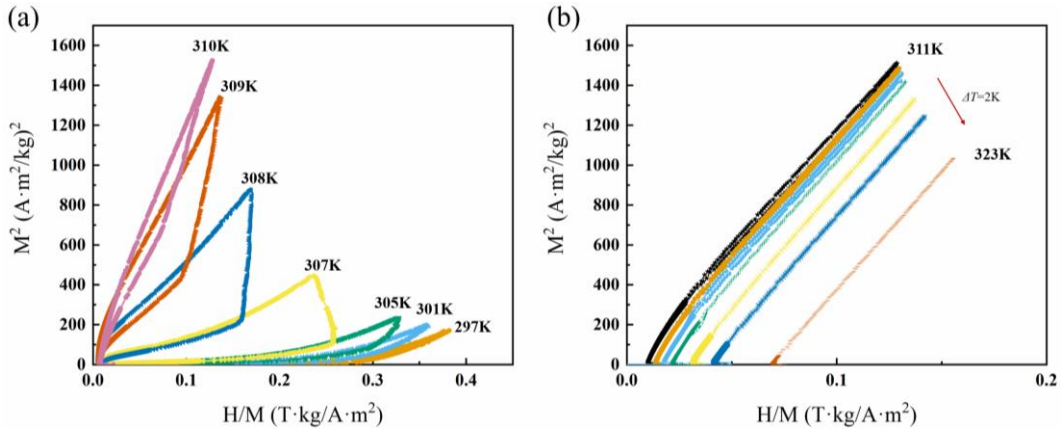

Fig. 4-23 Arrott curves under different testing temperatures for $Ni_{48}Mn_{38}Sn_{12}Cu_2$ alloy (a) 297 K≤T≤310 K; (b) 311 K≤T≤323 K

4.5.3 Full Magneto-Structural Coupling and Magnetocaloric Effect in Ni-Mn-Sn-Cu Alloys

Fig. 4-24(a) and (b) present the *M-H* curves of $Ni_{47}Mn_{38}Sn_{12}Cu_3$ alloy measured under a 5 T magnetic field within temperature ranges of 263−277 K and 278−326 K, respectively. To avoid spurious peaks, the sample was initially zero-field cooled to 150 K (more than 100 K below M_f) before being heated to the measurement temperature under zero field[167, 178]. With the increase of Cu doping to 3 at.%, the alloy demonstrates enhanced magnetization saturation capability. This phenomenon originates from the fact that in non-stoichiometric Ni-Mn-Sn-based alloys, excess Mn atoms tend to occupy Sn sites, resulting in

antiferromagnetic coupling between the magnetic moments of Mn atoms and those occupying Sn sites. This effect has been previously discussed in Chapter 3 regarding first-principles calculations. Cu doping can transform the antiferromagnetic Mn-Mn interactions into ferromagnetic. While the Cu content in the $Ni_{47}Mn_{38}Sn_{12}Cu_3$ alloy sample is insufficient to complete this transformation, it can effectively weaken the Mn-Mn interactions, exhibiting short-range ferromagnetic ordering. Within the temperature range where phase transition occurs, the critical magnetic field for reverse martensitic transformation decreases as the temperature increases.

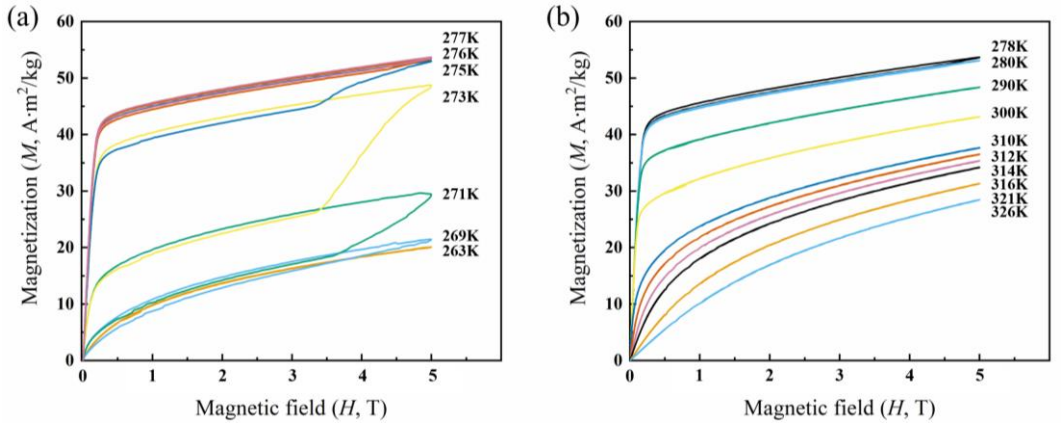

Fig. 4-24 *M-H* curves of $Ni_{47}Mn_{38}Sn_{12}Cu_3$ alloy under a magnetic field cycle of 0 T−5 T−0 T (a) 263 K≤T≤277 K; (b) 278 K≤T≤326 K

The *M-H* curves within the 269−276 K range exhibit distinct characteristics of metamagnetic martensitic transformation, where the applied magnetic field induces a transition from paramagnetic martensite to ferromagnetic austenite - a phenomenon beneficial for magnetocaloric effects (MCE). The observed hysteresis loops during field removal indicate the occurrence of magnetic hysteresis losses during the phase transition process. Below 263 K, the sample demonstrates weak magnetic properties, which aligns with the martensitic transformation temperature determined from the *M-T* curves in Fig. 4-19. Fig. 4-24(b) presents the isothermal

M-H curves of austenite at various temperatures. As the temperature increases from 278 K to 326 K, the alloy's saturation magnetization decreases, manifesting a transition from ferromagnetic to paramagnetic states.

To more precisely determine the magnetic transitions, Arrott plots were derived from isothermal *M-H* curves in the vicinity of the martensitic transformation temperature. The Arrott curves in Fig. 4-25(a) exhibit upward-bending shapes with negative slopes from 269 K (slightly above M_s) to 277 K, confirming the occurrence of a first-order magnetic transition (FOMT). Above 280 K, the slope becomes positive, indicating a second-order magnetic transition (SOMT)[179]. As shown in Fig. 4-25(b), when the temperature exceeds 310 K, the Arrott plots display negative intercepts on the M^2 axis, establishing that 300 K<T_C^A<310 K[180]. Both the *M-T* curves and Arrott plots of the $Ni_{47}Mn_{38}Sn_{12}Cu_3$ alloy demonstrate the coupling between martensitic transformation and the magnetic transition of austenite within the temperature range below 310 K.

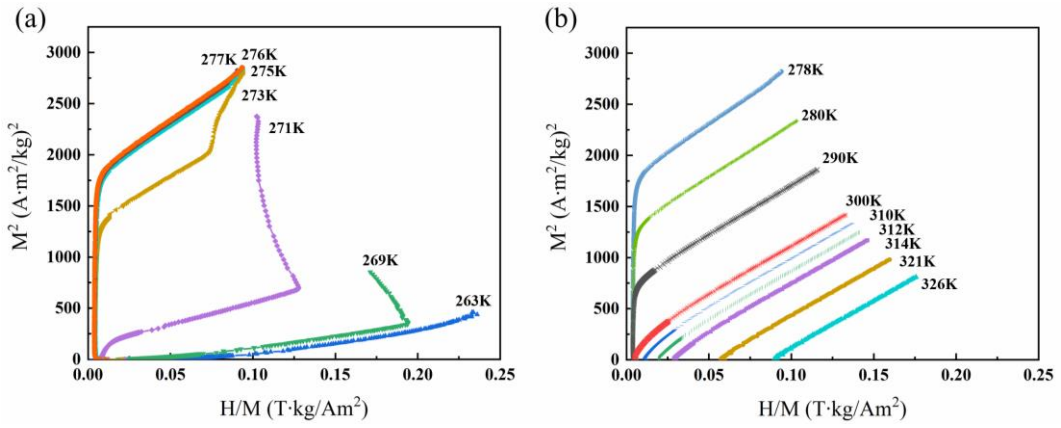

Fig. 4-25 Arrott curves under different testing temperatures for $Ni_{47}Mn_{38}Sn_{12}Cu_3$ alloy (a) 263 K≤T≤277 K; (b) 278 K≤T≤326 K

The hysteresis loss (*HL*) can be determined by integrating the area enclosed between the magnetization and demagnetization branches of the *M-H* curve, expressed by the following equation:

$$HL=\mu_0 \oint M\mathrm{d}H \tag{4.10}$$

The temperature dependence of hysteresis loss is illustrated in Fig.4-26. Meanwhile, the average hysteresis loss (*AHL*) can be obtained by integrating the area enclosed by the hysteresis loss curve over the refrigeration working temperature range, as expressed by the following equation:

$$AHL=\frac{1}{T_{hot}-T_{cold}}\int_{T_{cold}}^{T_{hot}} HL\mathrm{d}T \tag{4.11}$$

The calculated results show that the x=3 alloy exhibits an *AHL* of 45 J/kg under a 5 T magnetic field. This value demonstrates competitive performance when compared with the average hysteresis losses of other Ni-Mn-based alloys, including $Ni_{40.6}Mn_{43.3}Sn_{10.0}Co_{6.1}$ alloy (*AHL*=99 J/kg under 5 T)[181], $Ni_{43}Mn_{46}Sn_{11}$ alloy (*AHL*=138 J/kg under 5 T)[182], and $Ni_{45}Co_5Mn_{40}In_2Sn_8$ alloy (*AHL*=78 J/kg under 3 T)[183].

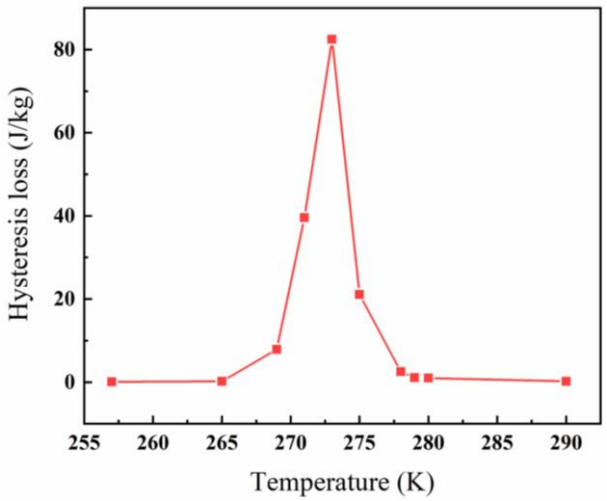

Fig. 4-26 Magnetic hysteresis loss of $Ni_{47}Mn_{38}Sn_{12}Cu_3$ alloy under a magnetic field of 5 T

The magnetic entropy change curves for x=2, 3, 4, and 5 alloys were calculated using the Maxwell relation integration method[184], as shown in Fig. 4-27. Comparative analysis reveals that both the peak values of magnetic entropy change and their corresponding temperatures slightly decrease with increasing

magnetic field, primarily due to the occurrence of metamagnetic transition[185]. Under a 5 T magnetic field, the peak magnetic entropy changes for x=2, 3, 4, and 5 alloys are 10.3, 21.2, 16.9, and 11.2 J/kg·K, with corresponding peak temperatures at 308, 274, 254, and 228 K, respectively. This demonstrates that Cu doping can effectively regulate the magnetic entropy change in $Ni_{50-x}Mn_{38}Sn_{12}Cu_x$ alloys by modulating the magneto-structural transition. The alloy with 3 at.% Cu doping exhibits the highest magnetic entropy change.

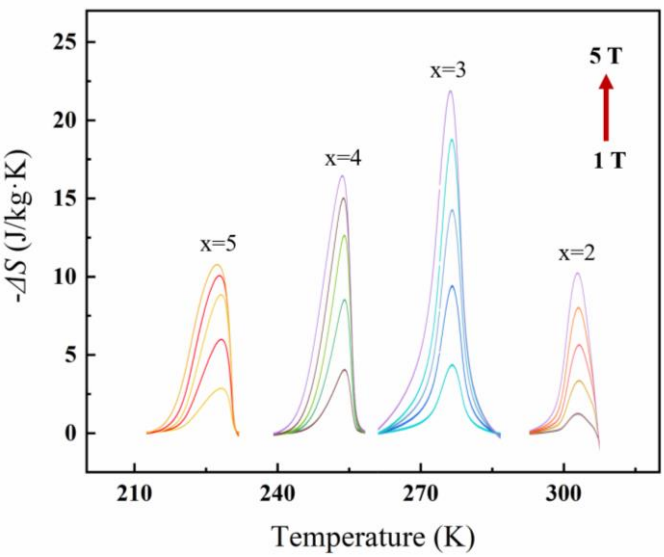

Fig. 4-27 ΔS_m as a function of temperature for $Ni_{50-x}Mn_{38}Sn_{12}Cu_x$ alloy under magnetic fields of 1−5 T

4.5.4 Comparative Study on Magnetocaloric Properties of $Ni_{47}Mn_{38}Sn_{12}Cu_3$ Alloy

In the previous section, ΔS_m was calculated using a series of *M-H* curves at different temperatures through the Maxwell's equations (Eq. 1.33) integration method[184]. According to research reports, when paramagnetic martensite and ferromagnetic austenite coexist in the alloy before applying a magnetic field, using the Maxwell relation to calculate ΔS_m may overestimate the values, and the resulting ΔS_m-*T* curve may exhibit artificial "peaks"[186, 187]. To obtain reliable

phase transition entropy changes and to describe the evolution of austenite mass fraction during the phase transition process, this section employs different methods to comparatively study the magnetocaloric properties (ΔS_m) of the $Ni_{47}Mn_{38}Sn_{12}Cu_3$ alloy.

The magnetocaloric entropy change $\Delta S_{m(c\text{-}c)}$ is calculated using the Clausius-Clapeyron equation, expressed as follows[187, 188]:

$$\Delta S_{m(c\text{-}c)} = -\Delta M \cdot \frac{\mu_0 dH}{dT} \tag{4.12}$$

where $\mu_0 dH/dT$ is the sensitivity parameters of critical magnetic field to temperature, ΔM is the magnetization difference between the two phases.

Even in the two-phase coexistence state, this equation can accurately determine $\Delta S_{m(c\text{-}c)}$. Fig. 4-28(a) presents the magnetic entropy change of $Ni_{47}Mn_{38}Sn_{12}Cu_3$ alloy calculated by this method under a 5 T magnetic field, showing good agreement with the results obtained from the Maxwell method in Fig. 4-27.

Furthermore, the phase transition progress can be determined by quantifying the transformation fraction of austenite during the phase transition, which in turn allows for the calculation of the magnetic entropy change[13, 189, 190]. Based on this approach, the expression for ΔS_m during the magnetic field increase is as follows:

$$\Delta S_m = \Delta S_{m(c\text{-}c)} \cdot df = \Delta S_{m(c\text{-}c)} \cdot [f(T, H+dH) - f(T, H)] \tag{4.13}$$

where df is the transformation fraction of austenite phase, $f(T, H)$ is the mass fraction of austenite at a certain temperature and magnetic field, $\Delta S_{m(c\text{-}c)}$ is the entropy change under a given magnetic field.

In order to further investigate the process of magnetic field induced phase transition, the concept of phase transition fraction is used to describe the mass fraction of austenite during magnetic field induced phase transition. The

relationship between the mass fraction of austenite and the applied magnetic field at a given temperature can be calculated through the *M-H* curve corresponding to that temperature, and the formula is as follows:

$$f(H)=\frac{M(H)-M_{\mathrm{Mar}}(H)}{M_{\mathrm{Aus}}(H)-M_{\mathrm{Mar}}(H)} \tag{4.14}$$

where $f(H)$ is the mass fraction of austenite under a certain magnetic field, $M(H)$ is the magnetization of the sample under this magnetic field, $M_{Mar}(H)$ is the magnetization of martensite, and $M_{Aus}(H)$ is the magnetization of austenite.

From the *M-H* curves at 276 K and 277 K in Fig. 4-24, it can be observed that the two curves coincide near a magnetic field of 5 T, indicating that the sample is in the austenitic state under a 5 T field. Therefore, the magnetization of the pure austenitic $Ni_{47}Mn_{38}Sn_{12}Cu_3$ alloy can be obtained by constructing a tangent to the *M-H* curve at 277 K. Similarly, the magnetization of the pure martensitic phase can be derived from the *M-H* curves. As seen in the low-field region of Fig. 4-24, the initial critical magnetic fields within the martensitic transformation temperature range are all around 0.2 T. Thus, the magnetization of the pure martensitic phase can be determined by constructing a tangent to the *M-H* curve.

The austenite phase transition fraction at different temperatures was calculated according to Eq. (4.5), with the results shown in Fig. 4-28(b). At 273 K, the $Ni_{47}Mn_{38}Sn_{12}Cu_3$ alloy achieved the maximum austenite phase fraction, corresponding to a peak ΔS_m value of 21.4 J/kg·K. At 271 K, the transformation fraction was 55%, yielding an estimated ΔS_m of 11.7 J/kg·K, while at 269 K, the transformation fraction was 33%, resulting in an estimated ΔS_m of 7.0 J/kg·K.

The ΔS_m values calculated using the phase transition fraction method are also plotted in Fig. 4-28(a). As seen in the figure, the ΔS_m values obtained from the three methods—Maxwell relation integration, the Clausius-Clapeyron equation, and the

phase transition fraction method—exhibit strong mutual consistency. This agreement arises because the $Ni_{50-x}Mn_{38}Sn_{12}Cu_x$ alloys were first cooled to 150 K (well below the M_s temperature) and held at this temperature before each magnetic field measurement to ensure a pure martensitic state. This procedure prevented the coexistence of martensite and austenite phases prior to testing, thereby ensuring that the ΔS_m values derived from the Maxwell relation matched well with those obtained from the other two methods. This consistency further validates the reliability of all three ΔS_m calculation approaches.

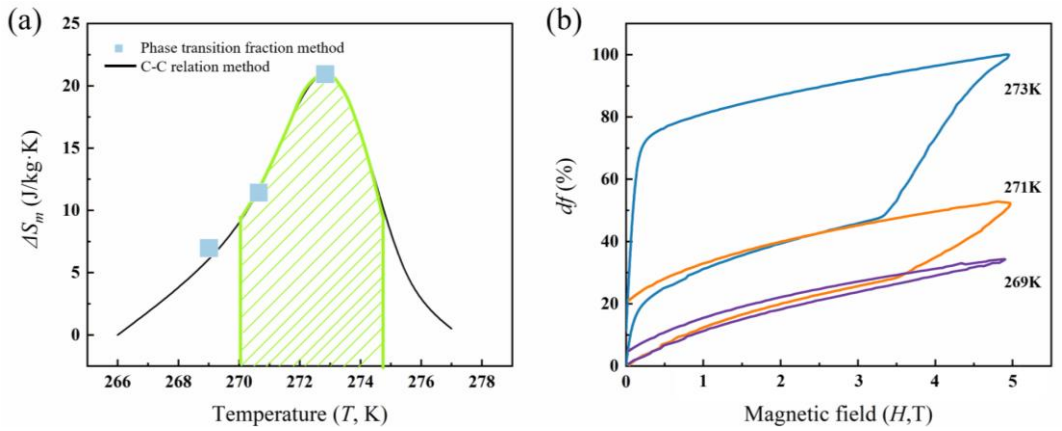

Fig. 4-28 ΔS_m and austenite phase transition fraction in $Ni_{47}Mn_{38}Sn_{12}Cu_3$ alloy (a) Magnetocaloric entropy change of $Ni_{47}Mn_{38}Sn_{12}Cu_3$ as a function of temperature under a magnetic field of 5T; (b) Fraction of austenite *df* in $Ni_{47}Mn_{38}Sn_{12}Cu_3$ at different temperatures as determined from the *M-H* curves

Refrigeration capacity (*RC*) and relative cooling power (*RCP*) serve as critical parameters for evaluating refrigeration performance, whose physical significance and characterization methods have been described in Chapter 1. Within the applied magnetic field range of 0−5 T, the $Ni_{47}Mn_{38}Sn_{12}Cu_3$ alloy demonstrates *RC* and *RCP* values of 92 J/kg and 108 J/kg, respectively. These values exhibit notable advantages when compared to other reported Ni-Mn-Sn-based alloys, such as $Ni_{42}Cu_2Co_6Mn_{39}Sn_{11}$ (μ_0H=1.5 T, *RCP*=42 J/kg)[191], $Mn_{39.5}Fe_{8.5}Ni_{41}Sn_{11}$ (μ_0H=1.4 T, *RCP*=40 J/kg)[192]and $Ni_{49.6}Mn_{37.3}Cr_{0.7}Sn_{12.4}$ (μ_0H=5.0 T, *RC*=49 J/kg)[193].

4.6 Summary

This chapter systematically investigates the reversible and nonreversible components during martensitic transformation. A series of $Ni_{50-x}Mn_{38}Sn_{12}Cu_x$ (x=0, 2, 3, 4, 5, 6) alloys were prepared to study the effects of Cu doping on their microstructure, martensitic transformation, mechanical properties, elastocaloric effect, and cyclic stability. By tuning the alloy composition, both partial and full magneto-structural coupling states were achieved. The main conclusions are as follows:

(1) Using modulated differential scanning calorimetry (MDSC), a small sinusoidal temperature oscillation was superimposed on a constant heating rate to separate the reversible and nonreversible components of the martensitic transformation. The nonreversible component originates from energy dissipation during phase transition and influences transformation hysteresis, while the reversible component determines the alloy's cooling performance, allowing for more accurate characterization of the adiabatic temperature change.

(2) For $Ni_{50-x}Mn_{38}Sn_{12}Cu_x$ (x=0, 2, 3, 4, 5, 6) alloys, Cu doping significantly refines grain size. When Cu doping reaches 6 at.%, a secondary phase precipitates and disperses within the alloy matrix. Cu doping also markedly enhances mechanical properties—the $Ni_{47}Mn_{38}Sn_{12}Cu_3$ alloy exhibits compressive fracture strength and strain of 912 MPa and 6.9%, respectively, representing an over 1.8-fold increase compared to the undoped alloy (493 MPa and 2.6%).

(3) The $Ni_{47}Mn_{38}Sn_{12}Cu_3$ alloy demonstrates excellent elastocaloric performance, with an adiabatic temperature change of 10.3 K under 500 MPa stress, closely matching the theoretical value (10.1 K) estimated from the reversible component of martensitic transformation. The elastocaloric effect remains stable

for ~30 cycles but then degrades significantly, with the adiabatic temperature change dropping from 3 K to 1.8 K after 30 cycles.

(4) The $Ni_{48}Mn_{38}Sn_{12}Cu_2$ alloy achieves partial magneto-structural coupling, exhibiting an entropy change (ΔS_m) of 10.3 J/kg·K under a 5 T magnetic field. With 3 at.% Cu doping, the alloy attains full magneto-structural coupling, yielding ΔS_m=21.2 J/kg·K, an average hysteresis loss of only 45 J/kg, and a relative cooling capacity of 108 J/kg.

Chapter 5 Multi-field Regulated Caloric Effect of Cu and B Co-doped Ni-Mn-Sn Alloy

5.1 Introduction

Excellent room-temperature refrigeration materials require not only large and reversible magnetocaloric and elastocaloric effects, but also a broad operating temperature window. Ni-Mn-Sn-based magnetic alloys, which simultaneously exhibit ferromagnetic and ferroelastic ordering[194], possess magnetocaloric, elastocaloric, and barocaloric effects. These characteristics provide a fundamental basis for achieving caloric effects through multi-field regulation. Therefore, conducting research in this area to optimize the performance of materials is highly significant.

As previously mentioned, Cu doping plays a regulatory role in the phase transition temperature, magnetic properties, and mechanical properties of Ni-Mn-Sn alloys. When the Cu content reaches approximately 3 at.%, coupling between the martensitic transformation and magnetic transition is achieved. However, due to the intrinsic brittleness of Ni-Mn-based magnetic alloys, further improvements in stress cycling stability of the materials are required. Processing bulk alloys into small-sized materials can effectively reduce the number of grain boundaries, thereby decreasing resistance and energy dissipation during phase transitions. Furthermore, such dimensional control enables grain size to match certain characteristic dimensions of the material (such as particle size in powders, diameter in microwires, or thickness in ribbons/thin films). Under these conditions, grains become surrounded by free surfaces rather than other grains, significantly reducing the resistance to twin boundary motion.

This chapter first analyzes the effects of B doping on the microstructure, phase transition temperature, and magnetic properties of Ni-Mn-Sn-Cu alloys. A systematic investigation was conducted on the magnetocaloric and elastocaloric properties of the optimized $(Ni_{47}Mn_{38}Sn_{12}Cu_3)_{99.4}B_{0.6}$ alloy. The "phase transition distribution function" and "transformation fraction" models were applied to describe the influence of simultaneously applied uniaxial stress and magnetic field on the martensitic transformation fraction, thereby explaining the resulting multi-field regulated caloric effect. The effects of combined hydrostatic pressure and magnetic field on the operating temperature window and refrigeration capacity of caloric effects were studied. This multi-field regulated caloric effect is expected to provide a new approach for developing novel solid-state refrigeration materials that combine large magnetocaloric and elastocaloric effects with a broader operating temperature window.

Moreover, the alloy was prepared in ribbon shape using the single-roller melt-spinning technique, and the influence of heat treatment processes on grain size was investigated. Furthermore, the anisotropic magnetic properties and magnetocaloric effects of textured ribbons were examined.

5.2 Martensitic Transformation and Mechanical Properties of Ni-Mn-Sn-Cu-B Alloy

5.2.1 Microstructure of Ni-Mn-Sn-Cu-B Alloy

To investigate the influence of B doping on the microstructure of Ni-Mn-Sn-Cu alloys. Fig. 5-1 presents optical micrographs of the $(Ni_{47}Mn_{38}Sn_{12}Cu_3)_{100-z}B_z$ (z=0, 0.2, 0.4, 0.6) magnetic alloys after quenching treatment following 24-hour annealing at 1173 K. As shown in Fig. 5-1(a), the undoped $Ni_{47}Mn_{38}Sn_{12}Cu_3$ alloy exhibits grain sizes of approximately 200 μm. With increasing B content, a small

amount of secondary phase precipitation becomes observable along grain boundaries.

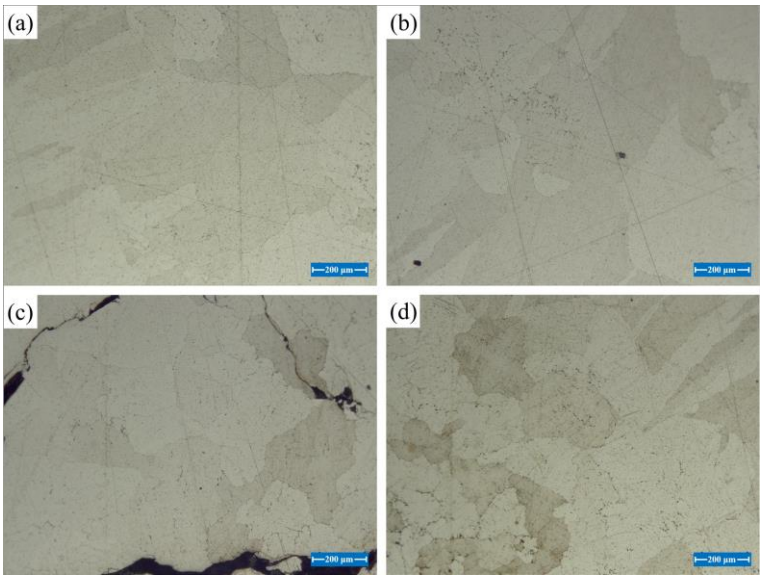

Fig. 5-1 Optical microscope images of $(Ni_{47}Mn_{38}Sn_{12}Cu_3)_{100-z}B_z$ (a) z=0; (b) z=0.2; (c) z=0.4; (d) z=0.6

The characteristic X-ray energies of light elements (those with atomic numbers smaller than Na) are too low to be accurately detected by EDS, including B. Therefore, in this study of boron doping, inductively coupled plasma mass spectrometry (ICP-MS) was employed to determine the B content. Quantitative analysis of B concentration in the alloy matrix revealed good agreement between nominal and actual compositions. However, due to the limited solubility of B in the alloy matrix, additional B doping (exceeding 0.6 at.%) during the melting process failed to further increase the actual boron content in the as-cast alloys.

The microstructure and precipitates of $(Ni_{47}Mn_{38}Sn_{12}Cu_3)_{99.4}B_{0.6}$ were analyzed using TEM. Fig. 5-2(a) shows a low-magnification bright-field image revealing the presence of $L2_1$ austenite and a small amount of 10M martensite. B doping was found to induce the formation of minor precipitates in the alloy. As shown in the magnified view of the precipitate-surrounding area (in Fig. 5-2(b)), these precipitates were predominantly distributed along grain boundaries. Selected-

area electron diffraction (SAED) analysis identified the precipitates as having a face-centered cubic structure. Fig. 5-2(c) confirms the $L2_1$ austenitic matrix of the alloy. Fig. 5-2(d) presents a high-resolution TEM image of the 10M martensite in the alloy, displaying its characteristic periodic atomic stacking structure. The inset SAED pattern of the five-layered orthorhombic 10M martensite phase shows four equally spaced superlattice spots (indicated by white arrows) between two bright spots, dividing the inter-spot distance into five equal segments. This observation is consistent with the periodic atomic stacking structure of 10M martensite described in Section 4.3. Microstructural analysis indicates that the alloy at room temperature consists of $L2_1$ austenite phase[172], five-layered orthorhombic 10M martensite[173], and trace amounts of precipitates.

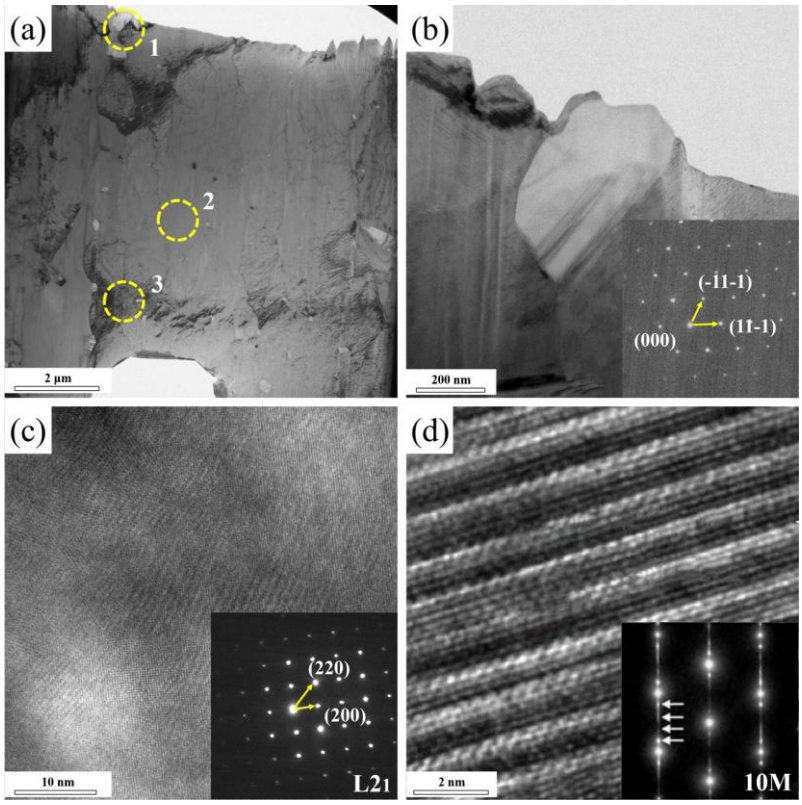

Fig. 5-2 TEM bright field images and electron diffraction patterns
(a) TEM bright-field images of $(Ni_{47}Mn_{38}Sn_{12}Cu_3)_{99.4}B_{0.6}$ alloy at room temperature; (b) the enlarged view of region 1 focusing on a single precipitate phase; (c) and (d) HRTEM images of 10M martensites and $L2_1$ austenite taken from region 2 and 3

5.2.2 Martensitic Transformation Behavior of Ni-Mn-Sn-Cu-B Alloy

The MT temperatures and latent heats of the $(Ni_{47}Mn_{38}Sn_{12}Cu_3)_{100-z}B_z$ (z=0, 0.2, 0.4, 0.6) alloys were measured using both DSC and MDSC, with the obtained DSC curves presented in Fig. 5-3. The results demonstrate a slight decrease in martensitic transformation temperatures with increasing B content. Among these four compositions, each 0.2 at.% increment in boron doping reduced the martensitic transformation temperatures by approximately 1.5 K. Fig. 5-4 shows the variation of transformation latent heat with B content, revealing a gradual decrease in total latent heat with increasing B concentration, a trend that is consistent with the results shown in Fig. 5-3.

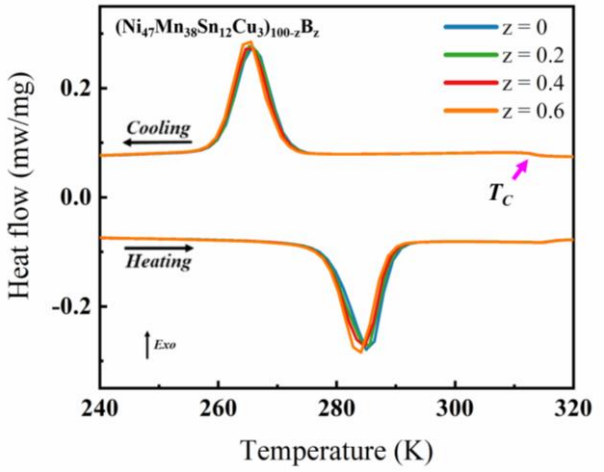

Fig. 5-3 DSC curves of $(Ni_{47}Mn_{38}Sn_{12}Cu_3)_{100-z}B_z$ alloys

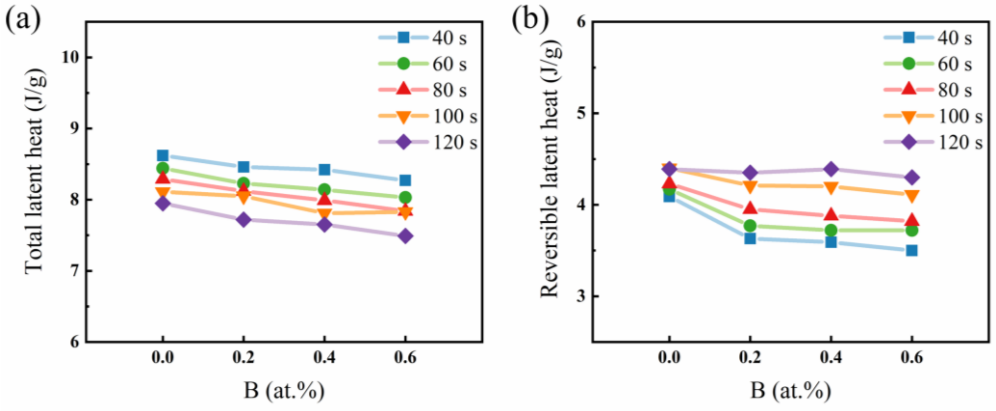

Fig. 5-4 Latent heat of $(Ni_{47}Mn_{38}Sn_{12}Cu_3)_{100-z}B_z$ alloys under different modulation periods (a) total latent heat; (b) reversible latent heat

It is noteworthy that the reversible latent heat also decreases with increasing B content. Between z=0 and z=0.2, the reversible latent heat exhibits a sharp decline, showing a more pronounced reduction trend compared to the total latent heat. However, as the B doping level increases to 0.6 at.%, the reversible latent heat remains nearly unchanged. This phenomenon can be attributed to the secondary phases formed by B addition, which impose constraints on the matrix and hinder the shear strain associated with martensitic transformation, thereby increasing frictional dissipation during interfacial motion during the transformation process. On the other hand, with increasing boron content, the gradually formed secondary phases do not participate in the martensitic transformation. Based on these two aspects, it can be inferred that the transformation entropy also slightly decreases with increasing B content.

Functional fatigue resistance is crucial for the practical application of solid-state refrigeration technology. The alloy must demonstrate excellent functional stability during both magnetic field cycling and thermal cycling. As shown in Fig. 5-5(a), $(Ni_{47}Mn_{38}Sn_{12}Cu_3)_{99.4}B_{0.6}$ alloy underwent 500 thermal cycles, during which the peak heights and widths of both martensitic transformation and reverse transformation remained essentially unchanged. Taking A_f temperature as an example, it shifted by approximately 2 K toward lower temperatures after 500 thermal cycles, demonstrating the alloy's stability during thermal cycling.

The $(Ni_{47}Mn_{38}Sn_{12}Cu_3)_{99.4}B_{0.6}$ alloy was subjected to 10^5 magnetic field cycles under a 5 T magnetic field. Fig. 5-5(b) compares the *M-T* curves of the alloy measured under 200 Oe and 5 T magnetic fields before and after the 10^5th magnetic cycling. The results show excellent overlap demonstrating remarkable stability in the alloy's phase transition behavior under magnetic field cycling.

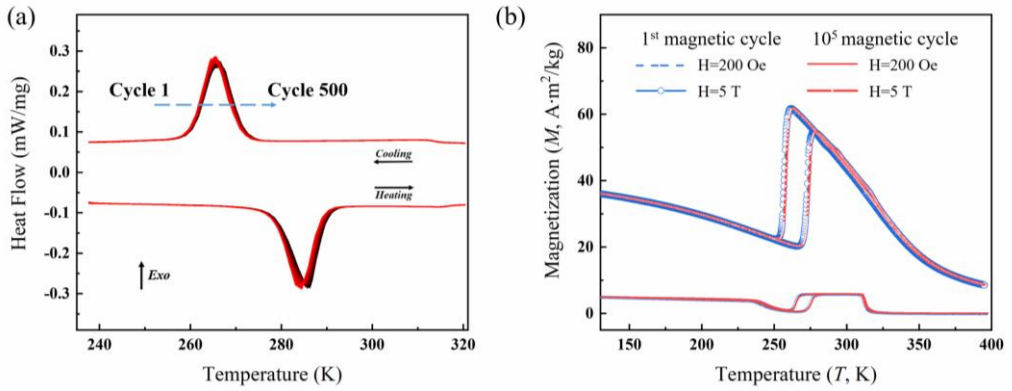

Fig. 5-5 Martensite transformation process of $(Ni_{47}Mn_{38}Sn_{12}Cu_3)_{99.4}B_{0.6}$ alloy
(a) 500 DSC cycles; (b) *M-T* curves before and after 10^5 magnetizing/demagnetizing cycles

A comparison between the *M-T* curves of $(Ni_{47}Mn_{38}Sn_{12}Cu_3)_{99.4}B_{0.6}$ alloy (Fig. 5-4(b)) and $Ni_{47}Mn_{38}Sn_{12}Cu_3$ alloy (Fig. 4-24) reveals that B doping has negligible influence on the magnetic-field-induced transformation behavior of the alloy. This observation can be attributed to the minimal B content dissolved in the alloy matrix, which produces insignificant effects on the alloy's properties from both energetic and magnetic moment perspectives. Consequently, in subsequent investigations, B doping is considered to have no substantial impact on either the martensitic transformation behavior or magnetic response characteristics of $Ni_{47}Mn_{38}Sn_{12}Cu_3$ alloy, with its primary role being the enhancement of mechanical properties and cyclic stability of caloric effects.

5.2.3 Mechanical Properties of Ni-Mn-Sn-Cu-B Alloy

Both adiabatic temperature change and the cyclic stability of elastocaloric effect are closely related to the mechanical properties of the alloy. The compression curves of $(Ni_{47}Mn_{38}Sn_{12}Cu_3)_{100-z}B_z$ alloys were measured at 350 K, with the results shown in Fig. 5-6. As inferred from the results in Fig. 5-3, at 350 K the alloy is in an environment approximately 60 K above the A_f temperature, making stress-induced martensitic transformation unlikely to occur at this temperature and thus avoiding confusion between the stress yield plateau and superelastic plateau. With

increasing B content, the yield strength of the austenitic phase gradually increases. These results demonstrate that boron doping can further improve the mechanical properties of $Ni_{47}Mn_{38}Sn_{12}Cu_3$ alloy - enhancing both yield strength and fracture strength - without significantly affecting its transformation temperature. This improvement suggests that B-doped alloys may withstand higher stresses and more loading-unloading cycles, which could facilitate the achievement of large ΔT_{ad}.

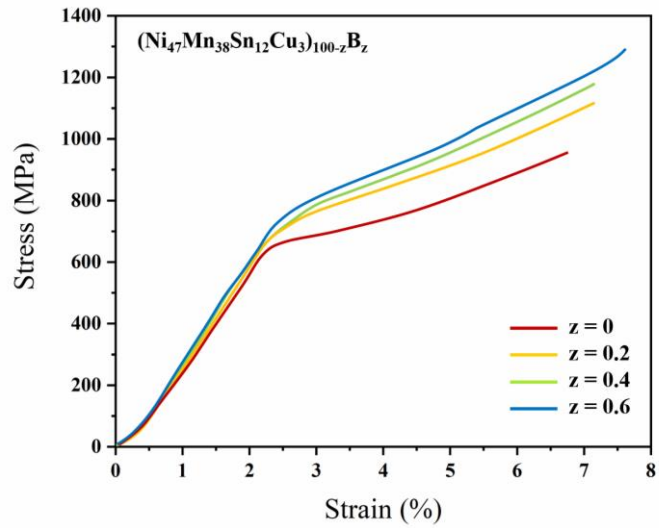

Fig. 5-6 Compressive stress-strain curves of $(Ni_{47}Mn_{38}Sn_{12}Cu_3)_{100-z}B_z$ alloys under 350 K

To investigate the effects of Cu and B doping on mechanical properties, the $(Ni_{47}Mn_{38}Sn_{12}Cu_3)_{99.4}B_{0.6}$ alloy was subjected to 200 stress loading-unloading cycles followed by TEM characterization. Fig. 5-7(a) reveals numerous dislocations within grains after cyclic loading, generated by the reciprocating motion of martensite-austenite phase interfaces during cycling, indicating good toughness and the occurrence of plastic deformation. Magnified analysis of the surrounding morphology in Fig. 5-7(b) and (c) shows that most dislocations have undergone climb motion, forming dislocation walls that transformed into subgrain boundaries, while some dislocations accumulated near precipitates with only a small fraction randomly distributed within grains. Comparative analysis between

Fig. 5-7(b) and Fig. 5-2(b) demonstrates no significant changes in precipitates after mechanical cycling. High-resolution TEM of the precipitate-matrix interface in Fig. 5-7(d) reveals considerable lattice mismatch. These observations collectively suggest that the secondary phases induced by B doping contribute only modestly to mechanical property enhancement.

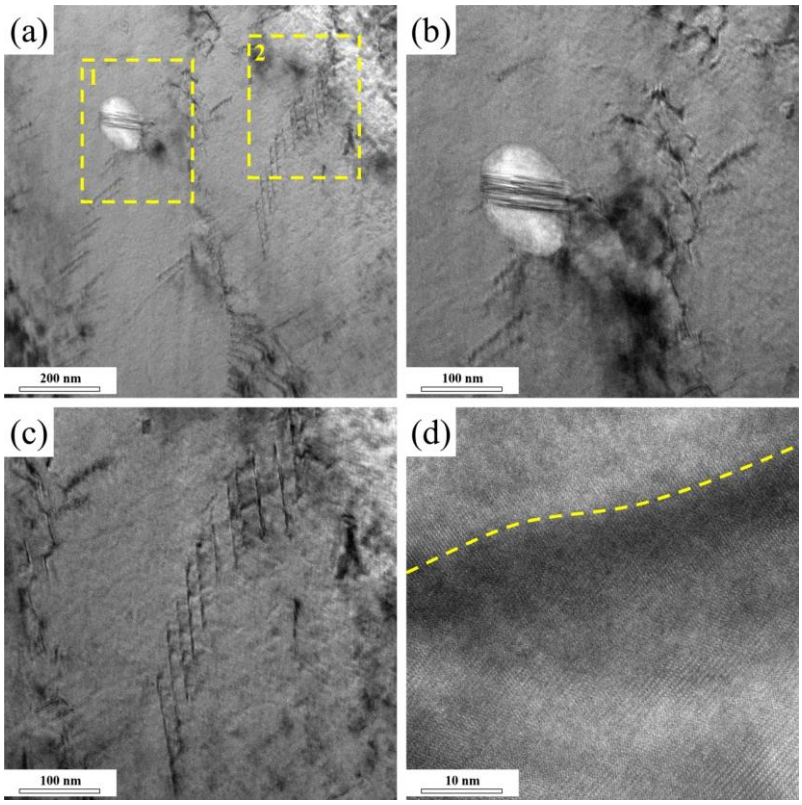

Fig. 5-7 TEM bright field images and corresponding electron diffraction patterns (a) the morphologies of $(Ni_{47}Mn_{38}Sn_{12}Cu_3)_{99.4}B_{0.6}$ alloy after superelastic cycling; (b) the enlarged view of (a) focusing on a single precipitate phase (region 1); (c) the enlarged view of (a) focusing on dislocation wall (region 2); (d) high-resolution TEM image of the interface between the precipitated phase and the matrix

Based on the first-principles calculation results of B doping in Section 3.4, B atoms preferentially occupy O−I interstitial sites. Literature reports indicate that B tends to form $NiBH^+$ complexes and segregate at grain boundaries[97], which reduces hydrogen diffusion along grain boundaries and decreases alloy brittleness. Therefore, it is concluded that the primary strengthening mechanism of B doping

originates from grain boundary strengthening caused by B segregation at grain boundaries.

5.3 Elastocaloric Effect of $(Ni_{47}Mn_{38}Sn_{12}Cu_3)_{99.4}B_{0.6}$ Alloy

5.3.1 Superelasticity of $(Ni_{47}Mn_{38}Sn_{12}Cu_3)_{99.4}B_{0.6}$ Alloy

Stress-induced martensitic transformation is a prerequisite for alloys to exhibit elastocaloric effect. To investigate the SIMT and its evolution during cyclic loading-unloading processes, isothermal compression stress-strain curves were measured at room temperature (296 K, above A_f=294 K) under 200 loading-unloading cycles with a strain rate of 3.3×10^{-4} s^{-1} for both loading and unloading. Fig. 5-8 presents the superelastic training curves of $(Ni_{47}Mn_{38}Sn_{12}Cu_3)_{99.4}B_{0.6}$ alloy during 200 loading-unloading cycles, demonstrating the stress-strain behavior under the conditions mentioned earlier.

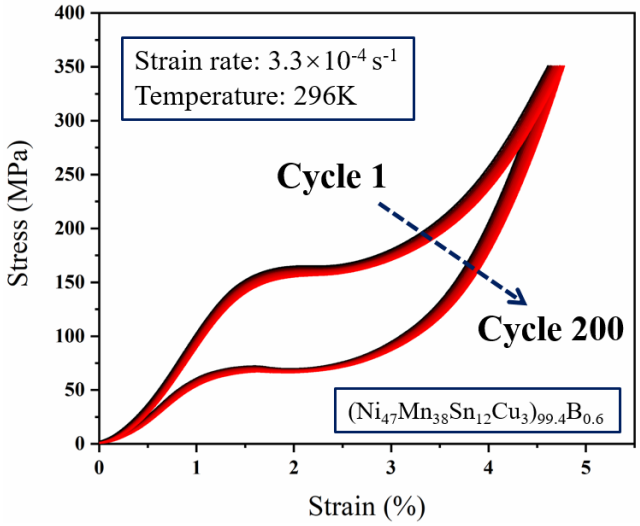

Fig. 5-8 Compressive stress-strain curves of $(Ni_{47}Mn_{38}Sn_{12}Cu_3)_{99.4}B_{0.6}$ alloy in 200 cycles at 296 K. The arrow shows the increase in the number of cycles

The stress-strain curves maintain consistent shape throughout all 200 cycles, exhibiting distinct superelastic plateaus during loading that correspond to SIMT. Complete reversibility is demonstrated by the absence of residual strain upon unloading. Through double-tangent method analysis of the stress-strain curves, two

key evolutionary trends are observed: the critical stress (σ_{Ms}) shows a gradual decrease from 154 MPa to 150.5 MPa with progressive cycling, while the maximum strain (ε_{max}) displays a near-linear increase from 4.61% to 4.83% with accumulating cycles.

To explore the temperature region where SIMT takes place, stress-strain tests with a strain rate of 3.3×10^{-4} s^{-1} were conducted at various temperatures ranging from 283 K to 318 K, as shown in Fig. 5-9. The stress-strain curves show a plateau after loading, which indicates the occurrence of SIMT from austenite to martensite. When the test temperature is above 295 K, as a result of the inverse change from martensite to austenite, the compressive strain is completely recovered after unloading.

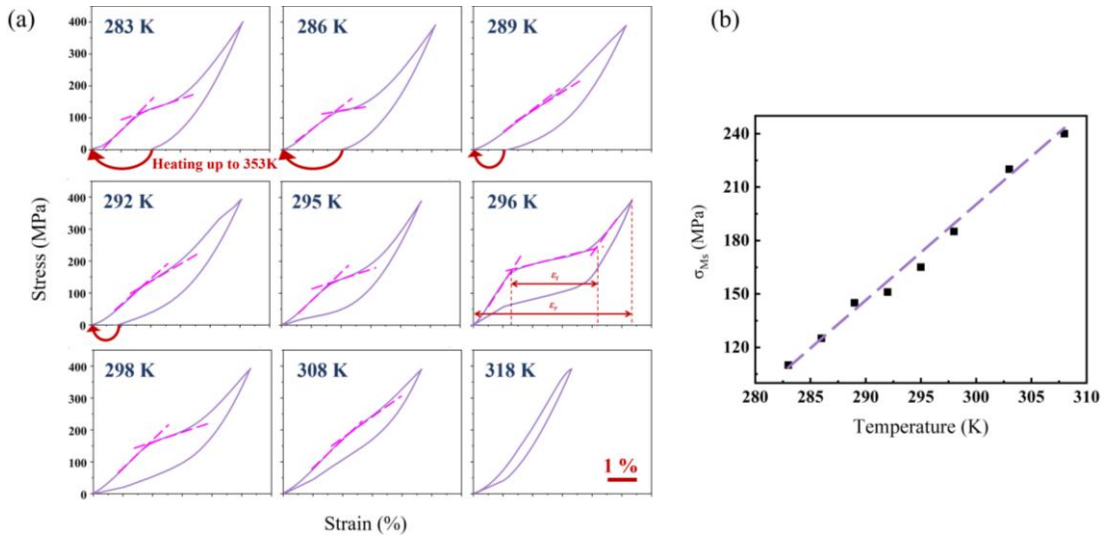

Fig. 5-9 $(Ni_{47}Mn_{38}Sn_{12}Cu_3)_{99.4}B_{0.6}$ alloy superelastic performance
(a) superelastic curves under different temperature; (b) temperature-dependent critical stress

As shown in Fig. 5-9(a), at a temperature of 296 K, the recovery strain (ε_r, the strain that is reversibly recovered when the applied load is removed) and associated transformation strain (ε_t, the plateau appearing in the superelastic stress-strain curve, and the length of the plateau can reflect the magnitude of the superelastic strain) are 5.2% and 3.0%, respectively, during the superelastic cycle. The plateau

gradually shifts to higher stress with increasing temperature, while the superelastic strain decreases. The temperature-dependent critical stress is depicted in Fig. 5-9(b), where σ_{Ms} rises linearly as the temperature in the region rises from 283 to 318 K, the slope of the fitted straight line ($d\sigma_{Ms}/dT$) is 5.36 MPa/K.

The isothermal entropy change ($\Delta S_{c\text{-}c}$) during SIMT process is expressed using the Clausius-Clapeyron equation:

$$\Delta S_{c\text{-}c} = -\varepsilon_t \times (d\sigma_{Ms}/dT) \times (1/\rho) \quad (5.1)$$

where $d\sigma_{Ms}/dT$ is the sensitivity parameter of critical stress to temperature, ε_t is the transformation strain, and ρ is the density of alloy.

Analysis based on the aforementioned equation reveals that, theoretically, a larger $d\sigma_{Ms}/dT$ value corresponds to higher isothermal entropy change and better elastocaloric performance. However, an excessively high $d\sigma_{Ms}/dT$ value would require prohibitively high stress to induce complete martensitic transformation, potentially causing material yielding and plastic deformation that would adversely affect elastocaloric performance. Therefore, the influence of $d\sigma_{Ms}/dT$ on elastocaloric properties must be considered dialectically. From Fig. 5-8, the isothermal entropy change $\Delta S_{c\text{-}c}$ of 20.6 J/kg·K under room temperature.

5.3.2 Reversibility and Cyclic Stability of Elastocaloric Effect

The ΔT_{ad} during superelastic test process was also monitored to directly reveal the eCE under room temperature (296 K). Before conducting the tests, the sample was subjected to superelastic cycles for 10 times to ensure that stable eCE was obtained. Fig. 5-10 shows the stress-strain curves under different stresses of 300, 400 and 500 MPa. The superelastic curve obtained under adiabatic conditions exhibits a steeper profile compared to that acquired under isothermal conditions in the previous section, which is consistent with literature[195].

A comparison of the three superelastic curves reveals that the increase in maximum stress leads to a widening of the stress hysteresis. This is attributed to the rapid movement of phase transition interfaces at high deformation rates, which enhances frictional resistance[196]. The stress hysteresis represents the energy dissipation during the phase transition process, indicating that the irreversibility of ΔT_{ad} also increases with strain.

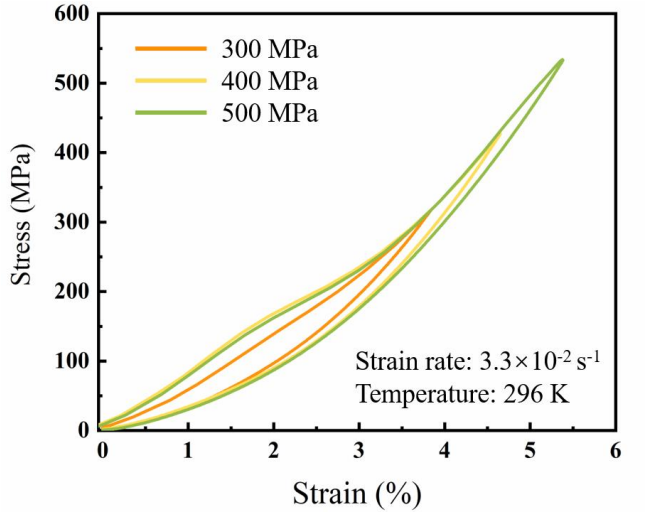

Fig. 5-10 Superelastic stress-strain curves under stresses of 300, 400, and 500 MPa in the $(Ni_{47}Mn_{38}Sn_{12}Cu_3)_{99.4}B_{0.6}$ alloy

Fig. 5-11 shows the ΔT_{ad}-time curve of $(Ni_{47}Mn_{38}Sn_{12}Cu_3)_{99.4}B_{0.6}$ alloy during the loading-holding-unloading process under 300 MPa stress. The evolution of surface temperature during adiabatic loading and unloading was simultaneously recorded using an infrared thermal imager, with the results presented in the inset of Fig. 5-11. The photo numbers correspond one-to-one with the points marked on the adiabatic temperature change-time curve. It should be noted that the temperature was calculated as the average value across the entire gauge section of the alloy sample in each infrared image.

During both martensitic transformation and reverse martensitic transformation, the sample temperature exhibited significant changes. However, a noticeable

temperature difference existed between the sample edges and the central region, attributable to heat exchange with the compression heads at the edges, resulting in partial heat loss. Under 300 MPa stress, the adiabatic temperature change reached 5.1 K. During the holding stage, the sample temperature gradually decreased and stabilized at room temperature after approximately 5 s. In the unloading stage, the stress rapidly decreased, and due to the reverse martensitic transformation, the sample temperature dropped significantly to 3.9 K before gradually rising back to equilibrium at room temperature.

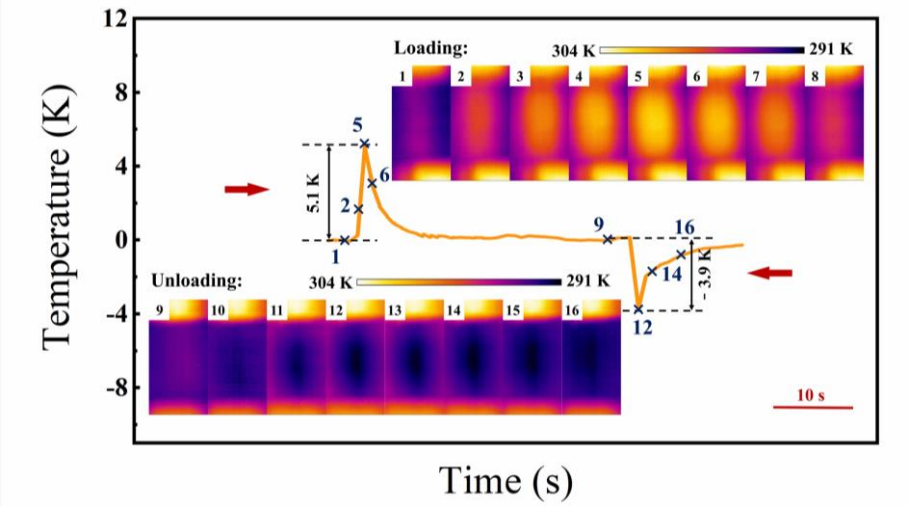

Fig. 5-11 A series of infrared images showing the temperature evolution under 300 MPa and corresponding ΔT_{ad}-time profiles

When the maximum applied stress reached 400 MPa, as shown in Fig. 5-12, the adiabatic temperature changes during loading and unloading were 7.8 K and 6.2 K, respectively. This is attributed to the increased strain accompanying higher stress levels, which promotes the transformation of more austenite into martensite. Observing insets 1 to 5, it can be observed that the spatial evolution of temperature changes during loading exhibits uniformity. The temperature band observed in the study by Ossmer et al.[197]did not occur in this work.

During the holding stage, inset 6 displays a triangular region near the contact

area between the alloy sample and the compression indenter, where the temperature was slightly lower than in adjacent zones. This indicates the formation of microcracks at the sample edge during holding, as marked by the arrow in the figure. The presence of microcracks also led to a more pronounced temperature change in this region during unloading compared to other areas. Furthermore, the nucleation and propagation of microcracks increased frictional dissipation, thereby reducing ΔT_{ad} during unloading.

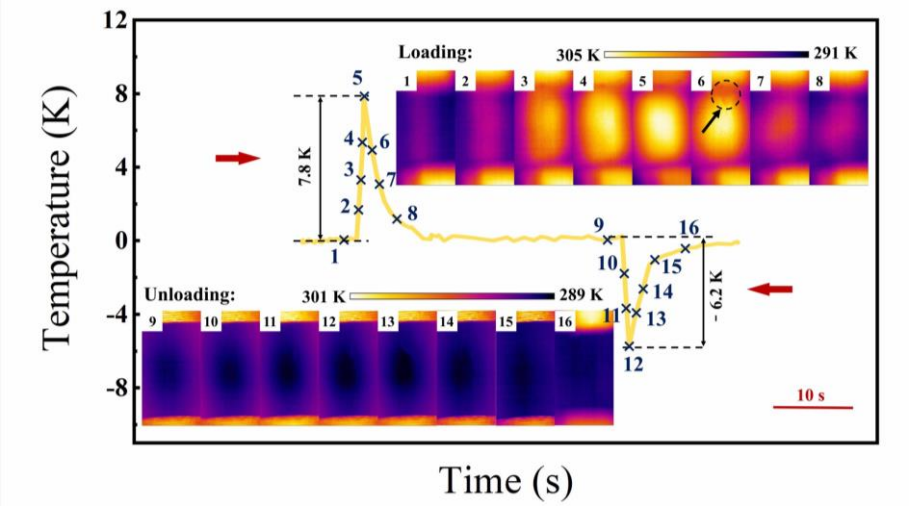

Fig. 5-12 A series of infrared images showing the temperature evolution under 400 MPa and corresponding ΔT_{ad}-time profiles

When the maximum applied stress was increased to 500 MPa, as shown in Fig. 5-13, ΔT_{ad} during loading and unloading increased to 10.3 K and 8.6 K, respectively. Comparing the elastocaloric effects under the three different maximum stresses reveals a gradual enhancement in ΔT_{ad}. The theoretical upper limit of ΔT_{cal} for the elastocaloric effect is evaluated as follows. As described in Section 1.2.4, according to the law of energy conservation, ΔT_{cal} and the entropy change ΔS under adiabatic conditions can be calculated using Eq. (1.14)[6]. Based on the heat capacity analysis results from Chapter 4, ΔS_{dsc} is taken as 22.1 J/kg·K and C_p as 500 J/kg·K. Substituting these values into Eq. (5.1) and have $\Delta T_{cal\text{-}DSC}$=12.1 K.

This fact confirms that the alloy undergoes almost complete SIMT to produce a high latent heat and a adiabatic temperature change. The values of ΔT_{ad} during the loading and unloading processes for the present alloy and some other Heusler-type alloys reported in the literature are listed in Table 5-1. The obtained ΔT_{ad} in the present $(Ni_{47}Mn_{38}Sn_{12}Cu_3)_{99.4}B_{0.6}$ alloy is comparable or higher than that reported in the well-studied Heusler-type alloys or compounds.

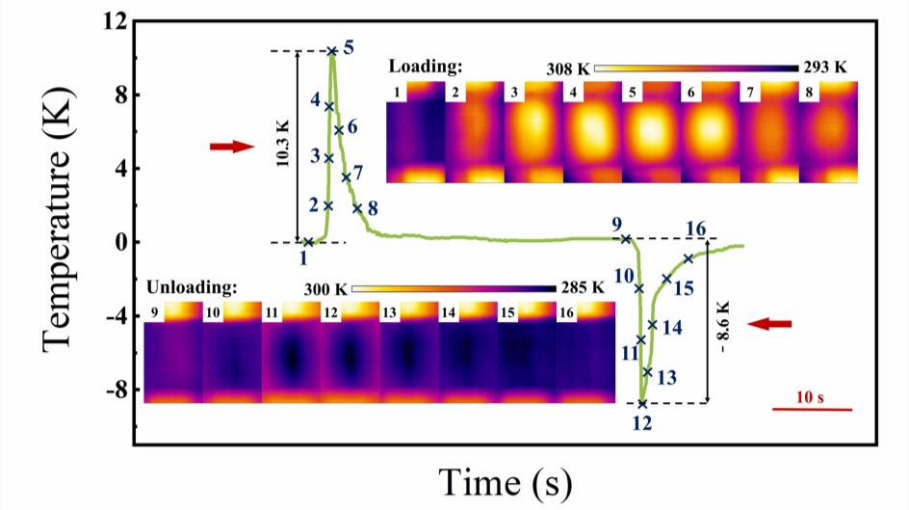

Fig. 5-13 A series of infrared images showing the temperature evolution under 500 MPa and corresponding ΔT_{ad}-time profiles

Table 5-1 Adiabatic temperature change during the loading ($\Delta T_{ad}^{loading}$) and unloading ($\Delta T_{ad}^{unloading}$) processes for $(Ni_{47}Mn_{38}Sn_{12}Cu_3)_{99.4}B_{0.6}$ alloy and some other Heusler-type alloys reported in literature

Alloys	$\Delta T_{ad}^{loading}$ (K)	Loading rate (s^{-1})	$\Delta T_{ad}^{unloading}$ (K)	Unloading rate (s^{-1})	Ref
$Ni_{45}Mn_{44}Sn_{11}$	4	0.85×10^{-2}	−5.7	0.85×10^{-2}	[34]
$Ni_{43}Co_6Mn_{40}Sn_{11}$	6.4	2.1×10^{-2}	−7.1	3.5	[16]
$Ni_{45.7}Co_{4.2}Mn_{37.3}Sb_{12.8}$	9.4	1.8×10^{-2}	−8.7	5×10^{-2}	[198]
$(Ni_{51.5}Mn_{33}In_{15.5})B_{0.3}$	6.6	4.2×10^{-2}	−6.2	4.2×10^{-2}	[97]
$Ni_{45.7}Mn_{36.6}In_{13.3}Co_{5.1}$	3.5	0.13	−3.5	0.13	[31]
$Ni_{45}Mn_{36.5}In_{13.5}Co_5$	8.6	5.66×10^{-2}	−5.8	5.66×10^{-2}	[32]
$(Ni_{47}Mn_{38}Sn_{12}Cu_3)_{99.4}B_{0.6}$	10.3	3.3×10^{-2}	−8.6	3.3×10^{-2}	This work

We further tested ΔT_{ad} at different temperatures of 306, 321 and 336 K, as shown in Fig. 6. At a low temperature of 306 K, ΔT_{ad} is 7 and 5.9 K during loading and unloading, respectively. When the test temperature is increased to 321 K, ΔT_{ad} obtained in the process of loading and unloading is 4.2 and 3.3 K respectively. The decrease in ΔT_{ad} is due to the increase of the critical stress for SIMT with increasing temperatures. At 336 K, the obtained ΔT_{ad} is 2.2 and 1.7 K during loading and unloading respectively. At all temperatures, the obtained ΔT_{ad} during loading process is larger than that during unloading process, also showing an irreversible nature.

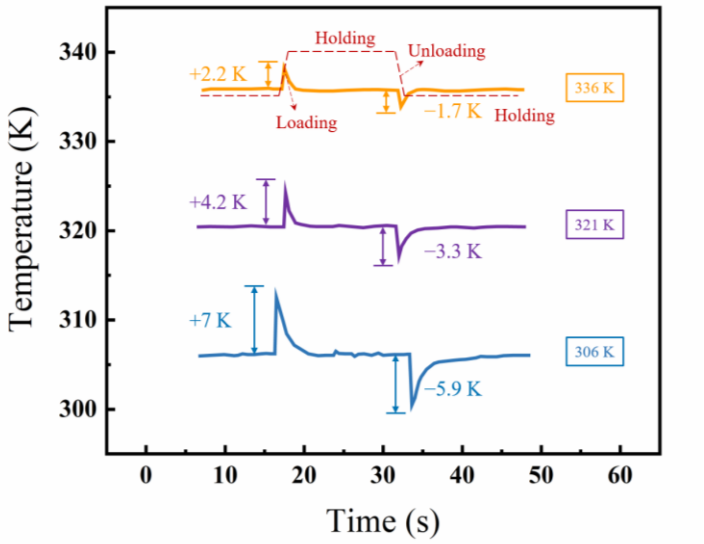

Fig. 5-14 Elastocaloric ΔT_{ad} of $(Ni_{47}Mn_{38}Sn_{12}Cu_3)_{99.4}B_{0.6}$ alloy during loading-unloading processes at different temperatures (306 K, 321 K, and 336 K)

Such irreversibility is related to the intrinsic frictional heat dissipation during superelastic process. That is to say, the heat dissipation aggravates the temperature rise during loading, and balances the temperature drop during partial unloading process, which results in the irreversibility of ΔT_{ad}. The frictional heat dissipation caused by stress hysteresis can be obtained by calculating the area enclosed by the loading and unloading curves. Accordingly, the irreversible temperature change (ΔT_{irr}) can be calculated by[199]:

$$\Delta T_{\mathrm{irr}}=\frac{T}{C_p}\Delta S_{\mathrm{irr}}=\frac{T}{C_p}\frac{Q_{\mathrm{hyst}}}{T}=\frac{1}{\rho C_p}\oint(\sigma\cdot \mathrm{d}\varepsilon) \tag{5.2}$$

where ρ is the alloy density (7.9 g/cm^3), c is the specific heat (500 J/(kg·K)). The determined ΔT_{irr} reaches 1.2 K based on Eq. (5.2), suggesting that the frictional heat dissipation is only one of the irreversible factors for eCE. Other factors including the temperature-dependent ferromagnetism of parent phase must be considered. In bulk Ni-Mn-based alloys, the total entropy change ($\Delta S_{\mathrm{total}}$) during phase transition includes the dominant lattice vibration component (ΔS_{vib}) and magnetic component (ΔS_{mag}). When the test temperature is close to the Curie point of the parent phase, the magnetic component slightly decreases due to reduced ferromagnetism of the parent phase, leading to an increase in the total entropy change during the phase transition. In the quasi-adiabatic tests, the sample temperature increases upon loading and approaches the Curie point of the parent phase, while the temperature decreases upon unloading and keeps away from the Curie point. Therefore, the total entropy change is different for the loading and unloading processes[200].

In practical applications of elastocaloric refrigeration, the loading and unloading processes would not be conducted at the slow rates used in superelasticity testing, as this would significantly compromise refrigeration efficiency. Therefore, to evaluate the cycling stability of the elastocaloric effect, the $(Ni_{47}Mn_{38}Sn_{12}Cu_3)_{99.4}B_{0.6}$ alloy must undergo rapid loading and unloading cycles. For this purpose, setting the applied stress at 300 MPa with both loading and unloading strain rates of 3.3×10^{-2} s^{-1}. The relationship between cyclic temperature variation and time is depicted in Fig. 5-15. The stable eCE is demonstrated in 200 cycles, implying promising application potential in $(Ni_{47}Mn_{38}Sn_{12}Cu_3)_{99.4}B_{0.6}$ alloys.

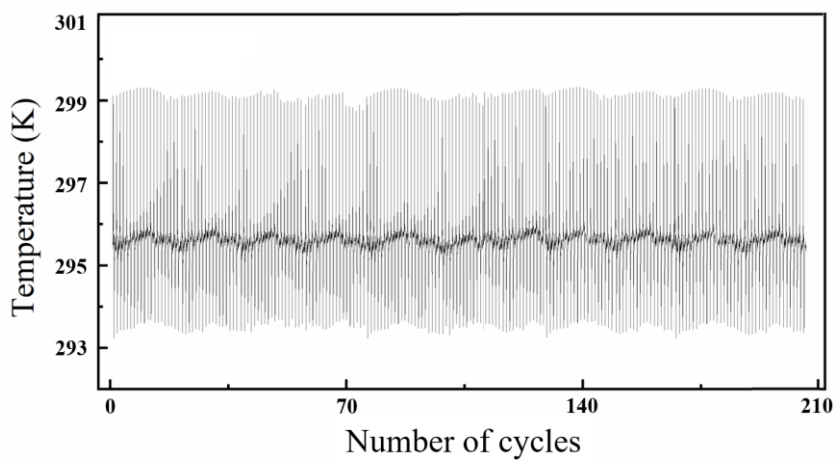

Fig. 5-15 Temperature variation in $(Ni_{47}Mn_{38}Sn_{12}Cu_3)_{99.4}B_{0.6}$ alloy during cyclic loading-holding-unloading for 200 cycles

5.4 Multi-field Regulated Caloric Effect

However, the working temperature range of refrigeration applications caused by these two caloric effects does not overlap. The working temperature range of MCE is lower than M_s of the alloy; while the reversible eCE appears above A_f. There is a "blank area" with a temperature span of about 10 K between these two temperature ranges. From another point of view, the magnetism and lattice structure of $(Ni_{47}Mn_{38}Sn_{12}Cu_3)_{99.4}B_{0.6}$ alloy have a strong coupling effect, so its magneto-structural transition is highly sensitive to both magnetic and stress fields. Uniaxial stress and magnetic field can be simultaneously applied to achieve the multi-field regulation of the coupled caloric effects, and the multicaloric effects could occur in the working temperature window of the "blank area". In this manner, it is expected to obtain a room-temperature magnetic refrigeration material with a wider working temperature range.

5.4.1 Transformation Distribution Model Describing the Multicaloric Effects

In the previous characterization of the MCE, the concept of "phase transition

fraction" has been mentioned. The variation of the external field influences the phase transition of the alloy, thereby regulating its caloric effect. This process essentially involves a change in the mass fraction of austenite participating in the phase transition[13]. The MCE of $(Ni_{47}Mn_{38}Sn_{12}Cu_3)_{99.4}B_{0.6}$ assisted by uniaxial stress can be established. From the phase transition parameters obtained previously, the field-induced austenite transformation fraction is phenomenologically modeled. The following equation can be used to explain this model:

$$v(T,H,\sigma)=\frac{1}{\delta\sqrt{2\pi}}\cdot e^{\frac{-\left(T-T_p-\frac{dT}{\mu_0 dH}\cdot H+\left(\frac{d\sigma_{Ms}}{dT}\right)^{-1}\cdot\sigma\right)^2}{2\delta^2}} \tag{5.3}$$

where ν is the transition distribution function. For the present alloy, δ is the transition interval (δ=5 K determined from the *M*-*T* plots), T_p represents the peak temperature ($T_{p(A\text{-}M)}$=262 K for martensitic transformation and $T_{p(M\text{-}A)}$=278 K for austenite transition), $dT/\mu_0 dH$=2 K/T and $d\sigma_{Ms}/dT$=5.36 MPa/K obtained from Fig. 5-9(b).

Based on the phase transition fraction model, the transition distribution functions are plotted in Fig. 5-16(a) and (b). It is found that the application of stress can increase the MT temperature, while the application of a magnetic field can reduce the phase transition temperature of the alloy. Since the stress and magnetic fields have opposite effects on the MT temperature, the strategy of the coupled caloric effects under the stress and magnetic fields can be applied to tailor the MT temperature, broadening the working temperature window.

From the transition distribution model, the austenite transformation fraction is determined, which is influenced by a combination of temperature, stress and magnetic field. Therefore, at a given temperature and stress, the austenite transformation fraction is affected by the variation of the magnetic field and can be

described by the following relationship:

$$\mathrm{d}f=f(T, H+\mathrm{d}H, \sigma)-f(T, H, \sigma)=\int_{-\infty}^{T} v(T, H+\mathrm{d}H, \sigma)\mathrm{d}T-\int_{-\infty}^{T} v(T, H, \sigma)\mathrm{d}T \qquad (5.4)$$

In section 4.5.4, it has been discussed that the entropy change can be obtained by the C-C relation. Here, the influence of low applied stress on entropy change can be neglected. Therefore, the adiabatic temperature change ΔT_{ad} under the simultaneous application of uniaxial stress and magnetic field can be calculated using the austenite transformation fraction:

$$\mathrm{d}T=\frac{T}{C_p}\cdot\Delta S\cdot\mathrm{d}f=\frac{T}{C_p}\cdot(-\Delta M)\cdot\frac{\mu_0\mathrm{d}H}{\mathrm{d}T}\cdot\mathrm{d}f \qquad (5.5)$$

Fig. 5-16(c) and (d) correspond to Fig. 5-16(a) and (b), respectively, showing the evolution of the austenite transformation fraction during the reverse martensitic transformation and martensitic transformation under a maximum uniaxial stress of 30 MPa and a magnetic field of 5 T. According to the previous discussion on the elastocaloric effect, it can be found that a uniaxial stress of 30 MPa has little effect on the austenite transformation fraction of the alloy. Therefore, the uniaxial stress of 30 MPa is only regarded as an external field that regulates the phase transition temperature range and does not contribute to the value of $\Delta S_{m,\sigma}$.

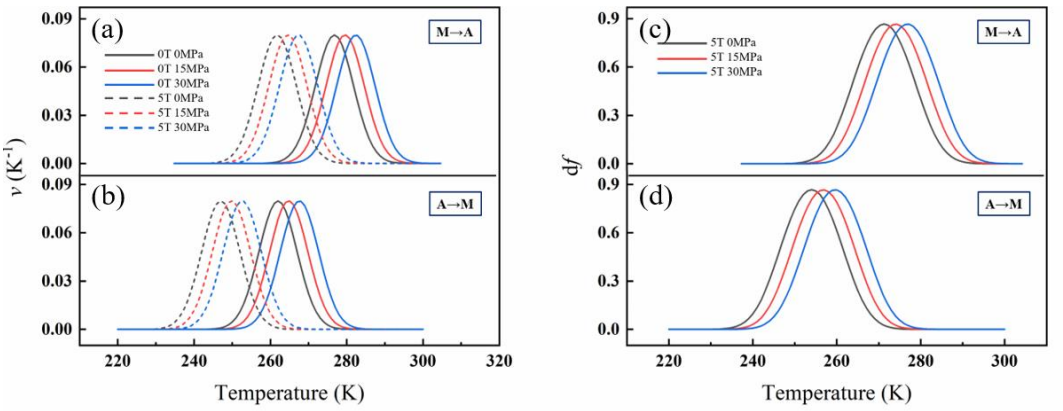

Fig. 5-16 Transition distribution function (v) and austenite transformation fraction (d*f*) changes as a function of temperature

(a) and (c) reverse martensitic transformation; (b) and (d) martensitic transformation

Based on the transition distribution model, $\Delta S_{m,\sigma}$ under the coupling of 30 MPa uniaxial stress and 5 T external field can be calculated, as shown in Fig. 5-17. The black and blue dashed lines indicate the entropic change of phase transition without and with 30 MPa uniaxial stress applied during the inverse martensitic phase transition under a 5 T magnetic field, respectively. The caloric effect operating temperature range (i.e., the half-height width of the curve) is ΔT_1, which also proves that the uniaxial stress only serves as an external field to regulate the caloric effect operating temperature range of the alloy without affecting the value of the entropy change.

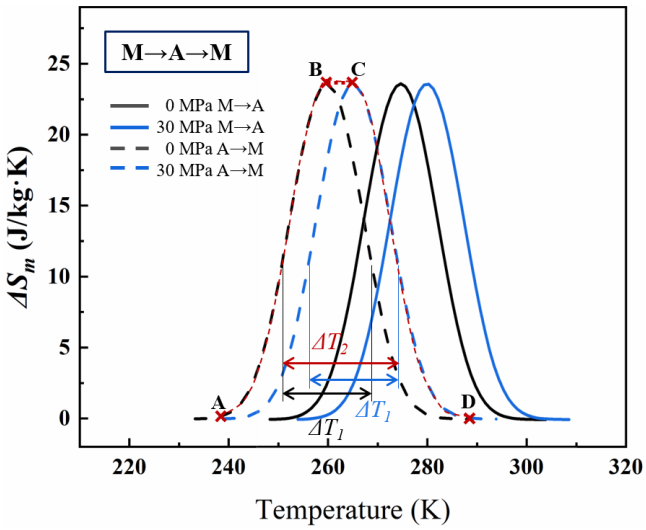

Fig. 5-17 Temperature dependence of $\Delta S_{m,\sigma}$ for the magnetization process (solid lines) and demagnetization process (dash lines) under different uniaxial stresses

The method of uniaxial stress regulation of the MSMA alloy's working temperature range is explained in detail using the reverse martensitic phase transition process as an example: The alloy only operates under an external field within the temperature range corresponding between point A to B. In the temperature range from point B to C, an adjustable uniaxial stress of up to 30 MPa is applied before the application of the magnetic field (and the uniaxial stress needs to be increased as the temperature rises in the temperature range), and a uniaxial

stress of 30 MPa is applied before the application of the magnetic field within the temperature range corresponding between point C to D. With this uniaxial stress-magnetic field coupling, the working temperature range of multicaloric effect is widened to ΔT_2.

5.4.2 Caloric Effects Under the Coupling of Magnetic Field and Hydrostatic Pressure

Similar to the uniaxial stress and magnetic field, hydrostatic pressure can also have some effects on the isothermal MT in polycrystalline MSMAs. But the effect of hydrostatic pressure on martensitic transformation is different from that of uniaxial stress and magnetic field. The lattice distortion during martensitic transformation is primarily accomplished through shear deformation, accompanied by minor volume changes. Due to the anisotropy of polycrystalline materials, under the combined effects of hydrostatic pressure and anisotropy, residual stresses between grains can generate shear stresses in appropriately oriented grains, triggering martensitic transformation. Notably, hydrostatic pressure impedes volume changes in the alloy, thereby suppressing martensitic transformation. Consequently, the response of martensitic transformation in magnetic alloys to hydrostatic pressure is weaker than that to uniaxial stress.

The change in MT temperatures induced by a bias hydrostatic pressure up to 10 kbar is shown in Fig. 5-18(a). With moderately increasing the external pressure, T_m increases significantly, implying that the coupling effects of stress and magnetic field is experimentally confirmed, and the temperature range of phase transition can be manipulated. It can also be found that the magnetization decreases with increasing hydrostatic pressure, which is due to the fact that the hydrostatic pressure reduces the Mn-Mn distance and the magnetic interaction changes. The

hydrostatic pressure may also enhance the antiferromagnetic interaction and reduce the net magnetization.

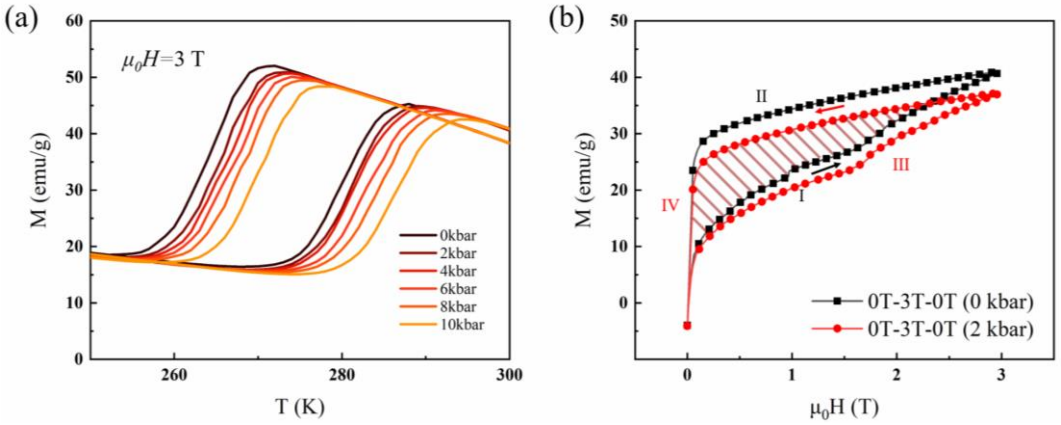

Fig. 5-18 *M-T* curves and *M-H* curves of $(Ni_{47}Mn_{38}Sn_{12}Cu_3)_{99.4}B_{0.6}$ alloy
(a) *M-T* curves under hydrostatic pressure up to 10 kbar; (b) *M-H* curves at 282 K

In addition to adjusting the phase transition temperature of the alloy, the path of the magneto-induced phase transition can be manipulated by applying stresses on the alloy, thereby improving the reversibility of the caloric effects. For example, at 282 K, the *M-H* curves are obtained by simultaneously applying hydrostatic pressure and magnetic field, and the coupling effect of hydrostatic pressure and magnetic field can be demonstrated, as shown in Fig. 5-18(b). When the sample is magnetized without an applied pressure (curve I) but demagnetized at an external hydrostatic pressure of 2 kbar (curve IV), the hysteresis and hysteresis losses (as indicated by the shadowed area in Fig. 5-18(b)) are significantly reduced. It is thus suggested that the coupling effects between the uniaxial stress and magnetic field could be also effective in tuning the alloy with a large and reversible caloric effect.

Using the measured *M-H* curves, the magnetic field-induced ΔS_m was calculated by numerical integration of the C-C relation. The isothermal magnetic entropy change was obtained as a function of temperature and magnetic field, as displayed in Fig.5-19(a). Under the same external magnetic field, the peak value of

ΔS_m decreases slightly with the increase of hydrostatic pressure. Compared with the value of 0kbar, the peak value of ΔS_m corresponding to 10kbar only decreases by 0.6 J/(kg·K), and the magnitude of the decrease is negligible. Additionally, the use of hydrostatic pressure improves the cooling efficiency by broadening the working temperature range. This is basically consistent with the results reported in literature[201, 202].

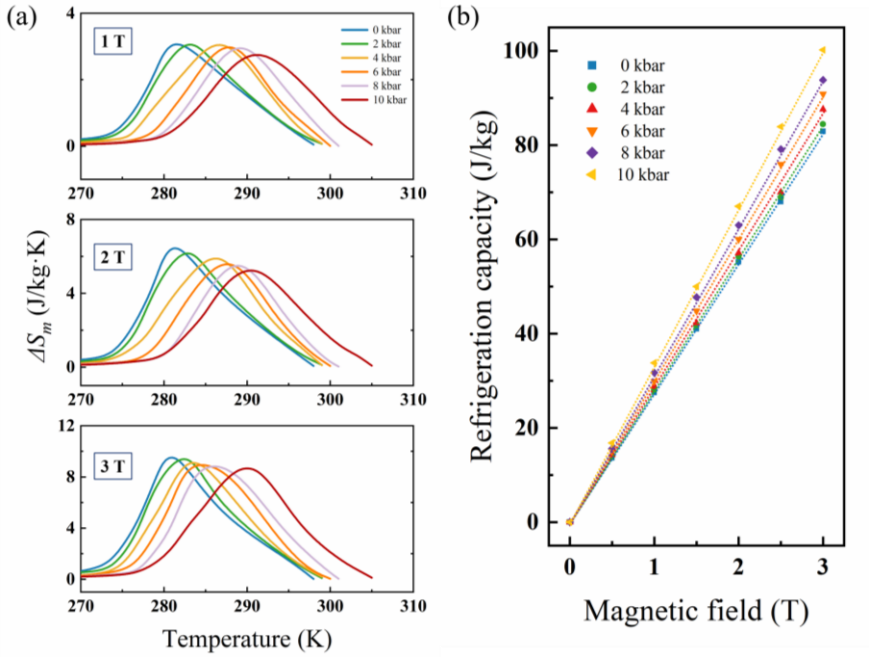

Fig. 5-19 ΔS_m and refrigeration capacity in $(Ni_{47}Mn_{38}Sn_{12}Cu_3)_{99.4}B_{0.6}$ alloy
(a) ΔS_m under various hydrostatic pressures; (b) refrigeration capacity

Fig. 5-19(b) shows the refrigeration capacity (*RC*, *RC* was calculated by integrating the ΔS_m-*T* curves over the full-width at half maximum) plotted as a function of magnetic field and applied pressure. The magnitude of *RC* is an approximately linear function of the applied field. Under the action of 0kbar, the response of the refrigeration capacity to the magnetic field is 27.39 J/(kg·T). When the hydrostatic pressure increases to 10 kbar, the response of refrigeration capacity to the magnetic field also increases to 33.42 J/(kg·T). Hydrostatic pressure coupled with a magnetic field increases the refrigeration capacity by 22%, this is because

the operating temperature window of the caloric effect under the action of hydrostatic pressure is effectively broadened. Therefore, the coupling of hydrostatic pressure can effectively regulate the MCE of the alloy. This demonstrates the two key advantages of employing multiple external fields to regulate caloric effects in this study, which is to broaden the working temperature range and reduce hysteresis.

5.4.3 Comparison with Other Typical Caloric Materials

To compare the caloric effect of $(Ni_{47}Mn_{38}Sn_{12}Cu_3)_{99.4}B_{0.6}$ with those of other typical Ni-Mn-based alloys, we plotted in Fig. 5-20 the magnetic-field-induced entropy change $|\Delta S_m|$ (blue area) [21, 80, 153, 203-208] and absolute adiabatic temperature change values $|\Delta T_{ad}|$ (pink area) [31, 198, 209-212] for different materials as a function of temperature. It can be found that ΔS_m at a magnetic field of 5 T is comparable to or exceeds those of other magnetocaloric materials.

As shown in Fig. 5-20, the adiabatic temperature changes and working temperature interval of $(Ni_{47}Mn_{38}Sn_{12}Cu_3)_{99.4}B_{0.6}$ are both at a high level among Ni-Mn-based alloys. Based on the transition distribution model, the multicaloric effect can be implemented in $(Ni_{47}Mn_{38}Sn_{12}Cu_3)_{99.4}B_{0.6}$ through a specifically designed operating route (A-B-C-D) illustrated in Fig. 5-20. Consequently, the operating temperature window of the caloric effects can span from 260 to 336 K. The operating route in achieving the multicaloric effect may be designed as follows: at the temperature between those of points A and B, the alloy is operated under the magnetic fields; at the temperature between those of points B and C, an adjustable uniaxial stress is preloaded on the alloy before the magnetic field is applied; at the temperatures above that of point C, the alloy is only operated under the applied stresses.

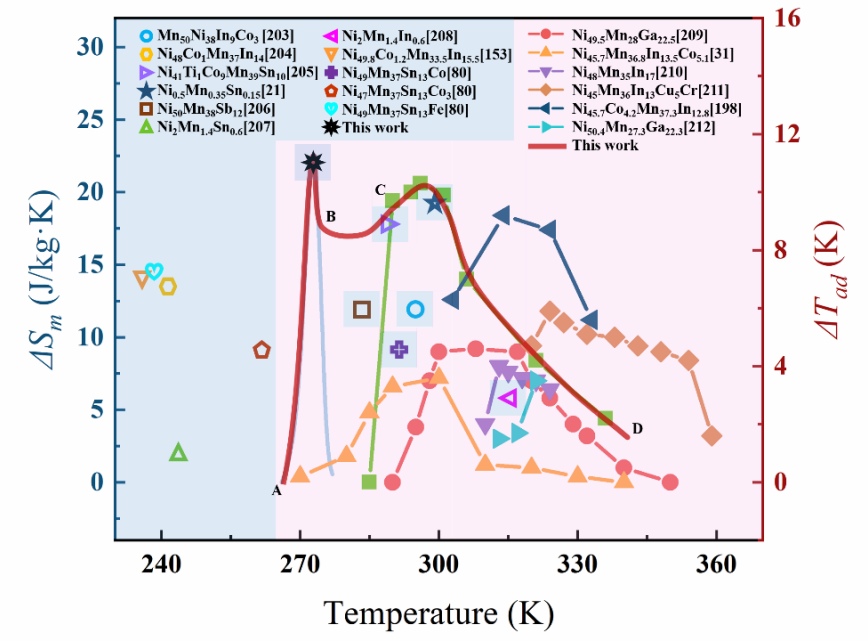

Fig. 5-20 Magnetic-field-induced entropy change $|\Delta S_m|$ under 5 T[21, 80, 153, 203-208] and reversible adiabatic temperature change $|\Delta T_{ad}|$ for elastocaloric effects[31, 198, 209-212] of Ni-Mn-based alloys as a function of temperature. The thick red lines are used to show the multicaloric effects

5.5 Fabrication and Magnetocaloric Properties of Ni-Mn-Sn-Cu-B Alloy Ribbons

The $(Ni_{47}Mn_{38}Sn_{12}Cu_3)_{99.4}B_{0.6}$ bulk alloy is fabricated into ribbons form to effectively reduce the number of grain boundaries, thereby decreasing the resistance and energy dissipation during phase transition. Meanwhile, by employing appropriate fabrication and heat treatment processes, the grain size of the ribbons can be controlled.

5.5.1 Investigation of Microstructural Evolution in Ni-Mn-Sn-Cu-B Ribbons

The fabrication parameters have a significant impact on the quality of the $(Ni_{47}Mn_{38}Sn_{12}Cu_3)_{99.4}B_{0.6}$ alloy ribbons. Appropriate fabrication techniques can yield ribbons with superior macroscopic quality. This section analyzes the

influence of various parameters on the ribbon formation morphology during the single-roller melt-spinning process, as well as the role of heat treatment parameters in adjusting grain size and martensitic transformation temperature.

5.5.1.1 Fabrication Process Optimization

Repeated melt-spinning experiments have demonstrated that the viscosity of the alloy during ejection significantly affects the forming quality of the ribbons. The alloy viscosity is primarily determined by the temperature of the molten metal, which is regulated by the heating power. Higher heating power enhances the fluidity of the molten metal, resulting in thinner ribbons, whereas lower heating power reduces the melt fluidity, allowing only a small amount of molten metal to be drawn out, thereby increasing ribbon thickness. When the heating power is too low, the molten metal tends to clog the quartz nozzle during ejection, causing the metal to solidify in droplet form, as shown in Fig. 5-21(a). Additionally, the melt may solidify into microwire structures, as illustrated in Fig. 5-21(b). Conversely, when the heating power is excessively high (15 kW or above), the molten metal exhibits extremely high fluidity. During ejection, the liquid metal fails to coalesce into a continuous ribbon, as depicted in Fig. 5-21(c). This phenomenon is similar to the results observed in the preparation of Ni-Mn-Ga microwire via melt-spinning[213].

Fig. 5-21 Macro morphology of Ni-Mn-Sn-Cu-B ribbons under different preparation parameters

Through fabrication process optimization, it was found that several factors significantly influence the quality of $(Ni_{47}Mn_{38}Sn_{12}Cu_3)_{99.4}B_{0.6}$ ribbons prepared by single-roller melt-spinning, including heating power, spray casting pressure, nozzle diameter, rotational speed, and the distance between the quartz nozzle and the roller surface. The optimized parameters for stable ribbon production are listed in Table 5-2. To ensure comparability of results, these fabrication parameters were kept constant in subsequent preparations. Fig. 5-22 shows the morphology of the Ni-Mn-Sn-Cu-B ribbons fabricated using the parameters specified in Table 5-2.

Table 5-2 Process parameters of rapid solidification

Nozzle diameter (mm)	Spray casting height (mm)	Vacuum (Pa)	Spray casting pressure (Pa)	Heating power (kW)	Rotational speed (rpm)
0.5	2	5×10^{-3}	2×10^{-2}	8	1800

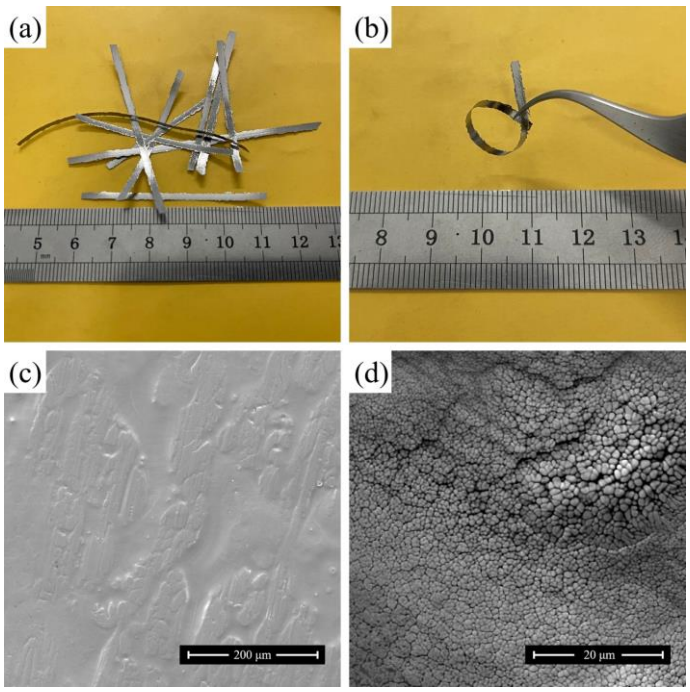

Fig. 5-22 Macro and micro morphology of the as-spun Ni-Mn-Sn-Cu-B ribbon
(a) and (b) as-spun ribbons; (c) contact surface; (d) free surface

Fig. 5-22(a) displays the macroscopic morphology of the Ni-Mn-Sn-Cu-B ribbon, the ribbon exhibits distinct metallic luster and good continuity. As shown

in Fig. 5-22(b), demonstrating its ability to undergo bending and curling with certain flexibility. The ribbon length generally does not exceed 120 mm, and no through holes are observed. Fig. 5-22 (c) shows the surface microstructure of the prepared ribbon on the side in contact with the copper roller, which has unevenly distributed protrusions on the surface, similar to the morphology obtained in melt-spun microwires[213]. Fig. 5-22(d) shows the surface microstructure of the as-spun ribbon on the side facing away from the copper roller, revealing numerous cellular crystals. The solidification rate also influences the free surface morphology: at higher rates, the free surface predominantly forms cellular crystals, whereas at lower rates, dendritic morphologies tend to appear[214].

Fig. 5-23 shows the SEM images of the fracture surface of the as-spun ribbons. As can be seen from Fig. 5-23(a), the as-spun ribbons exhibit uniform thickness, with an average thickness of approximately 20 μm. Along the growth direction of the ribbons, there are about 4−5 grains arranged, each with a diameter ranging from 5 to 10 μm.

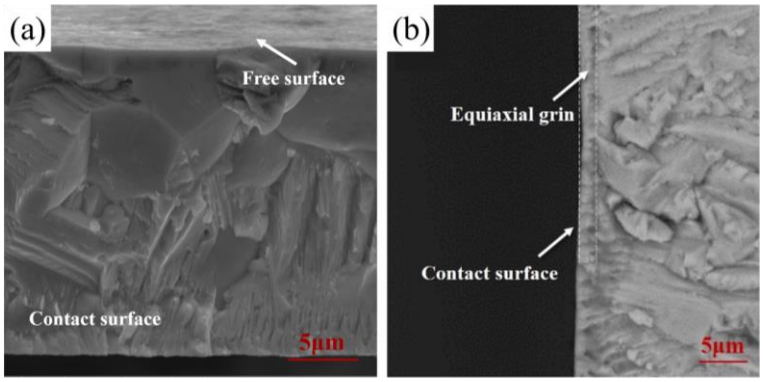

Fig. 5-23 SEM images of the as-spun Ni-Mn-Sn-Cu-B ribbon fracture morphology (a) cross section; (b) near the contact surface

Additionally, Fig. 5-23(b) reveals that within a region approximately 2 μm near the wheel-side surface, very fine equiaxed grains are present. As the distance from the wheel-side surface increases, the grains begin to grow gradually. This

phenomenon occurs because during the melt-spinning process, the temperature near the copper roller surface is low, and the grains instantly grow into equiaxed shapes. Once beyond a certain distance from the roller surface, the grains undergo significant growth along the direction of the temperature gradient.

5.5.1.2 Microstructural Evolution During the Grain Growth Heat Treatment Process

This section aims to obtain Ni-Mn-Sn-Cu-B alloy ribbons through a suitable single-roller melt-spinning process, and then obtain grains that penetrate the thickness direction of the ribbons through a suitable heat treatment process, thereby reducing the number of grain boundaries, lowering phase transition resistance, and reducing phase transition hysteresis. Using this textured material with structural anisotropy, the study will investigate the anisotropy in its magnetic and magnetocaloric properties.

Therefore, it is necessary to systematically investigate the evolution of grain during heat treatment and discuss the most suitable heat treatment process. The single-roller melt-spinning method is a rapid quenching technique, which introduces significant internal stresses and numerous crystalline defects in the as-spun alloy ribbons. These internal stresses and defects can increase the thermal hysteresis and magnetic hysteresis of the ribbons[215]. The rapid quenching process causes the metal droplets to solidify extremely quickly during ribbon fabrication, preventing many atoms (such as Mn and Sn atoms) from occupying their correct lattice sites. As a result, the atomic ordering degree (AOD) of the alloy ribbons is relatively low. A higher AOD value can effectively enhance the magnetization of the austenite phase[200, 154].

Based on the comprehensive analysis above, the as-spun ribbons require

suitable heat treatment processes to fulfill the following requirements: (1) releasing internal stresses, (2) reducing crystalline defects, (3) enabling sufficient atomic diffusion to allow atoms to reoccupy their proper positions in the solid solution lattice, and (4) adjusting grain size. These four requirements are addressed through two separate heat treatment processes: an annealing treatment is employed to optimize the crystal structure of the ribbons, while a grain growth heat treatment is applied to regulate the grain size of the ribbons.

To facilitate sufficient atomic diffusion, the as-spun alloy ribbons were maintained at 973 K for 2 hours. Subsequently, to release internal stresses, the alloy ribbons were further held at 773 K for 24 hours. These two heat treatment steps constitute the annealing process. Fig. 5-24 shows the room-temperature XRD patterns of Ni-Mn-Sn-Cu-B ribbons in both as-spun state and after the annealing treatment. AOD can be qualitatively evaluated by the relative diffraction intensity ratio $I(111)/I(220)$, where (111) is the most characteristic peak of the $L2_1$ phase and (220) is its strongest diffraction peak[216-218]. The results show that the as-spun ribbons exhibit a relatively low AOD value of 0.027. After annealing process, the AOD value increases to 0.08, demonstrating that the annealing process effectively enhances the AOD of the alloy ribbons.

To reduce grain boundary quantity and decrease phase transition hysteresis, a series of grain growth heat treatment processes were designed. The Ni-Mn-Sn-Cu-B ribbons were placed in quartz tubes under high-purity argon protective atmosphere and maintained at 1173 K for 10 min, 30 min, and 60 min respectively to facilitate grain growth. Following each grain growth heat treatment, an annealing process was performed to enhance AOD, with the results shown in Fig. 5-25. All ribbon samples exhibited similar thicknesses of approximately 20 μm. Fig. 5-25(a)

displays the grain morphology of as-spun ribbons, where grains with diameters around 4 μm were distributed along the ribbon growth direction with varied shapes. After 10 min of grain growth heat treatment, Fig. 5-25(b) reveals effective grain growth, with columnar crystals expanding laterally to about 6 μm while maintaining three to four layers along the ribbon thickness direction.

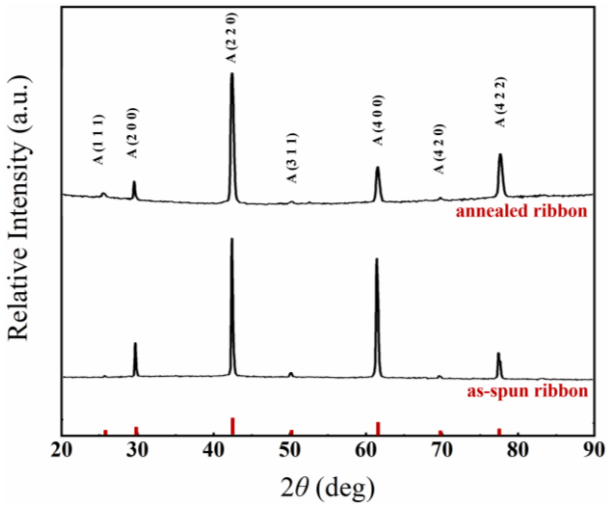

Fig. 5-24 X-ray diffraction patterns for the as-spun and annealed Ni-Mn-Sn-Cu-B ribbon

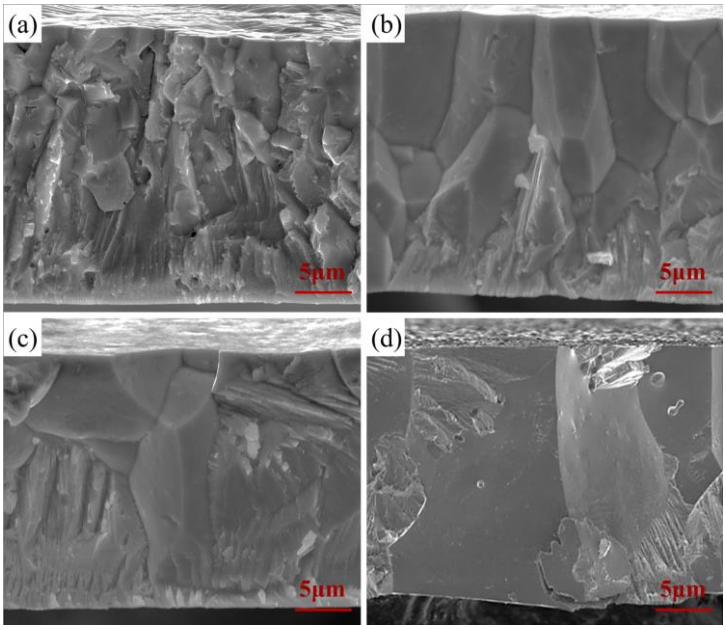

Fig. 5-25 SEM image of fracture surfaces

(a) as-spun; (b) 10 min annealed; (c) 30 min annealed; (d) 60 min annealed

When the holding time reached 30 minutes, the columnar grains further grew to an average diameter of approximately 10 μm while also extending longitudinally.

Consequently, only two layers of grains remained along the thickness direction of the ribbon, as shown in Fig. 5-25(c). After undergoing a 60-minute heat treatment, the ribbon's grains ultimately grew to an average diameter of 15 μm, with single grains completely spanning the entire thickness of the ribbon, as illustrated in Fig. 5-25(d). For the ribbons subjected to grain growth heat treatment, the grain size exhibited significant expansion in both diameter and length dimensions with increasing holding time.

5.5.1.3 Effect of Heat Treatment on the Martensitic Transformation Characteristics of Ribbons

The DSC curves of $(Ni_{47}Mn_{38}Sn_{12}Cu_3)_{99.4}B_{0.6}$ ribbons were measured and are presented in Fig. 5-26. It can be observed that compared to the polycrystalline bulk $(Ni_{47}Mn_{38}Sn_{12}Cu_3)_{99.4}B_{0.6}$ alloy, the characteristic martensitic transformation temperatures of the ribbons decreases. This phenomenon may be related to structural defects generated during the rapid cooling formation process of the ribbons[219, 160]. Fig. 5-26 also reveals that after the bulk alloy is fabricated into ribbons, the corresponding $T_C^A - T_A$ value increases, and the sensitivity parameter of the martensitic transformation temperature to magnetic fields also rises[220]. However, both the transformation hysteresis and the phase transition interval remain essentially the same for the two forms.

From the DSC curves, it is evident that the latent heat of transformation in the ribbons is reduced compared to that of the bulk alloy. This reduction is partly due to the relatively large difference between the Curie temperature and the reverse martensitic transformation peak temperature in the ribbons. The role of latent heat should be considered dialectically: on one hand, lower latent heat facilitates a larger $dT/\mu_0 dH$ in the ribbons[221]; on the other hand, it may constrain the theoretical

magnetic entropy change of the alloy[222]. The hysteresis of ribbon is also affected by heat treatment. From Fig. 5-26, it can be calculated that the hysteresis ΔT_{hys} of the heat-treated ribbon decreases from 26.3 K to 18.1 K.

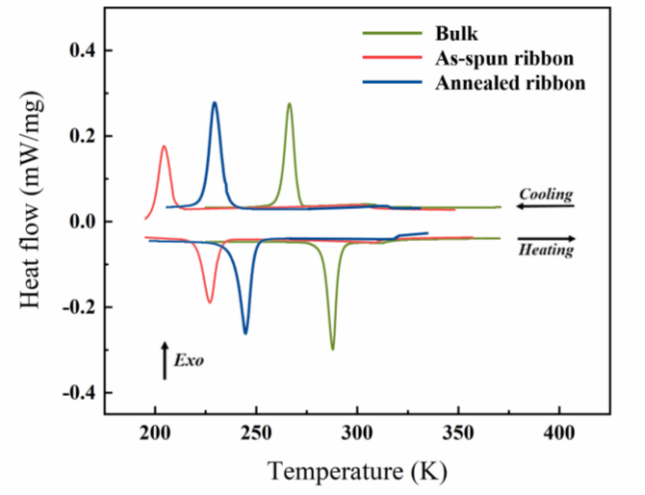

Fig. 5-26 DSC curves of the as-spun ribbon, annealed ribbon and bulk alloy

5.5.2 Magnetic Properties and Magnetocaloric Properties of Ni-Mn-Sn-Cu-B Ribbons

5.5.2.1 Anisotropic Magnetic Properties of Ni-Mn-Sn-Cu-B Ribbons

With the continuous development of magnetocaloric effect-driven magnetic refrigeration technology, research focus has shifted to exploring alloy systems that exhibit significant magnetocaloric within their phase transition temperature ranges. This trend has led to a core challenge for variable-field magnetic refrigeration technology: how to efficiently place and remove magnetocaloric materials from magnetic field. In 2010, Nikitin et al.[223] reported that $NdCo_5$ single crystals exhibit magnetization vector rotation, resulting in anisotropic magnetocaloric effects. Generally, structural anisotropy leads to functional anisotropy. The $(Ni_{47}Mn_{38}Sn_{12}Cu_3)_{99.4}B_{0.6}$ ribbons discussed in the previous section, after undergoing heat treatment, possess strong textures and are therefore expected to demonstrate significant magnetic anisotropy.

To study the magnetic anisotropic behaviors of $(Ni_{47}Mn_{38}Sn_{12}Cu_3)_{99.4}B_{0.6}$ ribbon, magnetic fields of different intensities were set in two directions parallel and perpendicular to the grain growth direction of the ribbon, and a series of *M-T* curves were obtained. The results are shown in Fig.5-27.

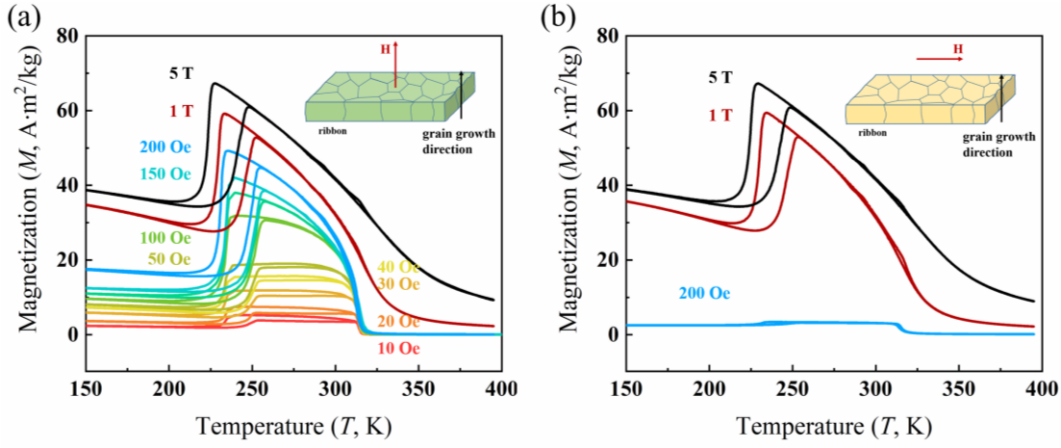

Fig. 5-27 Magnetization vs temperature at different magnetic field

(a) the parallel samples; (b) the perpendicular samples

It is worth noting that the ribbon exhibits significant differences in magnetization under low-intensity magnetic fields, especially within 200 Oe, showing significant anisotropy, as shown in Fig. 5-27(a) and (b). However, when the magnetic field strength was increased to 1 T or even 5 T, the differences in the *M-T* curves obtained under different field orientations became negligible. The ribbon exhibited a slightly higher ΔM under a parallel magnetic field, whereas the difference in magnetization of the paramagnetic martensite phase was insignificant. By calibrating the characteristic phase transition temperatures, it was observed that the martensitic transformation temperatures under the parallel magnetic field were marginally lower (by approximately 2 K).

As is well known, an external magnetic field tends to transform paramagnetic martensite into ferromagnetic austenite[13]. Therefore, the strong magnetic anisotropy exhibited by ribbons under low magnetic fields is closely related to the

phase transition fraction of ferromagnetic austenite undergoing phase transition. That is to say, for a given external magnetic field, ferromagnetic austenite is more likely to form in parallel samples. The driving force for this phase transition increases, resulting in a higher transformation fraction of austenite than that of perpendicular samples. However, when the magnetic field rises above 1 T, the martensitic transformation is almost complete, as shown in Fig. 5-28(a), and the difference in total magnetization change (ΔM) between austenite and martensite is relatively small.

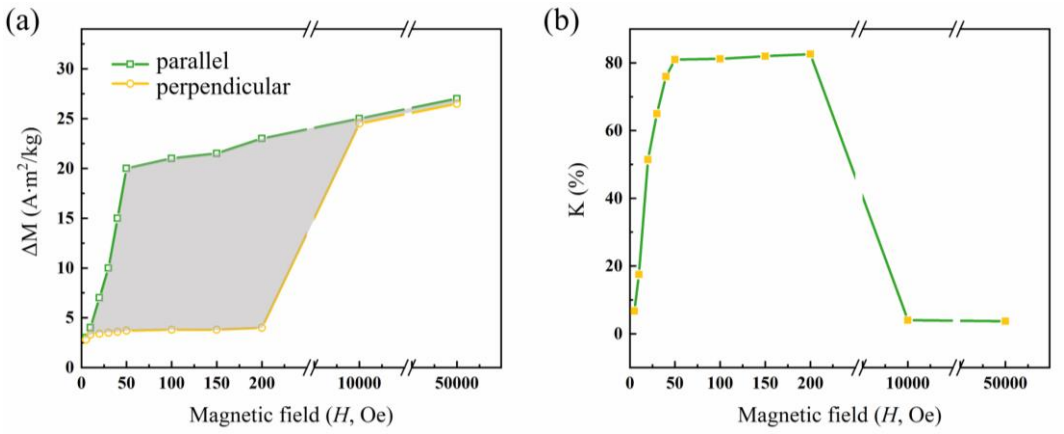

Fig. 5-28 The magnetization difference between the two phases and the corresponding ratio during phase transition for different directions

(a) ΔM-H curves; (b) K-H curves

As aforementioned, the driving force for magnetically induced martensitic transformation in Ni-Mn-X (X=In, Sn, Sb, Al) magnetic alloy comes from the Zeeman energy between austenite and martensite, and the value of Zeeman energy depends on the total magnetization change between the austenite and martensite phases. Therefore, the enhancement of the phase transition driving force of a parallel sample can be quantified by the relative ratio (K)[224]:

$$K=\frac{\Delta M_{\text{para}}-\Delta M_{\text{perp}}}{\Delta M_{\text{para}}}\times 100\% \tag{6.1}$$

where ΔM_{Para} and ΔM_{Perp} represent the total magnetization change during the MIMT

for the parallel and perpendicular samples, respectively.

These results show that in a considerably low magnetic field of 20 Oe, the value of *K* reaches over 50%, and reaches its maximum value of 80% at around 50 Oe to 200 Oe, as shown in Fig. 5-28(d). For practical applications, the magnetic anisotropy under low magnetic fields is of great significance for the practical application of ribbons in the refrigeration field, as it provides greater driving force for MIMT and requires less energy.

5.5.2.2 Anisotropic Magnetocaloric Properties of Ni-Mn-Sn-Cu-B Ribbons

To study $(Ni_{47}Mn_{38}Sn_{12}Cu_3)_{99.4}B_{0.6}$ ribbons' MCE properties under different directions of magnetic fields, the Loop method was used to measure the isothermal magnetization curves in the temperature range of 225−250 K, as shown in Fig. 5-29. For the *M-H* curve in the low field range (referring to the magnetic field range of 0−0.02 T), at each test temperature, the magnetization of the parallel sample increases rapidly with the increase of the magnetic field, and the magnetization is more likely to reach saturation. In the perpendicular sample, the magnetization reaches saturation around 0.5T.

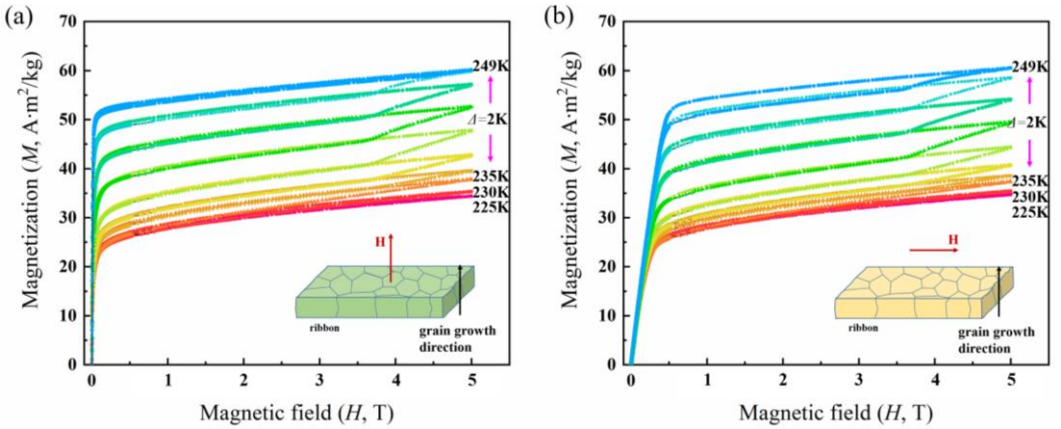

Fig. 5-29 *M-H* curves of $(Ni_{47}Mn_{38}Sn_{12}Cu_3)_{99.4}B_{0.6}$ ribbon under 5 T
(a) parallel direction; (b) perpendicular direction

Under high magnetic fields, the magnetization in both directions show no

significant difference. This further demonstrates that textured ribbons exhibit substantial magnetic anisotropy under low magnetic fields. The magnetic entropy change (ΔS_m-T) relationships under parallel and perpendicular magnetic fields were calculated separately from the magnetization curves, as shown in Fig. 5-30.

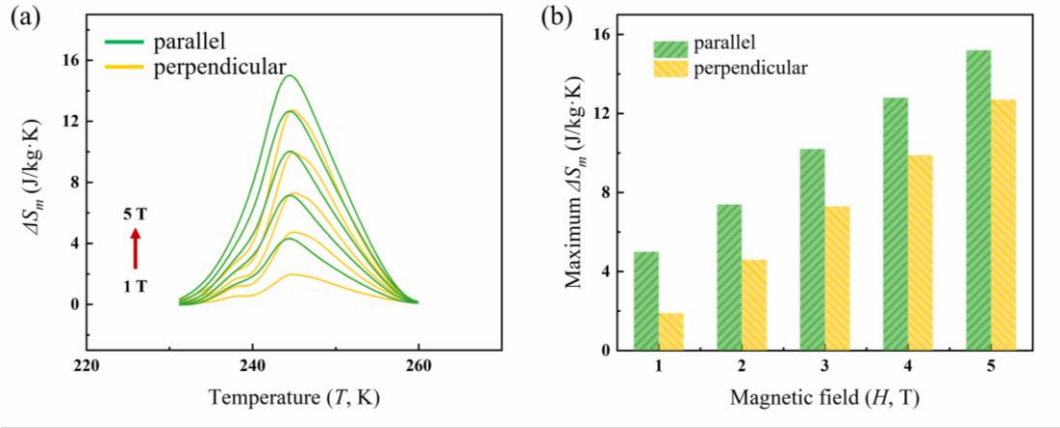

Fig. 5-30 Entropy changes of $(Ni_{47}Mn_{38}Sn_{12}Cu_3)_{99.4}B_{0.6}$ ribbon
(a) ΔS_m-T curves of $(Ni_{47}Mn_{38}Sn_{12}Cu_3)_{99.4}B_{0.6}$ ribbon for different directions; (b) maximum values of magnetic entropy change in different magnetic fields

Within the magnetic field variation range of 0−5 T, the maximum ΔS_m of the ribbon parallel to the magnetic field direction reaches 15.2 J/kg·K. Even under a magnetic field of only 2 T, ΔS_m attains 7.6 J/kg·K, which demonstrates advantages compared to the reported textured $Ni_{40}Mn_{50}In_{10}$ ribbons (ΔS_m=3.6 J/kg·K at 3 T) and $Ni_{45}Co_5Mn_{37.5}In_{12.5}$ single crystals (ΔS_m=6.3 J/kg·K at 2 T and 17.8 J/kg·K at 5 T) [225, 113]. This enhancement is attributed to the texture orientation being close to the easy magnetization axis. *RC* and *RCP* of the ribbons under different magnetic field directions were compared, with the calculation results summarized in Fig.5-31.

Within the applied magnetic field range of 0−5 T, the ribbons demonstrated *RC* values of 143 J/kg and 119 J/kg under parallel and perpendicular magnetic fields respectively, while achieving *RCP* values of 187 J/kg and 156 J/kg under the

corresponding field orientations. Comprehensive analysis reveals that the $(Ni_{47}Mn_{38}Sn_{12}Cu_3)_{99.4}B_{0.6}$ ribbons exhibit significant magnetic anisotropy in terms of magnetization, magnetic entropy change values, and refrigeration capacity. Notably, the ribbons display superior magnetocaloric performance when the magnetic field is aligned parallel to the texture direction.

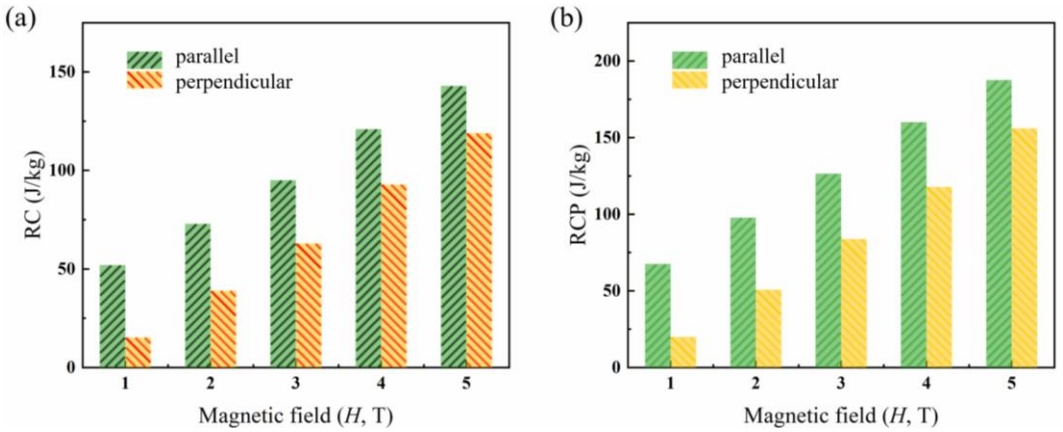

Fig. 5-31 Comparison of MCE in $(Ni_{47}Mn_{38}Sn_{12}Cu_3)_{99.4}B_{0.6}$ ribbon for different directions (a) *RC*; (b) *RCP*

5.6 Summary

By adjusting the B doping ratio based on the $Ni_{47}Mn_{38}Sn_{12}Cu_3$ alloy, we designed and prepared $(Ni_{47}Mn_{38}Sn_{12}Cu_3)_{100-z}B_z$ (z=0, 0.2, 0.4, 0.6) alloys. The effects of B alloying on martensitic transformation and the stability of the elastocaloric effect were systematically investigated, along with the refrigeration performance under multi-field regulation. Additionally, $(Ni_{47}Mn_{38}Sn_{12}Cu_3)_{99.4}B_{0.6}$ alloy ribbons were prepared using the single-roller melt-spinning method to study their magnetocaloric effects under different orientations. The main conclusions are as follows:

(1) Microalloying with B effectively suppressed intergranular fracture in the alloy. The $(Ni_{47}Mn_{38}Sn_{12}Cu_3)_{99.4}B_{0.6}$ alloy exhibited compressive fracture strength and strain of 1233 MPa and 7.4%, respectively. The martensitic transformation of

$(Ni_{47}Mn_{38}Sn_{12}Cu_3)_{99.4}B_{0.6}$ alloy demonstrated cycling stability over 500 thermal cycles (heating-cooling), 10^5 magnetic cycles, and 200 rapid adiabatic loading-unloading cycles.

(2) By utilizing the magnetocaloric effect below the alloy's M_s temperature, the refrigeration effect co-regulated by magnetic field and uniaxial stress between M_s and A_f temperatures, and the elastocaloric effect above A_f temperature, the working temperature range of $(Ni_{47}Mn_{38}Sn_{12}Cu_3)_{99.4}B_{0.6}$ alloy for refrigeration is 260–336 K.

(3) Under hydrostatic pressure, the magnetic entropy changes of $(Ni_{47}Mn_{38}Sn_{12}Cu_3)_{99.4}B_{0.6}$ alloy remained nearly unchanged, but the working temperature window for the caloric effect broadened. Under the combined action of a 3 T magnetic field and 10 kbar hydrostatic pressure, the refrigeration capacity reached 100.2 J/kg, representing a 22% increase compared to 0 kbar conditions.

(4) The heat-treated $(Ni_{47}Mn_{38}Sn_{12}Cu_3)_{99.4}B_{0.6}$ ribbon achieved saturation under a low magnetic field (0.02 T) parallel to the grain growth direction. The ΔS_m values reached 7.6 J/kg·K at 2 T and 15.2 J/kg·K at 5 T. The *RC* values obtained under magnetic fields parallel and perpendicular to the grain growth direction were 143 J/kg and 119 J/kg, respectively, while the *RCP* values were 187 J/kg and 156 J/kg, respectively.

Chapter 6 Conclusions and Future Work

6.1 Conclusions

Taking Ni-Mn-Sn magnetic alloys as the research object, we systematically investigated the crystal structure, magneto-structural transition, magnetic properties, and electronic structure of $Ni_{50}Mn_{37.5}Sn_{12.5}$ alloys doped with Fe and Cu elements using first-principles calculations, along with the effects of B doping on mechanical properties. Through a combined approach of theoretical computation and experimental verification, we studied the regulation of magneto-structural transition parameters, addressed the brittleness issue of the alloys, and improved stress cycling stability. The caloric effects were optimized through multi-field regulation, and the mechanisms for the influence of reversible components on caloric effects during martensitic transformation was revealed. The main conclusions are as follows:

(1) First-principles calculations reveal that in $Ni_{50}Mn_{37.5}Sn_{12.5}$ alloy, doped Fe or Cu atoms preferentially occupy the sublattice sites of Ni atoms. The energy difference between the austenite phase and non-modulated martensite phase gradually decreases with Fe or Cu doping, leading to a corresponding reduction in martensitic transformation temperature. When Fe doping exceeds 6 at.%, phase transition becomes difficult to occur. Fe doping can also enhance the phase stability and magnetic properties of the alloy. B atoms are most likely to occupy the O−I octahedral interstitial sites. B doping enhances the alloy's incompressibility, fracture resistance, and ability to resist shear deformation, but the alloy's magnetism remains insensitive to B doping.

(2) The study on $Ni_{50-y}Mn_{38}Sn_{12}Fe_y$ (y=0, 1, 2, 3, 4, 5) alloys demonstrates

that with increasing Fe content, the secondary phase content increases, the mechanical properties significantly improve, and the martensitic transformation temperature gradually decreases. Fe doping enables magneto-structural coupled regulation in the alloys, following a linear relationship fitted as $T_{A(y)}$=347−31.36y. Fe doping enables magneto-structural coupled regulation in the alloys. A complete magneto-structural coupling can be achieved within the Fe content range of 1.7–4.5 at.%. The $Ni_{47}Mn_{38}Sn_{12}Fe_3$ alloy undergoes two-step phase transitions during heating: 10M→$L2_1$ and 10M→4O, followed by 4O→$L2_1$. This two-step reverse martensitic transformations result in two ΔS_m peaks at 259 K (15.2 J/kg·K) and 267 K (9 J/kg·K), respectively, with an operating temperature range of 255–268 K and a refrigeration capacity of 142.5 J/kg.

(3) From a thermodynamic perspective, the martensitic transformation process can be decomposed into reversible and nonreversible components. By employing modulated differential scanning calorimetry, which superimposes a small sinusoidal temperature variation on a constant heating rate, these two components can be separated. The nonreversible component originates from energy dissipation during the phase transition and affects transformation hysteresis, while the alloy's refrigeration performance is determined by the reversible component. This approach enables more accurate characterization of the adiabatic temperature change. Using this method, the predicted adiabatic temperature change for the 3 at.% Cu-doped alloy was found to be close to that (10.3 K) obtained through direct measurement.

(4) The study on $Ni_{50-x}Mn_{38}Sn_{12}Cu_x$ (x=0, 2, 3, 4, 5, 6) alloys reveals that Cu doping significantly refines the grain size of the alloys. Through solid solution strengthening, Cu doping markedly enhances the mechanical properties of Ni_{50-}

$_x$$Mn_{38}Sn_{12}Cu_x$ alloys, with both compressive strength and strain increased by more than 1.8 times as compared to the undoped alloy. Cu doping improves the stress cycling stability of the alloys, during rapid adiabatic loading-unloading cycles, the 3 at.% Cu-doped alloy maintains stable elastocaloric effects even after approximately 30 cycles. The $Ni_{48}Mn_{38}Sn_{12}Cu_2$ alloy achieves partial magneto-structural coupling, exhibiting a ΔS_m of 10.3 J/kg·K under a 5 T magnetic field. The $Ni_{47}Mn_{38}Sn_{12}Cu_3$ alloy attains complete magneto-structural coupling, demonstrating a ΔS_m of 21.2 J/kg·K at 5 T with an average hysteresis loss of only 45 J/kg and a relative cooling power of 108 J/kg.

(5) The study on $(Ni_{47}Mn_{38}Sn_{12}Cu_3)_{100-z}B_z$ (z=0, 0.2, 0.4, 0.6) alloys demonstrates that B doping leads to the precipitation of a small amount of secondary phase. When the B doping content reaches 0.6 at.%, the martensitic transformation temperature decreases by approximately 1 K. B effectively suppresses the intergranular fracture tendency of the alloy, with the strengthening mechanism primarily attributed to grain boundary strengthening as induced by microalloying. The $(Ni_{47}Mn_{38}Sn_{12}Cu_3)_{99.4}B_{0.6}$ alloy exhibits excellent cycling stability in its martensitic transformation during 500 thermal cycles, 10^5 magnetic cycles, and 200 rapid adiabatic loading-unloading cycles.

(6) The study on multi-field regulated refrigeration effects in $(Ni_{47}Mn_{38}Sn_{12}Cu_3)_{99.4}B_{0.6}$ alloy reveals that stress assistance can broaden the working temperature range of caloric effects. Below the M_s temperature of the alloy, magnetocaloric refrigeration is employed; between M_s and A_f temperatures, refrigeration is achieved through combined regulation by magnetic field and uniaxial stress; above A_f temperature, elastocaloric refrigeration is utilized. This approach enables the $(Ni_{47}Mn_{38}Sn_{12}Cu_3)_{99.4}B_{0.6}$ alloy to achieve large and

reversible caloric effects within a temperature range of 260−336 K. Under hydrostatic pressure coupling, the magnetic entropy change of the alloy remains unchanged while the refrigeration working temperature window expands. At H=3 T, the refrigeration capacity reaches 100.2 J/kg under 10 kbar pressure, representing a 20.8% increase compared to the value at 0 kbar.

(7) The optimal preparation parameters for $(Ni_{47}Mn_{38}Sn_{12}Cu_3)_{99.4}B_{0.6}$ ribbons were determined to be: heating power ~8 kW and copper wheel speed ~1800 rpm. In the as-spun state, the ribbons contained approximately 4−5 grains arranged along the growth direction, while after heat treatment the grains grew to span the entire thickness of the ribbon. The heat-treated ribbons achieved magnetization saturation under low magnetic fields (0.02 T), with ΔS_m reaching 7.6 J/kg·K at 2 T and peaking at 15.2 J/kg·K under 5 T magnetic field. The *RC* values were measured at 143 J/kg (parallel field) and 119 J/kg (perpendicular field), while the *RC* values reached 187 J/kg and 156 J/kg for parallel and perpendicular field orientations respectively.

6.2 Future Work

Based on the research work presented in this Thesis, several unresolved issues remain, which warrant further in-depth investigation:

(1) In the work of Chapter 5, we prepared $(Ni_{47}Mn_{38}Sn_{12}Cu_3)_{99.4}B_{0.6}$ ribbons with relatively large specific surface areas using the melt-spinning method and investigated their magnetocaloric properties. However, the elastocaloric and barocaloric properties of these ribbons still require thorough study. Developing ribbon materials with stable refrigeration performance not only holds significant scientific importance for deepening the understanding of phase transition mechanisms but also opens new pathways for the practical application of novel

solid-state refrigeration technologies.

(2) Building on the research findings of $(Ni_{47}Mn_{38}Sn_{12}Cu_3)_{99.4}B_{0.6}$ ribbons, subsequent studies should focus on developing compatible miniature refrigeration devices. Among these efforts, achieving efficient heat exchange and optimizing system compactness are expected to emerge as two particularly valuable research directions.

References

[1] Kitanovski A, Plaznik U, Tomc U, et al. Present and future caloric refrigeration and heat-pump technologies[J]. International Journal of Refrigeration, 2015, 57: 288-298.

[2] Moya X, Kar-Narayan S, Mathur N D. Caloric materials near ferroic phase transitions[J]. Nat Mater, 2014, 13(5): 439-450.

[3] Tang X, Feng Y, Wang H, et al. Enhanced elastocaloric effect and cycle stability in B and Cu co-doping Ni-Mn-In polycrystals[J]. Applied Physics Letters, 2019, 114(3): 033901.

[4] Li D, Li Z, Yang J, et al. Large elastocaloric effect driven by stress-induced two-step structural transformation in a directionally solidified Ni55Mn18Ga27 alloy[J]. Scripta Materialia, 2019, 163: 116-120.

[5] Manosa L, Planes A. Materials with giant mechanocaloric effects: Cooling by strength[J]. Adv Mater, 2017, 29(11): 1603607.

[6] Bonnot E, Romero R, Manosa L, et al. Elastocaloric effect associated with the martensitic transition in shape-memory alloys[J]. Phys Rev Lett, 2008, 100(12): 125901.

[7] Zhao D, Liu J, Chen X, et al. Giant caloric effect of low-hysteresis metamagnetic shape memory alloys with exceptional cyclic functionality[J]. Acta Materialia, 2017, 133: 217-223.

[8] Trung N T, Ou Z Q, Gortenmulder T J, et al. Tunable thermal hysteresis in MnFe(P,Ge) compounds[J]. Applied Physics Letters, 2009, 94(10): 102513.

[9] Morellon L, Arnold Z, Magen C, et al. Pressure enhancement of the giant magnetocaloric effect inTb5Si2Ge2[J]. Physical Review Letters, 2004,

93(13): 137201.

[10] de Oliveira N A. Barocaloric effect and the pressure induced solid state refrigerator[J]. Journal of Applied Physics, 2011, 109(5): 053515.

[11] He X, Wei S, Kang Y, et al. Enhanced barocaloric effect produced by hydrostatic pressure-induced martensitic transformation for Ni44.6Co5.5Mn35.5In14.4 Heusler alloy[J]. Scripta Materialia, 2018, 145: 58-61.

[12] Moya X, Stern-Taulats E, Crossley S, et al. Giant electrocaloric strength in single-crystal BaTiO3[J]. Advanced Materials, 2013, 25(9): 1360-1365.

[13] Liu J, Gottschall T, Skokov K P, et al. Giant magnetocaloric effect driven by structural transitions[J]. Nat Mater, 2012, 11(7): 620-626.

[14] Neese B, Chu B, Lu S G, et al. Large electrocaloric effect in ferroelectric polymers near room temperature[J]. Science, 2008, 321(5890): 821-823.

[15] Reis M S. Magnetocaloric and barocaloric effects of metal complexes for solid state cooling: Review, trends and perspectives[J]. Coordination Chemistry Reviews, 2020, 417: 213357.

[16] Qu Y H, Cong D Y, Li S H, et al. Simultaneously achieved large reversible elastocaloric and magnetocaloric effects and their coupling in a magnetic shape memory alloy[J]. Acta Materialia, 2018, 151: 41-55.

[17] Fujita A, Fujieda S, Hasegawa Y, et al. Itinerant-electron metamagnetic transition and large magnetocaloric effects in La(FexSi1-x)13compounds and their hydrides[J]. Physical Review B, 2003, 67(10): 104416.

[18] Chen X, Chen Y, Tang Y. The effect of high-temperature annealing on LaFe11.5Si1.5 and the magnetocaloric properties of La1-xCexFe11.5Si1.5 compounds[J]. Rare Metals, 2011, 30(4): 343-347.

[19] Pecharsky V K, K. A. Gschneidner J. Giant magnetocaloric effect in Gd-5(Si2Ge2)[J]. Physical Review Letters, 1997, 78(23): 4494-4497.

[20] Arreguín-Hernández M L, Sánchez-Valdés C F, Llamazares J L S, et al. Magnetoelastic transition and magnetocaloric effect in induction melted Fe100-xRhx bulk alloys with x=50, 51[J]. Journal of Alloys and Compounds, 2021, 871: 159586.

[21] Krenke T, Duman E, Acet M, et al. Inverse magnetocaloric effect in ferromagnetic Ni-Mn-Sn alloys[J]. Nat Mater, 2005, 4(6): 450-454.

[22] Qian M, Zhang X, Wei L, et al. Tunable magnetocaloric effect in Ni-Mn-Ga microwires[J]. Sci Rep, 2018, 8(1): 16574.

[23] Zhang R, Zhang X, Qian M, et al. Effect of Co-doping on the microstructure, martensitic transformation behavior, and magnetocaloric effect of Ni-Mn-Sb-Si ferromagnetic shape memory alloys[J]. Metallurgical and Materials Transactions A, 2018, 49(12): 6416-6425.

[24] Imran M, Zhang X. Recent developments on the cyclic stability in elastocaloric materials[J]. Materials & Design, 2020, 195: 109030.

[25] Xiao F, Fukuda T, Kakeshita T. Inverse elastocaloric effect in a Ti-Ni alloy containing aligned coherent particles of Ti3Ni4[J]. Scripta Materialia, 2016, 124: 133-137.

[26] Bechtold C, Chluba C, Lima de Miranda R, et al. High cyclic stability of the elastocaloric effect in sputtered TiNiCu shape memory films[J]. Applied Physics Letters, 2012, 101(9): 091903.

[27] Mañosa L, Jarque-Farnos S, Vives E, et al. Large temperature span and giant refrigerant capacity in elastocaloric Cu-Zn-Al shape memory alloys[J]. Applied Physics Letters, 2013, 103(21): 211904.

[28] Xiao F, Fukuda T, Kakeshita T. Significant elastocaloric effect in a Fe-31.2Pd (at. %) single crystal[J]. Applied Physics Letters, 2013, 102(16): 161914.

[29] Xiao F, Jin M, Liu J, et al. Elastocaloric effect in Ni50Fe19Ga27Co4 single crystals[J]. Acta Materialia, 2015, 96: 292-300.

[30] Pataky G J, Ertekin E, Sehitoglu H. Elastocaloric cooling potential of NiTi, Ni2FeGa, and CoNiAl[J]. Acta Materialia, 2015, 96: 420-427.

[31] Lu B, Xiao F, Yan A, et al. Elastocaloric effect in a textured polycrystalline Ni-Mn-In-Co metamagnetic shape memory alloy[J]. Applied Physics Letters, 2014, 105(16): 161905.

[32] Zhao D, Liu J, Feng Y, et al. Giant elastocaloric effect and its irreversibility in [001]-oriented Ni45Mn36.5In13.5Co5 metamagnetic shape memory alloys[J]. Applied Physics Letters, 2017, 110(2): 021906.

[33] Huang Y J, Hu Q D, Bruno N M, et al. Giant elastocaloric effect in directionally solidified Ni-Mn-In magnetic shape memory alloy[J]. Scripta Materialia, 2015, 105: 42-45.

[34] Sun W, Liu J, Lu B, et al. Large elastocaloric effect at small transformation strain in Ni45Mn44Sn11 metamagnetic shape memory alloys[J]. Scripta Materialia, 2016, 114: 1-4.

[35] Guillou F, Porcari G, Yibole H, et al. Taming the first-order transition in giant magnetocaloric materials[J]. Adv Mater, 2014, 26(17): 2671-2675.

[36] Yan H, Wang L, Liu H, et al. Giant elastocaloric effect and exceptional mechanical properties in an all-d-metal Ni-Mn-Ti alloy: Experimental and ab-initio studies[J]. Materials & Design, 2019, 184: 108180.

[37] Huang X, Wang L, Liu H, et al. Correlation between microstructure and

martensitic transformation, mechanical properties and elastocaloric effect in Ni-Mn-based alloys[J]. Intermetallics, 2019, 113: 106579.

[38] Yan H, Zhao Y, Liu H, et al. Ab-initio revelation on the origins of Ti substitution for Ga, Mn and Ni on ferromagnetism, phase stability and elastic properties in Ni2MnGa[J]. Journal of Alloys and Compounds, 2020, 821: 153481.

[39] Chluba C, Ge W, Miranda R L d, et al. Ultralow-fatigue shape memory alloy films[J]. Science, 2015, 348(6238): 4.

[40] Graf T, Felser C, Parkin S S P. Simple rules for the understanding of Heusler compounds[J]. Progress in Solid State Chemistry, 2011, 39(1): 1-50.

[41] Sutou Y, Imano Y, Koeda N, et al. Magnetic and martensitic transformations of NiMnX (X=In,Sn,Sb) ferromagnetic shape memory alloys[J]. Applied Physics Letters, 2004, 85(19): 4358-4360.

[42] Liang X, Jiang X, Gu J, et al. 5M and 7M martensitic stability and associated physical properties in Ni50Mn35In15 alloy: first-principles calculations and experimental verification[J]. Scripta Materialia, 2021, 204: 114140.

[43] Krenke T, Acet M, Wassermann E F, et al. Martensitic transitions and the nature of ferromagnetism in the austenitic and martensitic states of Ni-Mn-Sn alloys[J]. Physical Review B, 2005, 72(1): 014412.

[44] Stager C V, CAMPBELL C C M. Antiferromagnetic order in the Heusler alloy, Ni2Mn(MnxSn1-x)[J]. Canadian Journal of Physics, 1978, 56: 674.

[45] Yan H, Huang X, Esling C. Recent progress in crystallographic characterization, magnetoresponsive and elastocaloric effects of Ni-Mn-In-Based Heusler alloys—A review[J]. Frontiers in Materials, 2022, 9: 812984.

[46] Li Y, Sun W, Zhao D, et al. An 8 K elastocaloric temperature change induced

by 1.3% transformation strain in Ni44Mn45-xSn11Cux alloys[J]. Scripta Materialia, 2017, 130: 278-282.

[47] Pecharsky V K, Gschneidner K A. Giant magnetocaloric effect in Gd5(Si2Ge2)[J]. Phys Rev Lett, 1997, 78: 4494-4497.

[48] Manosa L, Gonzalez-Alonso D, Planes A, et al. Giant solid-state barocaloric effect in the Ni-Mn-In magnetic shape-memory alloy[J]. Nat Mater, 2010, 9(6): 478-481.

[49] Fähler S. Caloric effects in ferroic materials: New concepts for cooling[J]. Energy Technology, 2018, 6(8): 1394-1396.

[50] Franco V, Blázquez J S, Ingale B, et al. The magnetocaloric effect and magnetic refrigeration near room temperature: Materials and models[J]. Annual Review of Materials Research, 2012, 42(1): 305-342.

[51] Stern-Taulats E, Castán T, Mañosa L, et al. Multicaloric materials and effects[J]. MRS Bulletin, 2018, 43(4): 295-299.

[52] Ossmer H, Wendler F, Gueltig M, et al. Energy-efficient miniature-scale heat pumping based on shape memory alloys[J]. Smart Materials and Structures, 2016, 25(8): 085037.

[53] Pataky G J, Ertekin E, Sehitoglu H. Infrared thermography videos of the elastocaloric effect for shape memory alloys NiTi and Ni2FeGa[J]. Data Brief, 2015, 5: 7-8.

[54] Dan N H, Duc N H, Yen N H, et al. Magnetic properties and magnetocaloric effect in Ni-Mn-Sn alloys[J]. Journal of Magnetism and Magnetic Materials, 2015, 374: 372-375.

[55] Bachaga T, Zhang J, Khitouni M, et al. NiMn-based Heusler magnetic shape memory alloys: a review[J]. The International Journal of Advanced

Manufacturing Technology, 2019, 103(5-8): 2761-2772.

[56] Zou J D, Shen B G, Gao B, et al. The magnetocaloric effect of LaFe11.6Si1.4, La0.8Nd0.2Fe11.5Si1.5, and Ni43Mn46Sn11 compounds in the vicinity of the first-order phase transition[J]. Advanced Materials, 2009, 21(6): 693-696.

[57] Aguilar-Ortiz C O, Camarillo-García J P, Vergara J, et al. Effect of solidification rate on martensitic transformation behavior and adiabatic magnetocaloric effect of Ni50Mn35In15 ribbons[J]. Journal of Alloys and Compounds, 2018, 748: 464-472.

[58] Xu Z. Classifacation of the martensitic transformations[J]. Acta Metall Sin, 1997, 01: 45-53.

[59] M. Reading, A. Luget, Wilson R. Modulated differential scanning calorimetry[J]. Thermochimica Acta, 1994, 238: 295-307.

[60] Qiu Z, Ikehara T, Nishi T. Melting behaviour of poly(butylene succinate) in miscible blends with poly(ethylene oxide)[J]. Polymer, 2003, 44(10): 3095-3099.

[61] Andrzej Orzeszko, Sikorski A. Reactivity of polyamic acids in thermal cyclization[J]. European Polymer Journal, 1993, 29(4): 593-596.

[62] W Chen, I.-K Moon, Wunderlich B. Study of crystallization kinetics by temperature-modulated DSC[J]. Polymer, 2000, 41(11): 4119-4125.

[63] B.B Sauer, W.G Kampert, E Neal Blanchard, et al. Temperature modulated DSC studies of melting and recrystallization in polymers exhibiting multiple endotherms[J]. Polymer, 2000, 41(3): 1099-1108.

[64] Els Verdonck, Ko Schaap, Thomas L C. A discussion of the principles and applications of Modulated Temperature DSC (MTDSC)[J]. International

Journal of Pharmaceutics, 1999, 192(1): 3-20.

[65] Xiao Hu, Christopher D. Breach, Young R J. Elucidation of the hard segment transition in a diacetylene-containing copolyurethane using modulated differential scanning calorimetry[J]. Polymer, 1997, 38(4): 981-983.

[66] Babita I, Patil S I, Ram S. First order structural transformation and inverse magnetocaloric effect in melt-spun Ni-Mn-Sn ribbons[J]. Journal of Physics D: Applied Physics, 2010, 43(20): 205002.

[67] Xuan H C, Zheng Y X, Ma S C, et al. The martensitic transformation, magnetocaloric effect, and magnetoresistance in high-Mn content Mn47+xNi43-xSn10 ferromagnetic shape memory alloys[J]. Journal of Applied Physics, 2010, 108(10): 103920.

[68] Xiao H B, Yang C P, Wang R L, et al. Effect of alloying element Al substitution on Ni-Mn-Sn shape memory alloy by first-principle calculations[J]. Journal of Applied Physics, 2012, 112(12): 123723.

[69] Tan C L, Huang Y W, Tian X H, et al. Origin of magnetic properties and martensitic transformation of Ni-Mn-In magnetic shape memory alloys[J]. Applied Physics Letters, 2012, 100(13): 132402.

[70] Roy T, Chakrabarti A. Possibility of martensite transition in Pt-Y-Ga (Y=Cr, Mn, and Fe) system: An ab-initio calculation of the bulk mechanical, electronic and magnetic properties[J]. Journal of Magnetism and Magnetic Materials, 2016, 401: 929-937.

[71] Xu X, Nagashima A, Nagasako M, et al. Martensitic transformation and phase diagram in ternary Co-V-Ga Heusler alloys[J]. Applied Physics Letters, 2017, 110(12): 121906.

[72] Ye M, Kimura A, Miura Y, et al. Role of electronic structure in the martensitic phase transition of Ni2Mn(1+x)Sn(1-x) studied by hard-X-ray photoelectron spectroscopy and Ab initio calculation[J]. Phys Rev Lett, 2010, 104(17): 176401.

[73] He W Q, Huang H B, Liu Z H, et al. First-principles investigation of magnetic properties and metamagnetic transition of NiCoMnZ (Z=In, Sn, Sb) Heusler alloys[J]. Intermetallics, 2017, 90: 140-146.

[74] Zhang Y, Liu J, Zheng Q, et al. Large magnetic entropy change and enhanced mechanical properties of Ni-Mn-Sn-C alloys[J]. Scripta Materialia, 2014, 75: 26-29.

[75] Krenke T, Acet M, Wassermann E F, et al. Ferromagnetism in the austenitic and martensitic states of Ni-Mn-In alloys[J]. Physical Review B, 2006, 73(17): 174413.

[76] Han Z D, Wang D H, Zhang C L, et al. Effect of lattice contraction on martensitic transformation and magnetocaloric effect in Ge doped Ni-Mn-Sn alloys[J]. Materials Science and Engineering: B, 2009, 157(1-3): 40-43.

[77] Khan M, Dubenko I, Stadler S, et al. Magnetic and structural phase transitions in Heusler type alloys Ni2MnGa1-xInx[J]. Journal of Physics: Condensed Matter, 2004, 16(29): 5259-5266.

[78] Chatterjee S, Giri S, De S K, et al. Kinetics of the field-induced resistivity jump inNi2Mn1.36Sn0.64-xGaxalloys[J]. Physical Review B, 2010, 81(21): 214441.

[79] Planes A, Mañosa L, Moya X, et al. Magnetocaloric effect in Heusler shape-memory alloys[J]. Journal of Magnetism and Magnetic Materials, 2007, 310(2): 2767-2769.

[80] Krenke T, Duman E, Acet M, et al. Effect of Co and Fe on the inverse magnetocaloric properties of Ni-Mn-Sn[J]. Journal of Applied Physics, 2007, 102(3): 033903.

[81] Wang D H, Zhang C L, Xuan H C, et al. The study of low-field positive and negative magnetic entropy changes in Ni43Mn46-xCuxSn11 alloys[J]. Journal of Applied Physics, 2007, 102(1): 013909.

[82] Khovaylo V V, Skokov K P, Gutfleisch O, et al. Peculiarities of the magnetocaloric properties in Ni-Mn-Sn ferromagnetic shape memory alloys[J]. Physical Review B, 2010, 81(21): 214406.

[83] Huang L, Cong D Y, Suo H L, et al. Giant magnetic refrigeration capacity near room temperature in Ni40Co10Mn40Sn10 multifunctional alloy[J]. Applied Physics Letters, 2014, 104(13): 132407.

[84] Jing C, Li Z, Zhang H L, et al. Martensitic transition and inverse magnetocaloric effect in Co doping Ni-Mn-Sn Heulser alloy[J]. The European Physical Journal B, 2009, 67(2): 193-196.

[85] Roy S, Blackburn E, Valvidares S M, et al. Delocalization and hybridization enhance the magnetocaloric effect in Cu-doped Ni2MnGa[J]. Physical Review B, 2009, 79(23): 235127.

[86] Gautam B R, Dubenko I, Mabon J C, et al. Effect of small changes in Mn concentration on phase transition temperatures and magnetic entropy variations in Ni2Mn0.75Cu0.25Ga Heusler alloys[J]. Journal of Alloys and Compounds, 2009, 472(1-2): 35-39.

[87] Wang J, Wang H, Jiang C. Microstructure and mechanical properties of a Ni30Cu20Mn41.5Ga8.5 dual-phase shape memory alloy[J]. Materials Science and Engineering: A, 2013, 578: 256-259.

[88] Feng X, Fang D, HWANG K. Mechanical and magnetostrictive properties of Fe-doped Ni52Mn24Ga24 single crystals[J]. Chinese Physics Letters, 2002, 19(10): 1547-1549.

[89] Cherechukin A A, Dikshtein I E, Ermakov D I, et al. Shape memory effect due to magnetic field-induced thermoelastic martensitic transformation in polycrystalline Ni-Mn-Fe-Ga alloy[J]. Physics Letters A, 2002, 291(2-3): 175-182.

[90] Wang H B, Chen F, Gao Z Y, et al. Effect of Fe content on fracture behavior of Ni-Mn-Fe-Ga ferromagnetic shape memory alloys[J]. Materials Science and Engineering: A, 2006, 438-440: 990-993.

[91] Feng Y, Sui J H, Gao Z Y, et al. Investigation on martensitic transformation behavior, microstructures and mechanical properties of Fe-doped Ni-Mn-In alloys[J]. Materials Science and Engineering: A, 2009, 507(1-2): 174-178.

[92] Nong N V, Tai L T, Huy N T, et al. Structural, magnetic and magnetocaloric properties of Heusler alloys Ni50Mn38Sb12 with boron addition[J]. Materials Science and Engineering: B, 2011, 176(16): 1322-1325.

[93] Prusik K, Matyja E, Zubko M, et al. Effect of the boron addition on the structure of the Ni-Mn-Co-in alloys[J]. Acta Physica Polonica A, 2016, 130(4): 1023-1025.

[94] Aydogdu Y, Turabi A S, Kok M, et al. Effects of the substitution of gallium with boron on the physical and mechanical properties of Ni-Mn-Ga shape memory alloys[J]. Applied Physics A, 2014, 117(4): 2073-2078.

[95] Zhang X, Liu Q, Zeng X, et al. Microstructure, mechanical properties and shape memory effect of Ni-Mn-Ga-B high-temperature shape memory alloy[J]. Intermetallics, 2016, 68: 113-117.

[96] Yang Z, Cong D, Yuan Y, et al. Ultrahigh cyclability of a large elastocaloric effect in multiferroic phase-transforming materials[J]. Materials Research Letters, 2019, 7(4): 137-144.

[97] Yang Z, Cong D Y, Sun X M, et al. Enhanced cyclability of elastocaloric effect in boron-microalloyed Ni-Mn-In magnetic shape memory alloys[J]. Acta Materialia, 2017, 127: 33-42.

[98] Czaja P, Chulist R, Tokarski T, et al. Superelastic behavior of a metamagnetic Ni-Mn-Sn single crystal[J]. Journal of Materials Science, 2018, 53(14): 10383-10395.

[99] Chernenko V A, Villa E, Salazar D, et al. Large tensile superelasticity from intermartensitic transformations in Ni49Mn28Ga23 single crystal[J]. Applied Physics Letters, 2016, 108(7): 071903.

[100] Wang J, Yu Q, Xu K, et al. Large room-temperature elastocaloric effect of Ni57Mn18Ga21In4 alloy undergoing a magnetostructural coupling transition[J]. Scripta Materialia, 2017, 130: 148-151.

[101] Dunand D C, Mullner P. Size effects on magnetic actuation in Ni-Mn-Ga shape-memory alloys[J]. Adv Mater, 2011, 23(2): 216-232.

[102] Ueland S M, Chen Y, Schuh C A. Oligocrystalline shape memory alloys[J]. Advanced Functional Materials, 2012, 22(10): 2094-2099.

[103] Zhukov A, Garcia C, Ilyn M, et al. Magnetic and transport properties of granular and Heusler-type glass-coated microwires[J]. Journal of Magnetism and Magnetic Materials, 2012, 324(21): 3558-3562.

[104] Zhukov A, Rodionova V, Ilyn M, et al. Magnetic properties and magnetocaloric effect in Heusler-type glass-coated NiMnGa microwires[J]. Journal of Alloys and Compounds, 2013, 575: 73-79.

[105] Zhukova V, Chernenko V, Ipatov M, et al. Magnetic properties of Heusler-type NiMnGa glass-coated microwires[J]. IEEE Transactions on Magnetics, 2015, 51(11): 1-4.

[106] Zhukova V, Ipatov M, Granovsky A, et al. Magnetic properties of Ni-Mn-In-Co Heusler-type glass-coated microwires[J]. Journal of Applied Physics, 2014, 115(17): 17A939.

[107] Zhukova V, Rodionova V, Fetisov L, et al. Magnetic properties of Heusler-type microwires and thin films[J]. IEEE Transactions on Magnetics, 2014, 50(11): 1-4.

[108] Zhang Y, Li M, Wang Y D, et al. Superelasticity and serration behavior in small-sized NiMnGa alloys[J]. Advanced Engineering Materials, 2014, 16(8): 955-960.

[109] Glock S, Zhang X X, Kucza N J, et al. Structural, physical and damping properties of melt-spun Ni-Mn-Ga wire-epoxy composites[J]. Composites Part A: Applied Science and Manufacturing, 2014, 63: 68-75.

[110] Ding Z, Zhu J, Zhang X, et al. 14% recoverable strain in Ni52.87Mn23.82Ga23.32 microwires[J]. Journal of Physics D: Applied Physics, 2017, 50(9): 095303.

[111] Li F Q, Qu Y H, Yan H L, et al. Giant tensile superelasticity originating from two-step phase transformation in a Ni-Mn-Sn-Fe magnetic microwire[J]. Applied Physics Letters, 2018, 113(11): 112402.

[112] Feng Y, Chen H, Gao L, et al. Effect of wheel speed and annealing temperature on microstructure and texture evolution of Ni45Mn36.6In13.4Co5 ribbon[J]. Materials Characterization, 2016, 122: 170-176.

[113] Hernando B, Sánchez Llamazares J L, Prida V M, et al. Magnetocaloric effect in preferentially textured Mn50Ni40In10 melt spun ribbons[J]. Applied Physics Letters, 2009, 94(22): 222502.

[114] Akkera H S, Singh I, Kaur D. Martensitic phase transformation of magnetron sputtered nanostructured Ni-Mn-In ferromagnetic shape memory alloy thin films[J]. Journal of Alloys and Compounds, 2015, 642: 53-62.

[115] Oliveira N A. Entropy change upon magnetic field and pressure variations[J]. Applied Physics Letters, 2007, 90(5): 052501.

[116] Planes A, Castán T, Saxena A. Thermodynamics of multicaloric effects in multiferroics[J]. Philosophical Magazine, 2014, 94(17): 1893-1908.

[117] Stern-Taulats E, Castán T, Planes A, et al. Giant multicaloric response of bulk Fe49Rh51[J]. Physical Review B, 2017, 95(10): 104424.

[118] Planes A, Castan T, Saxena A. Thermodynamics of multicaloric effects in multiferroic materials: application to metamagnetic shape-memory alloys and ferrotoroidics[J]. Philos Trans A Math Phys Eng Sci, 2016, 374(2074): 20150304.

[119] Kresse G, Furthmüller J. Efficiency of ab-initio total energy calculations for metals and semiconductors using a plane-wave basis set[J]. Computational Materials Science, 1996, 6(1): 15-50.

[120] Perdew J, Burke K, Ernzerhof M. Generalized gradient approximation made simple[J]. PHYSICAL REVIEW LETTERS, 1996, 77(18): 3865-3868.

[121] Kresse G, Furthmüller J. Efficient iterative schemes for ab initio total-energy calculations using a plane-wave basis set[J]. Physical Review B, 1996, 54(16): 11169-11186.

[122] Methfessel M, Paxton A T. High-precision sampling for Brillouin-zone

integration in metals[J]. Physical Review B, 1989, 40(6): 3616-3621.

[123] Wang X, Shang J, Wang F, et al. Effect of 3d transition elements substitution for Ni in Ni2Mn1+xSn1-x on the phase stability and magnetic properties: A first principle investigation[J]. Journal of Magnetism and Magnetic Materials, 2014, 368: 286-294.

[124] Kamarád J, Kaštil J, Friák M, et al. Effect of hydrostatic pressure on magneto-crystalline anisotropy of Heusler Ni2MnSn-based alloy[J]. High Pressure Research, 2021, 41(4): 405-413.

[125] Yan H, Zhang Y, Xu N, et al. Crystal structure determination of incommensurate modulated martensite in Ni-Mn-In Heusler alloys[J]. Acta Materialia, 2015, 88: 375-388.

[126] Yan H, Liu H, Zhao Y, et al. Impact of B alloying on ductility and phase transition in the Ni-Mn-based magnetic shape memory alloys: Insights from first-principles calculation[J]. Journal of Materials Science & Technology, 2021, 74: 27-34.

[127] Sokolovskiy V V, Buchelnikov V D, Zagrebin M A, et al. First-principles investigation of chemical and structural disorder in magnetic Ni2Mn1+xSn1-xHeusler alloys[J]. Physical Review B, 2012, 86(13): 134418.

[128] Sokolovskiy V, Zagrebin M, Buchelnikov V D. First-principles study of Ni-Co-Mn-Sn alloys with regular and inverse Heusler structure[J]. Journal of Magnetism and Magnetic Materials, 2019, 476: 546-550.

[129] Wu S K, Yang S T. Effect of composition on transformation temperatures of Ni-Mn-Ga shape memory alloys[J]. Materials Letters, 2003, 57(26-27): 4291-4296.

[130] Gruner M E, Fähler S, Entel P. Magnetoelastic coupling and the formation of adaptive martensite in magnetic shape memory alloys[J]. physica status solidi (b), 2014, 251(10): 2067-2079.

[131] Wang X, Shang J, Wang F, et al. The structural stability and magnetic properties of the ferromagnetic Heusler alloy Ni-Mn-Sn: A first principle investigation[J]. Journal of Magnetism and Magnetic Materials, 2014, 355: 173-179.

[132] Moriya T. Recent progress in the theory of itinerant electron magnetism[J]. Journal of Magnetism and Magnetic Materials, 1979, 14(1): 1-46.

[133] Sato K, Dederics P, Katayama-Yoshida H. Curie temperatures of III–V diluted magnetic semiconductors calculated from first principles[J]. Europhysics Letters, 2003, 61(3): 403-408.

[134] Wang X, Shang J, Wang F, et al. Origin of unusual properties in the ferromagnetic Heusler alloy Ni-Mn-Sn: A first-principles investigation[J]. Scripta Materialia, 2014, 89: 33-36.

[135] Li C, Luo H, Hu Q, et al. First-principles investigation of the composition dependent properties of Ni2+xMn1-xGa shape-memory alloys[J]. Physical Review B, 2010, 82(2): 024201.

[136] Czaja P, Przewoźnik J, Gondek Ł, et al. Low temperature stability of 4O martensite in Ni49.1Mn38.9Sn12 metamagnetic Heusler alloy ribbons[J]. Journal of Magnetism and Magnetic Materials, 2017, 421: 19-24.

[137] Miyakawa T, Ito T, Xu X, et al. Martensitic transformation near room temperature and hysteresis in (Ni-Co)50-Mn-Sn metamagnetic shape memory alloys[J]. Journal of Alloys and Compounds, 2022, 913: 165136.

[138] Wójcik A, Maziarz W, Szczerba M J, et al. Influence of Fe addition on the

martensitic transformation, structure and magnetic properties of metamagnetic Ni-Co-Mn-Sn alloys[J]. Acta Physica Polonica A, 2016, 130(4): 1026-1028.

[139] Lázpita P, Sasmaz M, Cesari E, et al. Martensitic transformation and magnetic field induced effects in Ni42Co8Mn39Sn11 metamagnetic shape memory alloy[J]. Acta Materialia, 2016, 109: 170-176.

[140] Fukushima K, Sano K, Kanomata T, et al. Phase diagram of Fe-substituted Ni-Mn-Sn shape memory alloys[J]. Scripta Materialia, 2009, 61(8): 813-816.

[141] Zhang Y, Bai J, Guo K, et al. An alloying strategy for tuning magnetism, thermal hysteresis, and mechanical properties in Ni-Mn-Sn-based Heusler alloys[J]. Journal of Alloys and Compounds, 2024, 979: 173593.

[142] Jiang C, Wang J, Li P, et al. Search for transformation from paramagnetic martensite to ferromagnetic austenite: NiMnGaCu alloys[J]. Applied Physics Letters, 2009, 95(1): 012501.

[143] Seiner H, Zelený M, Sedlák P, et al. Experimental observations versus first‐principles calculations for Ni-Mn-Ga ferromagnetic shape memory alloys: A review[J]. physica status solidi (RRL)-Rapid Research Letters, 2022, 16(6): 2100632.

[144] Pugh S F. Relations between the elastic moduli and the plastic properties of polycrystalline pure metals[J]. The London, Edinburgh, and Dublin Philosophical Magazine and Journal of Science, 2009, 45(367): 823-843.

[145] Schroers J, Johnson W L. Ductile Bulk Metallic Glass[J]. Physical Review Letters, 2004, 93(25): 255506.

[146] Ozdemir Kart S, Cagın T. Elastic properties of Ni2MnGa from first-

principles calculations[J]. Journal of Alloys and Compounds, 2010, 508(1): 177-183.

[147] Zheng H, Wang W, Yu J, et al. Martensitic transformation in melt-spun Heusler Ni-Mn-Sn-Co ribbons[J]. Journal of Materials Research, 2014, 29(7): 880-886.

[148] Zheng H, Wang W, Xue S, et al. Composition-dependent crystal structure and martensitic transformation in Heusler Ni-Mn-Sn alloys[J]. Acta Materialia, 2013, 61(12): 4648-4656.

[149] Zhang H, Qian M, Zhang X, et al. Martensite transformation and magnetic properties of Fe-doped Ni-Mn-Sn alloys with dual phases[J]. Journal of Alloys and Compounds, 2016, 689: 481-488.

[150] Tan C, Tai Z, Zhang K, et al. Simultaneous enhancement of magnetic and mechanical properties in Ni-Mn-Sn alloy by Fe doping[J]. Scientific Reports, 2017, 7(1): 43877.

[151] Wang J, Bai J, Liu D, et al. Understanding the magneto-structural coupling of Ni50Mn35.4In14.6 alloy from first-principles calculations[J]. Journal of Magnetism and Magnetic Materials, 2019, 488: 165339.

[152] Wang J, Bai J, Gu J, et al. Investigation of martensitic transformation behavior in Ni-Mn-In Heusler alloy from a first-principles study[J]. Journal of Materials Science & Technology, 2020, 58: 100-106.

[153] Huang L, Cong D Y, Ma L, et al. Large reversible magnetocaloric effect in a Ni-Co-Mn-In magnetic shape memory alloy[J]. Applied Physics Letters, 2016, 108(3): 032405.

[154] Qu Y H, Cong D Y, Chen Z, et al. Large and reversible inverse magnetocaloric effect in Ni48.1Co2.9Mn35.0In14.0 metamagnetic shape

memory microwire[J]. Applied Physics Letters, 2017, 111(19): 192412.

[155] Kustov S, Corró M L, Pons J, et al. Entropy change and effect of magnetic field on martensitic transformation in a metamagnetic Ni-Co-Mn-In shape memory alloy[J]. Applied Physics Letters, 2009, 94(19): 191901.

[156] Ito W, Imano Y, Kainuma R, et al. Martensitic and magnetic transformation behaviors in Heusler-type NiMnIn and NiCoMnIn metamagnetic shape memory alloys[J]. Metallurgical and Materials Transactions A, 2007, 38(4): 759-766.

[157] Recarte V, Pérez-Landazábal J I, Sánchez-Alarcos V, et al. Entropy change linked to the martensitic transformation in metamagnetic shape memory alloys[J]. Acta Materialia, 2012, 60(6-7): 3168-3175.

[158] Banerjee B K. On a generalised approach to first and second order magnetic transitions[J]. Physics Letters, 1964, 12(1): 16-17.

[159] Cugini F, Porcari G, Fabbrici S, et al. Influence of the transition width on the magnetocaloric effect across the magnetostructural transition of Heusler alloys[J]. Philos Trans A Math Phys Eng Sci, 2016, 374(2074): 1-15.

[160] Zhang Y, Zhang L, Zheng Q, et al. Enhanced magnetic refrigeration properties in Mn-rich Ni-Mn-Sn ribbons by optimal annealing[J]. Sci Rep, 2015, 5: 11010.

[161] Huang C, Wang Y, Tang Z, et al. Influence of atomic ordering on elastocaloric and magnetocaloric effects of a Ni-Cu-Mn-Ga ferromagnetic shape memory alloy[J]. Journal of Alloys and Compounds, 2015, 630: 244-249.

[162] Stadler S, Khan M, Mitchell J, et al. Magnetocaloric properties of Ni2Mn1-xCuxGa[J]. Applied Physics Letters, 2006, 88(19): 192511.

[163] Ortín J, Planes A. Thermodynamic analysis of thermal measurements in thermoelastic martensitic transformations[J]. Acta Metallurgica, 1988, 36(8): 1873-1889.

[164] Ortín J, Planes A. Thermodynamics of thermoelastic martensitic transformations[J]. Acta Metallurgica, 1989, 37(5): 1433-1441.

[165] Nespoli A, Passaretti F, Stortiero F, et al. Temperature-modulated differential scanning calorimetry for the study of reversing and nonreversing heat flow of shape memory alloys[J]. Journal of Thermal Analysis and Calorimetry, 2014, 116(2): 771-777.

[166] Antoni Planes E O, Alfons Gonzàlez-Comas, and Lluís Mañosa. Premartensitic transition driven by magnetoelastic interaction in bcc ferromagnetic Ni2MnGa[J]. PHYSICAL REVIEW LETTERS, 1997, 79(20): 3926-3929.

[167] Cong D Y, Huang L, Hardy V, et al. Low-field-actuated giant magnetocaloric effect and excellent mechanical properties in a NiMn-based multiferroic alloy[J]. Acta Materialia, 2018, 146: 142-151.

[168] Tong H C, Wayman C M. Characteristic temperatures and other properties of thermoelastic martensites[J]. Acta Metallurgica, 1974, 22(7): 887-896.

[169] Rama Rao N V, Manivel Raja M, Esakki Muthu S, et al. Pressure-magnetic field induced phase transformation in Ni46Mn41In13 Heusler alloy[J]. Journal of Applied Physics, 2014, 116(22): 223904.

[170] Wurm A, Schick C. Reversing and nonreversing contributions to polymer melting[J]. Colloid and Polymer Science, 2003, 281(2): 113-122.

[171] Hou H, Simsek E, Stasak D, et al. Elastocaloric cooling of additive manufactured shape memory alloys with large latent heat[J]. Journal of

Physics D: Applied Physics, 2017, 50(40): 404001.

[172] Esakki Muthu S, Rama Rao N V, Sridhara Rao D V, et al. Effect of Ni/Mn concentration on exchange bias properties in bulk Ni50-xMn37+xSn13 Heusler alloys[J]. Journal of Applied Physics, 2011, 110(2): 023904.

[173] Jing C, Yang Y J, Li Z, et al. Tuning martensitic transformation and large magnetoresistance in Ni50-xCuxMn38Sn12 Heusler alloys[J]. Journal of Applied Physics, 2013, 113(17): 173902.

[174] Ma J, Karaman I, Noebe R D. High temperature shape memory alloys[J]. International Materials Reviews, 2013, 55(5): 257-315.

[175] Hamilton R F, Sehitoglu H, Efstathiou C, et al. Pseudoelasticity in Co-Ni-Al single and polycrystals[J]. Acta Materialia, 2006, 54(3): 587-599.

[176] Snodgrass R, Erickson D. A multistage elastocaloric refrigerator and heat pump with 28 K temperature span[J]. Scientific Reports, 2019, 9(1): 18532.

[177] Yan J L, Li Z Z, Chen X, et al. Martensitic transition and magnetocaloric properties in Ni45Mn44-xFexSn11 alloys[J]. Journal of Alloys and Compounds, 2010, 506(2): 516-519.

[178] Caron L, Ou Z Q, Nguyen T T, et al. On the determination of the magnetic entropy change in materials with first-order transitions[J]. Journal of Magnetism and Magnetic Materials, 2009, 321(21): 3559-3566.

[179] Arrott A. Criterion for Ferromagnetism from Observations of Magnetic Isotherms[J]. Physical Review, 1957, 108(6): 1394-1396.

[180] Hughes R A, Britten J F, Dube P A, et al. Magnetocaloric effect in Ni-Mn-Ga thin films under concurrent magnetostructural and Curie transitions[J]. Journal of Applied Physics, 2011, 110(1): 013910.

[181] Zhang X, Zhang H, Qian M, et al. Enhanced magnetocaloric effect in Ni-

Mn-Sn-Co alloys with two successive magnetostructural transformations[J]. Sci Rep, 2018, 8(1): 8235.

[182] Şaşıoğlu E, Sandratskii L M, Bruno P. First-principles calculation of the intersublattice exchange interactions and Curie temperatures of the full Heusler alloys Ni2MnX (X=Ga,In,Sn,Sb)[J]. Physical Review B, 2004, 70(2): 024427.

[183] Guo Z, Pan L, Rafique M Y, et al. Metamagnetic phase transformation and magnetocaloric effect in quinary Ni45Co5Mn40InxSn10-x heusler alloy[J]. Journal of Alloys and Compounds, 2013, 577: 174-178.

[184] Tegus O, Brück E, Buschow K H J, et al. Transition-metal-based magnetic refrigerants for room-temperature applications[J]. Nature, 2002, 415(6868): 150-152.

[185] Gschneidner K A, Pecharsky V K. Magnetocaloric materials[J]. Annu Rev Mater Sci, 2000, 30: 387-429.

[186] Pecharsky V K, Gschneidner K A. Heat capacity near first order phase transitions and the magnetocaloric effect: An analysis of the errors, and a case study of Gd5(Si2Ge2) and Dy[J]. Journal of Applied Physics, 1999, 86(11): 6315-6321.

[187] Balli M, Fruchart D, Gignoux D, et al. The “colossal” magnetocaloric effect in Mn1-xFexAs: What are we really measuring?[J]. Applied Physics Letters, 2009, 95(7): 072509.

[188] Liu G J, Sun J R, Shen J, et al. Determination of the entropy changes in the compounds with a first-order magnetic transition[J]. Applied Physics Letters, 2007, 90(3): 032507.

[189] Shamberger P J, Ohuchi F S. Hysteresis of the martensitic phase transition

in magnetocaloric-effect Ni-Mn-Sn alloys[J]. Physical Review B, 2009, 79(14): 144407.

[190] Xu K, Li Z, Zhang Y, et al. An indirect approach based on Clausius-Clapeyron equation to determine entropy change for the first-order magnetocaloric materials[J]. Physics Letters A, 2015, 379(47-48): 3149-3154.

[191] Wójcik A, Maziarz W, Szczerba M J, et al. Transformation behavior and inverse caloric effects in magnetic shape memory Ni44-xCuxCo6Mn39Sn11 ribbons[J]. Journal of Alloys and Compounds, 2017, 721: 172-181.

[192] Ghosh S, Ghosh A, Mandal K. Reversible magnetocaloric effect and critical exponent analysis in Mn-Fe-Ni-Sn Heusler alloys[J]. Journal of Alloys and Compounds, 2018, 746: 200-205.

[193] Czaja P, Chulist R, Żywczak A, et al. The effect of a multiphase microstructure on the inverse magnetocaloric effect in Ni-Mn-Cr-Sn metamagnetic Heusler alloys[J]. Magnetochemistry, 2017, 3(3): 24.

[194] Planes A, Stern-Taulats E, Castán T, et al. Caloric and multicaloric effects in shape memory alloys[J]. Materials Today: Proceedings, 2015, 2: S477-S484.

[195] Ossmer H, Chluba C, Gueltig M, et al. Local Evolution of the Elastocaloric Effect in TiNi-Based Films[J]. Shape Memory and Superelasticity, 2015, 1(2): 142-152.

[196] Tobushi H, Shimeno Y, Hachisuka T, et al. Influence of strain rate on superelastic properties of TiNi shape memory alloy[J]. Mechanics of Materials, 1998, 30(2): 141-150.

[197] Ossmer H, Lambrecht F, Gültig M, et al. Evolution of temperature profiles in TiNi films for elastocaloric cooling[J]. Acta Materialia, 2014, 81: 9-20.

[198] Li Z, Li Z, Yang J, et al. Large elastocaloric effect in a polycrystalline Ni45.7Co4.2Mn37.3Sb12.8 alloy with low transformation strain[J]. Scripta Materialia, 2019, 162: 486-491.

[199] Tušek J, Engelbrecht K, Mikkelsen L P, et al. Elastocaloric effect of Ni-Ti wire for application in a cooling device[J]. Journal of Applied Physics, 2015, 117(12): 124901.

[200] Pérez-Sierra A M, Bruno N M, Pons J, et al. Atomic order and martensitic transformation entropy change in Ni-Co-Mn-In metamagnetic shape memory alloys[J]. Scripta Materialia, 2016, 110: 61-64.

[201] Albertini F, Kamarád J, Arnold Z, et al. Pressure effects on the magnetocaloric properties of Ni-rich and Mn-rich Ni2MnGa alloys[J]. Journal of Magnetism and Magnetic Materials, 2007, 316(2): 364-367.

[202] Mandal K, Pal D, Scheerbaum N, et al. Effect of pressure on the magnetocaloric properties of nickel-rich Ni-Mn-Ga Heusler alloys[J]. Journal of Applied Physics, 2009, 105(7): 073509.

[203] Yang Y, Li Z, Sánchez-Valdés C F, et al. Phase transformation and magnetocaloric effect of Co-doped Mn-Ni-In melt-spun ribbons[J]. Journal of Applied Physics, 2020, 128(5): 055110.

[204] Wang L, Li Z, Yang J, et al. Large refrigeration capacity in a Ni48Co1Mn37In14 polycrystalline alloy with low thermal hysteresis[J]. Intermetallics, 2020, 125: 106888.

[205] Qu Y H, Cong D Y, Sun X M, et al. Giant and reversible room-temperature magnetocaloric effect in Ti-doped Ni-Co-Mn-Sn magnetic shape memory

alloys[J]. Acta Materialia, 2017, 134: 236-248.

[206] Feng W J, Du J, Li B, et al. Large low-field inverse magnetocaloric effect in Ni50-xMn38+xSb12 alloys[J]. Journal of Physics D: Applied Physics, 2009, 42(12): 125003.

[207] Chernenko V A, Barandiarán J M, Rodriguez Fernández J, et al. Magnetic and magnetocaloric properties of martensitic Ni2Mn1.4Sn0.6 Heusler alloy[J]. Journal of Magnetism and Magnetic Materials, 2012, 324(21): 3519-3523.

[208] Singh S, Caron L, D'Souza S W, et al. Large magnetization and reversible magnetocaloric effect at the second-order magnetic transition in Heusler materials[J]. Adv Mater, 2016, 28(17): 3321-3325.

[209] Hu Y, Li Z, Yang B, et al. Combined caloric effects in a multiferroic Ni–Mn–Ga alloy with broad refrigeration temperature region[J]. APL Materials, 2017, 5(4): 046103.

[210] Huang Y J, Hu Q D, Bruno N M, et al. Giant elastocaloric effect in directionally solidified Ni–Mn–In magnetic shape memory alloy[J]. Scripta Materialia, 2015, 105: 42-45.

[211] Shen A, Sun W, Zhao D, et al. Influence of Cr on microstructure and elastocaloric effect in Ni–Mn–In–Co–Cr polycrystalline alloys[J]. Physics Letters A, 2018, 382(39): 2876-2879.

[212] Wei L, Zhang X, Gan W, et al. Hot extrusion approach to enhance the cyclic stability of elastocaloric effect in polycrystalline Ni-Mn-Ga alloys[J]. Scripta Materialia, 2019, 168: 28-32.

[213] Qian M F, Zhang X X, Witherspoon C, et al. Superelasticity and shape memory effects in polycrystalline Ni-Mn-Ga microwires[J]. Journal of

Alloys and Compounds, 2013, 577: S296-S299.

[214] Ström-Olsen J O, Rudkowska G, Rudkowski P, et al. Fine metallic and ceramic fibers by melt extraction[J]. Materials Science and Engineering: A, 1994, 179: 158-162.

[215] Hamilton R F, Sehitoglu H, Chumlyakov Y, et al. Stress dependence of the hysteresis in single crystal NiTi alloys[J]. Acta Materialia, 2004, 52(11): 3383-3402.

[216] Wu D, Xue S, Frenzel J, et al. Atomic ordering effect in Ni50Mn37Sn13 magnetocaloric ribbons[J]. Materials Science and Engineering: A, 2012, 534: 568-572.

[217] Liu J, Woodcock T G, Scheerbaum N, et al. Influence of annealing on magnetic field-induced structural transformation and magnetocaloric effect in Ni-Mn-In-Co ribbons[J]. Acta Materialia, 2009, 57(16): 4911-4920.

[218] Planes A, Manosa L, Vives E, et al. Neutron diffraction study of long-range atomic order in Cu-Zn-Al shape memory alloys[J]. Journal of Physics: Condensed Matter, 1992, 4(2): 553-559.

[219] Álvarez-Alonso P, Aguilar-Ortiz C O, Camarillo J P, et al. Adiabatic magnetocaloric effect in Ni50Mn35In15 ribbons[J]. Applied Physics Letters, 2016, 109(21): 212402.

[220] Gottschall T, Skokov K P, Benke D, et al. Contradictory role of the magnetic contribution in inverse magnetocaloric Heusler materials[J]. Physical Review B, 2016, 93(18): 184431.

[221] Li Z, Zhang Y L, Xu K, et al. Large magnetocaloric effect related to martensitic transformation in Ni50Co2Mn33In15 textured alloy[J]. Physica B: Condensed Matter, 2015, 476: 179-182.

[222] Ghosh A, Mandal K. Effect of Fe substitution on the magnetic and magnetocaloric properties of Mn-rich Mn-Ni-Fe-Sn off-stoichiometric Heusler alloys[J]. Journal of Applied Physics, 2015, 117(9): 093909.

[223] Nikitin S A, Skokov K P, Koshkid'ko Y S, et al. Giant rotating magnetocaloric effect in the region of spin-reorientation transition in the NdCo(5) single crystal[J]. Phys Rev Lett, 2010, 105(13): 137205.

[224] Hu Q, Zhou Z, Yang L, et al. On the driving forces of magnetically induced martensitic transformation in directionally solidified polycrystalline Ni-Mn-In meta-magnetic shape memory alloy with structural anisotropy[J]. Metallurgical and Materials Transactions A, 2017, 48(11): 5480-5491.

[225] Bourgault D, Tillier J, Courtois P, et al. Large inverse magnetocaloric effect in Ni45Co5Mn37.5In12.5 single crystal above 300 K[J]. Applied Physics Letters, 2010, 96(13): 132501.